

Durham E-Theses

Frequency-Resolved Photoelectron Spectroscopy of Nucleobase-Water Anion Clusters

CLARKE, CONNOR,JACK

How to cite:

CLARKE, CONNOR,JACK (2024) *Frequency-Resolved Photoelectron Spectroscopy of Nucleobase-Water Anion Clusters*, Durham theses, Durham University. Available at Durham E-Theses Online: <http://etheses.dur.ac.uk/15879/>

Use policy

The full-text may be used and/or reproduced, and given to third parties in any format or medium, without prior permission or charge, for personal research or study, educational, or not-for-profit purposes provided that:

- a full bibliographic reference is made to the original source
- a [link](#) is made to the metadata record in Durham E-Theses
- the full-text is not changed in any way

The full-text must not be sold in any format or medium without the formal permission of the copyright holders.

Please consult the [full Durham E-Theses policy](#) for further details.

Frequency-Resolved Photoelectron Spectroscopy of Nucleobase-Water Anion Clusters



Connor J. Clarke

2024

Department of Chemistry

Durham University

Submitted for qualification of *Doctor of Philosophy*

Table of Contents

List of Abbreviations.....	5
Declarations	6
Acknowledgements.....	7
Abstract.....	8
Chapter 1 – Introduction.....	9
1.1. Photoelectron Spectroscopy to study Anion Resonances	9
1.1.1. Photoelectron Imaging	10
1.1.2. Anion Resonances and their Dynamics.....	14
1.1.3. Frequency-Resolved Photoelectron Spectroscopy.....	20
1.1.4. Time-Resolved Photoelectron Spectroscopy	32
1.2. Non-valence States, Anion Clusters, and their Insight into DNA Damage	36
1.2.1. Identifying Non-valence States.....	37
1.2.2. Importance of Non-valence States	39
1.2.3. Photoelectron Spectroscopy of Anion-Water Clusters.....	40
1.2.4. Low-Energy Electron Attachment to DNA.....	42
Chapter 2 – Experimental	46
2.1. Laser Systems	47
2.1.1. Tuneable Nanosecond Pulses	47
2.1.2. New Nd:YAG Laser.....	50
2.1.3. Femtosecond Laser	50
2.2. The Cluster Instrument	54
2.2.1. The Even-Lavie Valve Source.....	54
2.2.2. Mass Spectrometry.....	56
2.2.3. Velocity Map Imaging.....	59
2.2.4. Reconstruction Algorithms	63
2.2.5. Ion Noise Reduction	68
2.3. The Electrospray Instrument.....	71
2.3.1. The ESI Source	71
2.3.2. Remaining Instrument and Recent Alterations	72
2.4. The Role of Electronic Structure Calculations	74
2.4.1. Solving the Schrödinger equation.....	74
2.4.2. Density Functional Theory	76
2.4.3. Basis Sets	77

2.4.4. Anion Resonances	78
Chapter 3 – Photodissociation of the Pyruvate Anion	81
3.1. Introduction	82
3.2. Methodology	84
3.2.1. Experimental	84
3.2.2. Computational	85
3.3. Photoelectron Spectroscopy of Pyruvate	89
3.3.1. Detachment and Excitation	89
3.3.2. A Mysterious Fragment	93
3.3.3. Photon Flux Dependence of the Methide Anion Peak	98
3.3.4. Time-resolved Photoelectron Spectroscopy	101
3.4. Closing Remarks	105
Chapter 4 – Determining the Valence Electron Affinity of Uracil	109
4.1. Introduction	110
4.2. Methodology	113
4.2.1. Experimental	113
4.2.2. Calibration	113
4.2.3. Computational	115
4.3. Uracil-Argon Cluster Anions	116
4.3.1. Photoelectron Spectra	116
4.3.2. Determination of the Valence Electron Affinity of Uracil	119
4.3.3. Large Anion Clusters	122
4.4. Effect of Changing Solvent	124
4.4.1. Uracil-Nitrogen Cluster Anions	124
4.4.2. Caveats of using Strongly Interacting Solvents	126
4.5. Competition with Autodetachment	130
4.6. Closing Remarks	133
Chapter 5 – Tracking Resonances of Hydrated Nucleobase Anions	135
5.1. Introduction	136
5.2. Methodology	138
5.2.1. Experimental	138
5.2.2. Computational	138
5.3. Identification of Anion Resonance States	140
5.3.1. FRPES of $U^-(H_2O)_2$	140
5.3.2. Ratio of Thermionic Emission to Direct Detachment	143

5.3.3. Kinetic Energy Shifts Arising from Autodetachment	145
5.3.4. Changes in Photoelectron Angular Distributions.....	146
5.4. Effect of Hydration	148
5.4.1. FRPES of $U^-(H_2O)_n$	148
5.4.2. Extrapolation of Resonance Energies	151
5.4.3. Electron Attachment to Aqueous Uracil	155
5.4.4. Decomposition of the Reorganisation Energy	158
5.5. Other Nucleobase-Water Clusters	160
5.5.1. Thymine-Water Anion Clusters	160
5.5.2. Adenine-Water Anion Clusters.....	165
5.6. Closing Remarks.....	174
Chapter 6 – Solvent-Mediated Formation of a Hydrated Electron from a Contact Pair	177
6.1. Introduction.....	178
6.2. Methodology	180
6.2.1. Experimental	180
6.2.2. Computational.....	180
6.3. The Non-Valence States of $U(H_2O)_n^-$	183
6.3.1. Characterising $U(H_2O)_1^-$	183
6.3.2. Non-valence States of Larger Cluster Anions, $U(H_2O)_n^-$	188
6.3.3. From Contact Pair to Hydrated Electron	195
6.4. Closing Remarks.....	199
Chapter 7 – Conclusion	201
References.....	203

List of Abbreviations

2DPAD	Two-dimensional photoelectron angular distribution
2DPES	Two-dimensional photoelectron spectrum/spectra
ADE	Adiabatic detachment energy
CTTS	Charge-transfer-to-solvent
DBS	Dipole-bound state
DCO	Discretised continuum orbital
eBE	Electron binding energy
eKE	Electron kinetic energy
FCF	Franck-Condon factor
FRPES	Frequency-resolved photoelectron spectroscopy
FWHM	Full-width-at-half-maximum
HOMO	Highest occupied molecular orbital
IVR	Intramolecular vibrational redistribution
MCP	Microchannel plate
ME	Maximum entropy
MO	Molecular orbital
NEA	Nuclear ensemble approach
OPA/OPO	Optical parametric amplifier/oscillator
PAD	Photoelectron angular distribution
RCB	Repulsive Coulomb barrier
TOF	Time-of-flight
TRPES	Time-resolved photoelectron spectroscopy
VAD	Vibrational autodetachment
VAE	Vertical attachment energy
VDE	Vertical detachment energy
VMI	Velocity map imaging

Declarations

The work outlined below was performed by the author, unless otherwise indicated. This thesis has not been previously submitted for any degree.

Copyright Notice

The copyright of this thesis rests with the author. No quotation from it should be published without the author's prior written consent and information derived from it should be acknowledged.

Acknowledgements

My deepest gratitude goes to my supervisor for the past four years, Jan Verlet. Your passion for science is obvious to anybody you meet, and has been deeply inspiring. Very few PhD students are fortunate enough to work for such an enthusiastic researcher and exceptional person.

Thank you to the past and current members of the Verlet group. In particular:

Caleb for introducing me to the laser lab;

Aude for helping me become a gas-phase chemist;

Cate for tolerating my endless questions about calculations;

Jemma for figuring out the lab with me;

And Michi for avidly taking the reins.

Equally important throughout my degree was my support system. My best mates, Dom and Ben, who are there for me to do dumb stuff with. My Dad, whose takes on football are only marginally better than his takes on science. And my Mum, for endlessly being there with love and advice in stressful moments.

Finally, I have profound appreciation and adoration for my partner, Kristine. You have made this journey tremendously easier with your loving support, and unimaginably more enjoyable with your company. Thank you.

Abstract

Frequency-resolved photoelectron spectroscopy enables anion resonance states to be accessed and probed. In the first instance, we applied this technique to the atmospherically abundant pyruvate anion, which was observed to exhibit ultrafast dissociation upon photoexcitation with UV light. Our focus then shifted to study the anion resonance states of nucleobases, which are postulated to play a crucial role in low-energy electron attachment to DNA, inducing strand breakages and mutagenesis. Clusters of the uracil anion, U^- , with weakly solvating molecules (Ar and N_2) were investigated, shedding light on how the anion resonance states can be incrementally stabilised with respect to the neutral species, and offering the most accurate determination of the valence electron affinity of U to date. Uracil-water cluster anions, $U^-(H_2O)_{n=1-35}$ were studied, yielding n -dependent electron binding energies and resonance photoexcitation energies that were extrapolated to the bulk aqueous limit. We showed that each of the three lowest-lying π^* resonances of $U^-_{(aq)}$ become bound states, but with accountment for the anion-to-neutral reorganisation energy (within a linear response model), the upper two remain accessible via low-energy electron attachment to $U_{(aq)}$. The thymine nucleobase exhibited similar behaviour. Altogether, our results connect the known anion resonance energies of the isolated nucleobases with a condensed-phase picture that is better representative of the native DNA environment, offering insight into which anion resonances may participate in the electron-induced DNA damage mechanism. Finally, we studied kinetically trapped non-valence states of $U^-(H_2O)_n$, bearing resemblance to water cluster anions, $(H_2O)_n^-$. Multiple isomers were observed with different electron binding energies, and the structures thereof were assigned with the aid of computations. The non-valence electron was found to shift further from the U molecule with increasing hydration, analogous to a diffusion-controlled dissociation process of a molecule-electron contact pair into a hydrated electron.

Chapter 1 – Introduction

1.1. Photoelectron Spectroscopy to study Anion Resonances

Negatively charged ions (anions) are ubiquitous throughout nature, but are more commonly observed in condensed-phase environments. This is because the excess charge is stabilised by the surroundings, such that the anion is stable with respect to electron loss. In the gas phase, where such stabilisation is absent, fewer molecules are capable of forming stable anions. Despite this, isolated anions remain a blooming subject of study.^{1,2} Modern ion sources (e.g. electrospray ionisation) access an abundance of molecules that form stable anions,³ and this number is further increased in molecular clusters, where microsolvation can render an excess electron bound.^{4,5} For an anion, the ‘boundedness’ of the excess electron to the molecule is quantified through its electron affinity, which in the context of photoelectron spectroscopy (as studied in this thesis) can be defined by the adiabatic detachment energy:

$$\text{ADE} = E_n - E_a, \quad (1.1)$$

where E_a and E_n represent the ground-state electronic energies of the anion and the neutral species, respectively. A bound anion is thus characterised by a positive ADE, which is typically quite small (< 3 eV).

Anion photoelectron spectroscopy has long been the experimental tool of choice in the determination of ADE.⁶ In anion photoelectron spectroscopy, an electron is removed from an anion upon absorption of a photon with known energy $h\nu > \text{ADE}$. The outgoing kinetic energy of the electron, eKE, is measured, and therefore the initial binding energy of the electron to the molecule can be determined. Information on the electronic and nuclear (vibrational) structure of an anion can be attained through the measurement of the photoelectron spectrum, and additional insight can be gleaned from the photoelectron angular distributions. Moreover,

photoelectron spectroscopy offers a unique pathway to probe excited states of anions, which are often unbound with respect to electron loss (due to the low associated ADEs). These studies typically come in two flavours: frequency- or time-resolved photoelectron spectroscopy, which provide complimentary information on the excited states and their dynamics.

1.1.1. Photoelectron Imaging

A simple schematic describing anion photoelectron spectroscopy is shown in Figure 1.1. Electrons (e^-) are detached from the sample of anions using a laser pulse with photon energy $h\nu$. The electrons leave with a distribution of eKEs, determined by the transition energies between individual electronic and vibrational states. A transition is more likely when there is better overlap between the participating vibrational wavefunctions, as quantified by the Franck-Condon factors (FCFs). The ADE is determined by the energy of the 0–0 transition, which does not necessarily have the largest FCF. The most probable transition (that leads to the maximum signal in the photoelectron spectrum) defines another useful property: the vertical detachment energy (VDE). A large disparity between the measured ADE and VDE is representative of a large difference in the relaxed geometries of the anion and neutral states (i.e. a more significant horizontal offset in the potential energy surfaces shown in Figure 1.1). As long as the equilibrium geometries are not too dissimilar, the vibrational structure of the neutral molecule may be observed in the photoelectron spectrum, directly providing energetic information relating to the active vibrational modes.

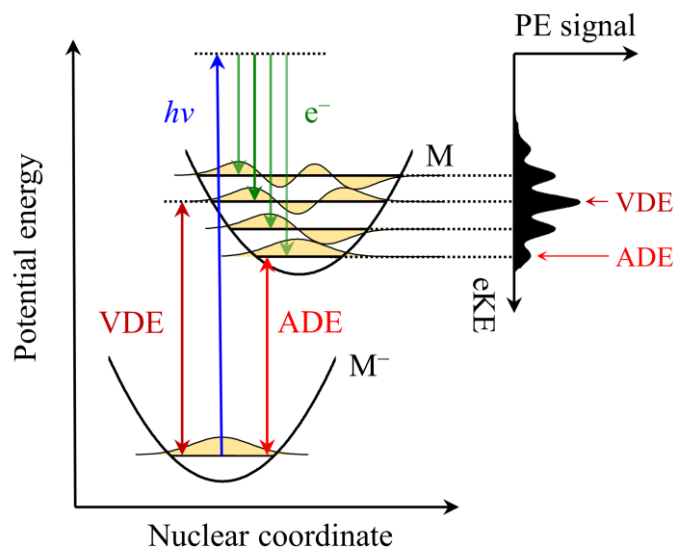


Figure 1.1: Schematic of photoelectron spectroscopy of an anion M^- , where an electron (e^-) is detached from M^- using a photon with energy $h\nu$. The outgoing electron kinetic energies (eKE) are determined from the anion-to-neutral transitions. The measured photoelectron (PE) signal is greatest at $eKE = h\nu - VDE$, due to maximal overlap of the participating vibrational wavefunctions (yellow). The ADE can be extracted from the 0-0 transition.

The advent of ion imaging allowed for efficient acquisition of angular information in gas-phase ion spectroscopy.^{7,8} In photoelectron spectroscopy, velocity map imaging (VMI) is now commonly applied to measure the directionality of the full 3D distribution of detached photoelectrons, whilst preserving information on the initial electron kinetic energies.^{8,9} In general, electrons are preferentially detached either along or perpendicular to a fixed light polarisation vector, giving rise to a distinct photoelectron angular distribution (PAD).¹⁰ As will be discussed, the PAD is determined from the electronic structure of the molecular orbital (MO) from which removal takes place, providing direct insight into the electronic character of the anion.

It is most informative to first consider the PADs arising from photodetachment of an atomic anion, which produces ‘well-behaved’ photoelectron partial waves (i.e. described by spherical harmonic functions). The partial waves can be labelled: s-wave, p-wave, d-wave, and

so on, denoting the associated angular momentum (with increasing quantum number l). Photodetachment from an s atomic orbital ($l = 0$), such as in the H^- anion, produces a pure p-wave photoelectron ($l = 1$), since the electron gains one quantum of angular momentum from the incident photon ($\Delta l = +1$). Photodetachment from a p atomic orbital, such as in the I^- anion, produces a combination of s- and d-waves, since the conservation of angular momentum permits $\Delta l = \pm 1$. From these two examples, it is already clear that different PADs are expected to arise from different atomic orbitals, lending credence to the idea that the initial electronic structure may be inferred from the PAD.

We now consider the experimental measurement and quantification of the PAD, in the context of a one-photon detachment process using linearly polarised light. In this case, the PAD is cylindrically symmetric about the fixed light polarisation vector $\boldsymbol{\varepsilon}$, and can therefore be described by a single ejection angle. This leads to the following expression for the PAD:¹¹

$$I(\theta) = \frac{\sigma}{4\pi} (1 + \beta_2 P_2(\cos(\theta))), \quad (1.2)$$

where θ is the angle the electron leaves with respect to $\boldsymbol{\varepsilon}$, and σ represents the photodetachment cross-section. The functionality of the PAD is dictated by P_2 , the second order Legendre polynomial, which acts as a $\cos^2(\theta)$ function. The coefficient thereof, β_2 , is simply referred to as the anisotropy parameter, and this encapsulates the degree of anisotropy in the PAD. The anisotropy parameter is limited in the values it can take: $-1 \leq \beta_2 \leq +2$. A distribution which is predominantly parallel to $\boldsymbol{\varepsilon}$ is quantified by a positive β_2 , whereas a predominantly perpendicular distribution has a negative β_2 . For an isotropic distribution, $\beta_2 = 0$.

Returning to our earlier examples, in the photodetachment of H^- , a pure p-wave photoelectron is produced along the direction of light polarisation, corresponding with the maximal value of $\beta_2 = +2$. The photodetachment of I^- requires more consideration. Interference between the outgoing s- and d-waves results in photoelectron emission which is primarily

oriented perpendicular to $\mathbf{\epsilon}$. At the maximum level of interference, this corresponds with the minimal value of $\beta_2 = -1$.¹² However, the photodetachment cross-section of an anion is both energy- and l -dependent, via the Wigner threshold law:¹³

$$\sigma \propto eKE^{l+1/2} . \quad (1.3)$$

This shows that at low eKE (i.e. $h\nu$ only slightly exceeding the ADE), photoelectron partial waves with lower angular momentum are produced preferentially. Therefore, for near-threshold photodetachment from Γ^- , the PAD will appear more isotropic ($-1 < \beta_2 < 0$).¹² Conversely, d-waves dominate the s-waves at higher eKE , and β_2 can even become positive.

For polyatomic molecular anions, the MO from which the electron is detached can no longer be described by a single value of l . However, as Jordan and Burrow succinctly explain,¹⁴ a qualitative picture of the MOs can reveal the value(s) of l which are most important to the description. This is demonstrated in Figure 1.2, which shows the dominant angular momentum quantum numbers for the HOMO (highest occupied molecular orbital) of a few simple anions. Beginning with (a) O_2^- , the HOMO resembles two adjacent p orbitals separated by a node, which taken together, bear resemblance with an atomic d orbital, and so $l = 2$ is the dominant description of this MO.¹⁵ In a heteronuclear diatomic molecule such as (b) NO^- , the HOMO electron density is similar to that of O_2^- , but skewed towards one side, and therefore a combination of $l = 1$ and $l = 2$ is required to describe this MO.¹⁶ Finally, larger molecules such as (c) $C_6H_5O^-$ can also be given this treatment, but the partial components of the overall angular momentum are less clear.

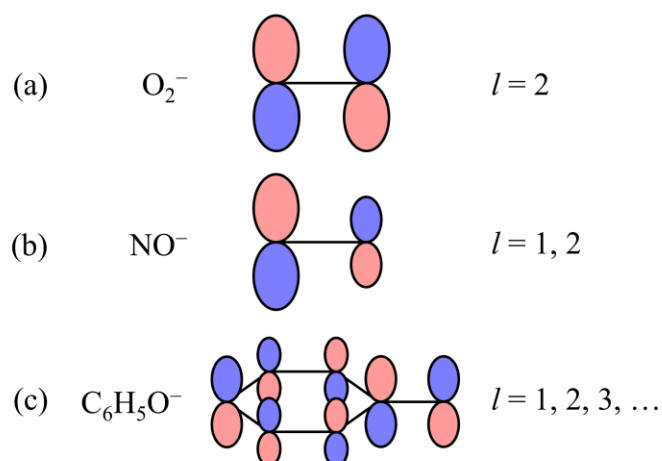


Figure 1.2: Dominant angular momentum quantum numbers l for the HOMOs of some molecular anions.

Although the PADs arising from larger molecular anions are of greater complexity, qualitative predictions can be made, particularly at low electron kinetic energies where outgoing waves with small l dominate.^{17,18} For instance, detachment from an MO of π character will typically result in a negative value of β_2 . When a more quantitative evaluation is required, (approximate) analytical models can be applied in some simple cases,^{12,18,19} or the computational state-of-the-art Dyson orbital approach can be taken.^{20–23} Notably, in much of the work included in this thesis, the characteristic anisotropic PADs arising from photodetachment of non-valence state anions (as described in Section 1.2.1) will be observed. Altogether, successful prediction of the PAD can be incredibly useful in distinguishing between (isoenergetic) electronic states, particularly in studies on molecular dynamics.^{24–27}

1.1.2. Anion Resonances and their Dynamics

Most electronically excited states of anions are unstable with respect to electron loss. Since it is possible to temporarily form this category of (unstable) anion state through resonant

electron attachment to the corresponding neutral molecule, they are referred to as anion resonance states (or more simply, resonances). Anion resonances are susceptible to spontaneous electron loss, and this process is termed autodetachment. There are two main categories of anion resonances: shape resonances and Feshbach resonances, which can be distinguished by the electronic structure of the neutral autodetachment product. Upon loss of the excess electron, a shape resonance forms the *ground-state* neutral species. Therefore, in the conventional anion-formation picture of electron attachment into an MO of a neutral molecule, it is a shape resonance that is formed. Conversely, autodetachment from a Feshbach resonance leads to an *excited* state of the neutral species. Therefore, Feshbach resonances tend to have longer autodetachment lifetimes than shape resonances (when the neutral forms in its ground state). This is summarised pictorially in Figure 1.3, where the two shape resonances undergo fast autodetachment into the ground-state neutral species, but similar autodetachment of the Feshbach resonance is less efficient.

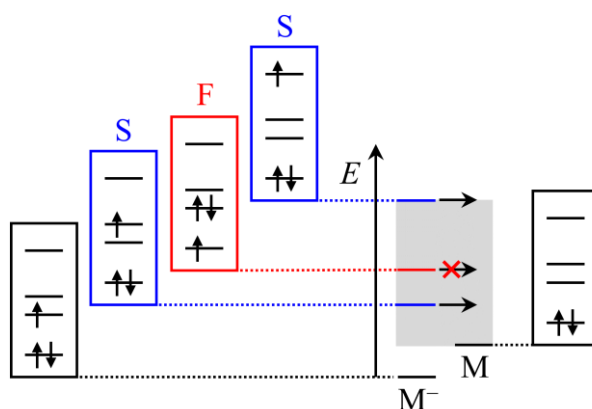


Figure 1.3: Electron configurations of shape (S; blue) and Feshbach (F; red) anion resonances. Electron loss from a shape resonance results in the electron configuration of the neutral ground state (M), and thus is generally faster than electron loss from a Feshbach resonance, which requires additional electron rearrangement to form the neutral ground state.

Autodetachment from a shape resonance is observed to occur on timescales up to picoseconds.^{28,29} The finite lifetime is due to the prevalence (and ‘shape’) of a centrifugal

barrier in the electronic energy landscape which the electron must tunnel through to escape. The barrier forms via the interplay of short-range attractive forces and long-range repulsive forces,³⁰ as shown in Figure 1.4. The short-range attraction originates from the polarisation potential common to covalent molecules, which scales with the atom-electron distance as $-r^{-4}$. The long-range repulsion experienced by the electron is due to the centrifugal potential, described by $l(l+1)/2r^2$. The height of the centrifugal barrier is therefore dependent on the angular momentum of the electron, which in turn is responsible for the l -dependence of the Wigner threshold law (see Eq. (1.3)).¹³ Owing to the finite lifetime provided by the centrifugal barrier, anion resonances often undergo a multitude of other mechanisms for decay, in competition with autodetachment.³¹

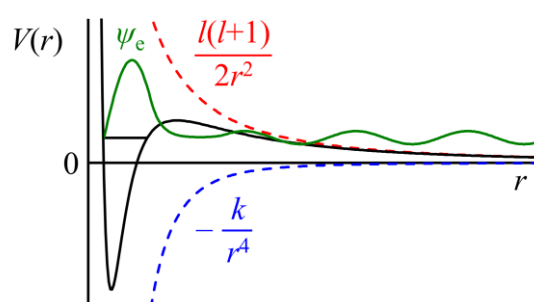


Figure 1.4: Wavefunction of an electron (ψ_e ; green) within a shape resonance, where r represents the electron-molecule distance. There are two contributions to the potential (V) which result in a barrier: the repulsive centrifugal potential (red); and the attractive polarisation potential (blue). As demonstrated, the electron is able to tunnel through the finite barrier.

Internal Conversion

An integral mechanism to photochemistry is the nonadiabatic transition from one electronic state to another, driven by changes in the molecular geometry.³² Such a transition fundamentally violates the Born-Oppenheimer approximation,³³ i.e. during a nonadiabatic transition, the motion of the nuclei is not separable from the motion of the electrons. As a matter of nomenclature, nonadiabatic transitions are termed internal conversion when the participating

electronic states have the same spin multiplicity, and are termed intersystem crossing when the spin multiplicities differ. The rate of internal conversion between two electronic states is inversely proportional to their energy gap,³⁴ and therefore the topography of the corresponding potential energy surfaces plays a crucial role in the associated state-hopping dynamics.

Anion resonance states can be generated through photoexcitation of a ground-state anion, or through electron attachment to a ground-state neutral molecule. In either case, the resonance typically forms outside of its preferred molecular geometry. That is to say, the potential energy surface of the resonance is offset with respect to the ground-state anion and the ground-state neutral, and therefore a potential gradient will initiate changes in the geometry of the molecule. An example of this is shown in Figure 1.5. The excited molecule distorts to lower the electronic energy, bringing together the surfaces of the populated resonance and a lower-lying electronic state. This intersection can take the form of an avoided crossing, or more interestingly (in the case of a polyatomic anion), a conical intersection (see Figure 1.5).³⁵ At a conical intersection, two or more electronic states are degenerate and nonadiabatically coupled, facilitating ultrafast (down to a few femtoseconds³⁶) internal conversion.^{35,37,38} Therefore, access to a conical intersection has a considerable influence on the relaxation dynamics of an anion resonance, allowing internal conversion to outcompete autodetachment. Moreover, the lowering of the electronic energy through combined geometric changes and internal conversion can render the anion resonance state vertically bound with respect to electron loss, greatly enhancing the lifetime of the anion. Such stabilisation of the anion is integral to the electron-accepting capabilities of corresponding neutral molecule, granting time for further processes to occur such as (reactive) charge-transfer, dissociation, or radiative emission.

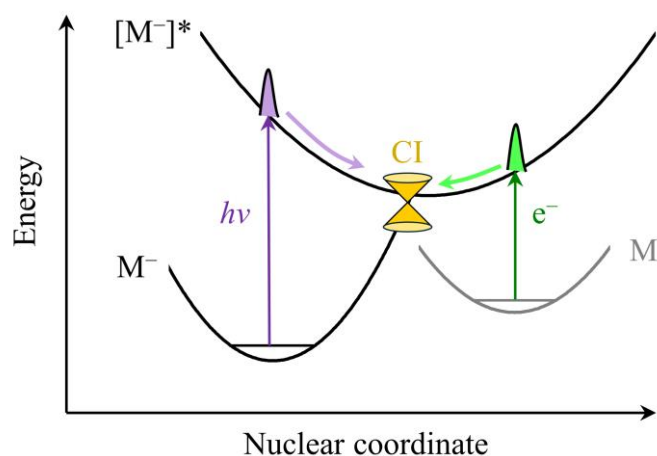


Figure 1.5: An anion resonance state $[M^-]^*$ being accessed through either photoexcitation ($h\nu$) from the anion ground state, or electron attachment to the neutral ground state. Either way, the potential gradient of the resonance prompts geometric changes. A conical intersection (CI) between the resonance and the ground-state anion facilitates ultrafast internal conversion.

Intramolecular Vibrational Energy Redistribution

Upon formation of an anion resonance state, specific vibrational modes associated with the initial perturbation are excited.³⁹ Due to anharmonic coupling between other vibrational modes, the initially localised energy is rapidly transferred to other moieties throughout the molecule,³⁹⁻⁴¹ in a process known as intramolecular vibrational energy redistribution (IVR). Some modes are more strongly coupled than others, such that the timescale for IVR is mode-specific.^{42,43} Eventual breakdown into a statistical distribution of vibrational energy amongst all modes is generally faster for larger molecules, which have more vibrational modes. IVR accompanies other resonance decay processes.

Dissociation

Driven by the topography of the resonance potential energy surface, an excited anion can stretch along a repulsive nuclear coordinate, leading to bond dissociation. This often results in fragmentation (unimolecular dissociation) of the anion, forming a smaller anion and one or more neutral fragments. Such photodissociation dynamics have implications for fundamental chemical reactivity and its controllability.⁴⁴ But even if the excited-state potential energy surface is not repulsive, fragmentation may still occur. The anion resonance population may first undergo internal conversion to the ground-state anion, where it now is able to access a repulsive region of the ground-state potential energy surface, triggering fragmentation.^{45–47} The newly generated anion will have a different ADE to the parent anion, and may therefore be stable with respect to autodetachment (especially as some internal energy is imparted into the neutral fragments). Moreover, the fragment anion should be distinguishable from the parent using photoelectron spectroscopy, allowing the dissociation dynamics of the excited parent anion to be tracked using time-resolved techniques, discussed in Section 1.1.4.

Luminescence

The excess electronic energy of an anion resonance state can also be removed radiatively, via luminescence. Through Kasha's rule,⁴⁸ luminescence predominantly transpires from the lowest excited state of the anion (for each spin multiplicity), upon trapping of the excited-state population within a minimum of the potential energy surface. Luminescence tends to occur on a longer timescale (nanosecond and higher⁴⁹) than the dynamical processes outlined above, including autodetachment. In the context of photoelectron spectroscopy experiments, luminescence is not directly observed, and its effect is often negligible.

1.1.3. Frequency-Resolved Photoelectron Spectroscopy

Before studying the dynamical behaviour of anion resonances, it is useful to first map out their energies. Electron scattering experiments are very suitable for this task, where changes in the electron-molecule scattering behaviour are observed for resonant kinetic energies of the incident electrons.^{50–53} It is also possible to deduce resonance energies starting from a stable anion state. One general technique involves scanning the wavelength of a photoexcitation laser pulse, and tracking at which wavelengths some measurable action occurs.⁵⁴ In the context of photoelectron spectroscopy, the fundamental action is the increase or decrease of total photoelectron signal as a resonance is populated. Such electronic action spectroscopy can be a very useful tool for mapping out the location of anion resonances.⁵⁵ However, by tracking only the total electron signal, electronic action spectroscopy disregards important information: the photoelectron spectrum at each wavelength. The omission is a practical one, as there is not sufficient time to accumulate the photoelectron spectra during a single wavelength scan.

Frequency-resolved photoelectron spectroscopy (FRPES) compromises by measuring a series of photoelectron spectra across a range of closely-spaced wavelengths. This approach essentially retains the information of the photoelectron action spectrum, albeit at discrete photon energies. Although FRPES is time-consuming, it has several clear benefits.⁵⁶ Autodetachment and other electron loss channels are directly observable in resonant photoelectron spectra, providing insight into the populated excited states through the measured distribution of eKEs and, in the case of photoelectron imaging, the PADs.

FRPES produces many photoelectron spectra (acquired at different photon energies), and the results are stacked in order of increasing $h\nu$. The spectra can therefore be displayed as a contour plot (with axes: eKE, $h\nu$, and photoelectron signal), known as a two-dimensional photoelectron spectrum (2DPES). An illustrative 2DPES is shown in Figure 1.6, exhibiting

several features (labelled **A–E**) that are discussed in detail below. In this example, an anion resonance is vertically accessible at $h\nu = 3.0$ eV, and features are discussed in the context of photodetachment/photoexcitation using nanosecond laser pulses.

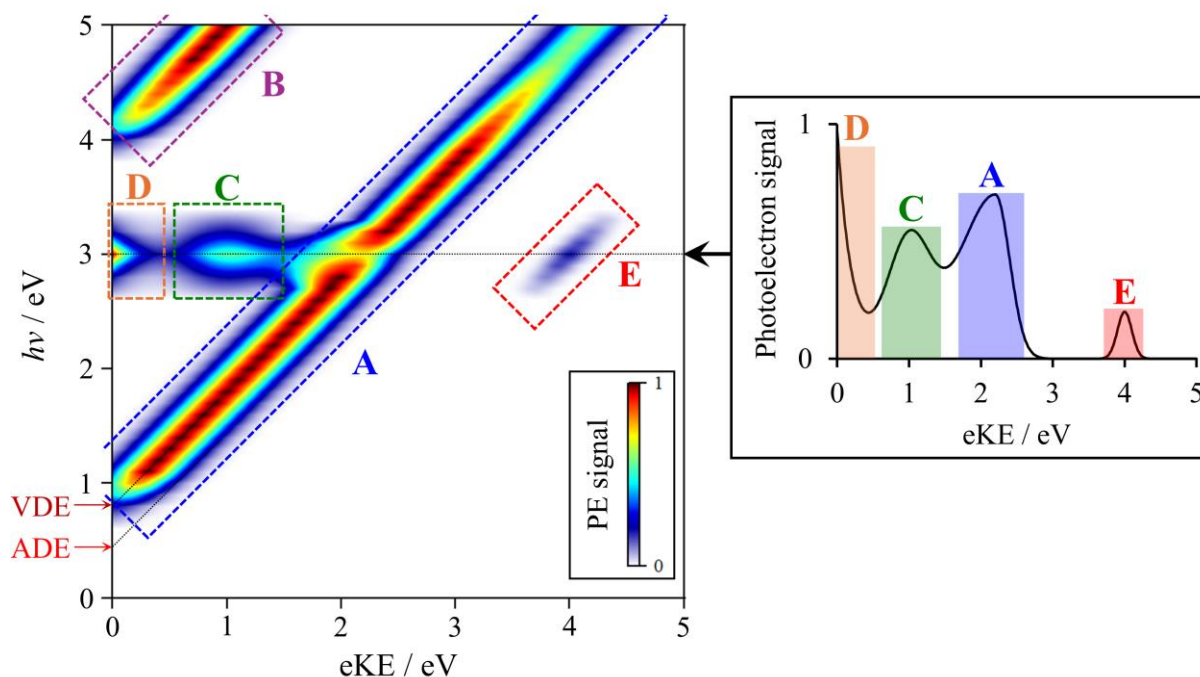


Figure 1.6: Exemplar two-dimensional photoelectron spectrum (2DPES), showing five main contributions (labelled **A–E**). Each horizontal slice of the 2DPES represents a single photoelectron spectrum acquired at the specified photon energy $h\nu$. Features **A** and **B** arise from direct photodetachment of the ground-state anion. The other features only appear in coincidence with photoexcitation around $h\nu = 3.0$ eV: features **C** and **D** arise from electrons lost through autodetachment and thermionic emission, respectively; and feature **E** is produced by direct detachment of a photofragment. The photoelectron spectrum at the central photoexcitation wavelength is shown on the right, with each present feature highlighted.

Direct Photodetachment

Direct electron detachment from an anion takes place at photon energies above the ADE and results in a spectral feature with maximum intensity around $eKE = h\nu - VDE$. Therefore, with increasing $h\nu$, the direct photodetachment feature shifts to higher eKE at an equal rate, and so appears as a diagonal signal (**A**) in the 2DPES. Figure 1.6 demonstrates how the ADE

and VDE of the anion may be easily extracted from the vertical intercept ($eKE = 0$) of the diagonal feature. Of course, the ADE and VDE can also be extracted from the individual photoelectron spectra. At higher photon energies, additional diagonal features (**B**) can appear, produced by direct photodetachment to an electronically-excited neutral state (Figure 1.7). The relative photoelectron signal between these features reflects their ($h\nu$ -dependent) relative photodetachment cross-sections, which are largely determined by Koopmans' correlations (i.e. a preference for electron loss from the anion, depending on the similarity between the underlying electronic structure of the anion and neutral species). As the photon energy becomes resonant with an excited state ($h\nu = 3.0$ eV), depletion and broadening of the direct detachment feature can occur: the signal can deplete due to competition between photoexcitation and direct photodetachment; and broadening towards lower eKE is observed due to fast autodetachment processes (discussed below), as well as changes in the FCFs associated with detachment from the different electronic state.

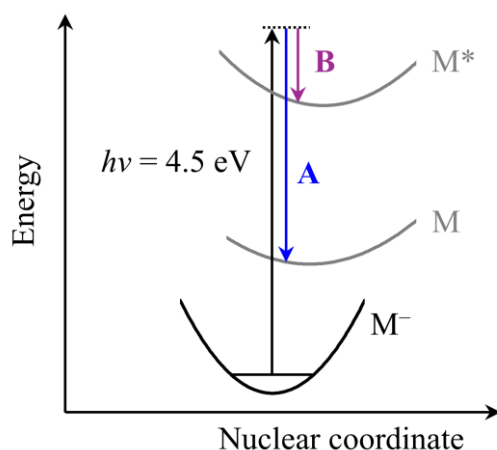


Figure 1.7: Direct photodetachment of an anion M^- to produce the corresponding neutral in either its ground state (M) or an excited state (M^*), giving rise to features **A** (blue) and **B** (purple) in the 2DPES, respectively.

Autodetachment

Upon photoexcitation to a resonance state, the anion is unstable with respect to electron loss. Nuclear motion acts to stabilise the new state of the anion, reducing the energy gap between the anion and neutral potential energy surfaces (Figure 1.8). Therefore, autodetached electrons are lost with less eKE than the directly detached electrons described above. If the excited-state population relaxes into a minimum on the resonance potential energy surface (following IVR), autodetachment can appear as a distinct new feature (C) in the photoelectron spectrum, reflecting the corresponding energy gap between the anion resonance and neutral state. Since this gap is fixed, the central eKE of an autodetachment feature is often unresponsive to increases in the photon energy, and thus autodetached electrons do not appear as a diagonal feature in the 2DPES.

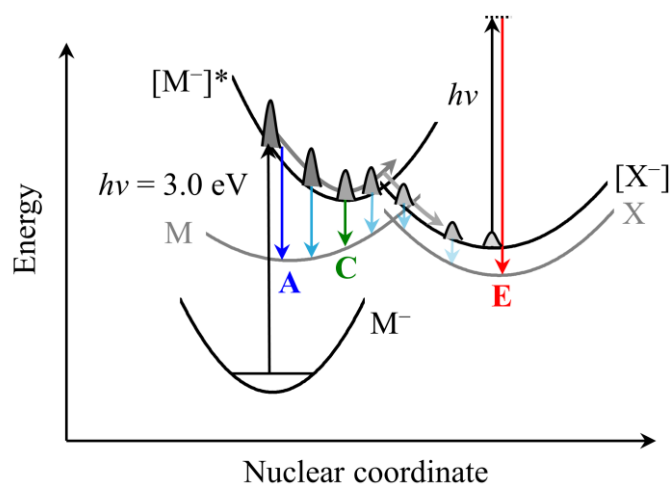


Figure 1.8: Photoexcitation of an anion M^- , generating $[M^-]^*$ which undergoes autodetachment (cyan and green arrows). Where the excited-state population becomes trapped in the minimum of the potential energy surface, autodetachment is more prominent and produces feature C (green) in the 2DPES. The fragmentation (dissociation) pathway to form a new anionic species X^- is also shown, where a second photon may be absorbed, producing the photofragment feature E (red) in the 2DPES.

Autodetachment also occurs at intermediate nuclear geometries (i.e. before the excited-state population is able to settle into a minimum), generating photoelectron signal that

spans the eKE range between features C and A. This can be considered ‘fast’ autodetachment, occurring on the timescale of initial nuclear motion. Of course, the resonance population does not necessarily need to become trapped in a minimum of the potential energy surface, and may instead continue along a repulsive nuclear coordinate or undergo nonadiabatic transition to a lower electronic state. The latter pathway can also lead to autodetachment from the newly populated lower state, which may be distinguishable in the photoelectron spectrum through differences in the eKE distribution and PADs. Nuclear rearrangement can also cause the resonance state to become vertically bound with respect to electron loss, greatly increasing the lifetime of the anion with respect to electron loss, and suppressing autodetachment.

Thermionic Emission

Bulk metals emit electrons when sufficiently heated, and correspondingly, thermally-excited metal clusters have been shown to lose electrons through thermionic emission.^{57–59} The same is true of hot molecular anions (and clusters thereof), with thermionic emission being a common phenomenon in anion spectroscopic studies involving photoexcitation,^{60–66} particularly when high laser powers are invoked.⁶⁷ A Jablonski diagram of the basic mechanism is shown in Figure 1.9. The anion is first photoexcited to a higher electronic state, then undergoes relaxation to the ground state of the anion (e.g. through internal conversion), producing a (vibrationally) hot ground-state anion with internal energy exceeding its ADE, from which the excess electron is lost.⁶⁸ Owing to the statistical manner of electron loss, thermionic emission typically occurs on timescales upwards of microseconds,⁶⁹ although the exact lifetime depends on properties of the anion such as the electron binding energy and nuclear degrees of freedom.⁶⁸ Thermionic emission is considered to be a ground-state process,

as generally there is plentiful time for electronic and nuclear (i.e. IVR) relaxation prior to electron loss.

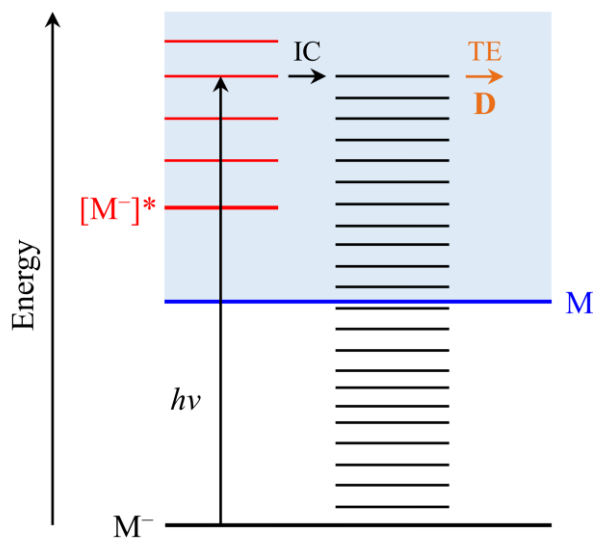


Figure 1.9: Illustrative Jablonski diagram for thermionic emission. Photoexcitation ($h\nu$) to an anion resonance $[M^-]^*$ leads to internal conversion (IC) back to the ground-state anion M^- , which undergoes statistical thermionic emission (TE) of electrons, generating the characteristic low-energy feature **D** in the 2DPES.

Thermionic emission is governed by Boltzmann (thermal) statistics, and as such, the kinetic energy distribution ρ of the measured electrons can be modelled as:

$$\rho(eKE) = A \cdot \exp(-eKE/k_B T^*), \quad (1.3)$$

where k_B is the Boltzmann constant, A is a system-dependent pre-exponential factor, and T^* is the effective temperature of anion. Although this model neglects the dependence of A on the eKE ,^{70–72} it does capture the dominant behaviour observed in anion photoelectron spectra.⁵⁷ Overall, thermionically emitted electrons produce identifiable photoelectron signals that mostly follow an exponential distribution (Figure 1.6; **D**) and are isotropic ($\beta_2 = 0$ in the PAD).

Photoinduced thermionic emission only takes place if the imparted energy exceeds the ADE of the anion. Therefore, bound excited states of an anion (accessed with $h\nu < ADE$) do

not produce thermal electrons following absorption of a single photon. However, activation (or enhancement) of the thermionic emission pathway can be instilled by increasing the excitation laser flux, permitting absorption of multiple sequential photons. Using nanosecond (or longer) pulses, the mechanism is described as ‘photon cycling’. A first photon photoexcites the anion, which then relaxes into a vibrationally hot ground state, completing the first cycle. Assuming that reformation of the ground state occurs within the duration of the laser pulse, the anion is susceptible to absorption of a second photon, beginning another cycle. This process can repeat until the anion has sufficient energy for thermionic emission, allowing bound excited states of the anion to also be located through thermionic emission.

From the signature (exponential and isotropic) traits of the thermionic emission feature (**D**), it is fairly straightforward to distinguish thermionically emitted electrons from other low-eKE electrons in photoelectron spectra. For instance, detachment of low-energy electrons can also take place through vibrational autodetachment (VAD).^{73,74} In VAD, electron loss is facilitated by specific (excited) vibrational modes. Therefore, the eKE distribution of vibrationally-autodetached electrons tends to be highly structured, corresponding with energetic properties of the participating (anionic and neutral) vibrational modes. The question of whether an anion will undergo VAD or thermionic emission is interesting and has recently been explored in the context of nitroalkane molecules, where it was shown that only the smallest nitroalkane (CH_3NO_2) exhibited VAD instead of thermionic emission.⁷⁵ Nonetheless, the observation of electrons lost through either VAD or thermionic emission can equally be used to deduce the presence of an excited anion resonance, but only the observation of thermionic emission implies also reformation of a ground-state anion.

Photofragmentation

Photodissociation, or photofragmentation, is an accessible decay pathway for many excited anions. Assuming the electron is not lost during the dissociation (as in dissociative photodetachment⁷⁶), then a new anionic product is formed. In a nanosecond FRPES experiment, the photoproduct anion may be detached by a second photon within the same photoexcitation laser pulse, assuming the dissociation dynamics are sufficiently fast. The result is a new diagonal direct detachment feature (**E**) in the 2DPES (Figure 1.6), appearing when $h\nu$ is resonant with the excited state. Fragment anions often have smaller (or even negative) electron binding energies than the parent anion due to their smaller size. As shown in the example in Figure 1.8, this results in the direct detachment feature being located at higher eKEs than detachment from the parent anion. As the mechanism for dissociation-detachment necessitates the absorption of (at least) two photons, the associated photoelectron signal may be weaker compared to the remaining photoelectron spectrum. Fortunately, the photofragment detachment peak tends to be well-separated from other features in the spectrum, allowing even weak signals to be discernible.

In addition to generally being located at higher eKE, photofragment detachment features may be recognised through other spectral properties, such as their PADs and any exhibited vibrational structure. This allows for identification of the fragment anion, giving insight into the dissociation mechanism of the initially populated anion resonance (or bound excited state). However, it should be noted that fragmentation may only be observed across specific ranges of $h\nu$, even if the same resonance is being populated across a broader range. For example, if the resonance is accessed with very little vibrational excitation (i.e. on the lower limit of the photoexcitation energy), the generated anion resonance may not have sufficient internal energy to overcome an energy barrier for dissociation, and the feature will not be observed.

Photoelectron Angular Distributions

PADs offer a unique perspective into the electronic structure of the initial state being photodetached, and can therefore be very useful in the identification of anion resonances. In much the same way that the FRPES photoelectron signal can be represented in a two-dimensional contour plot (2DPES), the anisotropy parameters β_2 (measured at each $h\nu$) can be formatted similarly. The corresponding two-dimensional photoelectron angular distribution (2DPAD) is shown in Figure 1.10, where the anisotropies are only displayed in regions of significant photoelectron signal.

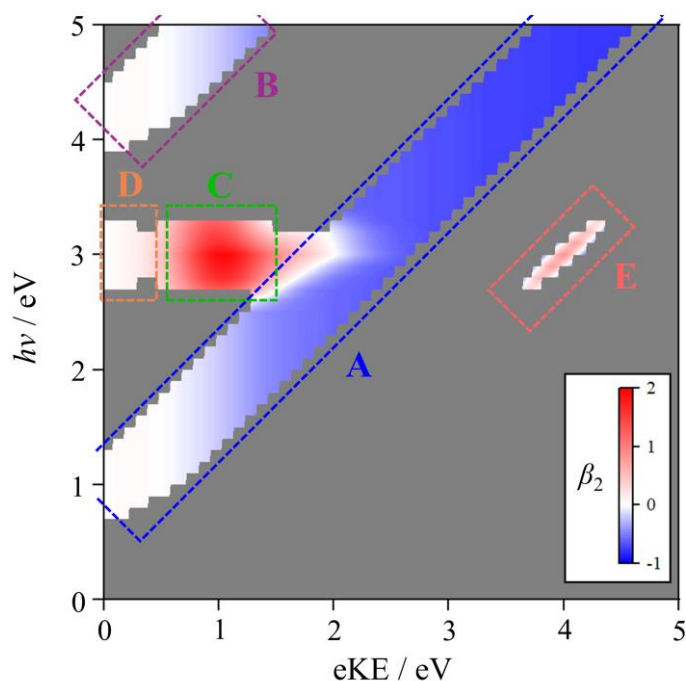


Figure 1.10: Two-dimensional photoelectron angular distribution (2DPAD), measured for the same exemplar system that produced the 2DPES in Figure 1.6. The PAD is quantified by the anisotropy parameter β_2 , which has limiting values -1 and $+2$. The anisotropy parameter is only shown in regions where there is significant photoelectron signal – other areas are greyed out.

Electrons arising from autodetachment (**C**) are expected to be expelled with different PADs than those arising from direct detachment of the anion ground state (**A**), since the detached electronic state is different in each case. Similarly, if the resonance population relaxes into a lower-lying electronic state, autodetachment from the new state can also produce a unique PAD. Of course, the same is true of detachment from a photofragment (**E**), and in general, the measured PADs can sensitively probe the electronic structure of the populated resonance states, as well as the starting anion. However, there is no guarantee that the PADs of different features will significantly differ, particularly if the electronic states share similar electronic character.¹⁰

The PADs of direct photodetachment features (e.g. **A**, **B**, and **E**) are expected to change gradually with increasing eKE (or equivalently, $h\nu$), as the emission of and interference between photoelectron partial waves changes smoothly with eKE. For instance, feature **A** in Figure 1.10 becomes more negative with increasing eKE. However, as $h\nu$ approaches the resonance excitation energy, electrons stemming from (fast) autodetachment also contribute to alter the PAD of the direct detachment feature. This effect is highlighted in Figure 1.11, which shows β_2 at the central eKE of feature **A**. The PAD changes smoothly and predictably until the resonance is populated, where there is a distinct shift towards a less negative β_2 . In general, sudden changes in the anisotropy are indicative of photoexcitation to a resonance. This can be particularly important when the autodetachment feature is isoenergetic with the direct detachment feature, such that the 2DPAD reveals changes that are indiscernible in the 2DPES.

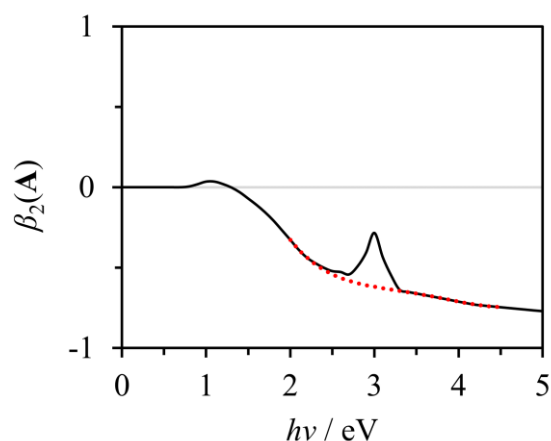


Figure 1.11: PAD of the direct detachment feature **A** (black curve). The red dotted curve represents the anisotropy that would be expected in absence of photoexcitation.

Multiply Charged Anions

As a final note on FRPES, it is interesting to consider the unique behaviour of multiply charged anions, which are dianions in the simplest case. Few molecular anions preferentially bind a second electron (i.e. few anions have a positive electron affinity) due to the inherent Coulombic repulsion between the two negative charges. However, a vast array of *metastable* dianions, with lifetimes upwards of milliseconds, have been observed and studied in the gas phase.⁷⁷⁻⁸¹ The origin of this enhanced kinetic stability is the repulsive Coulomb barrier (RCB), which inhibits electron loss.^{82,83} The RCB forms through the interplay of two opposing interactions: the long-range Coulomb repulsion between the (singly charged) anion and the additional electron; and the short-range attractive forces (e.g. polarisation) which seek to bind the extra electron. The repulsive contribution is demonstrated pictorially in Figure 1.12(a). There are clear similarities to the temporary stability of shape resonances described above (see Figure 1.4), but in the case of dianions, the Coulombic contribution is far stronger than the centrifugal potential. As such, RCB heights are typically on the order of several eV, causing metastable dianions to be very long lived.

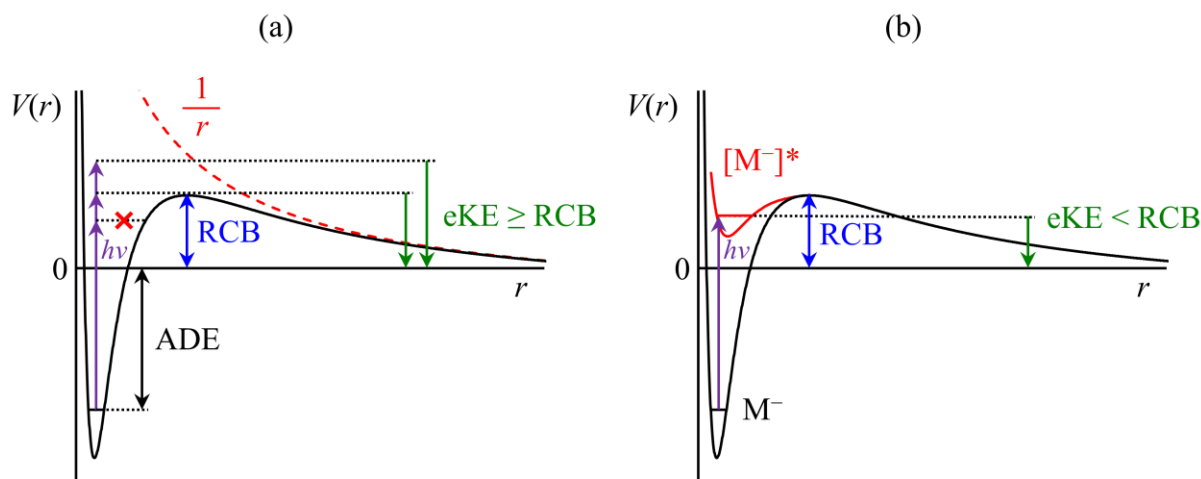


Figure 1.12: Schematics of FRPES on a dianion possessing a repulsive Coulomb barrier (RCB). (a) Directly detached photoelectrons are only measured when the photon energy $h\nu \geq \text{ADE} + \text{RCB}$. The Coulombic repulsion potential is shown as a red dashed line to highlight its importance to RCB formation. (b) Upon photoexcitation to an anion resonance $[\text{M}^-]^*$, an electron may have sufficient time to tunnel through the RCB (even if $h\nu < \text{ADE} + \text{RCB}$), producing a lower-energy photoelectron signal.

The RCB has constraining implications for photodetachment from a dianion. In order to be fully liberated from the dianion, the detached electron must have sufficient kinetic energy to overcome the RCB, as well as the electron affinity of the anion. Therefore in FRPES, direct detachment will only be observed once the photon energy exceeds the sum of the ADE and the RCB, as suggested in Figure 1.12(a). This leads to the sudden emergence of a direct detachment feature at $e\text{KE} \approx \text{RCB}$, once the threshold photon energy is reached. Hence, FRPES can be applied to measure RCB heights, which can give insight into the geometric charge separation in the dianion.⁷⁷ However, the height of the RCB also depends on the direction of electron emission, and thus a single dianion possesses a range of RCBs. For instance, if the electron propagates towards the other electron in the dianion, it will experience a greater Coulombic repulsion and therefore the RCB is larger in this direction. Consequently, the PADs (from an aligned sample) can provide further information into the three-dimensional nature of the RCB, and in turn, the electronic (and nuclear) structure of the initial dianion.⁸⁴

Photoexcitation to resonances of the dianion also produces quite unique features in FRPES, due to the RCB. As mentioned, an electron will not be photodetached from a dianion unless $h\nu \geq \text{ADE} + \text{RCB}$. However, if an anion resonance is populated at a lower photon energy than this, autodetachment may still take place. This counterintuitive process results from electron tunnelling,⁸⁵⁻⁸⁷ a schematic for which is shown in Figure 1.12(b). Following photoexcitation to the anion resonance state, the excited-state population may persist on a long enough timescale for an electron to tunnel through the RCB. Electron tunnelling is particularly enhanced when either the excited-state population reaches a minimum well on the potential energy surface, or the anion resonance energy is close to the crest of the RCB. In the 2DPES, electron tunnelling autodetachment manifests as a feature similar to C; the signal is fixed in eKE with increasing $h\nu$, and may appear in absence of the direct detachment feature (at lower $h\nu$). Conversely, thermionic emission is not observed from dianions, as the low-energy electrons are unable to overcome (or tunnel through) the RCB. Therefore, the observation of thermionic emission following photoexcitation of a dianion originates from a singly-charged species, which could either form through an initial electron loss (e.g. via autodetachment), or through fragmentation of the molecule.

1.1.4. Time-Resolved Photoelectron Spectroscopy

The development of ultrashort laser pulses enabled time-resolved photoelectron spectroscopy (TRPES) on the femtosecond timescale of nuclear motion,⁸⁸⁻⁹¹ affording a direct and unique perspective into the dynamical behaviour of electronically excited states. TRPES follows a pump-probe scheme, where a first ‘pump’ laser pulse ($h\nu_{\text{pump}}$) is used to generate an excited population in the sample, and then after a variable time delay Δt , a second ‘probe’ laser pulse ($h\nu_{\text{probe}}$) provokes photodetachment that is measured spectroscopically. Photoelectrons

arising from the probed excited state constitute the ‘pump-probe signal’, which is the primary action for monitoring the excited-state dynamics. Photoelectron spectra are acquired at a range of different Δt , allowing the excited state to be probed at different stages of its evolution (i.e. following the relaxation mechanisms described in the Section 1.1.2). Therefore, the excited-state dynamics are directly reflected in changes of the eKE distribution and PADs of the pump-probe signal, as outlined in the examples below.

We first consider TRPES in the context of photoexcitation to a bound excited state (with respect to electron loss). In the illustrative example shown in Figure 1.13(a), $h\nu_{\text{pump}}$ and $h\nu_{\text{probe}}$ are below the ADE of the molecule, so there is no (single-photon) photoelectron signal arising from either the pump or the probe pulse alone. Photoexcitation using a femtosecond laser pulse prepares a coherent superposition of vibrational states,⁹² i.e. a vibrational wavepacket, in the electronically excited state, $[M^-]^*$. Immediate probing of the wavepacket ($\Delta t \approx 0$) generates a pump-probe signal at high electron kinetic energy (Figure 1.13(b)). Later probing ($\Delta t > 0$) permits the wavepacket to first evolve on the excited state, typically increasing the energy gap between $[M^-]^*$ and the neutral ground state, and thereby reducing the measured eKE of the pump-probe signal. Probing at even later delays ($\Delta t \gg 0$) provides sufficient time for a transition to lower-lying electronic states, resulting in pump-probe signal with substantially different eKEs and PADs. Monitoring the photoelectron image with changing Δt thus reveals insight into the characteristic timescales for such relaxation processes. A multitude of other dynamical processes may also be tracked with TRPES, such as oscillatory wavepacket motion observed through periodically changing eKEs,⁹³ light-driven charge-transfer reactions,^{94,95} and photoinduced fragmentation processes.⁹⁶

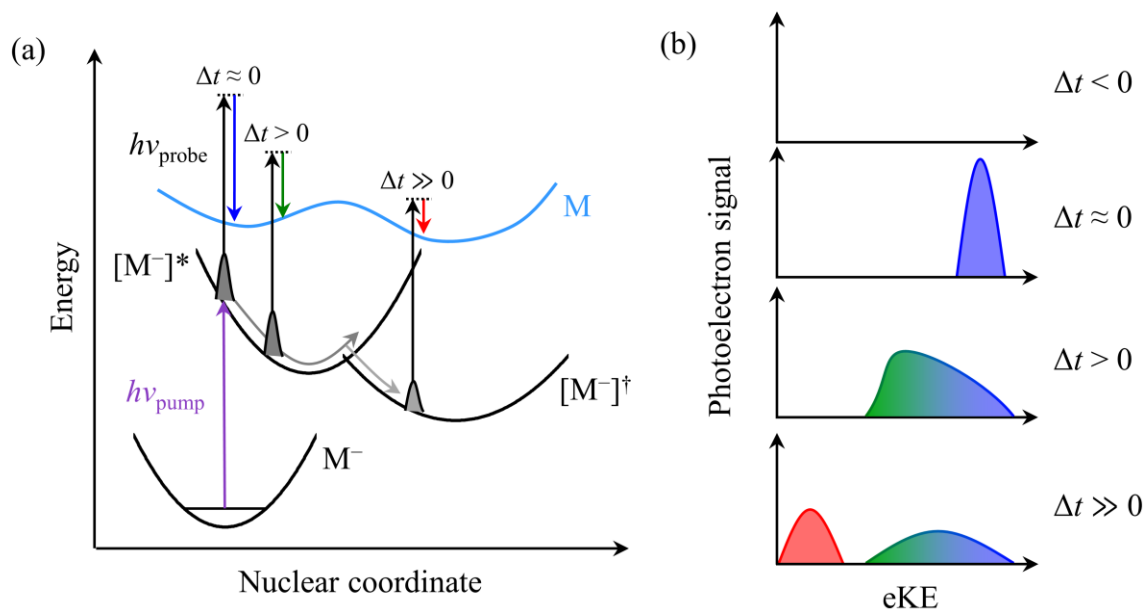


Figure 1.13: (a) Example of TRPES probing bound excited state dynamics. Photoexcitation using $h\nu_{\text{pump}}$ populates an excited state $[M^-]^*$, which eventually undergoes relaxation into a lower-lying excited state $[M^-]^\dagger$. Along the nuclear relaxation coordinate, the excited state population can be photodetached with $h\nu_{\text{probe}}$. (b) Evolution of the photoelectron spectrum with changing time delay Δt . Colours roughly correspond to the different detachment mechanisms shown in the left panel (a).

TRPES can also probe the dynamics of anion resonances (Figure 1.14(a)),²⁹ where a similar pump-probe signal can be obtained and tracked with changing Δt . Since the anion resonance state is unstable with respect to electron loss, the excited state can also decay through electron autodetachment, leading to a faster decay of the pump-probe signal. However, as autodetached electrons are also measured in the photoelectron spectrum (e.g. see Section 1.1.3), the timescales of autodetachment can be disentangled from competing relaxation dynamics. For instance, the autodetachment signal in Figure 1.14(b) exhibits an initial depletion at $\Delta t = 0$, but then a resurgence at $\Delta t > 0$ that is representative of the autodetachment lifetime. At longer times, nuclear motion may make the resonance state (or a lower-lying state that has been populated) vertically bound with respect to electron loss, such that autodetachment is no longer an accessible pathway. Time- and frequency-resolved photoelectron spectroscopy are complimentary: TRPES benefits greatly from the comprehensive understanding of resonance

energies that can be supplied through FRPES, and in turn, TRPES provides crucial information on the resonance relaxation dynamics that may only be indirectly observed in FRPES.

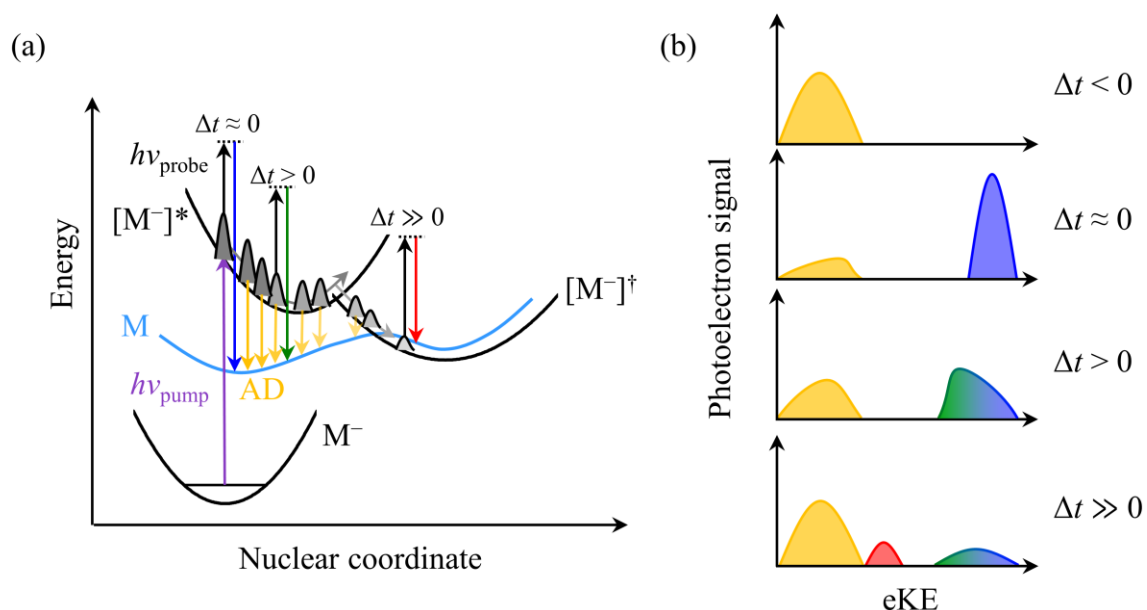


Figure 1.14: (a) Example of TRPES probing unbound (resonance) excited state dynamics. Photoexcitation using $h\nu_{\text{pump}}$ populates an excited state $[M^-]^*$, which eventually undergoes relaxation into a lower-lying excited state $[M^-]^\dagger$. Along the nuclear relaxation coordinate, the excited state population can be photodetached with $h\nu_{\text{probe}}$, and autodetachment (AD) occurs where the population is not vertically bound. (b) Evolution of the photoelectron spectrum with changing time delay Δt . Colours roughly correspond to the different detachment mechanisms shown in the left panel (a).

1.2. Non-valence States, Anion Clusters, and their Insight into DNA Damage

So far, the discussion of anions and their resonance states has been centred around the formation of traditional valence states, i.e. states described by electron occupancy of MOs within the covalent network of the molecule. However, molecules and their anions can also form more exotic electronic states: *non-valence* states. Neutral species possess an infinite number of non-valence states in the form of excited Rydberg states,⁹⁷ where an electron is distantly bound by its long-range Coulombic attraction to the cationic molecular core, akin to a hydrogenic species. Rydberg state energies converge to the ionisation threshold, and as such, the occupying electron is very weakly bound.

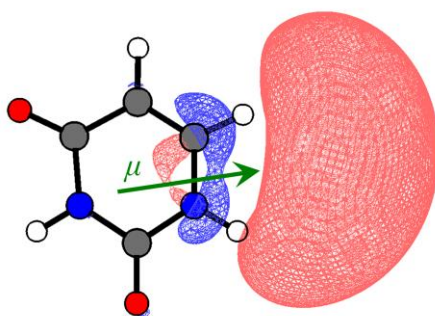


Figure 1.15: Computed isosurface (0.015) of electron density for the dipole-bound anion of the uracil nucleobase. The green arrow shows the orientation of the dipole moment μ of the neutral uracil core.

In a non-valence anion, the excess electron is also located in a diffuse orbital, distant from the covalent electronic structure of the molecule. However, the molecular core of a non-valence anion is neutral instead of positive, and thus the electron binding must be governed by weaker non-Coulombic interactions. The next longest-range interaction is between the excess electron and the dipole of the molecular core, decaying as r^{-2} , where r represents the charge-molecule separation distance. If the molecular core of the anion possesses a sufficiently strong dipole moment (typically >2.5 D),⁹⁸ the excess electron can be weakly bound towards the positive end of the molecule (see Figure 1.15) in a diffuse dipole-bound state (DBS).⁹⁹

However, a dipole is not mandatory for non-valence anion formation: quadrupole-bound states (scaling as r^{-3}) have been measured for a growing number of anions,^{100–104} and shorter-range electron correlation interactions (r^{-4} or shorter) can compound to produce a correlation-bound state.^{105–108} In many non-valence anions, it is a combination of these different interactions that dictate the electron binding.^{109,110} This is particularly interesting in anion clusters, where the geometry of the cluster steers which interactions permit non-valence electron binding.¹¹¹

1.2.1. Identifying Non-valence States

Non-valence anions can be formed through electron attachment to a neutral molecule, or through photoexcitation from a stable valence-bound anion. But how can one experimentally distinguish between a conventional valence anion and a diffuse non-valence anion, and moreover, measure the non-valence electron binding energy? The earliest observations of a DBS performed Rydberg electron transfer to dipolar CH_3CN .^{112,113} Non-valence anion formation is enhanced only at specific Rydberg quantum numbers (unlike for valence anion formation), which can be directly correlated with the electron binding energy of the non-valence state.¹¹⁴ As expected from the diffuse electronic structure of non-valence states, the associated binding energies are very small, such that non-valence anions are also distinguishable from valence states by their increased susceptibility to strong electric field-induced detachment.¹¹⁴ However, the clearest and most informative studies on non-valence anions typically utilise anion photoelectron spectroscopy.

Photodetachment from a non-valence state gives rise to a very characteristic photoelectron signal, as highlighted in Figure 1.16. There are three main identifiable attributes: (i) the measured eKE is only slightly lower than the detaching photon energy; (ii) the spectral linewidth tends to be very narrow; and (iii) the outgoing electron is imaged to be distinctly anisotropic. For the example of a DBS, these are explained as followed. The high eKE (i)

observed is due to the weak binding energy of the DBS electron (E_{DBS}). The two are related through $e\text{KE} = h\nu - E_{\text{DBS}}$, and thus it is straightforward to extract DBS binding energies from anion photoelectron spectroscopy. The narrow linewidth (ii) arises from the similarity of the DBS and neutral potential energy surfaces. Since the DBS electron resides far away from the neutral molecular core, it has a limited effect on the nuclear structure of the molecule. Therefore, the potential energy surface of a DBS is approximately parallel to the potential energy surface of the neutral species (at least near the minimum), with the two separated in energy by E_{DBS} . In turn, FCFs are greatest between unchanging vibrational levels (e.g. the 0-0 transition, or any other ν - ν transition), producing a very narrow photoelectron signal. Finally, the characteristic anisotropy (iii) of the DBS feature is determined from its unusual electronic structure. The very diffuse, isotropic DBS orbital (assuming it is the ground state) is akin to an atomic s orbital, described by $l = 0$. As earlier discussed, detachment from an s orbital produces a photoelectron partial p-wave, giving rise to a maximally anisotropic PAD: $\beta_2 \approx +2$, sketched in Figure 1.16(b). Very few valence states produce such a distinctly anisotropic PAD, and the three combined attributes outlined above enable effortless identification of photodetachment from non-valence states.

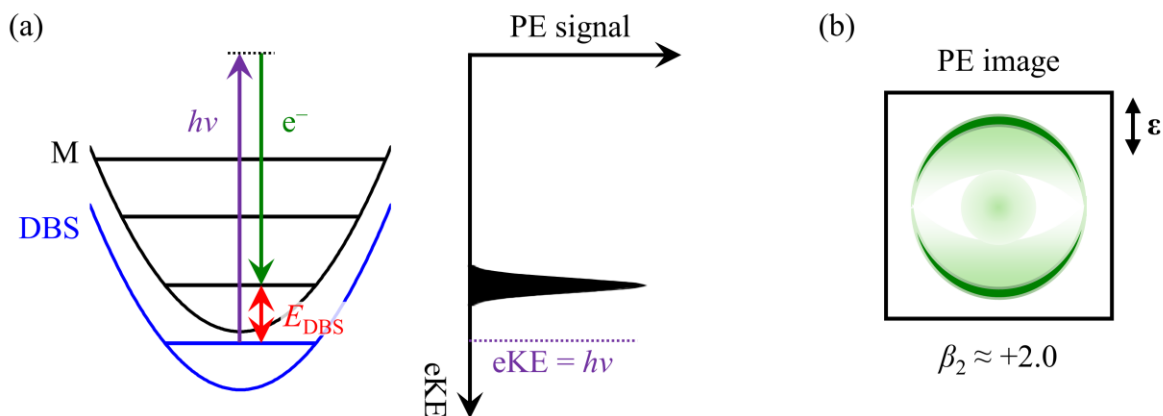


Figure 1.16: (a) Sketch of potential energy surfaces for a DBS and its neutral analog, M. The surfaces are approximately parallel near the minima, separated by E_{DBS} . The typical photoelectron (PE) spectrum resulting from detachment of a DBS is shown in the centre. (b) The corresponding PE image, demonstrating the characteristic anisotropy predominantly parallel to the laser polarisation axis ϵ .

1.2.2. Importance of Non-valence States

Non-valence anions have found application in the laboratory as a spectroscopic tool. As the excess non-valence electron does little to disturb the nuclear structure of the core molecule, the electron may be utilised as a spectroscopic ‘tag’. For example, the molecular vibrational modes (and frequencies thereof) are essentially the same whether the molecule is in its neutral form or in an anionic non-valence state.¹¹⁵ Therefore, beginning from a ground-state valence anion, vibrational levels of an excited non-valence anion (and approximately, the neutral molecule) can be probed by observing resonantly enhanced photodetachment as the photon energy of the input laser pulse is scanned (i.e. acquiring an action spectrum).⁸⁰ Moreover, vibrational autodetachment processes can be observed upon resonant excitation, providing further information on the vibrational properties.¹¹⁶ In general, experiments that perform photoexcitation of a non-valence anion have exciting potential to probe anion resonance states from the equilibrium geometry of the neutral molecule, i.e. the natural geometry important to electron attachment processes.

However, non-valence anions are more than just a useful physical curiosity. In particular, non-valence states are thought to act as ‘doorway’ states that facilitate electron attachment to neutral molecules.^{117–119} In this sense, the diffuse non-valence orbital provides an enhanced cross-section for electron capture, which proceeds to form a vibrationally-excited non-valence anion resonance, described as a vibrational Feshbach resonance. From here, the non-valence state may couple to and relax into a more adiabatically stable valence state – a process which has been observed in a number of systems^{95,119–122} – extending the lifetime of the anion. This has implications for anion formation in the interstellar medium,^{123,124} where several polyatomic anions have been discovered over the past few decades.^{125–130} In particular, polycyclic aromatic hydrocarbons (PAHs) are suspected to be important carriers of negative charge in space, contributing to diffuse interstellar bands.¹³¹ Many PAHs possess strong dipole or quadrupole moments, and thus correlation-supported non-valence states offer a facile route for electron attachment. The potential role of non-valence states in biological electron attachment processes, such as low-energy electron-induced DNA damage, has also been speculated,¹³² but it is generally conceded that such non-valence states are unlikely to prevail in a disrupting bulk environment.¹³³ To explore such solvation effects in more detail, one may turn to the study of anion-solvent clusters.

1.2.3. Photoelectron Spectroscopy of Anion-Water Clusters

The photodynamical behaviour of molecules is often critically dependent on the surrounding environment. For example, green fluorescent protein fluoresces brightly upon UV/visible irradiation,¹³⁴ yet the isolated chromophore responsible for its absorption band undergoes ultrafast internal conversion processes that inhibit such fluorescence.^{135,136} Clearly, it is necessary to develop techniques that connect the results of gas-phase studies to those in condensed phases, allowing the influence of the surroundings to be differentiated from the

intrinsic behaviour of the chromophore. Clusters provide an appealing opportunity to ‘bridge’ the two regimes.⁴ Anion clusters are charged and thus separable through mass spectrometry, allowing individual clusters to be studied in isolation, revealing the effects of incremental cluster growth.

As a fundamental example which relates to non-valence states, water cluster anions, $(\text{H}_2\text{O})_n^-$, have been extensively studied using photoelectron spectroscopy. The water dimer anion, $(\text{H}_2\text{O})_2^-$, is a DBS and produces the characteristic photoelectron signal associated with detachment from a non-valence state, i.e. narrow and at low electron binding energy.^{137,138} As water molecules are successively added to the cluster, the electron binding energy (or VDE) increases, demonstrating that hydration has a stabilising effect on the excess electron.^{138,139} When the cluster size reaches $(\text{H}_2\text{O})_6^-$, multiple structural isomers form and can be correlated to different electron binding motifs.¹⁴⁰ Vibrational spectroscopy has assigned many of these structures,^{141,142} and the most stable isomer binds the excess electron via a single water molecule that acts as a double hydrogen-bond acceptor.^{141,143} Therefore, even at small cluster size, the description of the non-valence electronic structure becomes less well-defined than a simple DBS. As the cluster size increases further, the electron binding energies of the different isomers diverge.¹⁴⁴ In the large cluster regime (tens of water molecules and greater), the VDE of the most stable isomer (which can be subdivided into more precise isomeric classes) increases linearly with cluster size, $n^{-1/3}$.^{144–146} Through a simple linear extrapolation to the bulk limit ($n = \infty$), the VDE of the hydrated electron, $e^-_{(\text{aq})}$, was determined as 3.60 ± 0.03 eV.¹⁴⁷ This cluster-based extrapolated value is in very good agreement with recent measurements utilising liquid microjets, which place the VDE of $e^-_{(\text{aq})}$ at 3.7 ± 0.1 eV.^{148,149} This is a fine example of how bulk properties, possibly immeasurable by other means, can be determined through the study of anion clusters.¹⁵⁰

Heterogeneous anion-water clusters (written as $X^-(\text{H}_2\text{O})_n$, although the charge may be delocalised throughout the cluster) allow exploration of solvation effects on anions. A well-studied exemplar system is iodide-water cluster anions, $\text{I}^-(\text{H}_2\text{O})_n$.^{151–153} The VDE of $\text{I}^-(\text{H}_2\text{O})_n$ increases with greater n ,¹⁵³ demonstrating that hydration stabilises I^- . Indeed, hydration-induced stabilisation is essentially a universal trait amongst anions.^{152,154–157} Extrapolation techniques have also been applied to measurements on $\text{I}^-(\text{H}_2\text{O})_n$, allowing the VDE, ADE, and various thermochemical properties of aqueous iodide to be determined.¹⁵³ Anion-solvent clusters also present an opportunity to probe more exotic species in solution. For instance, photoexcitation of $\text{I}^-_{(\text{aq})}$ (as well as other anions) below the detachment threshold can lead to the formation of a charge-transfer-to-solvent (CTTS) state – a metastable intermediate towards the production of $e^-_{(\text{aq})}$.¹⁵⁸ The $\text{I}^-(\text{H}_2\text{O})_n$ analogue to the CTTS state was found to be an excited non-valence state.¹⁵⁹ This allowed the nonadiabatic decay dynamics of CTTS state decay to be tracked by TRPES.^{160–163} Altogether, $\text{I}^-(\text{H}_2\text{O})_n$ represents one example where the great level of mechanistic detail offered by gas-phase experiments can be applied to condensed-phase systems through the study of anion-solvent clusters. We now move to consider how such clusters may be applied to offer a viewport into electron-driven processes in condensed-phase biological environments.

1.2.4. Low-Energy Electron Attachment to DNA

Just over 20 years ago, Sanche and coworkers demonstrated that low-energy electrons (< 20 eV) resonantly attach to plasmid DNA strands, inducing strand breakages (see Figure 1.17) that ultimately lead to mutagenesis or even cell death.¹⁶⁴ This observation prompted a pivotal shift in the fields of radiation and electron-driven (bio)chemistry, in which experiments pushed to identify the products of the DNA damage, and moreover, understand the full mechanism from electron attachment to subsequent lesion.^{165–168} The entire process

spans many orders of magnitude in both time and energy, and we focus specifically on the initial resonant electron attachment step.

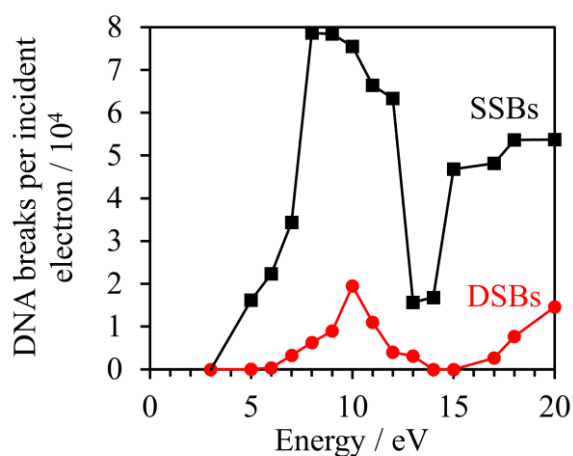


Figure 1.17: DNA strand breakages induced by incident low-energy electrons. Single- (SSB) and double- (DSB) strand breakages are distinguished by black squares and red circles, respectively. Adapted from ref. 164. Reprinted with permission from AAAS publishing.

Electrons were observed to induce DNA damage at specific incident energies, suggesting (transient) anion resonance states were forming on the DNA macromolecule. There are several moieties that are good candidates for accepting low-energy electrons: the phosphate backbone, the nucleobases, or the bridging sugar. Whilst both the nucleobase and the phosphate subunits can efficiently accept an electron, it is predominantly electron attachment to the *nucleobase* moieties that appear to lead to strand breakages and crosslinks.^{168,169} For incident electron energies ranging from 3–20 eV, Feshbach resonances of the nucleobase anions are populated.¹⁶⁹ At lower energies (< 3 eV), where resonant single-strand breakage has also been observed to occur,¹⁷⁰ shape resonances of π^* character have been implicated.¹⁷¹ In both cases, the accepted mechanism that leads to strand breakage is postulated to proceed as follows: charge-transfer occurs from a nucleobase π^* state (which can form directly, or in the higher energy case, via relaxation of a Feshbach resonance) to a σ^* orbital along the sugar-phosphate C–O bond, inducing cleavage.^{172,173} However, even in the case of sub-3 eV electron

attachment, it remains unclear which nucleobases, and moreover which π^* shape resonances, participate most.

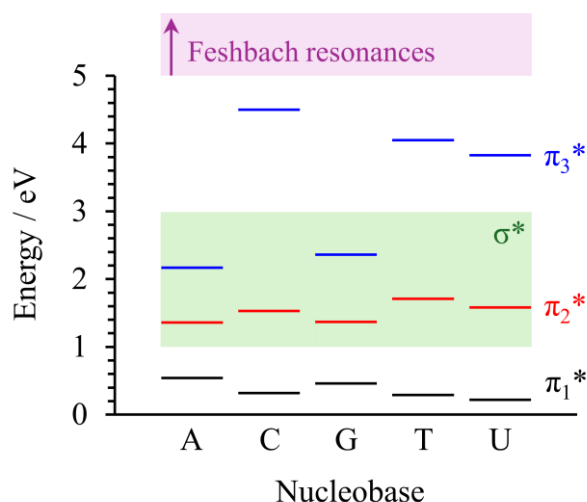


Figure 1.18: Anion resonance energies of isolated nucleobases: adenine (A), cytosine (C), keto-guanine (G), thymine (T), and uracil (U); relative to the neutral species.¹⁷⁴

For each of the five nucleobases (adenine, cytosine, guanine, thymine, and uracil), electron transmission spectroscopy has located the energetic positions of the lowest anion shape resonances with π^* character.¹⁷⁴ As summarised in Figure 1.18, three π^* resonances (labelled π_1^* – π_3^*) are accessible via electron attachment with sub-5 eV energies, for each nucleobase. Computational work has also identified the presence of σ^* states in this energy range.^{175–177} Although electron scattering from σ^* states has not been observed experimentally, they can participate in relaxation dynamics from populated π^* states, as demonstrated in dissociative electron attachment studies.^{178,179} Therefore, one may believe it straightforward to correlate the resonant energies of low-energy electron-induced DNA damage with the π_{1-3}^* resonances of the nucleobases. However, as discussed in the preceding section, water molecules in the proximity of an anion can provide a significant stabilising effect. It was recently shown that *excited* states of anions are similarly stabilised,⁶⁴ such that each of the π_{1-3}^* resonances can be expected to shift to lower energies due to the water molecules that infiltrate

the grooves of DNA. Conversely, the nearby phosphate backbone carries negative charge, which may act to destabilise the anion resonance states of the nucleobases. Undoubtedly, there is a need to investigate the behaviour of the π^* states of the nucleobases within condensed-phase environments.

Nucleobase-water anion clusters have been previously investigated using photoelectron spectroscopy by the Neumark and Bowen groups,^{180,181} although these studies did not find evidence of photoexcitation to anion resonance states. However, time-resolved photoelectron spectroscopy has been applied to iodide-nucleobase cluster anions, where near-UV excitation leads to the formation of a transient DBS anion of the nucleobase, or results in $\pi\pi^*$ excitation on the neutral nucleobase component, depending on the photon energy.^{120,182–184} For the uracil nucleobase, the DBS was observed to convert into the valence π_1^* state within hundreds of femtoseconds.¹⁸³ Similar experiments were extended to single-water clusters of the U-I⁻ complex, where conversion from the DBS to the π_1^* state was delayed, and the (long decay) lifetime of the subsequently formed π_1^* state was found to be substantially longer.^{185,186} These studies excellently highlight how the presence of even a single water molecule has a significant influence on the resonance dynamics of nucleobase anions. The work outlined in this thesis principally aimed to investigate the effect of hydration on nucleobase anions in more detail, hoping to elucidate which π^* resonances may accept low-energy electrons in aqueous conditions. To achieve this, our FRPES experiment was capable of accessing excited state resonances of nucleobase-water cluster anions by utilising photon energies that had not been previously applied. We exploited this to track the position of different anion resonance states of nucleobases with an increasing degree of hydration, shedding light on how an aqueous environment influences electron attachment to nucleobases. Additionally, water clusters of non-valence nucleobase anions were generated and measured for the first time, revealing the stabilising effect that water can exert on such delicate states.

Chapter 2 – Experimental

The Verlet group aims to investigate the photodynamical properties of anions, whether in isolation, in bulk solution, or at their dividing interface. The gas-phase laboratory is separated into two experimental setups, primarily differentiated by their anion source regions. One experiment utilises electrospray ionisation (ESI) to insert dissolved anions into a differentially pumped vacuum chamber. This is henceforth referred to as the *ESI instrument*. The second experiment generates anions through electron attachment to a molecular beam produced by an Even-Lavie pulsed valve. Within the supersonic expansion, molecular clusters (solvated molecules, or dimers, trimers, etc.) are formed, permitting the study of anion clusters. Due to this natural propensity to form anion clusters (and lack thereof in the ESI instrument), this molecular beam experiment is referred to as the *cluster instrument*.

The work included in this thesis was primarily carried out on the cluster instrument. Chapter 2 will highlight the current state of the experiments, with a particular focus on the more substantial adaptations which have been implemented on the cluster instrument. We begin by outlining the laser systems, one of which is new. The cluster instrument is then described in detail, and an overview of the ESI instrument is presented. Finally, the role of electronic structure calculations in aiding the interpretation of our experimental data is briefly discussed.

2.1. Laser Systems

There are currently three lasers available for use in gas-phase experiments within the Verlet lab: two Nd:YAG lasers, which each generate nanosecond laser pulses; and one Ti:Sapphire femtosecond system, which has seen little modification over the past few years.

2.1.1. Tuneable Nanosecond Pulses

The Q-switched Nd:YAG laser has been a staple of nanosecond experiments since its inception, and the Verlet group has employed one for many years in the form of the Continuum Surelite II. Q-switching is implemented to produce high-energy pulses (nominally 650 mJ) with a ~ 6 ns temporal FWHM (full-width at half-maximum). The fundamental wavelength of the laser is 1064 nm, but in typical operation the laser light undergoes frequency tripling to output 355 nm pulses (~ 150 mJ). The full output also contains residual 1064 nm and 532 nm light, the former of which is desirable for the subsequent wavelength-tuning step described below. The pulse repetition rate is 10 Hz.

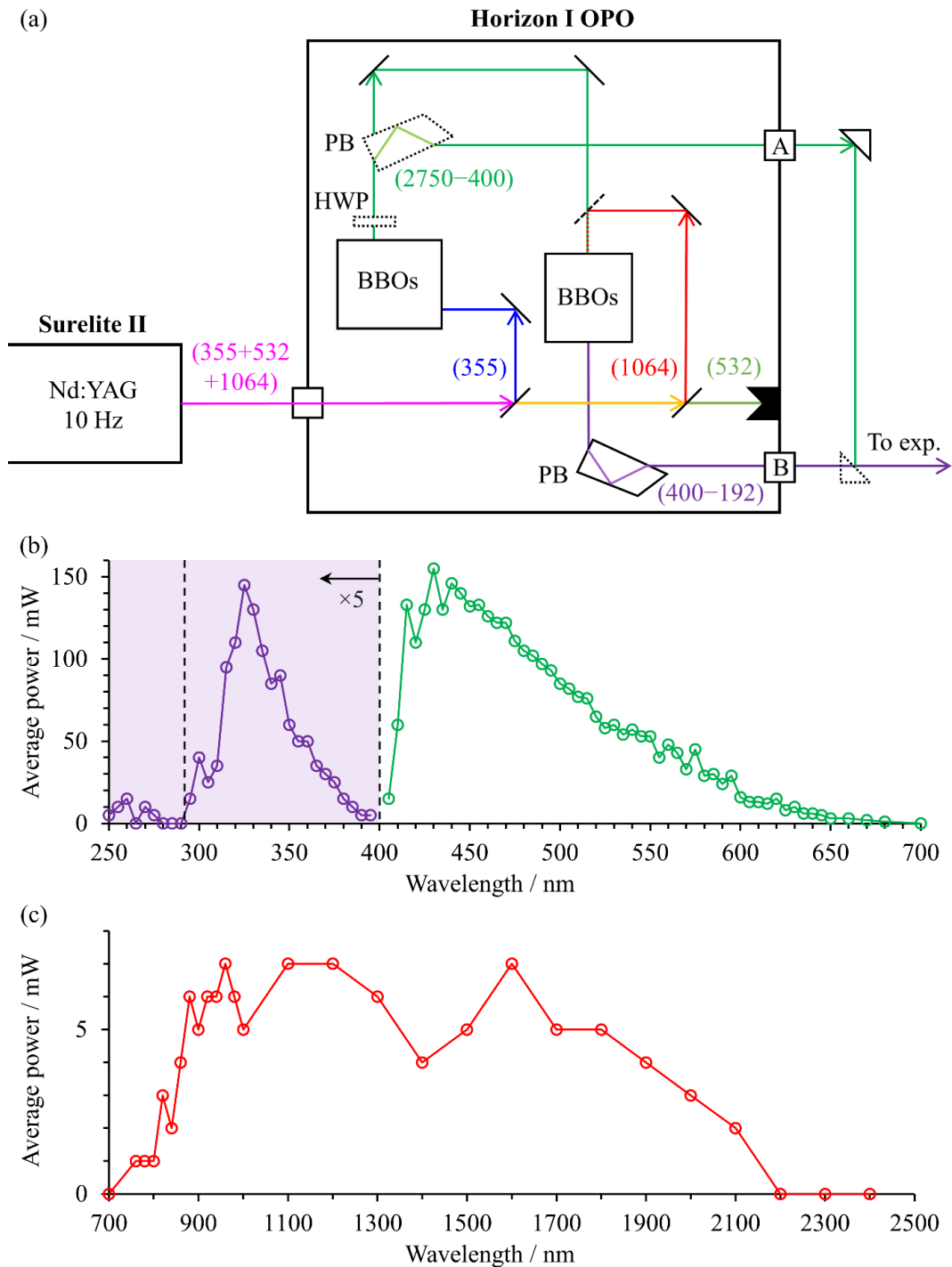


Figure 2.1: (a) Schematic of the Nd:YAG–OPO setup for the generation of nanosecond laser pulses with tuneable wavelength (2750–192 nm). The wavelength(s) of each path is given in parenthesis, with units of nm. HWP = half-wave plate, PB = Pellin-Broca prism, BBOs refers to the beta barium borate crystals which act as the necessary nonlinear optics. Dotted optics are removed depending on desired wavelength. Laser light leaves apertures A or B to be delivered to the experiment. (b, c) Measured power of resulting UV, visible, and near-IR pulses. Dotted lines indicate wavelengths at which the output power is expected to drop to zero due to the wavelength-tuning process.

Whilst the harmonic wavelengths of the Nd:YAG are useful for some experiments, tuneable-frequency pulses expand the limits on what can be studied, opening the door to, for instance, FPRES and various types of action spectroscopy. The output of the Surelite is coupled directly into a Horizon I (Continuum) optical parametric oscillator (OPO), accessing a near-complete range of wavelengths between 2750–192 nm. A simplified schematic of the setup is shown in Figure 2.1(a). The OPO converts the 355 nm pump pulses into two lower-energy waves of different frequency: the *signal* ($710 < \lambda_s < 400$ nm), and the *idler* ($2750 < \lambda_i < 710$ nm). As the signal and idler waves are produced with orthogonal polarisations, a combination of a half-wave plate (HWP) and a Pellin-Broca prism is used to selectively direct one of the beams towards aperture A (Figure 2.1(a)), for experimental use. For the generation of UV pulses in the $400 < \lambda_{UV} < 292$ nm range, the tuneable signal waves are mixed with residual 1064 nm fundamental light. Higher photon energies are similarly accessed, but require e.g. frequency-doubling of the signal. Ultraviolet pulses are directed to the alternate output – aperture B (Figure 2.1(a)). The measured laser power varies across the wide range of wavelengths, and the typical performance (as measured in 2023) is displayed in Figure 2.1(b) and 2.1(c). There is effectively zero output at 400 nm (3.10 eV), which is the visible-UV crossover.

The OPO is also capable of being continuously scanned, allowing for fast acquisition of photoelectron action spectra. This is particularly useful in determining the energetic position of anion resonance states, as there tends to be an increase in electron detachment yield when the photon energy becomes resonant with an excited state. This is demonstrated in greater detail in Chapter 5.

2.1.2. New Nd:YAG Laser

The second Nd:YAG laser is a Quantel Q-smart 450, and is a more recent addition to the laboratory. The primary distinguishing factor from the original Surelite Nd:YAG described above is that the Q-smart can run at a repetition rate of 20 Hz (rather than 10 Hz), delivering 450 mJ/pulse. The upshot of this increased rate is that our experiments can effectively acquire double the photoelectron signal with little-to-no drawback.

Like the Surelite, the new Q-smart laser generates nanosecond pulses (~ 5 ns FWHM) with a fundamental wavelength of 1064 nm. Higher harmonic generation is available, up to the fifth harmonic (213 nm). Additionally, the output of the Q-smart Nd:YAG can be coupled into a dye laser (Sirah, Cobra-Stretch), although this was not utilised for the work in this thesis. Like the OPO, the dye laser alters the wavelength of the input pulses. The advantage of the dye laser comes through the quality of the tuned laser pulses. First, the pulse power is far greater than the OPO is capable of, reaching up to 30% efficiency (of the 532 nm pump). And second, the linewidth of the tuned pulses is far more narrow (0.1 cm^{-1} at $\lambda = 625 \text{ nm}$, compared to $>3 \text{ cm}^{-1}$ for the OPO), allowing for selective photoexcitation of individual vibrational modes in target anions. However, the tuning range is far more limited: whilst the OPO spans 2750–192 nm (nearly) seamlessly, the dye laser only spans 920–370 nm, requiring different dye solutions at small wavelength intervals therein.

2.1.3. Femtosecond Laser

Over the past few years, there have been no significant alterations to the femtosecond laser system. Comprehensive descriptions of the current setup can be found in earlier PhD theses within the group.¹⁸⁷ Nonetheless, a summary of the system and its pulse properties are provided here. The primary purpose of femtosecond experiments are to record time-resolved

photoelectron spectra through a pump-probe scheme. A lesser secondary application is to compare photoelectron spectra acquired with nanosecond and femtosecond pulses of the same wavelength, which can give insight into photodetachment processes involving multiple photons and the intermediate excited state dynamics.

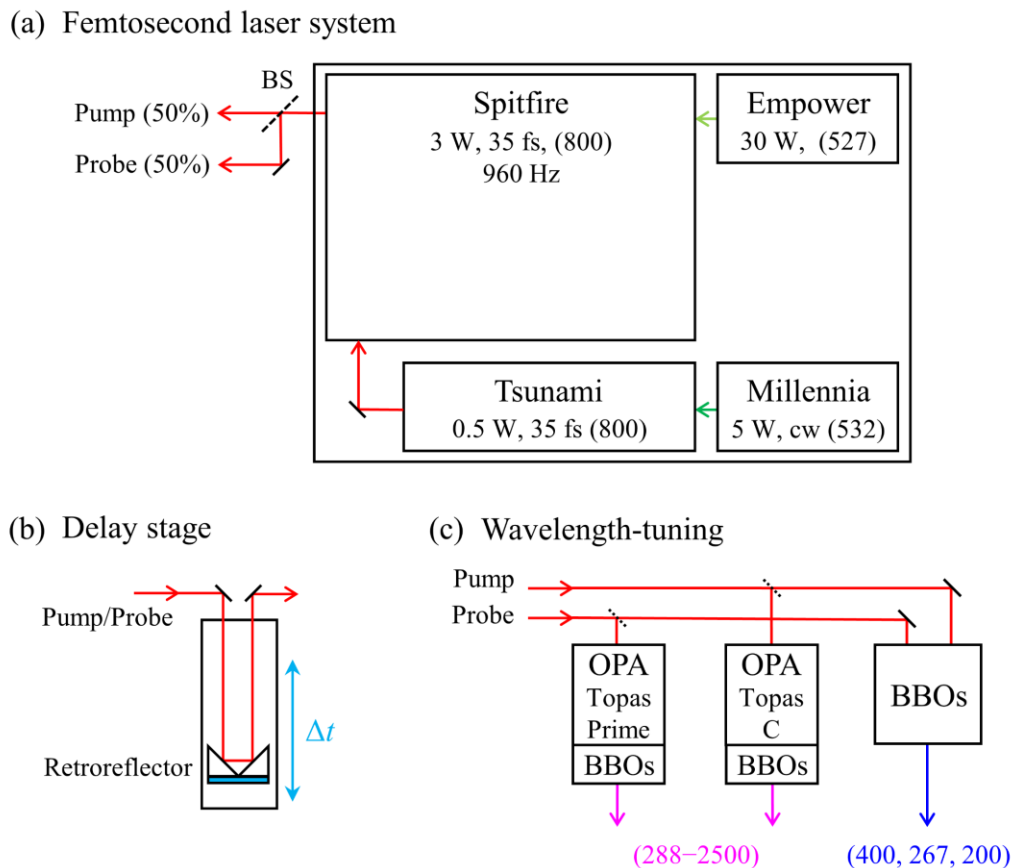


Figure 2.2: (a) A schematic of the current femtosecond laser setup, labelled with relevant beam properties. Pump and probe beamlines derive from the same output, where they are separated by a 50:50 beamsplitter (BS). (b) Sketch of the motorised stage used to generate a delay between the pump/probe pulses. (c) Setup for generating pump/probe pulses of different wavelengths.

A schematic of the femtosecond laser system is shown in Figure 2.2(a). The setup begins with a diode-pumped solid-state laser (Millennia, Spectra Physics). A continuous-wave beam at 532 nm is produced and pumps a mode-locked Ti:Sapphire oscillator (Tsunami, Spectra Physics), which emits ultrashort 800 nm pulses (FWHM = 35 fs) with an average power

of 0.5 W. Instead of directly using the output of the Tsunami for experiments, the pulses first undergo amplification to increase the power. This takes place in a Ti:Sapphire regenerative amplifier (Spitfire Pro, Spectra Physics), which is pumped by the second harmonic (527 nm) of a high-power Q-switched Nd:YLF laser (Empower, Spectra Physics) at with a repetition rate of 960 Hz. A Pockels cell dumps amplified pulses from the Spitfire cavity, generating a train of 800 nm, ~35 fs pulses, but an increased average laser power of 3 W. This output is separated into two equal parts: one to be used as a pump in TRPES experiments, and the other as a probe.

The pump and probe pulses take different paths through to the experiment, which naturally means that the pulses will not enter the experiment simultaneously. For TRPES, we must adjust the difference in arrival times, Δt , with femtosecond resolution. This is performed by directing one beam onto a delay stage (Figure 2.2(b)), consisting of a retroreflector mounted onto a one-dimensional motorised translation stage. The retroreflector is simply two mirrors oriented perpendicularly, reversing the direction of the incoming light. The translation stage adjusts the position of the retroreflector to sub-micrometer precision, altering the total pathlength of the beam. This affects the travel time of either the pump or probe laser pulses, offsetting them with respect to each other. Δt can be increased (or decreased) up to one nanosecond, with femtosecond resolution.

TRPES experiments generally require pump and probe pulses of specific wavelengths. Figure 2.2(c) outlines our current wavelength-tuning capabilities for the femtosecond laser. The laboratory has two optical parametric amplifiers (OPAs; Topas Prime and Topas C, Light Conversion) which can be used to tune the wavelength of the 800 nm pulses to the range of 2500–1150 nm. Combining the OPA outputs with sum-frequency generation (BBO) crystals, wavelengths between 2500–288 nm are achievable. Alternatively, harmonics of the initial 800 nm pulses can be generated, producing powerful femtosecond pulses of 400, 267, or 200 nm.

The pump and probe wavelengths must be selected carefully. The pump photon energy $h\nu_{\text{pump}}$ should be resonant with the excited state of interest (e.g. $S_1 \leftarrow S_0$), which can be located with a preceding FRPES experiment. The choice of probe photon energy $h\nu_{\text{probe}}$ is more involved. Inevitably, it must be sufficiently high to detach electrons from the excited state population, producing the pump-probe signal. However, if possible, $h\nu_{\text{probe}}$ should be below the electron affinity of the parent anion so as not to detach electrons from the ground-state population, which could obscure other, weaker features in the photoelectron spectrum. But note that with a ‘background’ subtraction, this adverse effect can be mitigated. Generally, the primary concern with choosing $h\nu_{\text{probe}}$ is to avoid the photon energy being resonant with other excited states of the anion. Transitions originating from the ground-state (e.g. $S_n \leftarrow S_0$) and transitions from the pump-induced population to higher states (e.g. $S_n \leftarrow S_1$) should both be avoided. Failure to do so will complicate the photoelectron spectrum and may affect interpretation of the excited state dynamics. Finally, both the pump and probe generally benefit from maximising the pulse power, and therefore it is preferable to use harmonics of the 800 nm output where possible.

2.2. The Cluster Instrument

Most of the data in this thesis was acquired on the cluster instrument,¹⁸⁸ which completed construction in 2016. A detailed description of the experiment, as well as a practical user guide, can be found in the PhD thesis of J. P. Rogers.¹²¹ This section will give a general overview of the experiment in its current state.

2.2.1. The Even-Lavie Valve Source

The ion source region features a high-temperature, high repetition rate, pulsed Even-Lavie valve.¹⁸⁹ Figure 2.3 shows an outline of the current setup. The desired molecule is contained within a high-pressure (>1 bar) inert backing gas and is delivered directly into ultrahigh vacuum (10^{-7} mbar) by the Even-Lavie valve. Gaseous samples can simply be mixed with the inert backing gas before entering the valve, whereas molecules which naturally exist in solid or liquid states must be vapourised in order to be carried by the backing gas. This can be easily achieved for sufficiently volatile liquids by inserting a small volume of the sample directly into the gas-line. On the other hand, solid samples may require sublimation through heating, which can be achieved directly inside the high-temperature valve (up to 240 °C). Less volatile liquids can also be studied via heating within the Even-Lavie valve, but should be inserted with a large quantity of glass wool.

The Even-Lavie valve is specifically designed to produce a translationally cold (few-Kelvin) and dense molecular beam through supersonic expansion. These conditions are ideal for the formation of weakly-bound molecular clusters, as internal energy in the target molecules is efficiently removed via collisions with the backing gas. In addition, our valve is optimised for high repetition rates (up to 1 kHz), allowing the cluster experiment to match the repetition

rate of the femtosecond laser, maximising efficiency of data acquisition. Generally, the valve is operated at lower repetition rates for experiments with the nanosecond lasers.

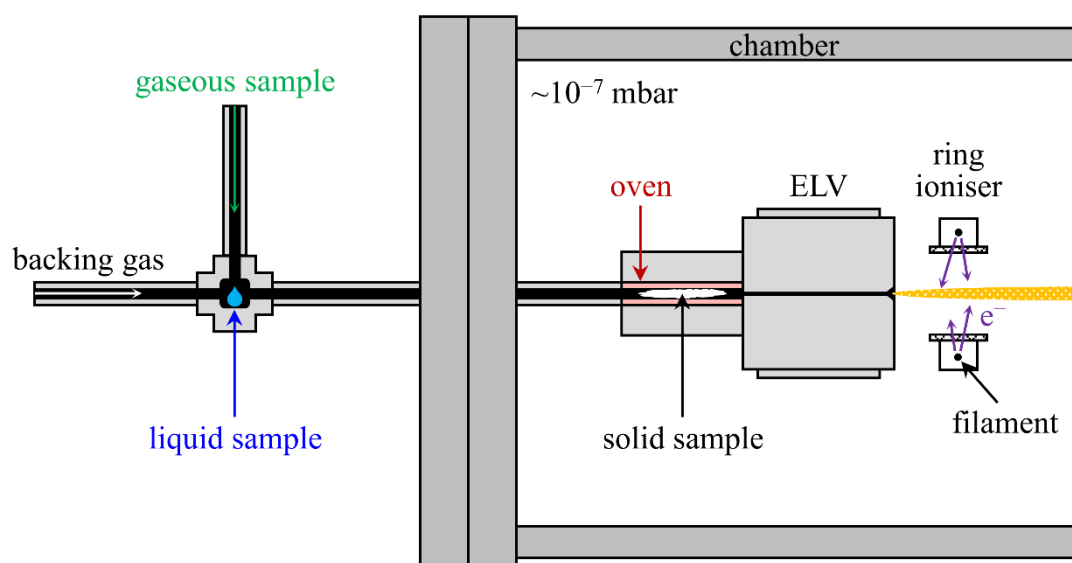


Figure 2.3: Schematic of the current source region of the cluster experiment, using the filament ring ioniser for injection of electrons into the supersonic expansion, which is generated by the pulsed Even-Lavie valve (ELV). Solid and volatile liquid samples are inserted into different areas of the gas line. Gaseous samples can be directly mixed with the backing gas.

The molecular beam comprises of neutral molecules (and clusters), so electrons must be attached to form the anions we desire. Various electron attachment schemes are available, and each method can result in a different distribution of anionic species and clusters. The original scheme, described in the thesis of J. P. Rogers,¹²¹ utilises an electron gun.

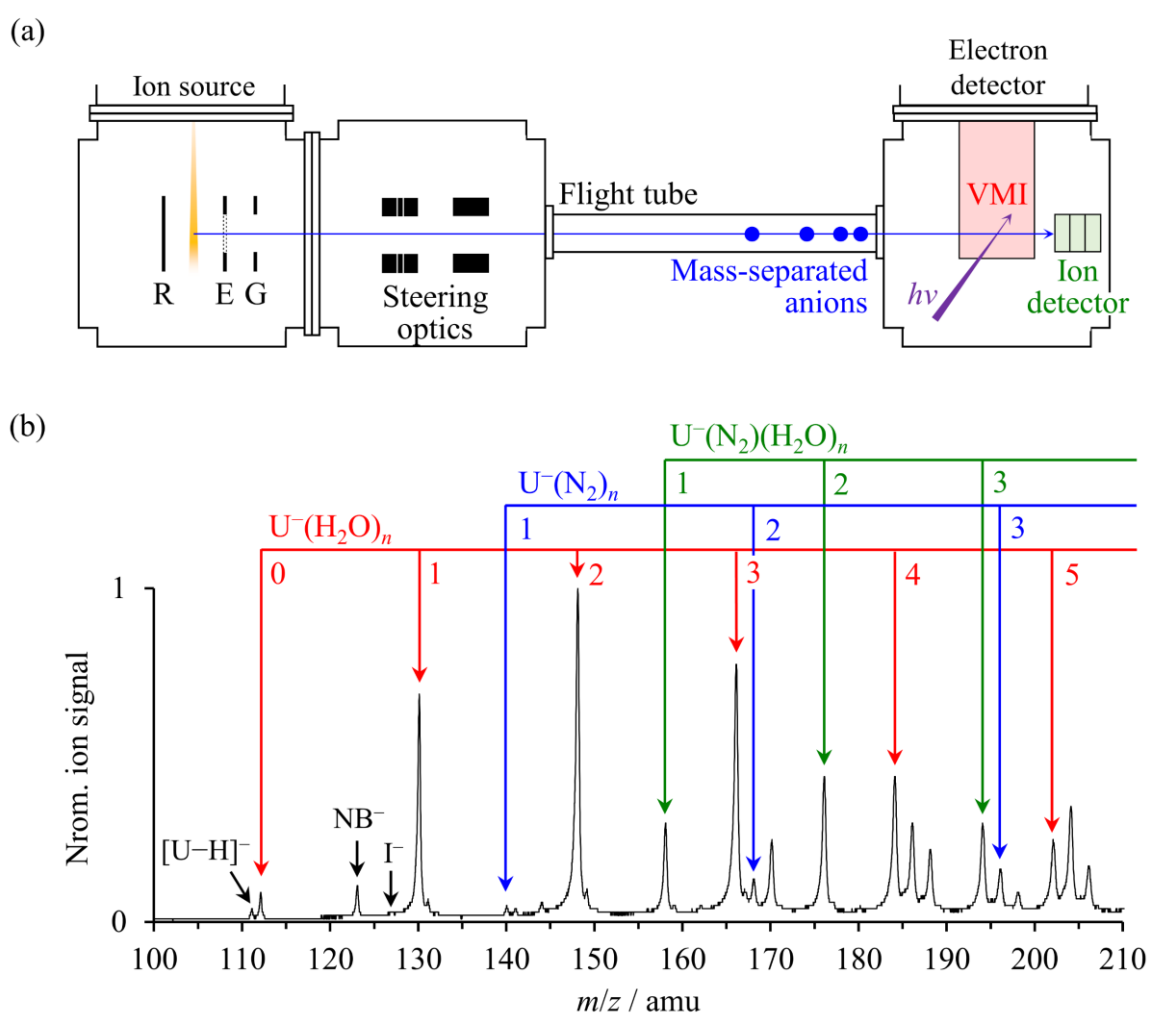
An alternative electron attachment source – the filament ring ioniser – was employed instead of the electron gun for the studies contained in this thesis. The ring ioniser contains a thoriated tungsten filament coiled around an empty aperture (1" diameter), and a high current is flowed through the filament to produce thermionic electrons. The ring is mounted onto the front of the Even-Lavie valve such that the molecular beam passes through the centre of the aperture. By applying a more negative voltage across the outer radius of the ring ioniser, the free electrons are accelerated towards the molecular beam, where a plasma is formed (with the

backing gas) and anions are generated. The ring ioniser can be translated along the axis of the molecular beam to offer some control over the point of attachment, but this naturally involves venting the experiment. In general, the ring ioniser tends to give more unstable ion currents than the electron gun, but the overall ion yields are greater.

2.2.2. Mass Spectrometry

Following the electron attachment scheme described above, the supersonic expansion will contain an assortment of different anions, as well as cations and neutral species. To perform photoelectron spectroscopy on a specific anion, a preceding separation stage is crucial. To achieve this separation, we use Wiley-McLaren time-of-flight (TOF) mass spectrometry.¹⁹⁰ The setup consists of only three stainless steel plates: the Repeller, the Extractor, and the Ground (see Figure 2.4(a)). The molecular beam bisects the Repeller and Extractor plates, which begin grounded (0 V) with respect to the valve and vacuum chamber. The grounded nature of the plates allow the charged species within the supersonic expansion to enter the TOF apparatus unperturbed. Once the dense packet of anions reaches the centre of the plates (typically a few hundred microseconds after the valve opening), the Repeller and Extractor are each pulsed to a high negative voltage, typically -3.0 kV and -2.6 kV, respectively. This creates a shallow potential gradient in the vicinity of the molecular beam, accelerating the anions orthogonally to the molecular beam axis. The anions fly through the aperture of the Extractor plate, which is covered with a high transmission mesh. Once through, the anions experience the enormous potential gradient between the Extractor and Ground plates, providing an even greater acceleration in the same direction. The anions then enter a long (~ 2 m) field-free region known as the flight tube. Various ion optics (deflectors and einzel lenses) help to steer the anions through the flight tube. As each anion was provided the same acceleration force, those with smaller m/z (mass-to-charge) ratios will travel faster through the flight tube, and reach the laser

interaction region (described below) earlier. The laser pulse is delayed to coincide with the mass-separated anion packet of interest. The pulsed voltages on the Repeller and Extractor plates are carefully tuned to temporally focus the chosen anion packet to the position of laser interaction. The mass-resolution with this setup is $m/\Delta m \approx 200$.



Beyond the laser interaction region rests an ion detector, which the mass-selected anion packets collide upon. Each collision triggers an electrical signal, giving live feedback on the anion time-of-flights and thus which anions are being produced. The ion detector is composed of three stacked elements. The front face (which the anions collide with) is a single microchannel plate (MCP). Upon ion impact, a cascade of electrons is generated through the MCP, exiting out the reverse side. The large number of electrons then impact the second element – a phosphor screen. This acts as a scintillator, emitting photons upon electron impact. These photons are detected by a photomultiplier tube at the end of the stack, converting the light signal into electronic signal readable by a standard oscilloscope.

Figure 2.4(b) shows an exemplar mass spectrum where the nucleobase uracil (U) was heated and sublimated within the Even-Lavie valve. The utilised backing gas was molecular nitrogen, N_2 (10 bar), and a small quantity of water was added to the backing line. The ring filament ioniser was used to attach electrons to the supersonic expansion, resulting in the production of U^- , and a notably larger quantity of cluster anions with larger m/z . The dominant progression in the mass spectrum (highlighted with red arrows) was constructed of uracil-water anion clusters, $U^-(H_2O)_n$. Clustering of the uracil anion with the backing gas was also present, although these $U^-(N_2)_n$ anion clusters formed in less yield compared to the uracil-water clusters, likely reflecting the weaker solvating power of N_2 compared to H_2O – the latter of which being polar and hydrogen bonding. Hybrid clusters also formed, and one example progression, $U^-(N_2)(H_2O)_n$, is highlighted with green arrows. Altogether, this mass spectrum demonstrates the propensity for cluster formation within the supersonic expansion, which allows solvation effects to be probed incrementally and with solvent specificity. As a final note, there is also the trace presence of iodide (I^-) and nitrobenzene (NB^-) anions, which have proven useful calibrants.

2.2.3. Velocity Map Imaging

The mass-separated anion of choice is intersected with a precisely delayed laser pulse at the centre of an electron spectrometer. Our experiment utilises a velocity map imaging (VMI) setup, which quickly became the dominant technique of photoelectron spectroscopy since its introduction by Eppink and Parker.⁸ VMI provides several key benefits over more traditional techniques, such as the magnetic bottle¹⁹¹ spectrometer: (i) the VMI spectrometer does not operate on the principle of electron time-of-flight, so low-energy electrons are mapped efficiently with good resolution; (ii) electrons are angularly resolved relative to the laser polarisation axis, offering insight into the electronic structure of the parent anion through the extracted PAD; and (iii) superior eKE resolution can be attained, provided with optimal electrode geometries and voltages. Details on the conversion of the velocity-mapped photoelectron image to the photoelectron spectrum (and PAD) is given in Section 2.2.4.

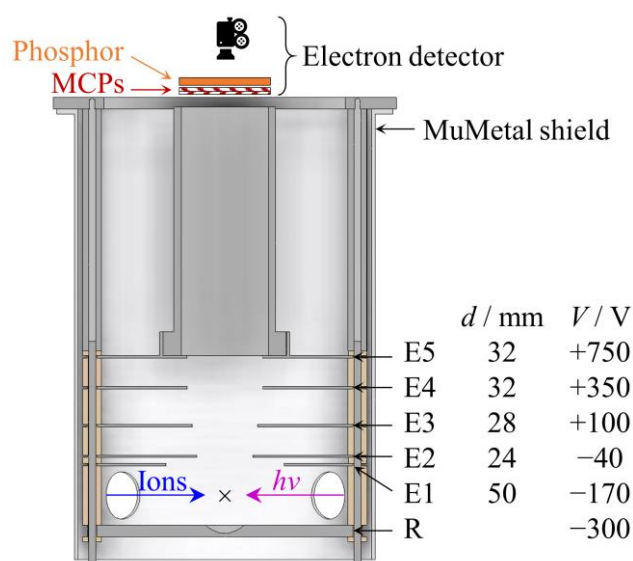


Figure 2.5: Current velocity map imaging (VMI) spectrometer design, featuring six electrode plates (R, E1–5). For each electrode, the diameter of the aperture, d , and typical applied voltage, V , is shown. Ions are perpendicularly intersected by the laser pulse $h\nu$ at the interaction region between electrodes E1 and R, which is highlighted with a cross. Detached electrons are accelerated upwards and detected at the top of the VMI stack.

The current VMI spectrometer consists of six stainless steel plate electrodes, mounted in series to the top flange of the detector chamber, as illustrated in Figure 2.5. This differs to the original VMI spectrometer described in the thesis of J. P. Rogers,¹²¹ which only implemented three plates. The ion-laser interaction region bisects the lowest two plates (R and E1), and generated photoelectrons are ejected upwards by pulsing the terminal plate (R) to a negative voltage. Each electrode above the interaction region contains an aperture, allowing the electrons to cleanly pass through. The voltage on each electrode is carefully adjusted (as guided via simulation using SIMION 8.0, in the first instance) to fulfil velocity-mapping conditions. As the electrons travel upwards, they spatially separate as an expanding Newton sphere. The electrode nearest the top flange is connected to a flight tube, providing a field-free region over which the Newton sphere of electrons can further expand. Upon reaching the top flange, the electrons impact the front face of an MCP. This is coupled to a second MCP, oriented such that the diagonal pores are in a chevron configuration. With a large (~ 1.4 kV) potential difference across the coupled MCPs, each electron impact generates a cascade of electrons within the MCP pores, greatly amplifying electron signal. Similar to the ion detector, a phosphor screen acts as a scintillator on the back side of the upper MCP. A fast-acquisition camera points down towards the back of the scintillator, measuring the two-dimensional position of each electron splat.

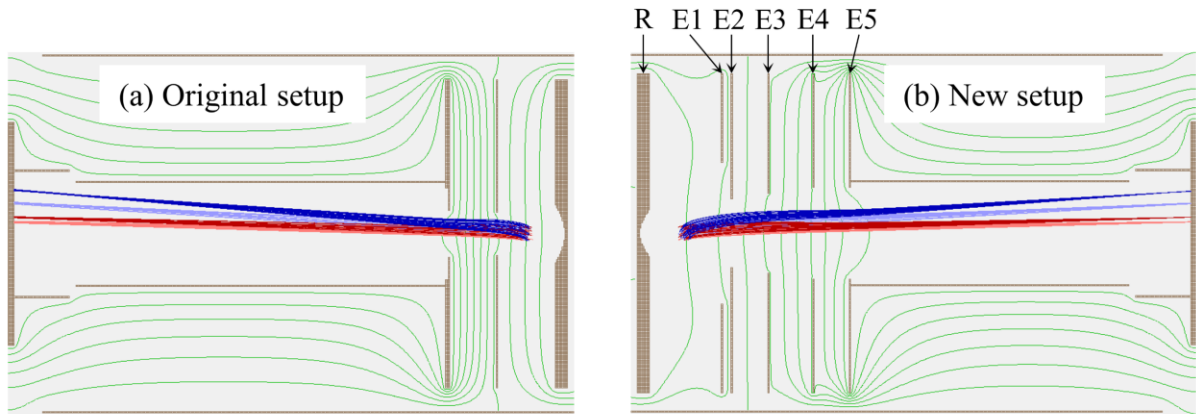


Figure 2.6: SIMION 8.0 simulated electron trajectories in the (a) original and (b) new velocity map imaging spectrometers. Electrons are initiated near the interaction region with $eKE = 0.5$ eV (red) or 5.0 eV (blue). The darker shade trajectories correspond to electrons with initial velocity vectors in the plane of the detector, whereas electrons shaded lighter began with velocity vectors at $\pm 45^\circ$ with respect to the detector plane.

Figure 2.6 displays electron trajectory simulations (performed using SIMION 8.0) that showcase the velocity-mapping capabilities of the original and new VMI designs. Uniformly spaced electric field lines are displayed in green, and give insight into the exerted force on the electrons at each point in the spectrometers. Qualitatively, the field lines are similar between the two setups. In both, the electric field gradient at the interaction region is small (distantly spaced electric field lines), giving the generated photoelectrons a relatively small initial acceleration. Moreover, an indentation in each repeller (R) plate gives the electric field lines a slight curvature at the interaction region. Later in the electron flight paths, there is a region of much greater potential gradient (densely packed electric field lines), curved such as to effectively produce an electrostatic focussing lens. This combination of slow initial acceleration into an electrostatic lens appears to fulfil velocity-mapping conditions, consistent with the observations of other groups.^{192,193} As mentioned earlier, the field-free flight tube simply allows for spatial separation of the electrons and therefore has no significant influence on the VMI capabilities.

The extra electrodes in the new VMI spectrometer provide additional control of the applied electric field, and their geometries (shape and position) were selected with care. Most notably, electrode E1 possesses a relatively large aperture and is in close vicinity to electrode E2. In this geometry and with a large potential difference between these two electrodes, the electric field curvature is more pronounced in the interaction region. In the electron flight simulations, this proved to be crucial in improving the VMI resolution. Additionally, it was found that a more disperse electrostatic lens offered better resolution, but to a lesser extent. Overall, the simulated electron kinetic energy resolution at $eKE = 0.5$ eV improved from approximately 3–5 % in the old spectrometer to <1 % in the new spectrometer (as determined by the FWHM).

Despite thorough optimisation of the applied voltages, the *experimental* VMI resolution could not be brought below 1%. We found that the VMI design was no longer the limiting factor in our resolution, but rather the detector setup. To illustrate this, the narrow photoelectron spectrum of the uracil anion is presented in Figure 2.7, in terms of (a) detector radius in units of pixels, and in terms of (b) electron kinetic energy. Two different VMI operating conditions were used: (i) applying voltages as listed in Figure 2.5; and (ii) halving those voltages. Under both of the operating conditions, the FWHM in units of pixels was 3.0, which is the approximate size of each detected electron impact. However, in terms of eKE (Figure 2.7(b)), the resolution was improved under the halved-voltage conditions (ii). Therefore, it appears that the spot size of our electron impacts are the new limiting factor of the VMI resolution. With efforts to reduce this spot size, the best spectral resolution that has been observed (so far) with the current VMI setup is < 2 %.

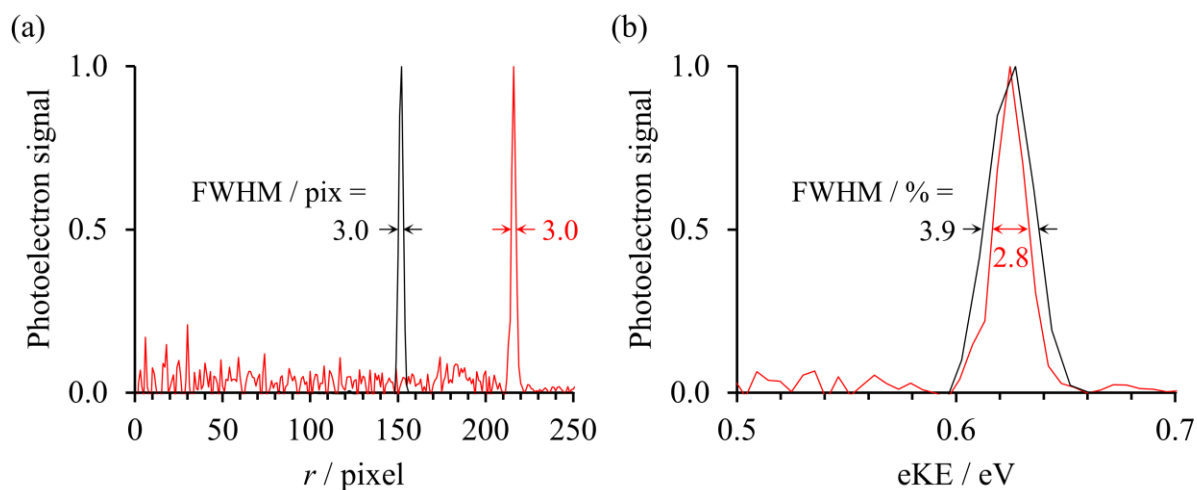


Figure 2.7: (a) Photoelectron spectra of U^- acquired at $h\nu = 0.7$ eV, plotted against image radius r in units of pixels. The VMI electrodes were operated at half-voltages for the spectrum plotted in red, compared to the spectrum plotted in black, expanding the photoelectron signal on the detector. The full-width-at-half-maximum (FWHM) in terms of r are the same for each spectrum. (b) The same photoelectron spectra plotted in terms of eKE. In this case, the FWHMs are representative of the VMI spectral resolution under these two operating conditions.

2.2.4. Reconstruction Algorithms

For conversion of the photoelectron image to a photoelectron spectrum (and PAD), an assortment of different reconstruction algorithms are available. Examples include pBASEX,¹⁹⁴ polar onion peeling (POP),¹⁹⁵ maximum entropy methods,^{196,197} and recently emerging artificial neural network programs.¹⁹⁸ These reconstruction algorithms primarily differ by how they circumvent the computationally expensive (and numerically unstable) Abel inversion that is required to convert the projected 2D image into the initial 3D distribution. The remainder of this subsection will offer a brief description on the POP and MELIXIR algorithms, which are utilised in later chapters.

The POP algorithm was developed within the Verlet group in 2009, and aimed to provide a faster, but equally accurate, alternative to pBASEX. A full description of POP can be found in ref. ¹⁹⁵, but an overview is presented here. The POP algorithm takes an ‘onion peeling’ approach, in that the 2D image is analysed from the outside inwards. The polar coordinate

system is therefore a natural choice to analyse the circular signals present in photoelectron images. Beginning from a large radius $r = R$, the photoelectron signal is assumed to represent the central slice of the Newton sphere at the corresponding $eKE = kR^2$, where k is an experimentally-determined calibration factor. This signal is then fit using a basis set of Legendre polynomials. The computational expense of performing the Abel inversion on this signal is avoided through the use of a ‘lookup table’. The lookup table contains, for each R , the expected contributions of the projected Newton sphere onto smaller radii $r < R$. Anisotropy is not contained within the lookup table, but is easily incorporated as a subsequent step. This new image of expected contributions at $r < R$ is subtracted from the original image, essentially removing all photoelectron signal arising from electrons with $eKE = kR^2$. The process is then repeated for $r = R-1$, where the corresponding signal is assumed to be the central slice of the $eKE = k(R-1)^2$ Newton sphere, and then the contributions of the other electrons are removed from the projected image. Iterations continue until the centre of the image is reached, and both photoelectron signal and anisotropy have been measured for every radius $r \leq R$. In addition to being computationally inexpensive, POP has minimal ‘smoothing’ effect on the experimental data.

Although the accuracy of POP compares well with other reconstruction algorithms, it tends to underperform with low-signal photoelectron images.¹⁹⁹ This largely arises from the retention of experimental noise when approximating the outer radius to the central slice of the corresponding Newton sphere. Moreover, noise accumulates as the POP algorithm works towards the centre of the image, so that weak features with low- eKE become obscured. Therefore, we looked to implement a second reconstruction algorithm into our analysis toolkit: MELEXIR (Maximum Entropy Legendre EXpanded Image Reconstruction), the most recent maximum entropy reconstruction method developed by Bernhard Dick.¹⁹⁷ Like POP, MELEXIR is computationally inexpensive but highly accurate. Unlike POP, MELEXIR has

been shown to perform very well in weak signal conditions, and does not suffer from noise accumulation as the algorithm progresses.

MELEXIR builds upon the earlier maximum entropy algorithms, MEVIR and MEVELER.¹⁹⁶ It is most useful to first discuss the general methodology common to each of the techniques, and then speak specifically of MELEXIR. The maximum entropy (ME) algorithms, unlike most reconstruction techniques, completely avoid the Abel inversion. Instead, the aim is to simulate a 3D velocity distribution \mathbf{Q} which, following (forward) Abel transformation, best describes the 2D experimental data \mathbf{D} . The forward Abel transform is much faster (and numerically well-behaved) than the Abel inversion, so this step takes little time. Although the ‘best’ choice of 3D velocity distribution might be thought to be the one which results exactly in the experimental data (this is the result of Abel inversion on \mathbf{D}), this tends to have unphysical contributions to both the photoelectron spectrum and PADs (due to the presence of experimental noise, for instance). The ME algorithms redefine the best \mathbf{Q} from being ‘*the \mathbf{Q} which reproduces the experimental data exactly*’ to ‘*the \mathbf{Q} which most likely results in the experimental data*’. Although this distinction is subtle, it can be used to prevent unphysical contributions and allows experimental noise to be incorporated in a simple way. To rephrase, the ME algorithms seek to maximise $\mathbb{P}(\mathbf{Q}|\mathbf{D})$, i.e. the probability of the simulated 3D velocity distribution being correct, given the experimental data. Dick applies Bayes’ theorem in order to assess this quantity;

$$\mathbb{P}(\mathbf{Q}|\mathbf{D}) = \frac{\mathbb{P}(\mathbf{D}|\mathbf{Q}) \mathbb{P}(\mathbf{Q})}{\mathbb{P}(\mathbf{D})}, \quad (2.1)$$

where $\mathbb{P}(\mathbf{D})$ is a constant for a given experiment. Clearly, $\mathbb{P}(\mathbf{Q}|\mathbf{D})$ is maximised by maximising the two-term product in the numerator.

The first term in the numerator, $\mathbb{P}(\mathbf{D}|\mathbf{Q})$, is dictated by the agreement between the simulated and experimental data, and is maximised with perfect agreement. This can be quantified, for example, by summing the squared residuals between the real and simulated projected images. Of course, the \mathbf{Q} which produces the greatest possible $\mathbb{P}(\mathbf{D}|\mathbf{Q})$ is simply the result of the Abel inversion on \mathbf{D} . However, this choice of \mathbf{Q} will introduce many new features to explain artefacts of noise in the experimental data. Intuitively, we can recognise this choice of \mathbf{Q} as being unlikely to be the true underlying velocity distribution, and it should correspondingly have a low $\mathbb{P}(\mathbf{Q})$. Indeed, the ME algorithms quantify $\mathbb{P}(\mathbf{Q})$ by the principles of entropy. The ‘default’ velocity distribution is taken to be completely featureless (flat). Deviation from the default distribution (introduction of new features) decreases the entropy in this choice of \mathbf{Q} , and consequently decreases $\mathbb{P}(\mathbf{Q})$. Accordingly, a balance is created: introducing new features in \mathbf{Q} leads to better agreement with \mathbf{D} but also reduces the entropy, so that $\mathbb{P}(\mathbf{D}|\mathbf{Q})$ increases but $\mathbb{P}(\mathbf{Q})$ decreases; whereas minimising the structure in \mathbf{Q} retains a high measure of entropy but offers a poorer description of \mathbf{D} , so that $\mathbb{P}(\mathbf{Q})$ increases but $\mathbb{P}(\mathbf{D}|\mathbf{Q})$ decreases. Unfortunately, the relative influence of these two contributions is dependent on many experimental factors, such that finding the optimal balance of new features is not trivial.

The method of maximum entropy is invoked to find the most appropriate distribution \mathbf{Q} . A pictorial representation of the decision process is shown in Figure 2.8. First, a selection of feasible \mathbf{Q} are generated, each satisfying the criterion that $\mathbb{P}(\mathbf{D}|\mathbf{Q}) \geq K$, for a chosen threshold value K . This can be thought of as allowing \mathbf{Q} to vary from the experimental data, but only to a collective extent. Therefore, only \mathbf{Q} which satisfactorily describe the experimental data (upon Abel transformation) are included in the subset of feasible choices, which can also be further constrained if necessary. From this subset of distributions, one \mathbf{Q} is selected as the most appropriate, which has the highest (maximum) entropy, and thus highest $\mathbb{P}(\mathbf{Q})$. All other feasible velocity distributions have a lower entropy, and as Dick states,¹⁹⁷ ‘contain information

for which there is no evidence in the experimental data'. Overall, the experimental data are only used to create the subset of feasible \mathbf{Q} , and the principles of maximum entropy make the final decision.

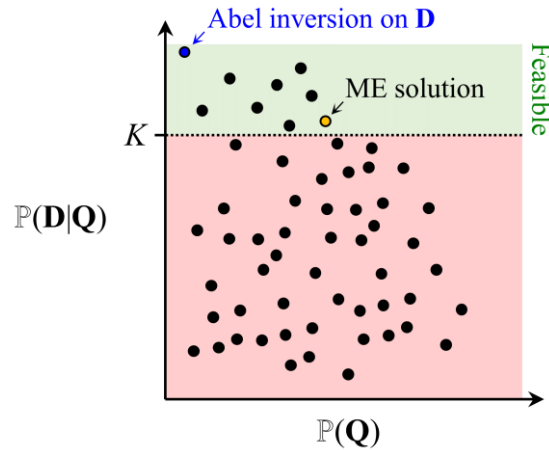


Figure 2.8: Picture describing the decision process in the maximum entropy (ME) algorithms. Black dots represent generated velocity distributions, \mathbf{Q} . Those which lead to sufficiently good agreement with the experimental image, \mathbf{D} , form the feasible subset of solutions (green area). The ME-determined \mathbf{Q} (gold) is the feasible solution with greatest entropy (and thus $\mathbb{P}(\mathbf{Q})$). The result of Abel inversion on \mathbf{D} (blue) maximises $\mathbb{P}(\mathbf{D}|\mathbf{Q})$, but is associated with a low $\mathbb{P}(\mathbf{Q})$.

Now to distinguish MELEXIR from the preceding maximum entropy methods. In MEVIR, the only constraint placed on the simulated velocity distribution (\mathbf{Q}) is that it is cylindrically symmetric, as is physically the case through the light-matter interaction in VMI. MEVELER constrains \mathbf{Q} further, restricting the 3D velocity distribution to being described by a series of Legendre polynomials. This is also true in most VMI experiments, including ours. MELEXIR generally takes a similar approach to MEVELER, but expands the 2D photoelectron image (raw data from experiment) into a 1D series of Legendre polynomials. This has been shown to be a valid expansion,²⁰⁰ and greatly reduces the number of data points required to be analysed in the maximum entropy algorithm. As such, MELEXIR improves upon the speed of the MEVELER algorithm whilst retaining comparative accuracy. MELEXIR can be applied to low-intensity images with signals down to 0.001 counts per pixel.

Figure 2.9 displays an example comparison between POP and MELEXIR, in low signal-to-noise conditions. Both algorithms were applied to the same photoelectron image, which contained a weak trace photoelectron signal arising from the uracil anion, which should be centred at an electron binding energy $VDE \approx 75$ meV. Using POP, the reconstructed peak is not particularly smooth and it is difficult to confidently determine the VDE. Smaller peaks are present at negative electron binding energies, where no signal is expected, showcasing the present level of noise. Conversely, the MELEXIR algorithm produces a Gaussian-like signal, with very little noise elsewhere. In this example, MELEXIR is clearly the superior choice in reconstruction algorithm, although this should not be treated as universally true.

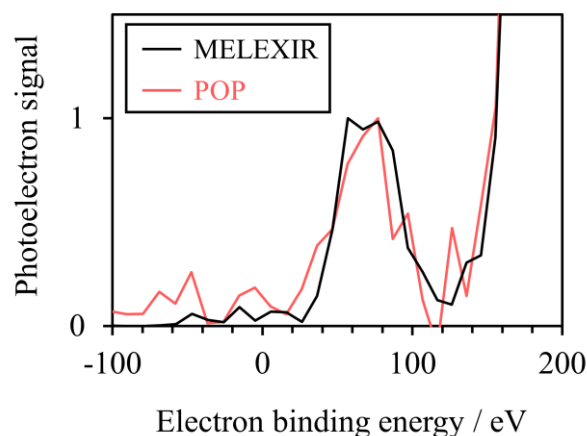


Figure 2.9: Comparison of the MELEXIR (black) and POP (red) algorithm performance on a photoelectron image that contained trace amounts of signal arising from the uracil anion.

2.2.5. Ion Noise Reduction

It was found that a larger backing pressure on the Even-Lavie valve was favourable for the formation of certain anion clusters, such as those described in Chapter 6. Unsurprisingly, this increases the pressure within the vacuum chamber during operation of the valve. In a typical experiment using 10 bar of N_2 backing gas, the pressure within the electron detector chamber typically exceeded 10^{-6} mbar. This is sufficiently high that a significant number of stray anions impact upon the MCP detector during low-signal experiments, causing

problematic noise levels. To combat this, we opted to pulse the bias across the two MCPs such that electrons (and stray ions) can only be detected for a short duration (~ 100 ns) after the laser pulse intersects the anion packet of interest. This is referred to as ‘gating’ the detector MCPs. Therefore, the electron detector now takes a default position of inactivity, and no longer measures background impacts in the time between valve openings.

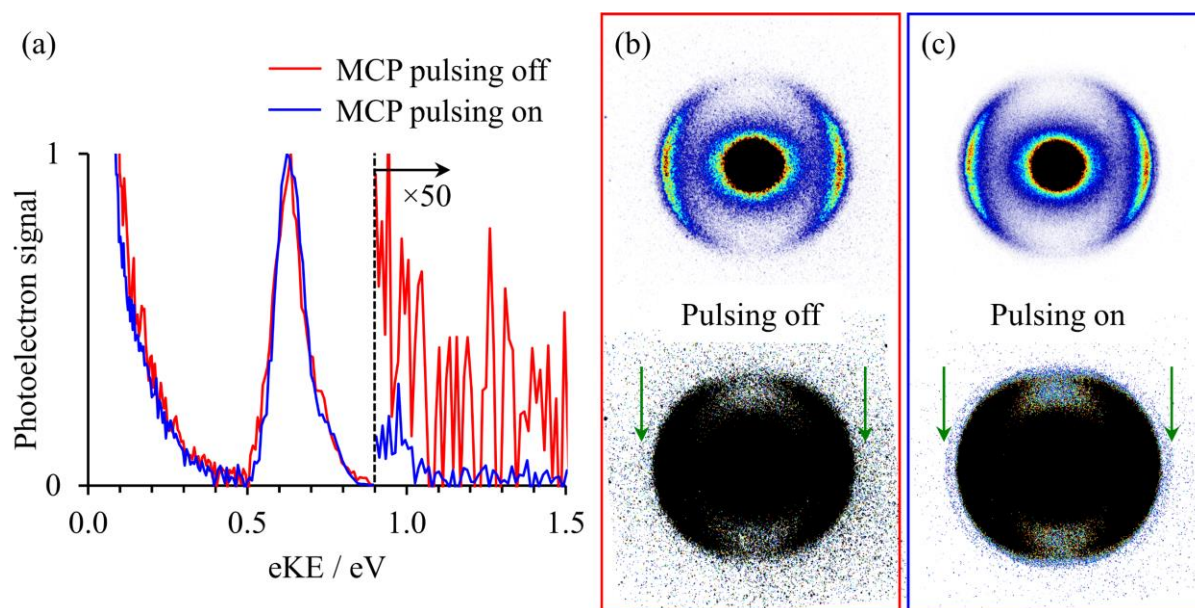


Figure 2.10: Demonstration of the noise-reduction when pulsing the gain across the MCPs of the electron detector. (a) Exemplar photoelectron spectra of the uracil dihydrate anion acquired with (blue) and without (red) pulsing the MCP detector. High-eKE (>0.9 eV) signal is magnified by a factor of 50 to accentuate the outermost feature. (b) and (c) show the corresponding photoelectron images, with the colour scale adjusted to highlight the $eKE \approx 0.7$ eV feature (top) and the outermost feature (bottom). Green arrows serve to highlight the radial position of the outermost feature, which is only clearly discernible when the MCPs are pulsed.

To assess the degree of noise reduction instilled by gating the MCPs, we acquired photoelectron images (using an equal number of shots) from a species which exhibits a very weak signal. The chosen anion was uracil dihydrate, $U^-(H_2O)_2$, which displays multiple photodetachment features when exposed to $h\nu = 1.0$ eV laser pulses. These features are discussed in more detail in Chapter 6, but here we focus on a very weak photoelectron signal between $0.9 < eKE < 1.0$ eV corresponding to detachment from the bare uracil anion, U^- , which

formed following evaporation of the clustered water molecules. As shown in Figure 2.10(a), signal arising from the U^- fragment was only discernible from background noise (which constitutes signal with $eKE > 1.0$ eV) when the MCP bias was pulsed. This is made more apparent in the photoelectron images, shown in panels (b) and (c) within Figure 2.10, particularly when saturating the colour scale of the images (lower half of panels).

2.3. The Electrospray Instrument

The following chapter showcases an experiment performed on the electrospray ionisation (ESI) instrument, for which a brief description is presented here. For further information, see ref. 25 and the various PhD theses of past members of the Verlet group.^{25,187,201–203} The general structure of the ESI instrument is similar to that of the cluster instrument: anions are produced in the source region, separated by time-of-flight, and photodetached inside a VMI electron spectrometer.

2.3.1. The ESI Source

The ESI instrument is primarily differentiated from the cluster instrument by its ion source region. Figure 2.11 shows a sketch of our ESI source. A dilute solution (usually a few mM in ammoniated methanol) of the target anion is injected through a narrow needle, forming a droplet that is exposed to a large potential gradient (5 kV). The electric field is biased such that anions are drawn to the surface of the droplet nearest the capillary opening of our vacuum chamber, where the droplet distorts into a Taylor cone.²⁰⁴ From here, aerosol droplets containing the target anion are sprayed toward the centre of the capillary opening. Solvent molecules evaporate away from the aerosol droplets as they travel towards the capillary, increasing the charge density of the droplets. Eventually, the Rayleigh limit is surpassed, inducing rapid fragmentation into much smaller droplets. As the small droplets proceed further into the differentially pumped vacuum chamber, the remaining solvent molecules also evaporate to surrender the bare monomer anion to the gas phase.

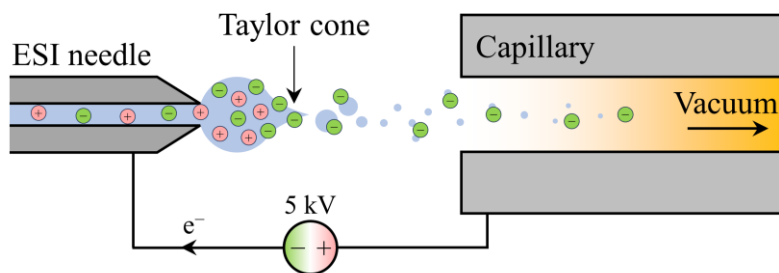


Figure 2.11: Schematic of the electro spray ionisation source used in the Verlet group. Anions are sprayed from the tip of the ESI needle towards the vacuum chamber, driven by the strong electric field applied.

Electrospray ionisation has become an increasingly attractive technique for anion generation in the field of photochemistry. Much of this drive is a consequence of ESI being a ‘soft ionisation’ technique, enabling the formation of very large and fragile anions in the gas phase.²⁰⁵ Generating large anionic species is far more difficult to achieve in molecular beam experiments, as they generally rely on harsher electron attachment schemes that can induce fragmentation. Since ESI preforms the anions in the solution phase, fragmentation is a lesser concern. Additionally, anions which preferentially form in solution, such as deprotonated species and multivalent anions, become far easier to study with ESI. This has even led to the creative technique of studying neutral molecules within a larger anion,²⁰⁶ in which a distant, spectating anionic group is tagged onto the neutral molecule to enable its formation through ESI and study with anion photoelectron spectroscopy.

2.3.2. Remaining Instrument and Recent Alterations

The ESI source operates continuously, whereas our laser systems are pulsed. Therefore, we accumulate the generated anions in an electrostatic trap to increase the ion packet density, and pulse open the trap at a repetition rate matching the laser. To achieve this, electro sprayed anions are directed through the vacuum chamber by RF (radio-frequency) ring electrodes,

which are biased along the ion propagation axis to transversely ‘push’ the anions forward. The RF field (and electrode geometry) acts to radially confine the anions during their flight. The terminal ring electrode is inversely biased, creating a transverse potential well which traps the anions. At the chosen repetition rate, the bias of the terminal ring electrode is reversed, driving the more dense ion packet out of the trap. For a standard experiment operated at 10 Hz, the ions are therefore allowed to accumulate for 100 ms. Throughout the accumulation period, a small amount of helium buffer gas is flowed into the trap, promoting vibrational cooling (and often collision-induced dissociation) of the target anions. Anions thermalise to approximately room temperature, and therefore clusters do not typically form. The remainder of the experiment is very similar to that described in the cluster instrument. Upon exiting the electrostatic trap, the anions enter a Wiley-McLaren time-of-flight mass spectrometer.¹⁹⁰ The mass-selected anions of interest are then intersected with a laser pulse at the centre of a VMI photoelectron spectrometer. The VMI electron kinetic energy resolution of the ESI instrument is poorer than that of the cluster instrument: approximately 5% (FWHM) across a large range of eKE.

An ion reflectron was recently added behind the VMI spectrometer, allowing us to identify anionic fragments which may form via photoexcitation. A potential use case for this is outlined at the end of Chapter 3. The reflectron also contains an MCP detector at its rear. This enables the further detection of neutral photodissociation products, which are unperturbed by the electric fields of the reflectron. Taken together, the VMI photoelectron imaging, and anion and neutral photofragment detection, should provide a more complete picture of dissociative photodetachment processes.

2.4. The Role of Electronic Structure Calculations

This chapter will close by emphasising the important role that electronic structure calculations, and other quantum chemical computations, play in the interpretation and prediction of the experimental traces of anions. Experiment and theory push each other to achieve better results, and the following chapters of this thesis showcase some examples of their mutual support. This section presents an introductory overview of some common techniques, but finer details on the exact methods used are outlined in the methodology sections of each subsequent chapter.

2.4.1. Solving the Schrödinger equation

One will be hard-pressed to find a quantum chemistry textbook that does not begin by introducing the time-independent non-relativistic Schrödinger equation:

$$H\psi = E\psi . \quad (2.1)$$

H is the Hamiltonian operator of the system, and the eigenequation determines the wavefunctions ψ and corresponding energy eigenvalues E . Electronic structure calculations aim to solve the Schrödinger equation, producing a set of ψ that describe the molecular orbitals. Within the Born-Oppenheimer approximation, the electronic Hamiltonian (in atomic units) takes the general form:²⁰⁷

$$H = -\sum_{i=1}^N \frac{1}{2} \nabla_i^2 - \sum_{i=1}^N \sum_{A=1}^M \frac{Z_A}{r_{iA}} + \sum_{i=1}^N \sum_{j>i}^N \frac{1}{r_{ij}} . \quad (2.2)$$

In this expression, indices i and A run over the total N electrons and M nuclei, respectively. The variable r represents the electron-nucleus or electron-electron distance, as labelled by the subscripts. The final term describes the inter-electron potential, which is the most difficult portion to treat computationally.

Solving the Schrödinger equation is not possible except for the simplest of systems, and thus computational chemistry searches for the best approximate solutions. Each individual electron is described by a spin orbital χ , which simply encapsulates the one-electron spatial wavefunction along with its binary (up or down) spin. In order to appropriately deal with electron exchange and satisfy the Pauli exclusion principle, the total N -electron wavefunction ψ can be approximated as a Slater determinant of the spin orbitals. This approximation is foundational to Hartree-Fock (HF) theory, which reframes the Schrödinger equation into N one-electron Hartree equations that are solved through self-consistent field methods.^{207,208} In accord with the variational principle,²⁰⁹ the best calculated wavefunction ψ is the one that minimises the electronic energy, E .

Hartree-Fock theory is the cornerstone of modern *ab initio* computational methods. However, the single-Slater determinant approximation is too restrictive in common scenarios: most importantly, the inter-electron potential is treated using a mean-field approximation, and therefore the effect of (Coulombic) electron correlation is completely neglected. So instead, a linear combination of Slater determinants can be used to describe ψ with accountment for electron correlation, as in the configuration interaction (CI) method.²¹⁰ Other post-HF methods alleviate this problem in different ways. For instance, Møller-Plesset (MP) theory²¹¹ treats correlation through perturbation of the electronic Hamiltonian, and coupled-cluster (CC) techniques²¹² apply an exponential operator to the HF wavefunction in order to construct a many-electron wavefunction that accounts for electron correlation. But common to all post-HF methods is a far greater computational cost, and therefore the correcting terms must be truncated.

2.4.2. Density Functional Theory

Density functional theory (DFT) also seeks to find a solution to the electronic Schrödinger equation, but takes advantage of the injectivity of the ground-state ψ to a minimal-energy functional of the electron density, $F[\rho]$. That is to say, the physically observable electron density ρ of a molecule, rather than its full electronic wavefunction, can equivalently be used to solve the Schrödinger equation for the ground state. Working with ρ has an important benefit over the *ab initio* techniques described above. DFT calculations are far more computationally efficient than competing *ab initio* techniques, since ρ depends on only three Cartesian coordinates whilst ψ depends on $3N$ dimensions (i.e. the coordinates of every electron).²¹³ However, the DFT functional that describes exchange and correlation interactions is not known *a priori*, and must be treated approximately.

Fortunately, modern quantum chemistry programs incorporate a wealth of reputable options. Approximate exchange functionals and correlation functionals can be combined into pure exchange-correlation functionals, such as PW91.²¹⁴ Hybrid exchange-correlation functionals, such as the now (relatively) famous B3LYP,^{215,216} treat a fraction of the exchange interactions exactly (i.e. using HF), and are empirically optimised to thermochemical measurements. For calculations on anions (which are highly polarisable), it is very important to treat long-range interactions successfully, and so more specialised functionals can be applied. The long-range corrected CAM-B3LYP functional uses different proportions of approximate and exact (HF) exchange, depending on the range of interaction.²¹⁷ Other long-range corrected functionals are also available (e.g. ω B97X-D),²¹⁸ and it is generally recommended to repeat DFT calculations using several different functionals to ensure reliable results.

2.4.3. Basis Sets

Having now discussed different levels of theory that can be applied for quantum chemical calculations, we now turn to the choice of basis set. In order to be computationally tractable, electronic wavefunctions must be described by a *finite* linear combination of functions that form the basis set. This imposes a new restriction on the electronic wavefunction that can be calculated, and therefore the correct choice of basis set is imperative for any calculation of electronic structure. Basis functions are typically constructed from primitive Gaussian type orbitals, described by the product of separate radial and angular (spherical harmonic) components.

A plethora of specialist basis sets are readily available;²¹⁹ the work outlined in this thesis utilises variants of the polarised, correlation-consistent Dunning basis set.^{220,221} The Dunning basis sets are denoted cc-pV ζ Z, where ζ denotes the number of basis functions that form each valence atomic orbital ($\zeta = D, T, Q, 5, \dots$; where D refers to double, T to triple, etc.). These basis sets can also be augmented with additional diffuse functions, denoted aug-cc-pV ζ Z. The augmented Dunning basis sets are particularly good at describing the diffuse and polarisable nature of anions, and have elsewhere been tagged the ‘gold standard’.²⁰³

However, sometimes even aug-cc-pV ζ Z is not sufficiently diffuse. Non-valence state anions (described in Section 1.2) have electron densities that can span many tens of Å, so require specialist basis sets.^{2,222–224} For a suitable treatment, the aug-cc-pV ζ Z basis set can be again augmented with extra-diffuse basis functions, which will be denoted, for instance, by aug-cc-pV ζ Z+*n*s*m*p, where an additional *n* s functions and *m* p functions are implemented.²²⁵ Typically, these extra-diffuse functions do not need to be added to every atom in the molecule, and can even be affixed onto a ghost atom if preferred. The number of additional functions, e.g. *n* and *m*, that is required will depend on the non-valence state system being studied. To

determine this number, the extra-diffuse basis set can be incrementally built up (aug-cc-pV ζ Z+1s1p, aug-cc-pV ζ Z+2s2p, etc.) until the energy of the non-valence anion state becomes stable.²²⁶ It is generally wise to keep the basis set minimal, as each subsequent diffuse function adds significantly to the computational cost.

2.4.4. Anion Resonances

Unfortunately, it can be very difficult to reliably calculate anion resonance states due to their instability towards electron loss. Any attempt to calculate the MOs of an unstable anion will also inevitably produce discretised continuum orbitals (DCOs), which are essentially solutions to the Schrödinger equation that represent the excess electron having left the molecule (i.e. neutral plus free electron).²²⁷ Discretisation of the continuum arises from the finite basis set being used, and therefore the number of undesirable DCOs increases with a more comprehensive basis set, particularly if more diffuse basis functions are added. This creates a tension between requiring an expansive basis set such that the electron density of the anion is accurately computed, but also wanting a restricted basis set to minimise contributions of DCOs.

This issue is elegantly summarised in a recent publication by T. C. Jagau,^{228,229} for which a pictorial representation of the interplay is reproduced in Figure 2.12. With a limited (or non-diffuse) basis set, the calculated energies of a metastable anion X^- (blue) and its neutral X (red) are poorly captured. As more (diffuse) basis functions are added, the calculated energetics improve, but new DCOs appear (grey). With too large a basis set, many representations of X^- appear, partially coupling to the continuum. In the theoretical limit of a complete basis (right of Figure 2.12), we can recognise that the anion resonance is truly represented by an increased density of (continuum) states at the electron attachment energy. To summarise, it is often practical to moderately restrict the basis set in the computation of anion

resonance states, and to be prudent with the quantitative determination of excitation energies involving resonance states.

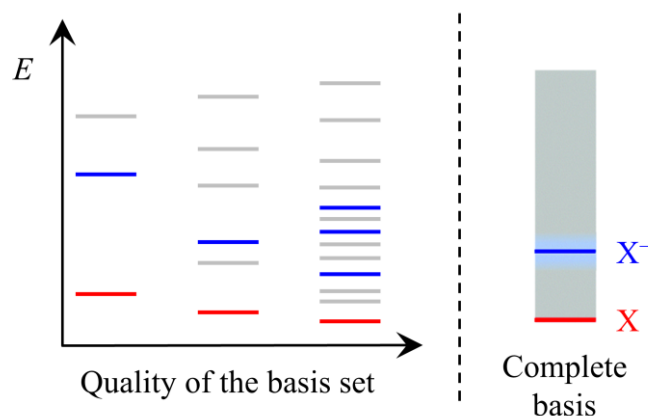


Figure 2.12: Schematic showing the effect that the quality of basis set can have on the calculated energy of a metastable anion X^- (blue) and its corresponding neutral X (red). DCOs (grey) emerge with a more diffuse basis set, and eventually multiple descriptions of the metastable anion are observed. A complete basis set recovers the continuum of states (right of dotted line), where the density of states increases near the energy of X^- . Adapted with permission from Chemical Communications.²²⁹

A useful technique for estimating electron attachment energies into anion resonance states is the stabilisation method.²³⁰ Beginning with the neutral molecule in its optimised geometry, a series of single-point energy calculations are performed using different basis sets. Each basis set only differs by a scaling factor α that is applied to the most diffuse basis functions on each atom. The energies of the computed virtual molecular orbitals are tracked with changing α , and respond differently depending on their electronic character. The energies of virtual orbitals that represent valence anion resonance states are fairly insensitive to the changing diffuseness of the basis set, since they are already accurately described by the more localised basis functions. Conversely, energies of virtual orbitals describing DCOs are heavily influenced by the spatial extent of the basis set, since the most diffuse basis functions control how far the electron is allowed to leave the molecule. Therefore, as α is decreased

(corresponding with a more diffuse basis set), DCOs are stabilised whilst the valence anion resonance states are essentially unperturbed. This leads to avoided crossings between these differently behaving orbitals, from which the energy of the anion resonance can be estimated.²³¹ An example of the stabilisation method being applied is given towards the end of Chapter 5.

In the context of anion photoelectron spectroscopy, we are more interested in excitation energies from a ground-state anion to a resonance (or bound excited) state. Time-dependent density functional theory (TDDFT) is a common technique for calculating excitation energies, owing to its efficiency.²³² However, in calculations involving anion resonances, one must remain cautious of excitation to contaminant DCOs, and be aware that self-interaction errors can be prevalent for long-range charge-transfer type excitations.²³³ Often, quantitatively accurate results can only be achieved through more specialised *ab initio* techniques,²⁰³ which are beyond the scope of this thesis.

Chapter 3 – Photodissociation of the Pyruvate Anion

This chapter details and builds upon the following publications:

²³⁴ C. J. Clarke, J. A. Gibbard, L. Hutton, J. R. R. Verlet and B. F. E. Curchod, *Nat. Commun.*, 2022, **13**, 937

All experimental work was performed by C. J. Clarke and J. A. Gibbard. All computational work was performed by B. F. E. Curchod and L. Hutton.

3.1. Introduction

There is an abundance of highly reactive molecules and ions in our atmosphere, leading to a complex cocktail of perpetual chemical reactions.^{235–237} As such, there is a large drive towards understanding the photochemistry of atmospheric molecules of biogenic or anthropogenic origins. The presence of clouds (and more generally, aerosols) means that atmospheric molecules do not exist solely in the gas-phase, but also within water droplets (of different sizes and compositions) and at their surfaces. In particular, hydration tends to stabilise charged species, allowing water droplets to promote the formation of many anions (and cations). In the context of acidic atmospheric molecules, the photochemistry of an anionic conjugate base may therefore be comparatively important to the neutral species.

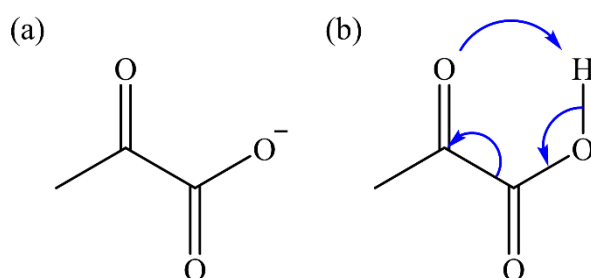


Figure 3.1: (a) Structure of the pyruvate anion. (b) Structure of pyruvic acid, highlighting the decarboxylation mechanism initiated by photoexcitation to the S_1 state. This mechanism involves a proton which the pyruvate anion lacks.

Pyruvic acid and its conjugate base, the pyruvate anion $\text{CH}_3\text{COCOO}^-$ (shown in Figure 3.1(a)), are pervasive throughout the atmosphere and elsewhere in nature (e.g. seawater).^{238,239} Their presence in atmospheric aerosols has attracted particular attention due to the rich photochemistry of pyruvic acid, which differs between the gas and solution phase and at their dividing interface,^{240–242} and because pyruvic acid serves as a representative α -dicarbonyl in atmospheric models.²⁴³ Of particular interest is the near-UV photoexcitation of pyruvic acid in water, populating the first excited singlet state, S_1 . This leads to decarboxylation

through an intramolecular proton transfer mechanism (Figure 3.1(b)), and eventual production of acetaldehyde (through a methylhydroxycarbene intermediate).²⁴⁴⁻²⁴⁸ In an aqueous environment, the photoproducts can react further, producing acetoin, lactic acid, acetic acid, and oligomers.²⁴³ This observation has triggered consideration of pyruvic acid as a precursor to primitive metabolism – an essential feature for life.²⁴⁹ But what of the conjugate base, which is also prevalent in aerosols and seawater?^{250,251} We aimed to investigate if the pyruvate anion could undergo photoinduced decarboxylation, despite the anion lacking the H atom involved in the intramolecular proton transfer step.

3.2. Methodology

3.2.1. Experimental

Deprotonated species are typically best studied with the electrospray ionisation (ESI) instrument, described in Chapter 2. Pyruvic acid (Sigma-Aldrich) was mixed with ammoniated methanol to undergo near-complete dissociation, forming a ~ 100 mM solution of pyruvate anions. The anions were electrosprayed into ultrahigh vacuum, accumulated in a collisional cooling trap, and ejected into a Wiley-McLaren time-of-flight mass spectrometer. A single intense peak with a mass to charge ratio of 87 was observed (Figure 3.2). FRPES was performed using nanosecond laser pulses, supplied by the Nd:YAG (Surelite) pumped OPO (Continuum). TRPES utilised femtosecond pulses (FWHM ~ 100 fs) of 400 nm (pump) and 800 nm (probe). Photoelectrons were collected in a VMI spectrometer with a spectral resolution of $\Delta eKE/eKE \approx 5\%$.²⁵² The polar onion-peeling (POP) algorithm was used for image reconstruction.¹⁹⁵ For the laser flux measurements, a thermopile power meter monitored the laser power at the backside of the experiment.

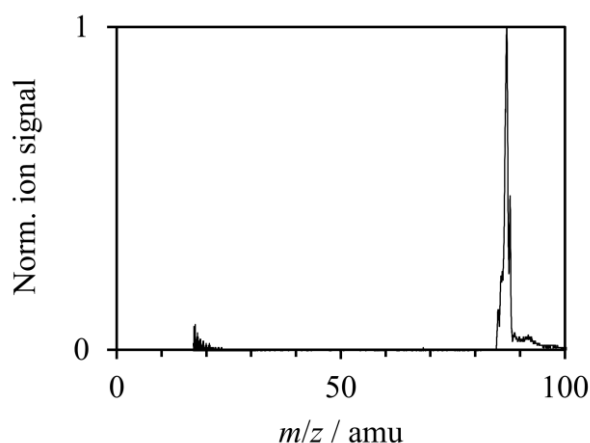


Figure 3.2: Mass spectrum of electrosprayed pyruvic acid solution, showing a dominant feature corresponding to the pyruvate anion.

3.2.2. Computational

The experimental results were supported by electronic structure calculations and simulations, provided by B. F. E. Curchod and L. Hutton. An overview of these computations will be provided here. To begin, the minimum electron binding energy of the pyruvate anion in its equilibrium geometry was calculated using (unrestricted) density functional theory (DFT) with the ω B97X-D functional²¹⁸ and the aug-cc-pVDZ basis set^{221,253}. The chosen functional treats long-range electron-electron interactions with full Hartree-Fock exchange to resolve self-interaction errors. As with any basis set, there is a compromise between ensuring high accuracy and minimising computational cost. Crucially, aug-cc-pVDZ is augmented with diffuse bases which are necessary to capture the broad electron density exhibited in anions. The calculated electron binding energy was verified with the *ab initio* method (U)CCSD(T)-F12/aug-cc-pVTZ,²⁵⁴ and both levels of theory showed excellent agreement to experiment and each other. Electron binding energies of possible photofragments were also calculated at the same levels of theory, and too showed good agreement. These are summarised in Table 3.1. The DFT calculations were performed using Gaussian09,²⁵⁵ whilst the more expensive *ab initio* results were computed with Molpro 2012.²⁵⁶

Table 3.1: Electron binding energies for the pyruvate anion and possible photofragments at their respective optimise ground state geometries, calculated with (unrestricted) ω B97X-D/aug-cc-pVDZ and CCSD(T)-F12/aug-cc-pVTZ.

Level of theory	Electron binding energy / eV		
	Pyruvate anion	Acetyl anion	Methide anion
ω B97X-D/aug-cc-pVDZ	3.786	0.606	0.381
CCSD(T)-F12/aug-cc-pVTZ	3.906	0.665	0.395

In order to simulate photoelectron spectra of the pyruvate anion and its potential photofragments, a nuclear ensemble approach (NEA) was taken. Generally, this technique works best when there is poor vibrational overlap between initial and final states, such as when the equilibrium geometries of the respective states show a large difference, or the target state is dissociative (or substantially anharmonic). A comparative schematic between the NEA and a more conventional approach based on Franck-Condon factors is shown in Figure 3.3. For the NEA taken in this study, 500 molecular geometries were sampled from a Wigner distribution around the initial anion in its equilibrium geometry at 0 K (ground vibrational state). The vibrational mode frequencies were calculated using ω B97X-D/aug-cc-pVDZ and the modes were treated as uncoupled harmonic oscillators for the construction of the Wigner distribution. To simulate the photoelectron spectra, the VDE was calculated for each sampled geometry. Since the oscillator strength associated with each transition differs, the signal arising from each transition was weighted by the norm of the associated Dyson orbital. The result is a ‘stick’ spectrum, representing the photoelectron signal as a function of electron binding energy. To produce a smooth function akin to that seen experimentally, each transition was broadened by a narrow Lorentzian function (0.05 eV width), and summed together. The Newton-X 2.0 package²⁵⁷ was used to produce the Wigner distribution, sample the geometries, and simulate the photoelectron spectra.

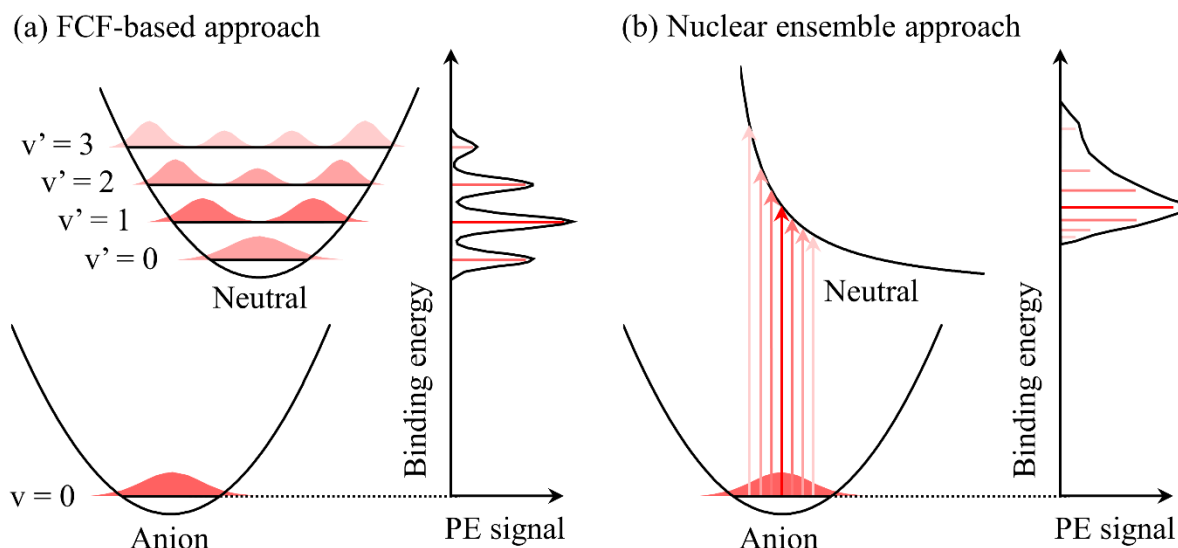


Figure 3.3: Visual representations of two methods which can be used to simulate photoelectron (PE) spectra. (a) Photoelectron ‘stick’ spectrum acquired by calculating vibronic transitions and their associated Franck-Condon factors (FCFs). (b) The NEA, where an ensemble of nuclear geometries is generated (from a Wigner distribution, in this work) around the equilibrium geometry of the anion. Vertical energy gaps to the anharmonic neutral state are calculated and the oscillator strength is given by the corresponding Dyson orbital norm. One ‘stick’ is produced per geometry. Photoelectron spectra are broadened according to experimental parameters.

The photoexcitation cross-section associated with the $S_1 \leftarrow S_0$ transition in pyruvate was also calculated with the NEA, using the same 500 geometries as for the simulated photoelectron spectrum (i.e. sampled with ω B97X-D/aug-cc-pVDZ). The $S_1 \leftarrow S_0$ transition energies and oscillator strengths were calculated with SCS-ADC(2)/cc-pVTZ. Note that the augmented diffuse functions have been removed in order to limit the contributions of DCOs. Turbomole 7.3.1²⁵⁸ was used for the more expensive SCS-ADC(2) calculations.

Although not presented in detail here, exploratory molecular dynamics simulations were performed to give mechanistic insight into the photodissociation process, and verify the fast S_1 decay observed in the TRPES experiment. The methodology behind these calculations is more complex and will only be summarised briefly for completeness – the reader is directed to the published article for more information.²³⁴ *Ab initio* molecular dynamics simulations were

initiated from ground state equilibrium geometry of the (fragment) acetyl anion, CH_3CO^- , with nuclear velocities sampled from a Boltzmann distribution at 2200 K. The energy of dissociation into CH_3^- and CO was then determined to be $\sim 100 \text{ kJ mol}^{-1}$ ($\sim 1 \text{ eV}$). Exploratory simulations probing the S_1 dynamics of pyruvate were performed but remain unpublished at present. Rapid decarboxylation was observed, congruent with production of the acetyl anion.

3.3. Photoelectron Spectroscopy of Pyruvate

3.3.1. Detachment and Excitation

Photoelectron images of the pyruvate anion were acquired following irradiation with nanosecond laser pulses at a series of different photon energies within the near-UV spectral region, $3.3 \leq h\nu \leq 4.3$ eV (in steps of 0.1 eV). The resulting photoelectron spectra were normalised to their maximum signal and are presented in Figure 3.4. There are two main features present in the FRPES data: a broad Gaussian-like feature which shifts higher in eKE with increasing photon energy – this is most clearly apparent in the $h\nu = 4.3$ eV spectrum; and low-energy electrons which are released with a Boltzmann distribution of energies (exponential decay trace), dominating the $3.3 \leq h\nu \leq 3.9$ eV spectra. The former broad peak arises from a direct photodetachment process from the S_0 ground state of the pyruvate anion, to the ground state of the resulting neutral, D_0 . The latter low-eKE trace is characteristic of electrons originating from thermionic emission.

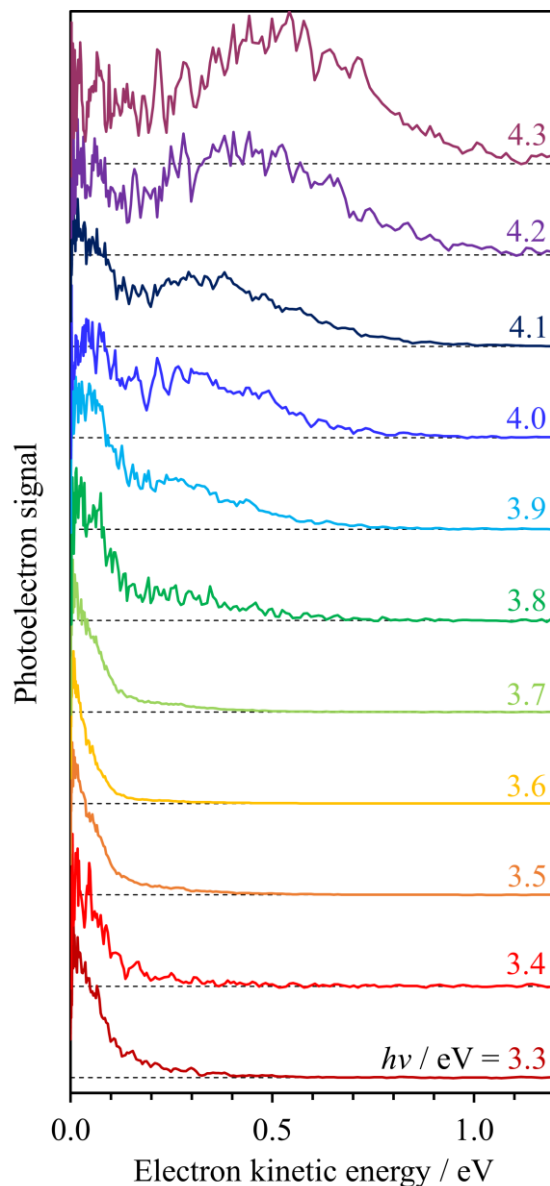


Figure 3.4: Photoelectron spectra of the pyruvate anion acquired with nanosecond laser pulses with a range of different photon energies $h\nu$. Each spectrum has been normalised to its maximum intensity, and so comparison of intensities across different spectra should be approached cautiously.

We begin by examining the direct photodetachment feature. There are two useful energy gaps which can be extracted – the vertical detachment energy (VDE) and the adiabatic detachment energy (ADE) of the pyruvate anion. As each photoelectron spectrum contains this information, we will focus on the spectrum which shows the direct photodetachment feature most clearly: $h\nu = 4.3$ eV. Figure 3.5(a) displays this spectrum with a reformatted horizontal

axis, quantified by the electron binding energy, $eBE = h\nu - eKE$. The VDE is given by the eBE at which there is greatest photoelectron signal: here, $VDE = 3.8 \pm 0.1$ eV. The lowest eBE at which there is significant photoelectron signal (which was chosen to be 10% of maximum signal) represents the ADE, which is found to be ~ 3.3 eV, comparable to the electron affinities of other carboxylates.

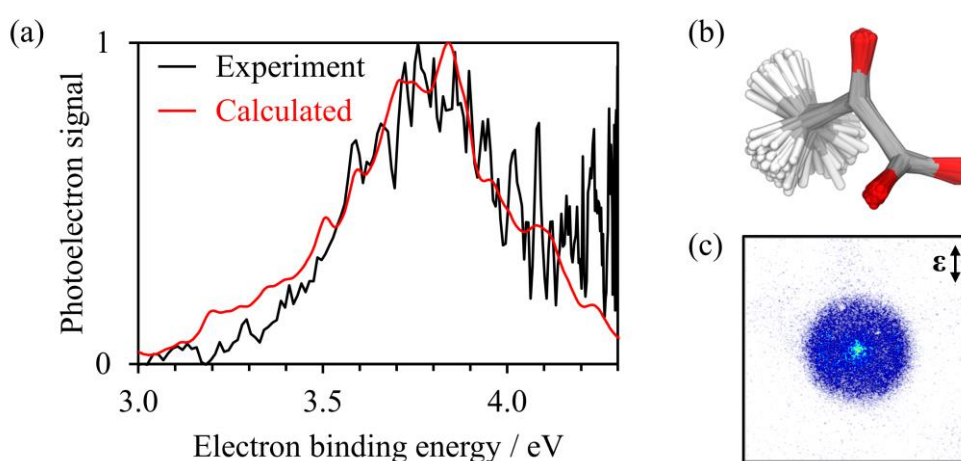


Figure 3.5: (a) Photoelectron spectrum of pyruvate acquired at $h\nu = 4.3$ eV (black), plotted against the electron binding energy, defined as $eBE = h\nu - eKE$. Overlaid in red is the calculated $D_0 \leftarrow S_0$ photoelectron spectrum, obtained with the nuclear ensemble approach (NEA) using $\omega B97X-D/aug-cc-pVDZ$. (b) The sampled geometries used in the NEA. (c) The corresponding measured photoelectron image. The direction of laser polarisation (ϵ) is indicated on the image, demonstrating a slight perpendicular anisotropy in the signal ($\beta_2 < 0$).

The large disparity in the ADE and VDE indicates that the equilibrium geometries between anionic and neutral pyruvate are substantially different. Furthermore, there is no distinct vibrational structure in the experimental data (at any of the implemented photon energies). This suggests that the photoelectron spectrum is most suitably simulated using a nuclear ensemble approach (NEA), rather than more conventional methods involving FCF calculations. Density functional theory at the $\omega B97X-D/aug-cc-pVDZ$ level was applied to calculate the photoelectron spectrum corresponding to the direct $D_0 \leftarrow S_0$ transition, using the NEA with 500 initial geometries (Figure 3.5(b)). The result is overlaid onto the experimental

measurement in Figure 3.5(a), demonstrating excellent overall agreement and confirming our assignment of this peak. The only substantial deviation is at higher eBE, and results from thermionic emission contributions (i.e. the low-eKE feature).

Photoelectron imaging also allows us to measure the photoelectron angular distribution (PAD) of the outgoing electrons. As discussed in Chapter 1, PADs are quantified by the anisotropy parameter, β_2 , which has limiting values of +2 and -1. Direct photodetachment of the pyruvate anion at $h\nu = 4.3$ eV produced a PAD described by $\beta_2 \approx -0.2$, i.e. detachment was preferentially perpendicular with respect to the fixed laser polarisation axis (Figure 3.5(c)). This is consistent with the predominantly non-bonding p-orbital nature of the S_0 state.

We now turn to the second feature: the low-eKE photoelectron signal arising from thermionic emission. In the mechanism of thermionic emission, the internal energy of the participating anion exceeds its electron binding energy, and an electron is lost from the anion in a statistical manner. The excess energy is provided through photoexcitation, and therefore the observation of thermionic emission reflects the presence of an electronically excited state of the pyruvate anion. Thermionic emission was strongest in the $3.3 \leq h\nu \leq 3.9$ eV spectra, so we deduce that the pyruvate anion has an excited state ~ 3.6 eV above S_0 , which is likely the S_1 ($n\pi^*$) state. To support this assignment, the $S_1 \leftarrow S_0$ photoexcitation cross-section was calculated using the NEA. The calculated photoexcitation cross-section, shown in Figure 3.6, displays significant intensity across the entire energy range over which thermionic emission was observed. Although $n\pi^*$ states are often optically dark, it appears the experiment was capable of accessing this excited state.

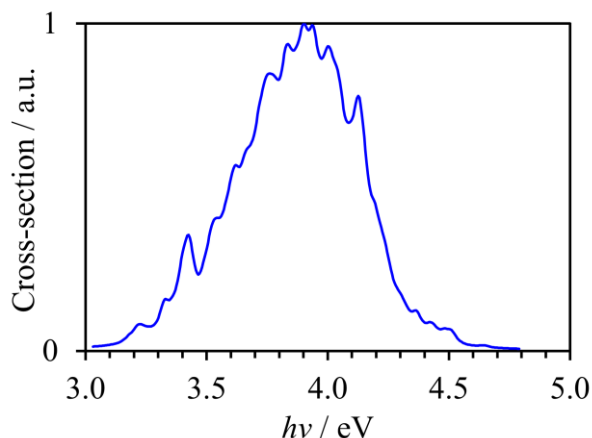


Figure 3.6: Calculated photoabsorption cross-section corresponding to the $S_1 \leftarrow S_0$ transition for the pyruvate anion. The nuclear ensemble approach (NEA) was applied with 500 geometries sampled from a Wigner distribution around the S_0 minimum geometry, where the necessary frequencies were obtained with ω B97X-D/aug-cc-pVDZ. Transition energies and oscillator strengths were calculated for each geometry using SCS-ADC(2)/cc-pVTZ.

3.3.2. A Mysterious Fragment

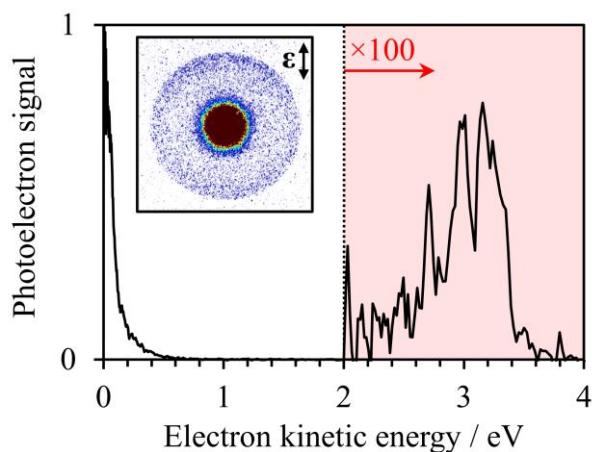


Figure 3.7: Normalised photoelectron spectrum of pyruvate acquired at $h\nu = 3.5$ eV, where the signal has been amplified by 100 in the red region (eKE > 2 eV). Inset is the photoelectron image: low-eKE signal has been saturated on the colour scale so that the weak high-eKE feature is visible.

A third feature was also present in the FRPES data – another Gaussian-like peak positioned at very high eKE. This is shown in Figure 3.7 for $h\nu = 3.5$ eV, the photon energy at which the peak was strongest. The corresponding photoelectron image is also displayed, where

there is a distinct ring at large radius (equivalent to a high eKE). At $h\nu = 3.5$ eV, the peak has a high-energy onset of eKE ≈ 3.4 eV, corresponding to a very low eBE ≈ 0.1 eV. This binding energy is far below the electron affinity of pyruvate (ADE ≈ 3.3 eV), so does not correspond to one-photon direct or indirect detachment from the parent anion. We first considered the possibility of simultaneous two-photon absorption of the pyruvate to detach an electron. This can occur when either the laser flux or photodetachment cross-section is particularly high. Therefore, the two-photon direct detachment feature is expected to essentially match that of the one-photon $D_0 \leftarrow S_0$ feature, but shifted $h\nu$ higher in energy. We can rule out this possibility in two ways. First, the outgoing eKEs do not quite match up – the feature is narrower than expected and positioned at significantly lower eKE. Second, the $h\nu$ dependence of the peak disagrees with that expected for a two-photon direct detachment. In particular, increasing the photon energy by 0.2 eV (to $h\nu = 3.7$ eV) shifts the peak higher by 0.2 eV. In a coincident two-photon absorption, the eKE is expected to change by twice this amount, so 0.4 eV. Figure 3.8 demonstrates that this is not the case over a large range of photon energies. With the possibility of a two-photon direct detachment process eliminated, we turn to other explanations for the high-eKE feature.

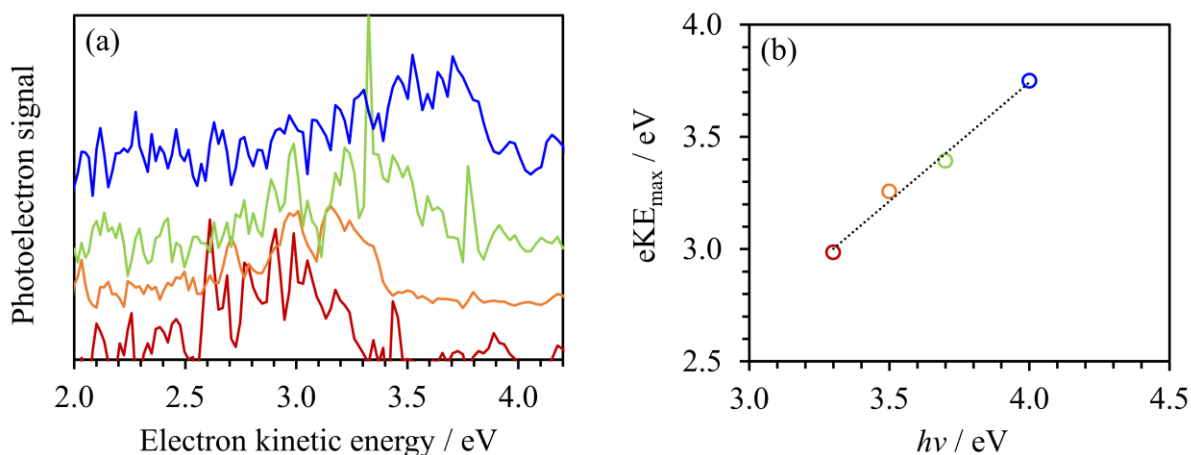
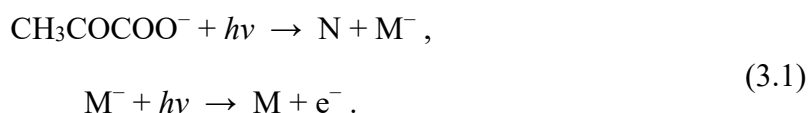


Figure 3.8: (a) Photoelectron spectra showing the high-eKE when acquired at different photon energies $h\nu$. The colours correspond to the FRPES photon energies shown in Figure 3.4: these are 3.3 (red), 3.5 (orange), 3.7 (green) and 4.0 (blue) eV. Each spectrum was normalised to the integral of the high-eKE feature, and then stacked in order of increasing $h\nu$. (b) eKE_{\max} represents the electron kinetic energy at which the third feature is strongest, for each $h\nu$. This was located by fitting one asymmetric Gaussian function to each spectrum. The linear fitting function (black dotted) has essentially unitary gradient (1.06).

The appearance of the high-eKE feature coincided with the presence of thermionic emission in the FRPES data, suggesting photoexcitation is playing a role. Following photoexcitation to the S_1 state, a number of different relaxation pathways will compete. Internal conversion back to the S_0 ground state is possible and may lead to the observed thermionic emission. Alternatively, nuclear dynamics prompted by photoexcitation will lead to geometric distortions, which may provoke dissociation of the molecule. For a monovalent species like pyruvate, only one of the resulting photofragments will be anionic. It is often the case that this smaller anion has a lower electron binding energy than the parent, such that photodetachment of the fragment produces a high-eKE feature like that seen in Figure 3.7. The proposed overall mechanism is therefore a two-photon process: the first photon populates the S_1 state in pyruvate; propagation of the nuclear geometry leads to dissociation; then finally, a second photon (within the same nanosecond laser pulse) photodetaches an electron from the resulting anionic fragment. This is summarised in Eq. 3.1, where N and M^- are the generated neutral and anionic photofragments, respectively.



It is important to note that this is a *sequential* two-photon process, and therefore will not necessarily exhibit the same $h\nu$ -dependence described above for the coincident two-photon absorption. Instead, excess energy from the first photon can be deposited into the partnered neutral fragment. Therefore, the outgoing eKE (following photodetachment of the anionic fragment) can increase at the same rate as the increasing photon energy. It appears so far the high-eKE feature is consistent with detachment from a photofragment, but what is the new species being detached?

Decarboxylation is a common photodissociation pathway observed in many anions, driven by the great thermodynamic stability of CO_2 . Moreover, photoexcitation of pyruvic acid to its S_1 state leads to loss of CO_2 with high efficiency, although pyruvate lacks the proton which promotes this pathway in the acid. Therefore, it seems very possible that pyruvate also undergoes decarboxylation, producing the acetyl anion, CH_3CO^- . To test if photodetachment from the acetyl anion was consistent with our low-eBE feature, we simulated its photoelectron spectrum, taking a NEA. The level of DFT implemented was $\omega\text{B97X-D/aug-cc-pVDZ}$, which earlier proved successful for the parent pyruvate. The result is displayed in Figure 3.9 (red) and compared to our high-eKE (low-eBE) feature (black). A photoelectron spectrum of the acetyl anion has also been measured by Nimlos *et al.*,²⁵⁹ and our simulated spectrum is in reasonable agreement: there is a small discrepancy in the electron binding energy (by ~ 100 meV), and the experimental data shows vibrational structure which cannot be captured by the NEA. Comparing the (calculated or experimental²⁵⁹) photoelectron spectrum of the acetyl anion to our photofragment feature reveals a greater deviation. Although there is some overlap between the two peaks, the low binding energy onset of the signal is mismatched by over 0.3 eV. Therefore, it appears that the acetyl anion is not the responsible photofragment.

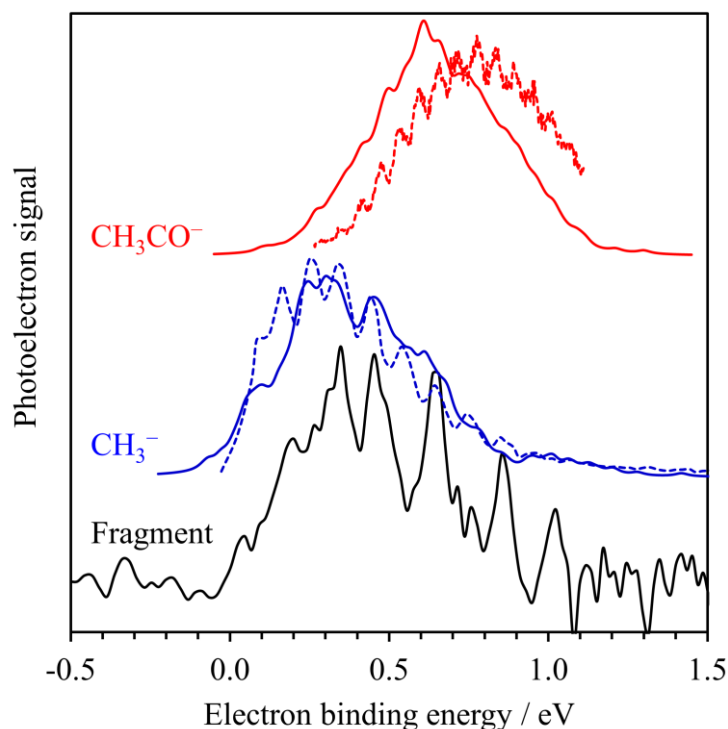
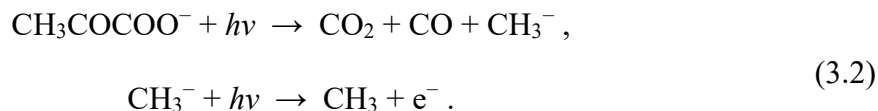


Figure 3.9: High-eKE feature in the $h\nu = 3.5$ eV photoelectron spectrum recast in terms of electron binding energy (black). Solid red and blue lines above show the simulated photoelectron spectra of two potential photofragments, CH_3CO^- and CH_3^- , respectively. These were calculated with the NEA using $\omega\text{B97X-D/aug-cc-pVDZ}$. Also shown is the previously measured photoelectron spectra for the potential photofragments (dashed). CH_3CO^- spectrum adapted with permission from Nimlos *et al.*,²⁵⁹ copyright 1989 American Chemical Society. CH_3^- spectrum adapted with permission from Oliveira *et al.*,²⁶⁰ copyright 2015 American Chemical Society.

Pyruvate is a small organic molecule, so there are a very limited number of sensible photodissociation pathways available. Since decarboxylation seems the likeliest dissociative process, we proceeded to consider the fate of the acetyl anion. Instead of living long enough to be detached by the second photon, what if CH_3CO^- also dissociates? Chemical intuition suggests that the C–C bond is the most likely to rupture in this case, producing CO and a methide anion, CH_3^- . Exploratory *ab initio* molecular dynamics simulations indeed confirmed this to be the case. Even at a relatively low temperature of 1400 K (bearing in mind that the pyruvate has absorbed a UV photon), the ground state acetyl anion was unstable with respect to CO loss. Once again, we applied the NEA to simulate the photoelectron spectrum of the

methide, which is shown in Figure 3.9 (blue). This time, there is excellent agreement between the calculation, an earlier measured photoelectron spectrum of CH_3^- by Oliveira *et al.*,²⁶⁰ and our observed high-eKE feature. We therefore assign the photofragment feature to direct photodetachment from the methide anion fragment. This follows the general mechanism outlined in Eq. (3.1), where there are two neutral fragments, $N = \text{CO}_2 + \text{CO}$:



It should be noted that the photodissociation process in the first step is not necessarily concerted. At this stage, we only conclude that in order to absorb the second photon in the same nanosecond laser pulse, the full photodissociation process from the parent pyruvate to CH_3^- must take place within approximately six nanoseconds (FWHM of the laser pulse).

To reinforce our identification of the photofragment, the measured PADs were examined. The corresponding anisotropy parameter at $h\nu = 3.5$ eV was determined to be $\beta_2 \approx +0.4$: a significant positive value. This is noticeable in the photoelectron image displayed in Figure 3.7, where there is more photoelectron signal parallel to the direction of the laser polarisation (top and bottom of ring). Oliveira *et al.* also investigated anisotropy in their photoelectron images of the methide anion,²⁶⁰ and found that β_2 could be appropriately modelled by a modified Wigner-Bethe-Cooper-Zare equation.¹⁸ The results of this equation, using empirically determined parameters for CH_3^- ,²⁶⁰ gives rise to a positive anisotropy parameter, in accordance with the measured PAD from our photofragment.

3.3.3. Photon Flux Dependence of the Methide Anion Peak

The flux dependence can generally be correlated with how many photons are involved in the overall photodissociation-detachment process. Following the scheme outlined in Eq.

(3.2), we might expect the flux measurements to indicate a two-photon process, or more if a photon cycling mechanism is required for dissociation.

To determine the photon flux dependence of the photofragment signal, we can acquire photoelectron spectra at different laser powers and compare the response of the photofragment peak to the response of a different peak in the photoelectron spectrum, acting as a reference signal. In particular, the $D_0 \leftarrow S_0$ direct detachment of pyruvate produces a strong signal in our photoelectron spectrum (at higher $h\nu$) and strictly arises from a one-photon absorption. Therefore, as the laser power (photon flux) is adjusted, any other photoelectron signal that arises from a one-photon process will scale at the same rate as the $D_0 \leftarrow S_0$ peak. Conversely, signal originating from a multiple photon process will typically scale differently.

Photoelectron spectra were acquired at $h\nu = 4.0$ eV with four different laser fluxes. The laser power was measured with a power meter positioned behind the interaction region. The integrated photoelectron signal corresponding to the CH_3^- detachment peak, I_M , was compared to the integrated $D_0 \leftarrow S_0$ (pyruvate) signal, I_D , by taking the ratio I_M/I_D . Each spectrum was normalised to the integral of the pyruvate detachment peak, such that $I_D = 1$. The results are shown in Figure 3.10, demonstrating a constant ratio with changing laser power. Surprisingly, this seems to suggest that only one photon is required for the dissociation-detachment mechanism. This seems impossible, as at least one photon is required for photodissociation, and a different photon is required to detach the resulting fragment. However, there is an alternative explanation for the constant flux relationship which does not contradict the mechanism in Eq. (3.2).

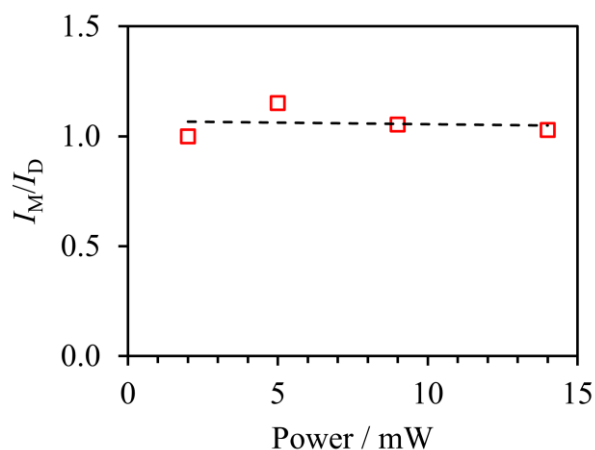


Figure 3.10: Integrated signal arising from direct detachment of the CH_3^- photofragment, I_M , relative to that of pyruvate, I_D . Laser power was monitored with a commercial power meter located at the back-end of the experiment. The dashed line represents the linear fit to the four data points: the gradient is approximately zero, indicating similar power dependences for I_M and I_D .

The dissociation-detachment process occurs sequentially, and therefore there are two distinct cross-sections at play associated with the different photon absorptions. The first is the photoexcitation cross-section associated with the $S_1 \leftarrow S_0$ transition. The second is the photodetachment cross-section of the methide anion. If either of these cross-sections are significantly smaller than the other, then the probability of that photon absorption will be the limiting factor in the overall mechanism. This is akin to a rate-determining step in a chemical reaction. Ultimately, the photon flux dependence will be similar to that of a single-photon process, since one of the photon absorptions is comparatively efficient. We have no reason to expect the two cross-sections to be similar, and therefore the photon flux dependence remains consistent with the dissociation-detachment mechanism. It is difficult to predict which is the higher cross-section from our data alone: photoexcitation to S_1 was sufficiently bright to observe thermionic emission across a broad range of photon energies, but photodetachment cross-sections of anions with low electron binding energies also tend to be large.

3.3.4. Time-resolved Photoelectron Spectroscopy

From the FRPES data, we have deduced that photoexcitation of pyruvate to its S_1 state leads to decarboxylation and ultimately the production of the CH_3^- anion within six nanoseconds. In order to probe the dynamics in more detail, we performed pump-probe TRPES experiments with femtosecond laser pulses. A pump wavelength of 400 nm (3.10 eV) was chosen and appeared to be resonant with S_1 state of pyruvate. The selected probe wavelength was 800 nm (1.55 eV) for two reasons: this is the fundamental wavelength of our Ti:Sapphire laser, providing the maximum possible power output; and the low photon energy inhibits probe-only photoelectron signal. The time resolution was limited by the ~ 100 fs (FWHM) temporal width of the 400 nm femtosecond laser pulses.

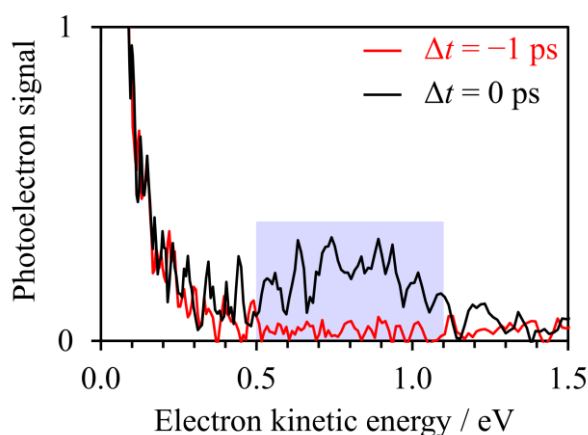


Figure 3.11: Time-resolved photoelectron spectra of the pyruvate anion acquired with femtosecond laser pulses. The 800 nm probe pulse was delayed with respect to the 400 nm pump by Δt . The red trace shows the photoelectron spectrum for a substantially negative time delay, where the probe arrives before the pump by 1 ps, providing a ‘pump-only’ photoelectron spectrum. The black trace shows the pump-probe spectrum when the two pulses are overlapped. Photoelectron signal within the blue shaded region was selected to track the S_1 population.

Figure 3.11 shows a photoelectron spectrum acquired with only the 400 nm pump pulse (red). In this case, the photon energy is less than the ADE of pyruvate so there is no feature arising from direct photodetachment. The spectrum shows a singular feature corresponding to thermionic emission, which was surprising to observe. Since $h\nu < \text{ADE}$, thermionic emission

from the parent pyruvate anion should only be accessible through a photon cycling mechanism, where multiple photons are absorbed in series to increase the internal energy of the ground state anion (see Section 1.1.3). However, given the short temporal width of the laser pulse used in this experiment, we do not expect two sequential absorptions to occur – internal conversion would be required to take place within 10s of femtoseconds (before the second photon absorption). We instead propose that the thermionic emission is largely occurring from the photofragment instead of the pyruvate anion. Excitation to the S_1 state of pyruvate has already been shown to produce the methide anion, and likely the CH_3CO^- anion as an intermediate. Both of these photofragments have very low electron binding energies and will be susceptible to electron loss through thermionic emission, due to the high internal energy instilled via photoexcitation. It therefore seems reasonable to conclude that photodissociation is again occurring and that the methide (or acetyl) anions are responsible for the observed thermionic emission. This implies the formation of the reactive methyl radical CH_3^\bullet is also a likely photoproduct upon UV absorption.

A photoelectron spectrum of pyruvate with both the pump and probe laser pulses in coincidence is also shown in Figure 3.11 (black). A new broad feature emerges around $e\text{KE} = 0.8$ eV. This aligns well with the expected pump-probe signal corresponding to photoexcitation to the S_1 state (pump) and subsequent photodetachment to the neutral species (probe). In particular, the peak should be approximately centred around $e\text{KE} \approx h\nu_{\text{pump}} + h\nu_{\text{probe}} - \text{VDE} = 0.85$ eV. The pump-probe signal thus provides a direct measure of the S_1 state population of the pyruvate anion. As the pump-probe time delay Δt is increased, the excited state population is given more time to evolve and decay before the probe pulse arrives.

The excited pyruvate anion is likely to evolve through two main pathways: (i) relaxation by internal conversion to the S_0 ground state will diminish the S_1 population and therefore

lower the measured pump-probe signal; and (ii) dissociation of the molecule within the S_1 state will lead to a different pump-probe signal, positioned at higher eKE due to the much weaker electron binding energies of the likely photofragments – CH_3CO^- and CH_3^- . Therefore, dissociation within S_1 will also result in a decrease in the pump-probe signal measured at $\text{eKE} \sim 0.8$ eV.

Figure 3.12 displays the integrated pump-probe signal as a function of the time delay between the two femtosecond pulses. Specifically, the S_1 population was represented by numerically integrating the photoelectron signal within the region $0.5 \leq \text{eKE} \leq 1.1$ eV (blue shaded area in Figure 3.11). As the two pulses overlap ($\Delta t \rightarrow 0$), the pump-probe signal rises to a maximum value. The rise is gradual over 10s of femtoseconds and is representative of the instrument response function, governed by the temporal width of the two femtosecond pulses. Over the next 200 fs, the signal declines almost as quickly as it grew in, indicating the S_1 state is depopulated within a few hundreds of femtoseconds. Only a small fraction of the pump-probe signal remains at $\Delta t = 175$ fs.

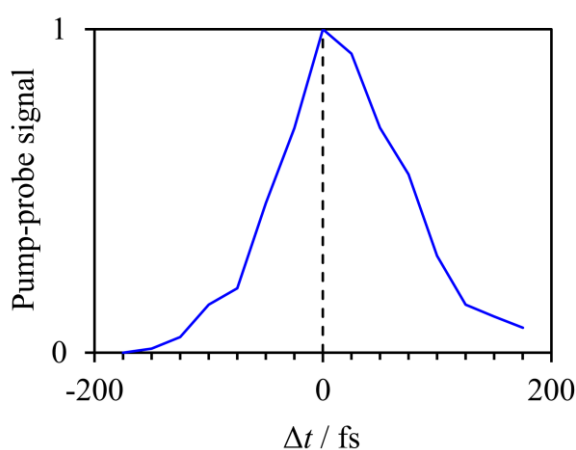


Figure 3.12: Evolution of the integrated pump-probe signal (within blue shaded region in Figure 3.11) as pump-probe delay Δt is altered. The signal is representative of the S_1 excited state population of the pyruvate anion.

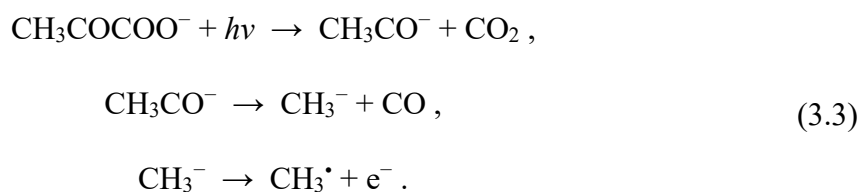
We were surprised to observe such a fast decay of the S_1 state, which was on the order of our experimental time resolution. The rapid depopulation suggests that the S_0 ground state is reformed nonadiabatically through a conical intersection close to the Franck-Condon geometry. The alternative would be that ultrafast photodissociation is taking place within the S_1 state, which seems unlikely because: the decay appears to be highly efficient – very little population remains trapped in the S_1 state at $\Delta t = 175$ fs; and we observe no probed signal from photofragments at any time delay, which would likely be present if the photodissociation were so efficient. It is important to note that the ultrafast reformation of S_0 can be followed by dissociation – nuclear dynamics will still take place on the ground state. The TRPES results suggest that the fragment methide anion that was observed with FRPES (using nanosecond laser pulses) was formed following dynamics on the athermal S_0 ground state of pyruvate. Such extensive dynamics on the ground state are not unprecedented, and similar decarboxylation mechanisms have been observed for the *p*-coumarate and octatrienoate anions.^{45,46} Unfortunately, as we do not observe the direct detachment of the methide (or acetyl) anion, the TRPES does not give insight into the timescale of the dissociation process.

The absence of a probed fragment peak, whilst disappointing, was not unexpected. Only a very weak signal corresponding to photodetachment of CH_3^- was observed with FRPES (with intensity <1% of the accompanying thermionic emission). It may also be that the timescale of dissociation was too long to be observed across the applied range of Δt . From our current results, we are limited to conclude that the S_1 excited state of pyruvate reforms the S_0 ground state within 100s of femtoseconds, and that the dissociation dynamics occur on the ground state, likely on a longer timescale.

3.4. Closing Remarks

Conclusions

To summarise, using FRPES, we showed that the S_1 excited state of the pyruvate anion is accessible via UV photoexcitation. Population of S_1 coincided with the spectral trace of a photofragment with low electron binding energy. With the aid of quantum chemical calculations using the nuclear ensemble approach, we identified the fragment to be the methide anion, CH_3^- . No acetyl anion intermediate, CH_3CO^- , could be clearly distinguished in the data, so is presumably very short lived. Attempting to further probe the dissociation dynamics, we also performed TRPES. It was found that the S_1 state is depopulated within a few hundred femtoseconds, corresponding to relaxation to the S_0 ground state. Unfortunately, the methide anion was unable to be probed in the time-resolved experiment, so the timescale of dissociation could not be more accurately determined. However, we were able to conclude that dissociation is a ground-state process. Overall, based on our results, the following photochemical processes are proposed:



Decarboxylation of pyruvic acid following actinic UV irradiation (accessing the S_1 state) is highly efficient (>97% in gas-phase), promoted by an intramolecular proton transfer mechanism.^{244–248} Despite the pyruvate anion lacking the participating proton, we observe decarboxylation and further dissociation upon excitation to the S_1 state. However, our experiment is unable to quantify the branching ratio of decarboxylation relative to reformation of the intact parent anion. Although the peak associated with direct photodetachment of CH_3^- was very weak, this was not necessarily an indicator of low quantum yield – observation of the

dissociation product requires a sequential two-photon process, which typically occurs with a small probability. For now, the baton is passed to computational chemists to explore the intrinsic dissociation mechanism and its efficiency.

Placing our findings into the context of atmospheric chemistry, we observe formation of the CH_3^- anion, the chemistry of which has been previously considered in the atmosphere of Titan.^{260,261} Moreover, we observed thermionic emission that likely arose from the methide anion, offering also a route for the formation of reactive methyl radicals CH_3^\cdot . These radicals can react with oxygen to produce methyl peroxide,²⁶² which in turn can generate more exotic species. A free (or partially solvated) electron is also formed, which too is highly reactive.^{263,264} Although we cannot provide a measure for the efficiency of photodissociation, we emphasise the relative ubiquity of pyruvate in solution compared to pyruvic acid, which is viewed as atmospherically relevant. The $\text{p}K_a$ of pyruvic acid is 2.5 and has been measured to be as low as 0.7 at the water-air interface.²⁶⁵ Therefore, in all but the most acidic aerosols, pyruvate will dominate. UVA radiation penetrates through to Earth's surface, so the photoactivity of pyruvate may also be accessed in seawater (and seawater sprays). It should be noted that the vapour pressure of the pyruvate anion will be considerably lower than that of the acid, so it is more difficult to compare the relative abundance of these species in isolation. However, it will be interesting to compare the rich photochemistry which pyruvate exhibits in the gas-phase to future studies in aqueous solution and at a water surface, in which the anion is expected to prevail.

Outlook

Inspired by our work, Cao *et al.* presented results on the photochemistry of microhydrated pyruvate anions, $\text{pyruvate}^-(\text{H}_2\text{O})_n$, with $n = 0-5$.²⁶⁶ Photoelectron spectroscopy was also implemented at a selection of different wavelengths, and excellent consistency with

our results was observed for the bare pyruvate anion ($n = 0$). The VDE was measured to be 3.75 eV, photodissociation was observed upon excitation to the S_1 state, and a CH_3^- photofragment was identified. A notable difference (to our results) was that the acetyl anion CH_3CO^- was measured, in addition to the methide anion. However, there are feasible explanations for this: Cao *et al.* stored the pyruvate anions in a cryogenic trap,²⁶⁶ substantially lowering the internal energy of the parent molecules; and, in our experiment, some of the photoelectron signal attributed to the photofragment on the higher-eBE side could have arisen from CH_3CO^- , but this was essentially indistinguishable from noise. Cao *et al.* found that production of CH_3^- was suppressed below $h\nu = 3.5$ eV, but the acetyl anion was still produced.²⁶⁶ With the addition of a water molecule to form the monohydrate ($n = 1$), this threshold shifted higher to $h\nu = 3.7\text{--}4.0$ eV. A second water molecule ($n = 2$) appeared to inhibit dissociation completely, such that even CH_3CO^- was not observed. This points towards a ‘caging’ effect from the microsolvating environment, and it was concluded that photodissociation of pyruvate is not an active channel in solution. It should be noted however, that suppression of the photofragment peaks in the $n = 1\text{--}2$ photoelectron spectra does not necessarily indicate total suppression of the photodissociation channel: solvent ‘caging’ may slow the fragmentation dynamics such that the timescale for decarboxylation exceeds nanoseconds, and therefore the acetyl/methide anions will not be detached within the same laser pulse. Nevertheless, supporting calculations by Cao *et al.* offer an explanation for the inhibition via the emergence of an activation barrier, as hydration is incrementally added.²⁶⁶ In addition, photolysis of pyruvate in water has been previously reported to be very limited,²⁶⁷ lending credence to the inhibition of photodissociation in the bulk. These complementary results give good insight into the of the photodissociation mechanism of (microsolvated) pyruvate, but ultimately, a full experimental determination requires time-resolved methods.

There is opportunity to improve upon our TRPES experiment. Although we could clearly demonstrate that the pyruvate anion relaxed out of the S_1 state in less than a picosecond, we were not able to probe the production of the acetyl or methide photofragments. The study by Cao *et al.*²⁶⁶ may have provided insight as to why. Photodissociation of pyruvate and of subsequent CH_3CO^- was dependent on photon energy. With $h\nu_{\text{pump}} = 3.1$ eV, it is possible that we were exciting the pyruvate anion to the S_1 state but with insufficient energy to trigger dissociation. Therefore, the TRPES experiment should be repeated at a higher photon energy for the pump. Although this will inevitably sacrifice pump laser power, the photoexcitation cross-section is expected to be higher at $3.3 \leq h\nu \leq 4.2$ eV (see Figure 3.6), so pump-probe signal may not be adversely affected. The observation of electrons detached from the photofragments will give the greatest insight into the timescales of the dissociative processes, and may unravel the underlying mechanism.

Finally, a short word on how recent modifications of the ESI instrument (described in Section 2.3.2) could prove useful for the experiment presented in this chapter. Through the detection of the high-eKE electrons and with the aid of supporting electronic structure calculations, we were able to identify the CH_3^- dissociation product. With the addition of the anion reflectron, this methide anion fragment could be detected directly. Additionally, if the lifetime of the CH_3CO^- intermediate was sufficiently long (up to a few microseconds), we could detect this fragment too. As the reflectron acts to separate the photodissociation products by their m/z , the signals arising from these photofragments would be easily distinguishable.

Chapter 4 – Determining the Valence Electron Affinity of Uracil

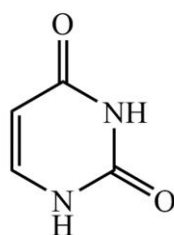
This chapter details and builds upon the following publications:

²⁶⁸ C. J. Clarke, E. M. Burrow and J. R. R. Verlet, *Phys. Chem. Chem. Phys.*, 2024, **26**, 20037–20045

All experimental work was performed by C. J. Clarke and E. M. Burrow. All computational work was performed by C. J. Clarke.

4.1. Introduction

Low-energy electrons can induce strand breaks in DNA, even at electron energies below the ionisation energy of individual components and below the dissociation energies of covalent bonds in the biopolymer.^{164,170,171} As discussed in Section 1.2.4, the initial step is believed to involve electron attachment into π^* valence states of DNA nucleobases, forming temporary negative ions that then lead to bond-rupture.^{173,269,270} In the gas phase, electron transmission spectroscopic experiments have mapped out the location of these π^* resonances (see Section 1.2.4).^{133,174} However, such experiments are not sensitive to the subsequent dynamics that could stabilise the generated temporary negative ions. In particular, nuclear dynamics can compete with autodetachment to decrease the energy gap between the anion valence state and the neutral ground state, leading to a highly reactive radical anion that is long-lived, especially if the anionic valence π^* state is adiabatically bound. So, a natural question then arises: what is the adiabatic electron affinity of the lowest valence state, EA_V , of a nucleobase? Even for the simplest nucleobase, uracil (U), this remains a debated question. Here, we seek to answer this question by applying anion photoelectron spectroscopy to a range of uracil clusters to determine EA_V of U.



Uracil (U)

Figure 4.1: Chemical structure of the uracil (U) nucleobase.

The U nucleobase, for which the chemical structure is shown in Figure 4.1, forms a stable anion in the gas phase, where the excess electron is weakly bound in a diffuse orbital by

the strong dipole moment of the molecule ($\mu \approx 4.5$ D).^{271,272} However, such a dipole-bound state (DBS)⁹⁹ is not a valence state and, while non-valence states can partake in electron attachment at very low electron energies^{95,119,122,273–275} and population can pass from valence to non-valence state and *vice versa*,^{276,277} they are not thought to be relevant in the context of DNA damage because the surrounding environment will disrupt the orbital.² From electron transmission spectroscopy, the lowest-energy shape resonance, π_1^* , is populated with incident electron energies around 220 meV.¹⁷⁴ Upon geometric relaxation, electronic states may stabilise by hundreds of meV, and the π_1^* valence state was suspected to be adiabatically bound with respect to electron loss. However, anion photoelectron spectroscopic studies reported observation of only the DBS of U^- .²⁷¹ This was rationalised as the DBS being more stable than the π_1^* state, and an upper-bound for the EA_V was found to be $EA_V < EA_D \approx +90$ meV, where EA_D is the electron binding energy of the uracil anion in its DBS. On the other hand, long-lived U^- in its π_1^* state was observed to form via Rydberg electron transfer to $U(\text{Ar})_n$ clusters, following evaporation of the solvating argon atoms.²⁷⁸ This was presented as confirmation that the π_1^* state is adiabatically bound with respect to electron loss, and Desfrancois *et al.* reported $EA_V = +62 \pm 32$ meV.²⁷⁸ Computationally, there have been a wide range of EA_V values reported ranging from negative^{225,279–283} to positive^{175,270,284–289}. The seemingly most comprehensive treatment has been performed by Gu *et al.*, who followed the WIBD composite method²⁹⁰ and found $EA_V = +24 \pm 13$ meV,²⁹¹ suggesting a weakly adiabatically bound π_1^* valence state.

Solvation stabilises valence-bound anions to a greater degree than dipole-bound anions.²⁹² Consequently, the ground state of uracil-water cluster anions, $U^-(\text{H}_2\text{O})_n$, is observed to be the π_1^* valence state (see Chapter 5), as easily distinguished in photoelectron spectra by its greater spectral width compared to the signal arising from a DBS.^{180,181,293} By plotting the n -dependent EA_V of these clusters, it therefore becomes possible to extrapolate towards $n = 0$ and obtain an estimate for the EA_V of U . Two studies have performed this procedure, both

yielding relatively large positive adiabatic electron affinities: $EA_V = +150 \pm 120 \text{ meV}$ ¹⁸⁰ and $EA_V = +159 \text{ meV}$ ¹⁸¹ (uncertainty not stated). However, the 0-0 transition for photodetachment from the π_1^* valence state could not be discerned clearly for any of the clusters, and moreover, the validity of performing such an extrapolation is questionable. Water molecules interact very strongly with the uracil anion through a multitude of interactions (e.g. hydrogen bonding and dipolar) so that a simple linear extrapolation is unlikely to be valid even for small clusters. In principle, these concerns can be alleviated through the study of uracil-solvent cluster anions with more weakly interacting solvent molecules. To this end, we performed anion photoelectron spectroscopy on two different series of uracil-solvent cluster anions: $U^-(Ar)_n$ and $U^-(N_2)_n$, and compared our findings to results on $U^-(H_2O)_n$. This approach, utilising spectroscopic tags, also offers colder clusters and allowed us to unambiguously identify the 0-0 transition for photodetachment from the π_1^* valence state. Our determination for EA_V is close to the ‘best’ computational predictions,^{270,291} and expands upon the results from Rydberg electron transfer experiments.²⁷⁸ Our study also establishes protocols for the determination of small (be they positive or negative) adiabatic electron affinities using photoelectron spectroscopy of anion clusters.

4.2. Methodology

4.2.1. Experimental

The cluster instrument was used to perform the experiments outlined below.¹⁸⁸ A solid sample of uracil (U) was placed inside a pulsed Even-Lavie valve¹⁸⁹ and heated to approximately 220 °C. The valve was backed with argon or nitrogen at ~10 bar pressure to produce the desired series of molecular clusters, $U(\text{Ar})_n$ or $U(\text{N}_2)_n$. To induce formation of uracil-water clusters, $U(\text{H}_2\text{O})_n$, a drop of water was added to the backing line. The molecular beam passed through a (thoriated tungsten) filament ring ioniser held at high current, attaching electrons and generating the corresponding progressions of cluster anions. A Wiley-McLaren time-of-flight mass spectrometer¹⁹⁰ separated the cluster anions by their mass-to-charge ratio (m/z), and the targeted anion packet was intersected with a delayed laser pulse at the centre of a velocity map imaging electron spectrometer. Nanosecond laser pulses were sourced from an Nd:YAG laser (Quantel, Q-smart 450), at the fundamental (1064 nm) or second harmonic (532 nm) wavelengths. Photoelectron spectra and angular distributions were reconstructed from the resulting photoelectron images using the polar onion peeling (POP) algorithm.¹⁹⁵ The well-known energetics of atomic I^- were used for calibration of electron energies.

4.2.2. Calibration

As shown in the following section, an electron binding energy for the DBS of U was extracted: $E_{\text{AD}} = +75 \pm 6$ meV. Other experimental studies are in agreement with this value,^{272,278} but some report a slightly higher binding energy (~90 meV).^{180,271} Therefore, further details of the calibration process are included here. Following photodetachment with 266 nm laser pulses ($h\nu = 4.661$ eV), two peaks are observed in the photoelectron spectrum of I^- (Figure 4.2(a)), corresponding to formation of neutral I in either the $^2P_{3/2}$ (ground) or $^2P_{1/2}$

(excited) state. The electron affinity of I is $EA(\text{I}) = 3.0590 \text{ eV}$,²⁹⁴ and the spin-orbit splitting between the two peaks is $E_{\text{SO}} = 0.9427 \text{ eV}$.²⁹⁵ The two peaks were fit with Gaussian functions, allowing the necessary calibration factor to be deduced.

Immediately after measurement of I^- , the photoelectron spectrum of U^- (Figure 4.2(b)) was acquired with 1064 nm laser pulses ($h\nu = 1.165 \text{ eV}$). The photon energy was lowered due to the smaller electron binding energy for U^- . Resultantly, the central electron kinetic energy (eKE) of the DBS peak was between the eKEs of the two I^- features, ensuring that the calibration was not subject to radial dependencies in the image. The fitted central electron binding energy was found to be $EA_{\text{D}} = +75 \text{ meV}$. Although the DBS peak had a notable width ($\sigma = 13 \text{ meV}$), the peak centre was determined to a greater precision. An uncertainty of $\pm 6 \text{ meV}$ was extracted using the standard error on the mean (which is displayed inset of Figure 4.2(b)). Repeated measurements at different wavelengths also produced consistent values for EA_{D} .

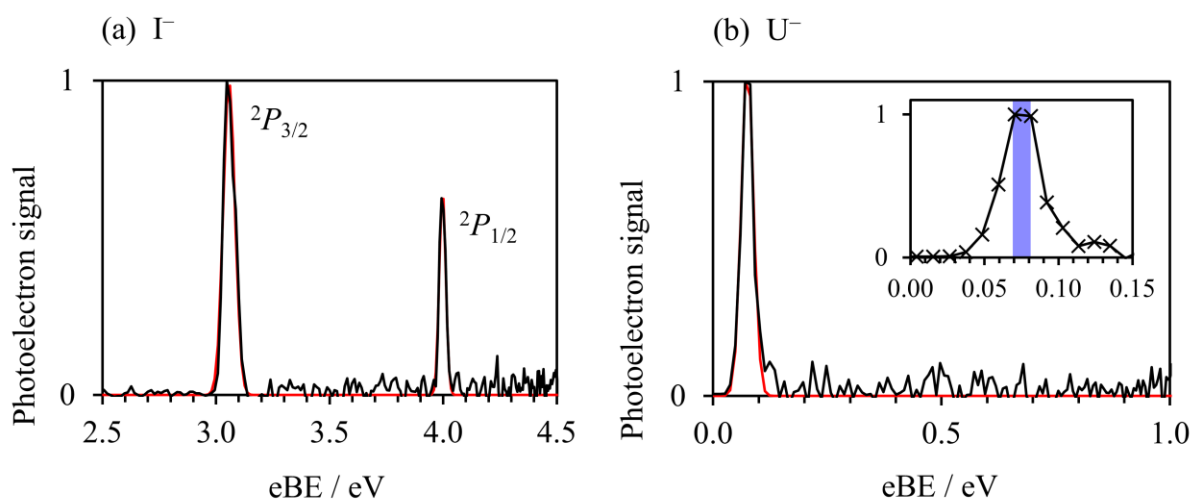


Figure 4.2: Photoelectron spectra of (a) I^- and (b) U^- . Gaussian fits to each peak are shown in red. Inset of (b) shows an expanded view of the DBS peak, with the stated range for EA_{D} highlighted in blue.

4.2.3. Computational

Density functional theory (DFT) tends to produce a bound π_1^* state of the uracil anion,²⁹¹ making it an ideal choice for calculating the vibronic spectrum of valence U^- . We opted for the long-range corrected CAM-B3LYP functional,²¹⁷ with the diffuse aug-cc-pVDZ Dunning basis set.²²¹ By omitting the extra-diffuse basis functions that are often added into calculations on U^- , such as in the calculations performed in Chapter 6, the optimised anion geometry settled into the buckled π_1^* valence state, and a minimum was confirmed through vibrational frequency analysis. The planar equilibrium structure of neutral uracil was also calculated, allowing the vibronic spectrum associated with the $S_0 \leftarrow \pi_1^*$ transition to be computed. Each transition was broadened by a Gaussian function with standard deviation $\sigma = 20$ meV, and summed to produce a representative photoelectron spectrum. The simulated spectrum was shifted to align with the measured 0-0 transition of $U^-(Ar)_3$. All calculations were performed with Gaussian 16.²⁹⁶

4.3. Uracil-Argon Cluster Anions

4.3.1. Photoelectron Spectra

Photoelectron spectra of a series of uracil-argon cluster anions, $U^-(Ar)_n$ where $n \leq 25$, were acquired using nanosecond laser pulses with photon energy $h\nu = 1.165$ eV. Figure 4.3(a) shows all spectra up to $n = 18$. Photoelectron signal is plotted in terms of electron binding energy, defined as $eBE = h\nu - eKE$. As found in earlier photoelectron spectroscopy experiments,^{180,271,293} the photoelectron spectrum of U^- exhibits a single, sharp peak at low electron binding energy. This is the characteristic photoelectron signal arising from photodetachment of a DBS to reach the ground-state neutral, as the excess electron only weakly interacts with the neutral core. We additionally confirm that the electron emission is highly anisotropic ($\beta_2 = +2.0$, see Figure 4.3(b)) as expected from an s-like non-valence orbital.^{297,298} As described in Section 4.2.2, we determine that $EA_D = +75 \pm 6$ meV.

The photoelectron spectra of $U^-(Ar)_1$ and $U^-(Ar)_2$ are similar to the spectrum of U^- . The low-energy electrons ($eBE > 0.5$ eV) were produced from a small contamination of uracil-water cluster anions of similar masses to $U^-(Ar)_{1-2}$, but given that this signal does not interfere with the low binding energy peak associated with the dipole-bound state, the contamination has no impact on the current discussion. It is clear that formation of the DBS of U^- remains favourable in the presence of one or two argon atoms, and solvation appears to only increase EA_D by a few meV per argon atom.

Upon the addition of a third solvating argon atom, the photoelectron spectrum changes drastically. $U^-(Ar)_3$ exhibits a broad, structured photoelectron signal, with a far more isotropic PAD ($\beta_2 \approx +0.4$, see Figure 4.3(b)). The signal arises from photodetachment of the π_1^* valence state and suggests that it has become the ground electronic state of the anion due to stabilisation from the solvating argon atoms. This agrees well with an earlier photoelectron spectroscopic

measurement of the π_1^* valence state of $U^-(Xe)_1$,²⁹³ which also shows a broad feature with underlying vibrational structure (although the structured peak was partially obscured by photoelectron signal arising from some accompanying DBS). The considerable spectral width of the π_1^* detachment feature arises from the substantially different equilibrium geometries between the anionic and neutral form of the U molecule: the neutral molecule is planar while the anion buckles to become non-planar.²²⁵

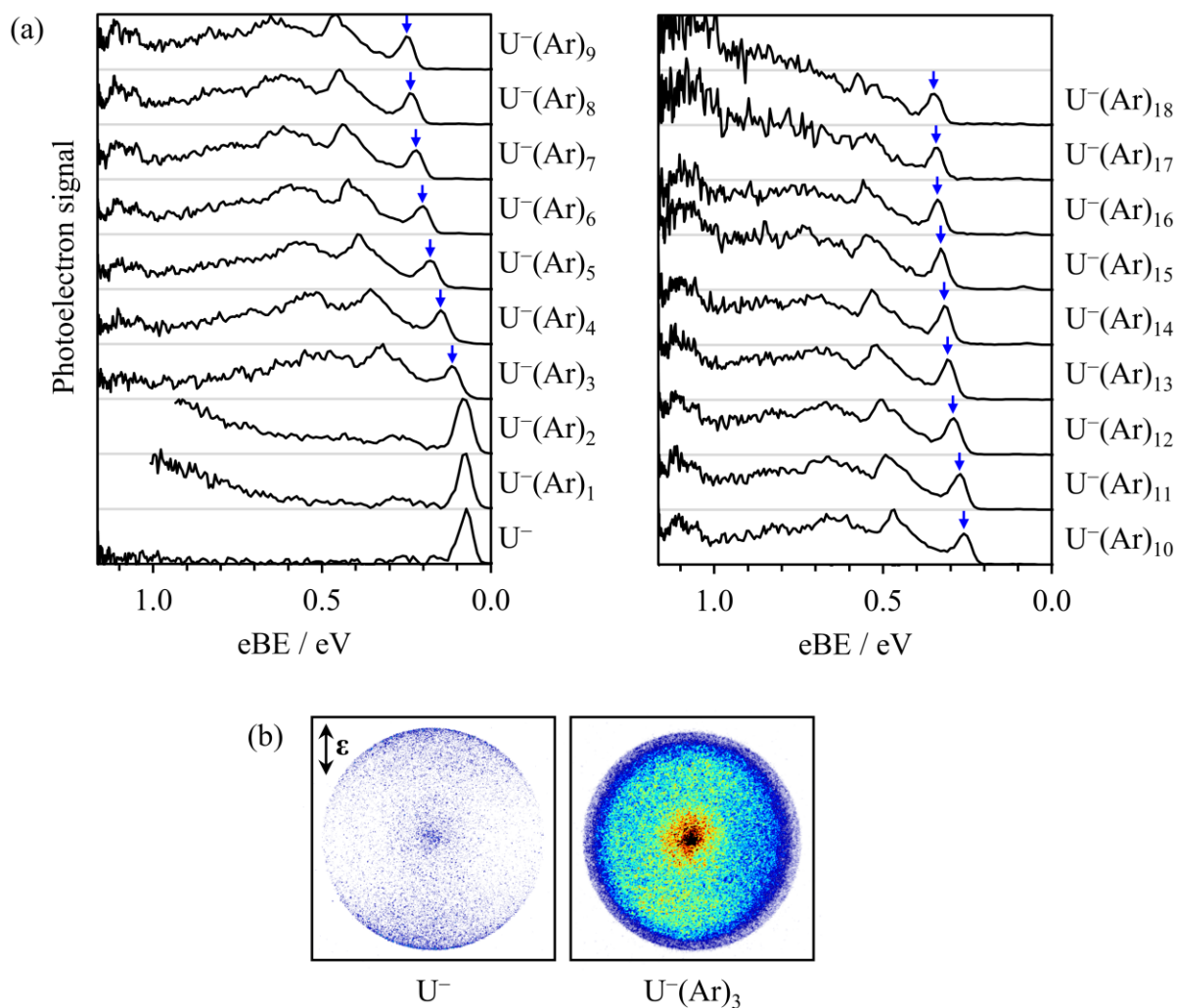


Figure 4.3: (a) Photoelectron spectra of uracil-argon cluster anions, $U^-(Ar)_n$, acquired using nanosecond laser pulses with $h\nu = 1.165$ eV. Blue arrows highlight the electron binding energy (eBE) associated with the 0-0 transition from the π_1^* valence state to the neutral ground state. (b) Corresponding photoelectron images from dipole-bound U^- (left) and valence-bound $U^-(Ar)_3$ (right). The fixed direction of laser polarisation vector is represented by ϵ .

Despite the disparate geometries, it appears that a peak corresponding to the 0-0 transition is resolved in Figure 4.3 (blue arrows), which represents a direct measure of EA_V associated with the π_1^* state of $U^-(Ar)_{n \geq 3}$. To reinforce assignment of the 0-0 transition peak, Figure 4.4(a) recasts the photoelectron spectrum of $U^-(Ar)_3$ with an overlay of a computed (DFT/(U)CAM-B3LYP/aug-cc-pVDZ) vibronic spectrum of the π_1^* valence state of U^- . As the excess charge is expected to localise on the nucleobase component, exclusion of the argon in the calculations was considered acceptable. Indeed, the vibrational structure displayed in photoelectron spectra of the larger $U^-(Ar)_{n > 3}$ clusters are very similar, demonstrating the negligible effect of the argon atoms. The calculated vibronic spectrum shows good overall agreement, although the vibrational structure in the experimental spectrum was not perfectly captured. Nevertheless, the dominant vibrational mode can be clearly identified as ν_{15} , which corresponds to an out-of-plane motion (displacement vectors shown in Figure 4.4(b)). Some disparity between experimental and calculated structures might be expected due to differences in anion-neutral geometries, which results in a broad Franck-Condon window made up of many combined excitations, as well as the neglect of anharmonicity. In the context of this study, it is more critical that we can conclude that the 0-0 transition is clearly distinguishable in the photoelectron spectra of $U^-(Ar)_n$, and therefore the associated EA_V can be accurately determined for each cluster.

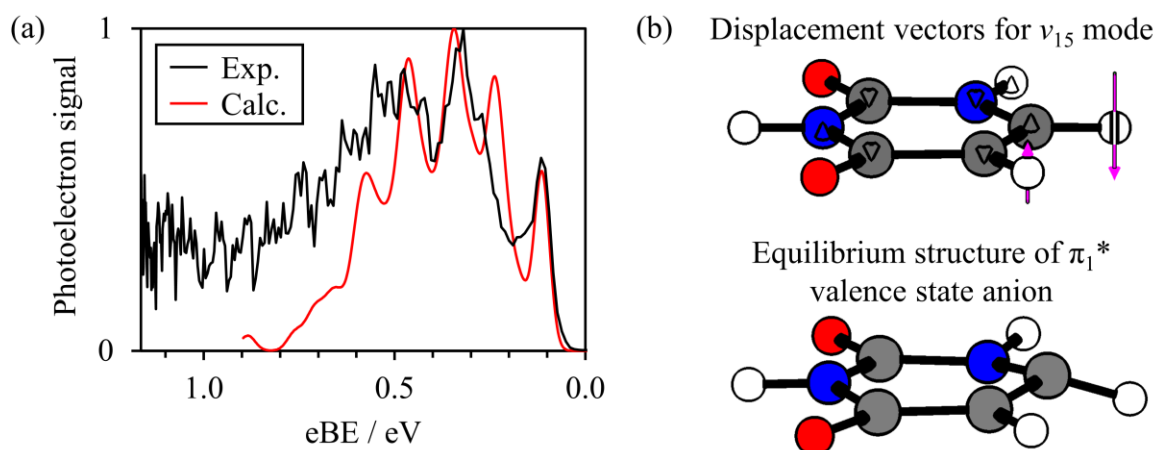


Figure 4.4: (a) Measured photoelectron spectrum of $U^-(Ar)_3$ (black), overlaid with the calculated (CAM-B3LYP/aug-cc-pVDZ) vibronic spectrum (red) of the π_1^* valence state of U^- , which was horizontally shifted to align the 0-0 transitions. (b) Calculated displacement vectors (pink) for the ν_{15} vibrational mode (top), that contributed most to the calculated vibronic spectrum. For comparison, the buckled optimised geometry of U^- in its π_1^* valence state is also shown (bottom).

4.3.2. Determination of the Valence Electron Affinity of Uracil

With increasing cluster size, the 0-0 transition shifts to higher electron binding energy. This demonstrates that EA_V increases with each incrementally added argon atom, directly reflecting the imposed anion-stabilising effect. In particular, U^- is stabilised through favourable interactions between the excess negative charge and the polarisability of the argon atoms. From the measured 0-0 transition energies, it is possible to extrapolate the measured $EA_V(n)$ to the isolated U^- limit (i.e. $n = 0$), obtaining an estimate for EA_V of U. However, in order to perform such an extrapolation, the expected behaviour of $EA_V(n)$ should be considered in detail.

Figure 4.5 presents a compilation of the argon-induced anion-stabilising effect, $E_{stab}(n) = EA_V(X(Ar)_n) - EA_V(X)$, from a number of photoelectron spectroscopic studies on valence-bound $X^-(Ar)_n$ clusters, where $X = O$,²⁹⁹ NO ,³⁰⁰ Cl ,³⁰¹ Br ,³⁰² I ,³⁰² I_2 ,³⁰³ and pyrazine.³⁰⁴ It is apparent that the more electron-dense anions are stabilised to a greater degree by the clustered argon atoms. The trend in $E_{stab}(n)$ (and therefore also EA_V) for each anion cluster appears approximately linear at small n , but curves slightly at larger n , where the $E_{stab}(n)$

increases by a smaller amount per successive argon atom added. This curvature has been explained to result from various many-body interactions (mostly between the charged anion and the clustered argon atoms),^{301,302} ultimately adding a small destabilising effect to the anion with respect to the neutral form. Through least-squares fitting, we found the power function $E_{\text{stab}}(n) \sim n^{0.95}$ to reproduce the exhibited curvature very well for each series of anion clusters. The only exception to this is $\text{O}^-(\text{Ar})_n$ (where the curvature is more pronounced), but O^- interacts most strongly with the solvating Ar atoms. In the case of U, $E_{\text{stab}}(n)$ for $\text{U}^-(\text{Ar})_n$ is the most comparable to $\text{Br}^-(\text{Ar})_n$, suggesting that the U^- -Ar interaction strength is similar to Br^- -Ar and the above power function is appropriate to use for extrapolation purposes.

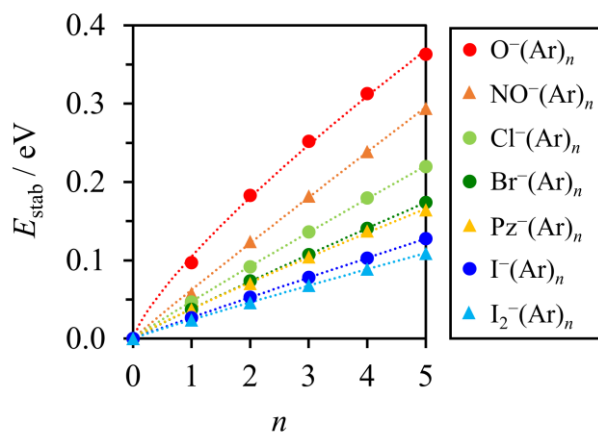


Figure 4.5: Stabilisation energy $E_{\text{stab}} = EA_{\text{V}}(\text{X}(\text{Ar})_n) - EA_{\text{V}}(\text{X})$, associated with the clustering of n argon atoms to different anions X. Circles and triangles are used to distinguish between atomic and molecular anions, respectively. The dotted lines show fitted power functions of n associated with each series of anion clusters. Adapted from ref.²⁹⁹⁻³⁰⁴, with the permission of AIP publishing.

Figure 4.6 presents the experimentally determined EA_{V} associated with each measured $\text{U}^-(\text{Ar})_n$ cluster, demonstrating a slightly curved behaviour at small cluster size. There is a distinct ‘kink’ in the trend around the $\text{U}^-(\text{Ar})_{12}$ cluster, indicative of the (partial) closing of a solvation shell around U^- ,^{299,300} which is briefly discussed in Section 4.3.3. For now, we focus on the EA_{V} values of the small clusters. The EA_{V} values of $\text{U}(\text{Ar})_{3-5}$ were fit to the empirical

function $EA_V(n) = k_{Ar}n^{0.95} + EA_V$, where k_{Ar} was an optimised constant associated with the interaction strength between U^- and Ar. Only clusters consisting of up to five argons were included in the fit, since a second less-defined kink may be present at $n = 6$. The fitting function, extrapolated to $n = 0$, is shown in Figure 4.6. Extrapolation to $n = 2$ suggests that $EA_V(2)$ is below the electron binding energy of the DBS for this cluster, consistent with the absence of the π_1^* valence state signal in the photoelectron spectrum of $U^-(Ar)_2$. From the full extrapolation, we find that $EA_V = -6 \pm 24$ meV, where the uncertainty in EA_V was determined by the combined contributions of our experimental resolution and the extrapolation process. It should also be noted that applying a linear extrapolation ($n = 3-5$) instead obtains $EA_V = +2$ meV, showing that the slight curvature has little effect on the extrapolated energy. Unfortunately, our results on the $U^-(Ar)_n$ clusters were unable to conclusively determine whether the π_1^* state of U^- is adiabatically bound or not. Nevertheless, we can conclude that EA_V is very small. By directly observing the 0-0 transition associated with the π_1^* valence state in weakly perturbed clusters, our extracted value is currently the most accurate experimentally determined EA_V , and is slightly lower than the most reliable theoretical determination.²⁹¹

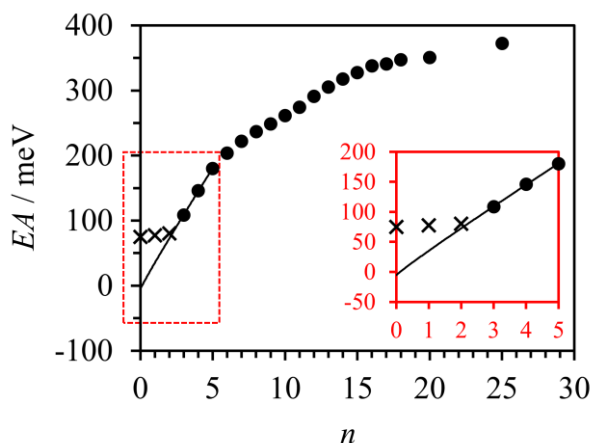


Figure 4.6: Adiabatic electron affinity (EA) of uracil-argon clusters, $U(Ar)_n$, extracted from photoelectron spectroscopy on the corresponding anions. Dots indicate $EA_V(n)$ associated with the π_1^* valence state of $U^-(Ar)_n$, whereas the crosses show the measured electron binding energies of the DBS anions, EA_D . An extrapolation using the $EA_V(n)$ of $U(Ar)_{3-5}$ is overlaid (black line). Inset is a magnified view for small n (red dashed area).

4.3.3. Large Anion Clusters

As an anion-solvent cluster grows larger, it is expected that the solvent molecules will form solvation shells around the anion, providing enhanced stabilisation. Upon formation of a particularly stable anionic structure, such as a partial or fully-completed solvation shell, the electron binding energy of the anion cluster increases substantially.¹⁵¹ For $U^-(Ar)_n$, this leads to the observed kinks in the functionality of $EA_V(n)$. This is more clearly observed by inspecting the stepwise change in adiabatic electron affinity: $\Delta EA_V(n) = EA_V(n) - EA_V(n-1)$, as in Figure 4.7. There is a distinct increase in EA_V upon addition of the 12th argon atom. Interestingly, a similar observation has been previously made for oxygen-argon cluster anions, where $O^-(Ar)_{12}$ was observed to be particularly stable,²⁹⁹ which was attributed to the icosahedral structure that forms as the first solvation shell. For $U^-(Ar)_{12}$, it is unlikely that the charged nucleobase can be fully enclosed with just 12 argon atoms, owing to steric effects. However, it is possible that local sites of the uracil ring, such as the densely charged oxygen atoms, became fully solvated. Alternatively, the 12th argon atom may have completed a partial solvation shell, more akin to a hemisphere than a conventional solvation sphere. Ultimately, the exact structure can only be speculated upon from this study alone. Further experimental investigation could take the form of IR spectroscopy, although vibrational modes of the argon solvent are likely to be challenging to measure; computational study would also prove useful, but quantum chemical calculations on such large cluster structures become prohibitively expensive (e.g. 12×18 electrons for Ar alone).

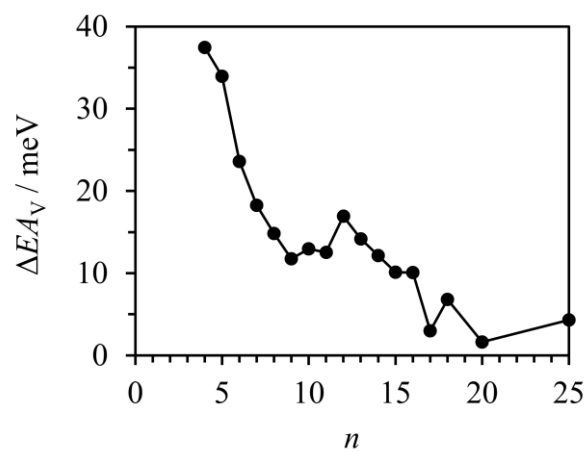


Figure 4.7: Stepwise change in adiabatic electron affinity (EA_v) associated with the π_1^* valence state of $U^-(Ar)_n$, defined as $\Delta EA_v(n) = EA_v(n) - EA_v(n-1)$.

4.4. Effect of Changing Solvent

4.4.1. Uracil-Nitrogen Cluster Anions

Further estimates for EA_V can be obtained by repeating the above procedure with different solvent molecules. Figure 4.8 displays photoelectron spectra ($h\nu = 1.165$ eV) of $U^-(N_2)_n$, with $n \leq 6$. The vibrational structure in the detachment from the π_1^* valence state is very similar to that observed from $U^-(Ar)_n$, allowing $EA_V(n)$ to be extracted from the distinct 0-0 transition feature in each spectrum. The nitrogen molecules interact more strongly with the uracil anion than do the argon atoms, as reflected in the greater degree of stabilisation per added solvent molecule, as well as in the observation of the π_1^* valence state for $U^-(N_2)_2$. The stabilisation is greater because, despite the similar polarisabilities of N_2 and Ar,³⁰⁵ the inherently anisotropic charge distribution of diatomic nitrogen allows for additional interactions with U^- , e.g. through its significant quadrupole.³⁰⁶ The observed 0-0 transitions in the photoelectron spectra of $U^-(N_2)_n$ are also broader than in the case of $U^-(Ar)_n$, and so the uncertainty associated with finding EA_V was slightly larger. This spectral broadening again correlates with stronger interactions between the anion and N_2 , consistent with previous studies on NO^- cluster anions.³⁰⁰ In particular, stronger interactions between U^- and N_2 (compared to U^- and Ar) can act to both: encourage excitation of lower-frequency vibrational modes which cannot be spectrally resolved; and increase the degree of structural rearrangement in the transition from anion to neutral, leading to a broader Franck-Condon window. Additionally, some of the broadening may be attributed to the presence of multiple structural isomers for each anion cluster, as the N_2 molecules preferentially bind to different sites of the uracil anion (with facile interchange), resulting in subtly different binding energies for the excess electron between isomers.

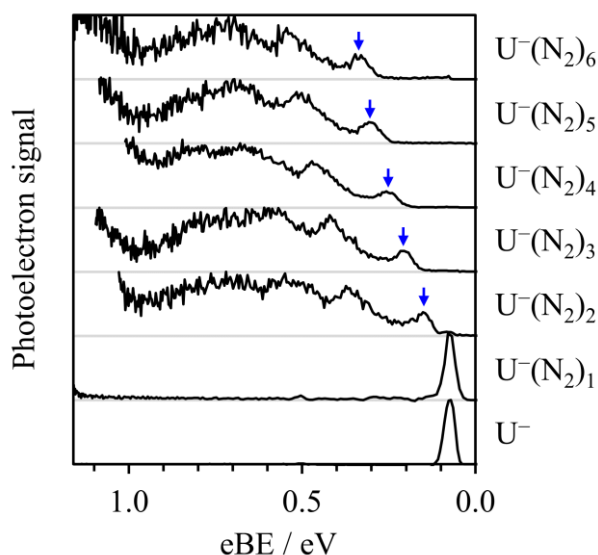


Figure 4.8: Photoelectron spectra of uracil-nitrogen cluster anions, $U^-(N_2)_n$, acquired using nanosecond laser pulses with $h\nu = 1.165$ eV. Blue arrows highlight the electron binding energy (eBE) associated with the 0-0 transition from the π_1^* valence state to the neutral ground state.

Figure 4.9 presents the extracted $EA_V(n)$ of the $U(N_2)_n$ clusters, alongside the earlier results on $U(Ar)_n$. Over the range of small clusters measured, the curvature exhibited in the plot of $EA_V(n)$ was exacerbated with the N_2 solvent. Once more, this follows from stronger intermolecular forces within the clusters. In fact, the strength of interaction between U^- and N_2 is comparable to the $O^-(Ar)_n$ anion clusters shown in Figure 4.5, which also expressed a pronounced curvature (compared to the more weakly interacting anion-argon clusters). However, there is an important difference between the $U^-(N_2)_n$ and $O^-(Ar)_n$: the latter series of clusters are comprised of atomic subunits, whereas both uracil and molecular nitrogen are polyatomic. Therefore, the many-body interactions that govern the exhibited curvature of the $O^-(Ar)_n$ clusters are completely absent in $O^-(Ar)_1$, and so approximately linear behaviour is expected in the range $0 \leq n \leq 2$ for these atomic clusters. In the case of $U^-(N_2)_n$, the curvature results from a combination of many intermolecular interactions (e.g. between dipoles, quadrupoles, polarisabilities), which all remain present even in $U^-(N_2)_1$. Consequently, there is no reason to suspect the exhibited curvature not to persist to the $n = 0$ limit. We found a

relationship, $EA_V(n) = k_{N_2}n^{0.7} + EA_V$, to fit the data appropriately (fit included in Figure 4.9), with the optimised coefficient $k_{N_2} > k_{Ar}$. A value $EA_V = +1 \pm 26$ meV was extracted, consistent with the EA_V derived from the $U^-(Ar)_n$ series of clusters, and providing further evidence that the excess electron in the π_1^* valence state of U^- is very weakly bound, if at all.

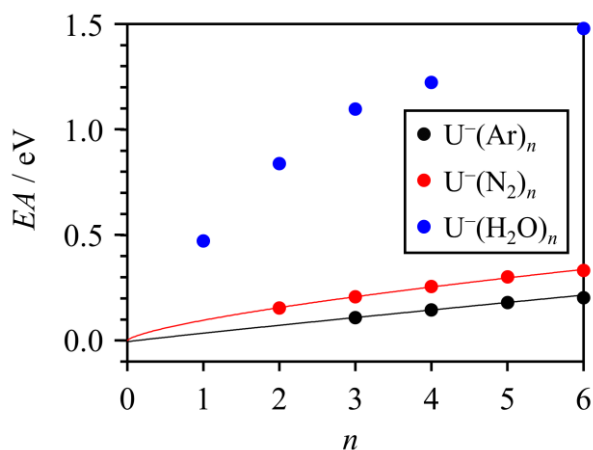


Figure 4.9: Adiabatic electron affinities (EA) for a selection of uracil-solvent clusters, $U(Ar)_n$ (black), $U(N_2)_n$ (red), and $U(H_2O)_n$ (blue), extracted from photoelectron spectroscopy on the corresponding anions. Extrapolations are overlaid as solid lines. Uncertainties in each data point were smaller than the size of the data point symbols for the $U^-(N_2)_n$ and $U^-(H_2O)_1$ clusters. The uncertainties for $U^-(H_2O)_{2-6}$ were larger (due to absence of the 0-0 transition), around 0.1 eV.

4.4.2. Caveats of using Strongly Interacting Solvents

Solvation-induced stabilisation of U^- has been most extensively studied in uracil-water cluster anions (see Chapter 5),^{180,181,307} where even a single water molecule sufficiently stabilises the π_1^* valence state to become the ground state of the uracil anion. A photoelectron spectrum of $U^-(H_2O)_1$ is shown in Figure 4.10 ($h\nu = 1.165$ eV), where the 0-0 transition peak arising from the π_1^* valence state was distinct but broad. Through its characteristic spectral signature, the formation of the solvent-stabilised DBS of $U^-(H_2O)_1$ in our ion source was also observed: this is the subject of Chapter 6. From the 0-0 transition associated with the π_1^* valence state, the solvating power of H_2O is demonstrably much greater than either Ar or N_2 .

Indeed, the anion-stabilising effect of a single water molecule exceeded that of 25 argon atoms: $EA_V(U(H_2O)_1) > EA_V(U(Ar)_{25})$. It is unsurprising that the interactions of U^- with H_2O are so vastly stronger, as clustering with water is additionally supported by long-range charge-dipole interactions as well as hydrogen bonding.

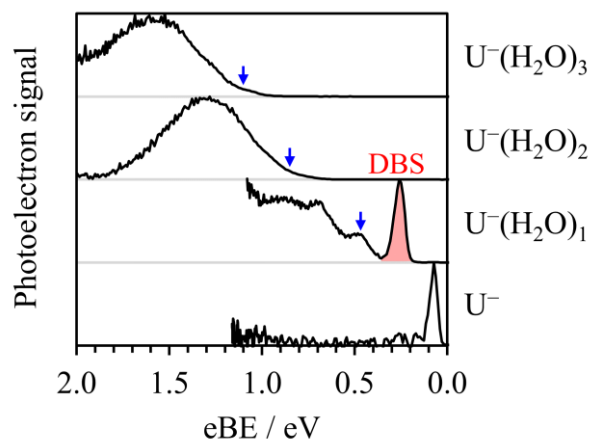


Figure 4.10: Photoelectron spectra of small uracil-water cluster anions, $U^-(H_2O)_n$, acquired using nanosecond laser pulses with $h\nu = 1.165$ eV ($n = 0, 1$) and $h\nu = 2.230$ eV ($n = 2, 3$). Blue arrows highlight the electron binding energy (eBE) associated with the 0-0 transition from the π_1^* valence state to the neutral ground state. The contribution from the DBS of $U^-(H_2O)_1$ is highlighted in red.

Larger clusters of $U^-(H_2O)_{n \geq 2}$ are discussed in depth in Chapter 5. In the context of this study, they did not produce distinguishable 0-0 transition features due to further spectral broadening, and therefore each $EA_V(n)$ associated with these clusters was estimated from the onset of the Gaussian-like photoelectron signal (taken as 10% of peak height). The resulting $EA_V(n)$ values are also displayed in Figure 4.9, and exhibit an even more pronounced curvature across n . We do not present an extrapolation to the monomeric limit ($n = 0$) using the uracil-water cluster $EA_V(n)$ for several reasons: (i) there was no simple power function which suitably captured the experimental data; (ii) the 0-0 transition was not observable in all but one of the clusters, restricting accurate determination of the EA_V ; and (iii) water molecules are far more selective towards the binding site of U^- (or to other H_2O molecules in the cluster), largely

due to their tendency for hydrogen bonding. Nonetheless, linearly extrapolating the $EA_V(n)$ of the smallest $U^-(H_2O)_n$ clusters results in an estimated $EA_V \approx +177$ meV, similar to the electron affinities obtained in earlier studies that performed this procedure.^{180,181} Our results on the $U^-(Ar)_n$ and $U^-(N_2)_n$ clusters highlight the problems associated with performing such a linear extrapolation: in particular, the EA_V for some of the argon- and nitrogen-stabilised clusters are measurably lower than 177 meV. We conclude that, in general, linear behaviour of the electron binding energy should not be assumed in clusters containing a polyatomic anion and a strongly solvating species such as water. In the case of U^- , this leads to systematic errors up to hundreds of meV.

Extrapolating adiabatic electron affinities of anion-solvent clusters must be performed with due consideration of the strength of the anion-solvent interaction. As shown above, strong interactions lead to significantly non-linear behaviour, and a linear extrapolation to $n = 0$ is inappropriate. If the interactions are too weak, then many solvent molecules may be required to render the anion a bound (or kinetically-trapped metastable) state, causing greater uncertainty in the extrapolated EA . For instance, $U^-(He)_n$ and $U^-(Ne)_n$ anion clusters can also provide an estimate for the EA_V of U , but the weak solvating power of He and Ne means that the π_1^* valence state is unlikely to be observed until $n \geq 4$, necessitating a more extreme extrapolation that may lead to poorer determination of EA_V . Overall, the ideal solvent must strike a balance between strongly and weakly solvating the anion, permitting an approximately linear extrapolation from small clusters. In addition to argon and nitrogen, xenon also appears to be a suitable solvent probe for U^- ; as mentioned earlier, the valence state of $U^-(Xe)_1$ had been measured with photoelectron spectroscopy, although with some obfuscation from the co-generated DBS.²⁹³ From our clear characterisations of the 0-0 transition present in the photoelectron spectra of $U^-(Ar)_n$ and $U^-(N_2)_n$, we can infer that $EA_V(U(Xe)_1) \approx 120$ meV.²⁹³ By then comparing the general anion solvating power of xenon with that of other solvent

molecules,³⁰⁰ which is stronger than argon but weaker than water, it appears that an extrapolation from the electron affinities of $U^-(Xe)_n$ is also likely to yield a value of EA_V close to zero.

4.5. Competition with Autodetachment

The observed vibrational structure in the photoelectron spectra of $U^-(Ar)_n$ and $U^-(N_2)_n$ also provides insight into the nuclear rearrangement undergone by uracil in the transition from its neutral to anionic valence state. The vertical detachment energy (VDE) of each anion cluster can be extracted from the eBE at which there was most (fitted) photoelectron signal, and for both $U^-(Ar)_n$ and $U^-(N_2)_n$, is found to decrease with smaller n at the same rate as $EA_V(n)$. From the appropriate extrapolation, we find that $VDE(U^-) = +210 \pm 30$ meV. The extracted detachment energies of U^- (EA_D , EA_V , and VDE) can be used to draw a schematic of the relevant diabatic potential energy surfaces along the ring-buckling coordinate that connects the neutral (S_0) and anionic (π_1^*) equilibrium geometries (Figure 4.11) in a harmonic approximation. Encouragingly, electron transmission spectroscopy has measured the vertical attachment energy (VAE) of the π_1^* valence state of U to be very close to our extracted VDE: $VAE = 220$ meV.¹⁷⁴ Assuming the same harmonic diabatic surfaces for S_0 and π_1^* valence states allows us to connect the buckling coordinate in a consistent picture as shown in Figure 4.11. In the context of low-energy electron attachment into the π_1^* resonance, U^- forms in the planar geometry, but will rapidly stabilise via the buckling distortion. With only the slightest buckling away from planarity, the π_1^* valence state energy approaches that of the neutral S_0 state and then becomes vertically bound with respect to electron loss, greatly enhancing the lifetime of the generated anion. Regardless of whether the π_1^* state is adiabatically bound in its minimum energy (fully-buckled) structure (i.e. $EA_V < 0$ or $EA_V > 0$), its vertical binding exceeds 200 meV and U^- formed by electron attachment via the π_1^* resonance is expected to persist on a timescale greatly surpassing the sub-picosecond lifetimes expected from shape resonance autodetachment.^{28,29,95}

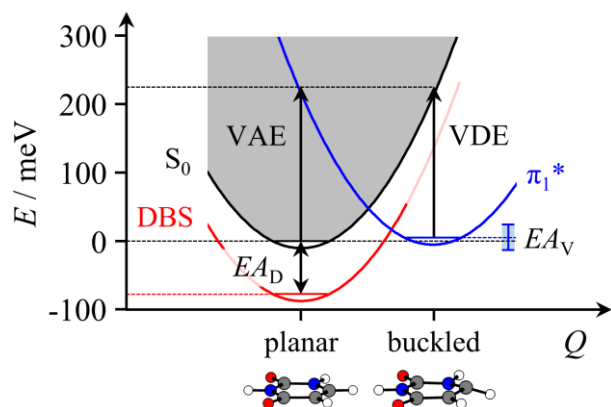


Figure 4.11: Schematic showing diabatic potential energy surfaces of neutral (S_0) and anionic (π_1^* and DBS) uracil along the ring-buckling coordinate, Q , treated within a harmonic approximation. Energy gaps reflect the experimentally determined values, and the grey region represents the electron detachment continuum. Uncertainty in the measured value of EA_V is shown with blue bars.

A competing decay pathway for the π_1^* state is through internal conversion to the DBS.²⁷⁶ Within the harmonic approximation displayed in Figure 4.11, an energetic barrier is expected to separate the two states, limiting the rate of internal conversion from the π_1^* state to the DBS. Numerous computational studies have attempted to calculate the height of this barrier, with estimates ranging from tens to hundreds of meV.^{175,283,308} Within our simple linear response model in Figure 4.11, it appears the barrier height is on the order of 10s of meV. This barrier held important consequences for the earlier Rydberg electron transfer experiments that had suggested a positive value for the EA_V .²⁷⁸ These experiments attached electrons to $U(\text{Ar})_n$ clusters, and following evaporation of the clustered argon atoms, formed U^- in the π_1^* state. U^- was kinetically trapped in the valence state for many microseconds (in order to be mass-separated), which is consistent with our combined observations of (i) a large vertical binding energy (VDE), and (ii) the suggested presence of a barrier between the valence- and dipole-bound states. We note that the lower threshold of their stated EA_V (+30 meV) was derived from the intermolecular binding energy between uracil and argon, which was explained to be less than EA_V such that even the smallest generated $U^-(\text{Ar})_n$ clusters could then have

sufficient internal energy to evaporate off the clustered argon atom(s), but not enough to undergo autodetachment. Our extracted EA_V for U^- is also consistent with this picture, despite being less than 30 meV. Our extrapolation predicts that $EA_V \sim 35$ meV for $U^-(Ar)_1$ so that both electron and argon loss result in similarly stable products. But it should also be noted that these loss channels will differ in their kinetics. In particular, electron loss from the valence state of any $U^-(Ar)_n$ cluster is driven by a buckled-to-planar transformation of the uracil ring, which is expected to be inhibited by an energetic barrier. Therefore, we do not expect autodetachment to occur for up to many microseconds, giving sufficient time for competitive loss of the solvating argon.

4.6. Closing Remarks

Conclusions

The π_1^* valence state of the uracil anion is significantly stabilised by clustered solvent molecules, even in the weakly-interacting case of $U^-(Ar)_n$. Earlier estimates for the EA_V of isolated uracil utilised linear extrapolation techniques from the $EA_V(n)$ of uracil-water clusters, in which the solvent interacts strongly with the nucleobase anion. We demonstrate that such linear extrapolations are, in general, not accurate and should not be applied in the context of a polyatomic anion and a strongly-interacting solvent. Instead, weakly-interacting solvent molecules induce a nearly linear increase in the $EA_V(n)$, and can be used to perform a more suitable extrapolation. Our photoelectron spectroscopic measurements on $U^-(Ar)_n$ and $U^-(N_2)_n$ clusters resolved the 0-0 transition corresponding to photodetachment of the π_1^* valence state of U^- , allowing for an accurate determination of the associated EA_V . With accountment for the subtle non-linearity in $EA_V(n)$ with increasing cluster size, our extrapolated value for the adiabatic electron affinity associated with the π_1^* state of bare uracil, $EA_V = -2 \pm 18$ meV, using the combined values from $U^-(Ar)_n$ and $U^-(N_2)_n$. Within the uncertainty of our experiment, we are unable to conclude that the π_1^* state is adiabatically stable, which has elsewhere been suggested by Rydberg electron transfer experiments,^{278,309} and extrapolations from $U^-(H_2O)_n$.^{180,181} Nonetheless, our results demonstrate the magnitude of EA_V is very small and that any potential binding of the excess electron in the π_1^* valence state of U^- must be very weak. This finding appears to reveal why computational attempts to calculate (the sign of) EA_V have shown such disagreement. Nevertheless, our reported value is close to the most rigorous computational predictions.²⁹¹ We also offer insight into the barrier connecting the valence and non-valence states along the nuclear buckling coordinate, and our extracted energies are consistent with earlier results from electron transmission spectroscopy.

Outlook

As utilised in this photoelectron spectroscopic study, anion-solvent clusters can reveal the adiabatic electron affinities associated with unstable anions via extrapolation. In addition, a similar technique can be applied to the measured VDEs of the clusters, providing an extrapolated spectral width associated with photodetachment of the bare anion, which can be related back to geometric changes incurred in the molecule. In the case of uracil, electron attachment into the π_1^* state induces a notable buckling distortion. This is reflected in the disparity between the extrapolated EA and VDE, and the corresponding reorganisation energy for U can be estimated: $\lambda \approx \text{VDE}(\text{U}^-) - EA_{\text{v}} = 0.2$ eV. Within large clusters or a bulk solvent environment, the reorganisation energy is expected to increase substantially, as solvent molecules rearrange to accommodate the additional negative charge of the anion. This is considered in more detail in Chapter 5 (where large uracil-water cluster anions are examined). For now, it should be noted that the use of weakly solvating species are essential for an accurate determination of the EA and the VDE, and thus also the reorganisation energy associated with the bare U^- anion.

The valence electron affinities of the other nucleobases are expected to be similar to or slightly higher than that of U.¹⁷⁴ In the context of electron attachment to DNA, the energetic position of these low-lying anion resonances will surely be influenced by the surrounding protein environment, through hydrogen bonding and π -stacking interactions,³¹⁰ as well as proximity to the negatively charged phosphate backbone. Therefore, it is unlikely that the exact sign of EA_{v} in the gas phase will hold much consequence for DNA damage mechanisms. To better understand such processes, the electronic energetics and dynamics of nucleobases should be explored in environments more representative of *in vivo* DNA.

Chapter 5 – Tracking Resonances of Hydrated Nucleobase Anions

This chapter details and builds upon the following publications:

³⁰⁷ G. A. Cooper[†], C. J. Clarke[†] and J. R. R. Verlet*, *J. Am. Chem. Soc.*, 2023, **145**, 1319-1326

³¹¹ G. A. Cooper, C. J. Clarke and J. R. R. Verlet*, *J. Phys. B: At. Mol. Opt. Phys.*, 2023, **56**, 185102

[†] Authors contributed equally.

All experimental work was performed by C. J. Clarke and G. A. Cooper. All computational work was performed by C. J. Clarke.

5.1. Introduction

The threat that high-energy ionising radiation poses to living cells is largely an indirect one. For instance, high-energy radiation can be absorbed by intracellular water molecules to produce hydroxyl radicals (and other species), which go on to damage nearby DNA strands.³¹² Low-energy electrons (<20 eV) can also be produced in great numbers (~40,000 / MeV),³¹³ and participate in further reactions. In particular, Sanche and coworkers have observed low-energy electrons to induce lesions in DNA, such as single- and double-strand breakages.^{164,169,170,314} This has prompted much interest in the underlying electron attachment mechanism to DNA, notably for potential applications to the development of radiosensitisers in cancer therapy.^{315,316} As described in Section 1.2.4, the main postulated mechanism involves initial electron capture into the antibonding π^* resonances on the nucleobases, followed by nonadiabatic charge transfer to a σ^* state across the C–O sugar-phosphate bond, inducing strand cleavage.^{173,317} However, understanding exactly which π^* states participate in the initial capture requires further investigation into the influence of the DNA environment on the nucleobase anion resonance energies.

Through the study of anion-solvent clusters in the gas-phase, the effects of solvation can be probed with great mechanistic detail. To this end, Kočišek *et al.* performed an elegant (electron impact) ion yield spectroscopic study on uracil- and thymine-water clusters, $U(H_2O)_n$ and $T(H_2O)_n$, respectively.³¹⁸ Although it was already well-known that the bare U and T nucleobases undergo dissociative electron attachment upon exposure to low-energy electrons (< 3 eV),^{319–322} Kočišek *et al.* showed that this channel was suppressed when the nucleobases were clustered with water, and instead the only dissociation channel observed was (full or partial) evaporation of the clustered water molecules, leaving the anionic nucleobase intact.³¹⁸ This emphasises how the behaviour of gas-phase species can change substantially with even a

small degree of solvation. Unfortunately, relating these results to specific anion resonance states is very difficult, as the neutral clusters under study were not mass-separated.

In the studies presented in this chapter,^{307,311} the anion resonance states of nucleobase-water clusters are directly probed via photoexcitation from the ground state anion. Since mass-selection is naturally implemented, and the photon energy can be tuned to populate specific resonance states, the behaviour of targeted resonances can be tracked with the incremental addition of water, and related to bulk aqueous conditions through extrapolation.

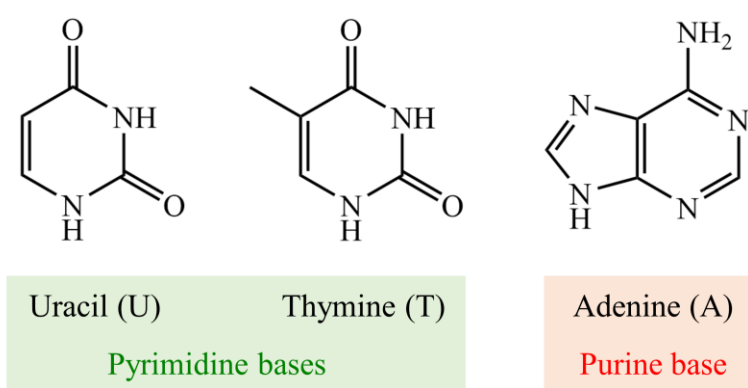


Figure 5.1: Canonical structures of the nucleobases under examination.

Three different nucleobases were studied: uracil (U), thymine (T) and adenine (A). The chemical structures of these species are shown in Figure 5.1. Uracil-water cluster anions, $U^-(H_2O)_n$, happened to be generated with the greatest ease, and therefore take the primary focus. Small uracil-water cluster anions ($n \leq 7$) have been previously studied by photoelectron spectroscopy in other groups.^{180,181} They found that, despite the ground state of the bare uracil anion U^- being a weak dipole-bound state, the addition of even a single water molecule sufficiently stabilises the lowest electronic shape resonance, π_1^* , to become the ground state of $U^-(H_2O)_n$. We now explore if the other shape resonances follow in this stead.

5.2. Methodology

5.2.1. Experimental

The cluster instrument was used to perform the experiments outlined below.¹⁸⁸ A solid sample of U, T, or A was placed inside a pulsed Even-Lavie valve¹⁸⁹ and heated to approximately 220 °C. The valve was backed with nitrogen at ~5 bar pressure, flowed over a drop of water in the backing line, inducing formation of the corresponding nucleobase-water clusters. The corresponding anions were formed via electron attachment to the clusters using a ring filament ioniser. The anion clusters then underwent mass separation, and were intersected by a timed laser pulse. All (two-dimensional) photoelectron spectra were acquired using tuneable wavelength nanosecond laser pulses from the OPO. The POP algorithm was applied for image reconstruction.¹⁹⁵

5.2.2. Computational

To aid interpretation of the experimental 2DPES of $A^-(H_2O)_n$, Gaussian 16²⁹⁶ calculations were performed for the three main prototropic tautomers of adenine (N3, N7 and N9). Anionic and neutral molecular structures were optimised using DFT/CAM-B3LYP/aug-cc-pVDZ.^{217,221} Anion resonance positions, relative to the energy of the neutral species, were estimated using a stabilisation method.²³⁰ Starting with the optimised neutral geometry above, single point energy calculations were repeated with the CAM-B3LYP functional, but with a modified aug-cc-pVDZ(α) basis set, where α represents an adjustable scaling factor. In particular, the exponents of the most diffuse s and p functions on all C and N atoms, and the most diffuse s function on all H atoms, were multiplied by α . The range of α chosen for this analysis was 0.3–2.0, in increments of 0.05. The energies of the virtual molecular orbitals were extracted and plotted against α , revealing avoided crossings at energies that were consistent

with those of the anion resonance states. Estimates for the anion resonance energies were simply taken as the midpoint of the avoided crossings.^{176,323}

To help validate that the estimated $\pi_3^* \leftarrow \pi_1^*$ excitation energy associated with the N3 tautomeric anion was in reasonable agreement with the experimental evidence for UV photoexcitation, time-dependent DFT calculations were carried out using the B3LYP^{215,216} and CAM-B3LYP²¹⁷ functionals, with the cc-pVDZ basis set.²²⁰ The less diffuse basis set was selected to limit the number of discretised continuum orbital solutions, which otherwise interfered with the excited state calculations. To assess the character associated with the valence excitations, natural transition orbitals were calculated.

5.3. Identification of Anion Resonance States

Excited anion resonance states can be observed through multiple experimental signatures in FRPES. One of these – the appearance of thermionic emission – was already utilised in Chapter 3 to deduce the approximate energetic position of a resonance of the pyruvate anion. This section describes how the degree of thermionic emission can be more precisely quantified, taking the uracil dihydrate cluster anion, $\text{U}^-(\text{H}_2\text{O})_2$, as an example. Two other spectral signatures of resonance excitation are also characterised and quantified, and altogether provide consistent excitation energies. Further application and comparison of the three resonance identification techniques outlined in this section can be found in Section 5.4, within the context of larger $\text{U}^-(\text{H}_2\text{O})_n$ clusters.

5.3.1. FRPES of $\text{U}^-(\text{H}_2\text{O})_2$

The 2DPES of $\text{U}^-(\text{H}_2\text{O})_2$ across a photon energy range of $1.2 \leq h\nu \leq 5.2$ is presented in Figure 5.2(a). Photoelectron images were acquired in steps of $\Delta h\nu = 0.1$ eV. Unlike in Chapter 3, the FRPES is best represented as a 2DPES due to the large number of closely-spaced spectra being displayed. Each individual photoelectron spectrum can be recognised as a horizontal slice through the 2DPES at the appropriate photon energy.

The dominant feature in Figure 5.2(a) is a diagonal photoelectron signal starting around $h\nu \approx 1.5$ eV. This corresponds to direct photodetachment of $\text{U}^-(\text{H}_2\text{O})_2$ in its π_1^* ground state, forming the neutral in its S_0 ground state. The feature appears as diagonal in the 2DPES because, with an increase in $h\nu$, there is an equal corresponding increase in the eKE of the measured electrons. A second diagonal feature is present too, emerging at a higher photon energy of $h\nu \sim 4.6$ eV. This also follows from direct photodetachment of the π_1^* state, but to an excited triplet state (T_1) of $\text{U}(\text{H}_2\text{O})_2$.

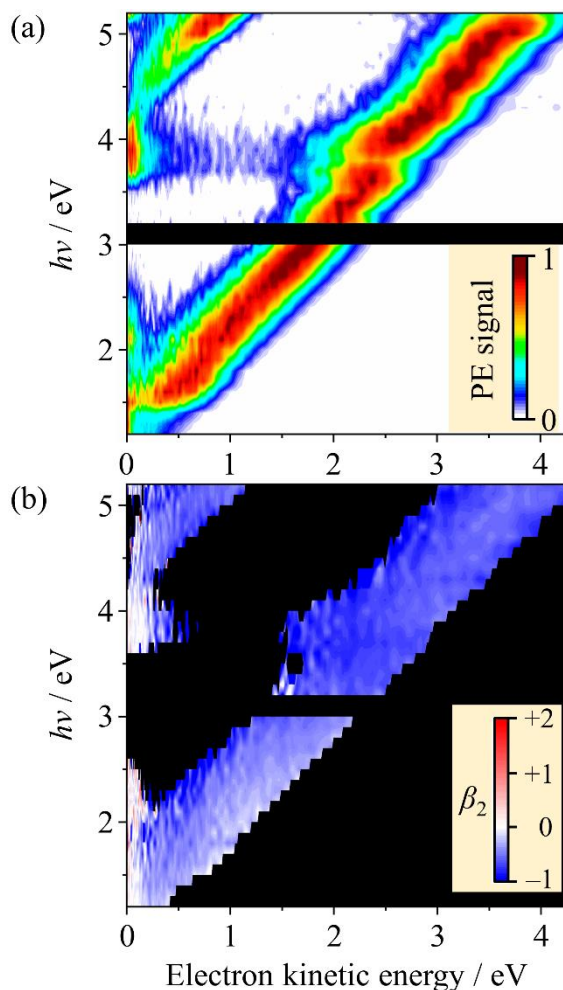


Figure 5.2: (a) 2D photoelectron spectrum of the uracil dihydrate cluster anion, $U^-(H_2O)_2$. Each spectrum has been normalised to its maximum intensity. No spectrum was acquired for the photon energy $h\nu = 3.1$ eV due to poor laser output from the OPO. (b) Corresponding photoelectron angular distributions for the 2DPES in (a). PADs are not shown for regions with little photoelectron signal ($<10\%$).

In Figure 5.2(a), there is clear evidence of photoexcitation to anion resonance states. The main telltale sign is the observation of thermionic emission. At a narrow window of photon energies around $h\nu = 3.9$ eV, there is electron emission centred on $eKE = 0$ eV with a Boltzmann distribution of electron kinetic energies. As described in Section 1.1.3, this is the characteristic spectral trace of electrons lost through (statistical) thermionic emission. At a range of lower photon energies, $h\nu < 3.0$ eV, thermionic emission is also observed but with less intensity compared to the $S_0 \leftarrow \pi_1^*$ direct detachment feature. Using the results of earlier electron transmission spectroscopy experiments,¹⁷⁴ we can correlate the resonant transition at

$h\nu = 3.9$ eV to the $\pi_3^* \leftarrow \pi_1^*$ photoexcitation, and the broad resonance at lower photon energies to the $\pi_2^* \leftarrow \pi_1^*$ photoexcitation. Further information regarding this assignment is provided in Section 5.4.1. Both π_2^* and π_3^* are shape resonances, so it is unsurprising that each can be accessed via photoexcitation with relative ease.

In Figure 5.2(a), a second indicator of photoexcitation to an anion resonance is observed through shifts in the eKE distribution of the $S_0 \leftarrow \pi_1^*$ direct detachment feature. Around $h\nu = 3.9$ eV, the mean eKE associated with direct detachment is lower than expected, resulting in a ‘wiggle’ in the diagonal feature. As described in Section 1.1.3, these lower-eKE electrons arise due to autodetachment: photoexcitation transitions the anion from the π_1^* to the π_3^* state, intermediary dynamical processes begin to transpire (e.g. internal conversion to lower energy resonances), and then electrons are subsequently lost from an anion resonance state. Although the shift in mean eKE is relatively clear in the vicinity of the π_3^* resonance, autodetachment does not appear to be as prevalent for photoexcitation to the π_2^* resonance.

The third indicator of resonance excitation is contained within the photoelectron angular distributions (PADs). Figure 5.2(b) displays a 2D contour plot of the PADs measured at each (eKE, $h\nu$) coordinate. Photodetachment from the π_1^* state of $U^-(H_2O)_2$ results in photoelectrons emitted with negative anisotropy (preferentially perpendicular to the laser polarisation axis), as typically expected for detachment from a state with π^* character. In the vicinity of the π_3^* resonance, the PADs of the direct detachment feature appear to change subtly. PADs can be very sensitive to the electronic structure of state being detached, so although the excited resonance is also of π^* character, it is not unexpected to see its introduction reflected in the angular distribution.

5.3.2. Ratio of Thermionic Emission to Direct Detachment

The observation of thermionic emission reliably implies that an excited state is being populated, although the converse is not necessarily true. In the mechanism of thermionic emission, following photoexcitation, a vibrationally-hot ground state of the anion is formed through energy redistribution (IVR) and nonadiabatic processes, wherefrom the electron is lost statistically (see Section 1.1.3). If the dynamics of the initially excited state do not result in ground state (re)formation, thermionic emission should not be observed. Fortunately, both the π_2^* and π_3^* resonances of the $\text{U}^-(\text{H}_2\text{O})_2$ anion appear to undergo such relaxation processes on a timescale fast enough to observe thermionically emitted electrons.

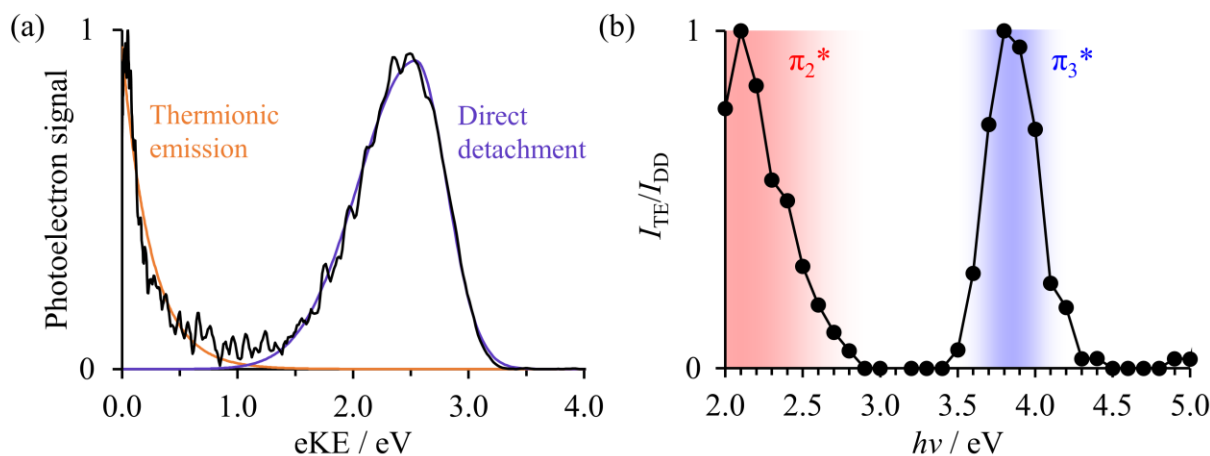


Figure 5.3: (a) Photoelectron spectrum of $\text{U}^-(\text{H}_2\text{O})_2$ acquired at $h\nu = 3.9$ eV. Orange and purple curves show the underlying fits to the thermionic emission and direct detachment features, respectively. (b) Ratio of integrated photoelectron signal associated with thermionic emission to direct detachment. As the photon energy approaches $h\nu \sim 3.85$ eV, the π_3^* resonance (blue) is accessed and the yield of thermionically emitted electrons increases. Excitation to the π_2^* resonance (red) occurs at $h\nu < 2.8$ eV.

The energetic position of the π_3^* resonance relative to the π_1^* ground state can be determined by tracking the number of thermionically emitted electrons as $h\nu$ is scanned. To quantify the amount of thermionic emission, we compared the total yield of thermionically emitted electrons to those lost to direct photodetachment ($\text{S}_0 \leftarrow \pi_1^*$). More precisely, the amount

of thermionic emission was quantified by taking the ratio of photoelectron signal associated with thermionic emission to that of the direct detachment: I_{TE}/I_{DD} . Figure 5.3(a) highlights these two contributions to the photoelectron spectrum of $U^-(H_2O)_2$ at $h\nu = 3.9$ eV. The photoelectron signal of each feature can be appropriately measured either through: (i) the peak heights; (ii) integration of the photoelectron signal in the appropriate eKE ranges; or (iii) integration of fits to the peaks. All three methods of quantification were found to give similar results for I_{TE}/I_{DD} .

Figure 5.3(b) shows I_{TE}/I_{DD} as a function of $h\nu$ using quantification method (iii), where the thermionic emission signal was fit to a decaying exponential function (Figure 5.3(a), orange), and the direct detachment signal was fit to an asymmetric Gaussian function (Figure 5.3(a), purple). One sharp peak is present, centred between $3.8 < h\nu < 3.9$ eV. This indicates that the vertical excitation energy of the $\pi_3^* \leftarrow \pi_1^*$ transition is approximately 3.85 eV. It should be noted that this vertical energy gap is in the equilibrium geometry of the $U^-(H_2O)_2$ anion, and is therefore expected to differ from the vertical electron attachment energy that would be observed in electron scattering studies on $U(H_2O)_2$.

The excitation energy associated with the $\pi_2^* \leftarrow \pi_1^*$ transition is more difficult to distinguish. Although it is clear that the degree of thermionic emission increases substantially at $h\nu < 2.8$ eV, the peak shown in Figure 5.3(b) is very broad. The lowest photon energy chosen for the I_{TE}/I_{DD} analysis described above was $h\nu = 2.0$ eV, and the degree of thermionic emission remained high at that wavelength. For $h\nu < 2.0$ eV, the direct detachment feature is centred at such low eKE (< 0.6 eV) that the associated photodetachment cross-section diminishes substantially, in accordance with the Wigner threshold law.¹³ As such, no lower edge of the π_2^* resonance excitation could be determined.

5.3.3. Kinetic Energy Shifts Arising from Autodetachment

Autodetachment can result in changes in the shape of the photoelectron spectrum, as the FCFs associated with the $S_0 \leftarrow \pi_3^*$ transition differ to those of the $S_0 \leftarrow \pi_1^*$ transition, and nuclear dynamics lead to a reduction in the energy gap between the autodetaching resonance and the neutral ground state. Figure 5.4(a) presents the central measured electron kinetic energy associated with the (fitted) $S_0 \leftarrow \pi_1^*$ direct detachment peak with changing $h\nu$. The central eKE increases linearly until the photon energy is in the range of accessing the π_3^* resonance, at which there is a notable shift towards lower eKE. This shift is emphasised in Figure 5.4(b) by plotting the residuals between the measured and ‘unperturbed’ central eKEs, where the ‘unperturbed’ eKEs are extrapolated from the data at non-resonant wavelengths. At a photon energy of $h\nu = 3.9$ eV, there is the greatest deviation in eKE. This is further corroborated by tracking the width of the direct detachment feature (Figure 5.4(c)). Upon excitation to the π_3^* resonance, the feature also broadens due to changing FCFs and the increased emission of lower-eKE electrons. Once again, at $h\nu = 3.9$ eV there is greatest deviation from the value at non-resonant wavelengths. It should be noted that no significant eKE shift or broadening is exhibited upon excitation to the π_2^* resonance, suggesting that the autodetachment is less prominent from this state, or suppressed through competing dynamical processes.

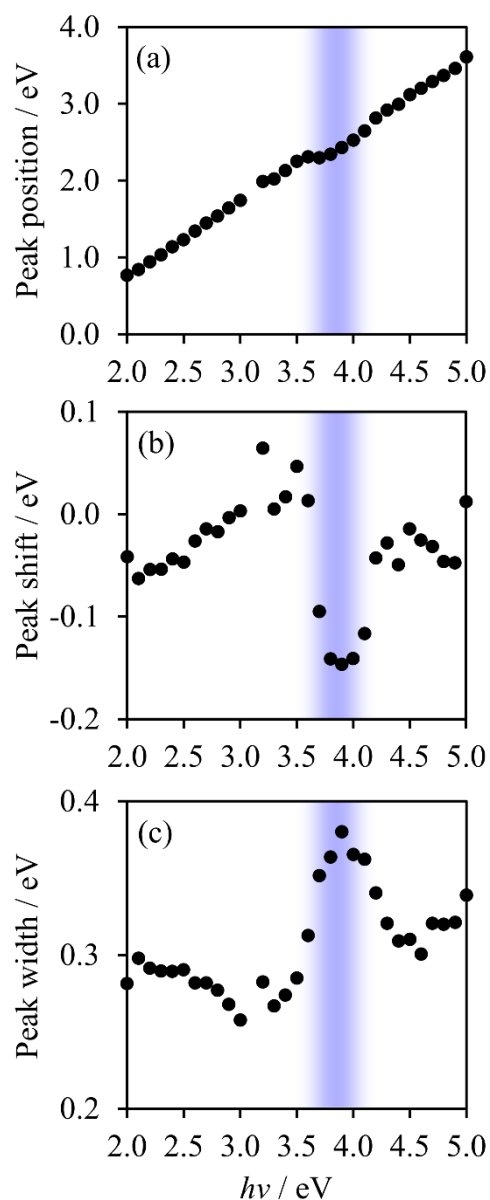


Figure 5.4: (a) Central eKE position of the $S_0 \leftarrow \pi_1^*$ direct detachment feature of $U^-(H_2O)_2$. (b) The deviation of the central eKE position to the expected position (in absence of excited states). (c) The associated change in the peak width of the direct detachment feature. The blue shaded region highlights changes induced by photoexcitation to the π_3^* resonance.

5.3.4. Changes in Photoelectron Angular Distributions

The PADs also appear to mildly change in the vicinity of the π_3^* resonance. To quantify the anisotropy at each photon energy, the β_2 parameters were averaged across the eKE window of the direct detachment feature. In the averaging procedure, the contribution of β_2 was

weighted by the corresponding photoelectron signal at the appropriate eKE. This ensured that the averaged anisotropy correctly accounted for the number of photoelectrons being measured. The resulting averaged $\beta_2(h\nu)$ are presented in Figure 5.5.

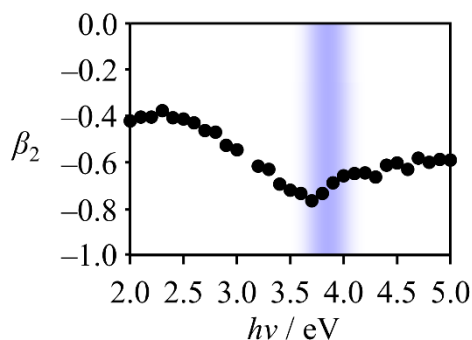


Figure 5.5: Averaged β_2 anisotropy parameters across the $S_0 \leftarrow \pi_1^*$ direct detachment feature for different photon energies. Blue shaded region highlights the position of photoexcitation to the π_3^* resonance found by tracking the thermionic emission and shifts in eKE.

Throughout the range of applied photon energies, the averaged β_2 parameter was negative, consistent with detachment from either π_1^* or π_3^* orbitals. The PAD is known to depend on the outgoing eKE, so it is unsurprising that gradual changes in β_2 are observed with increasing photon energy. However, on the lower edge of the π_3^* resonance ($h\nu \sim 3.7$ eV), there is a notable ‘kink’ in the anisotropy parameter. This kink can arise from the activated photoexcitation pathway to the π_3^* resonance. Although both states are expected to produce photoelectrons with $\beta_2 < 0$, the magnitude of these parameters may be quite different. It appears in this case, electron detachment following excitation to the π_3^* resonance is producing a slightly more isotropic PAD. Although the PADs may be used to locate the π_3^* resonance of $U^-(H_2O)_2$, it is apparent that the contrast is far less clear than through the other two techniques described above. Excitation to the π_2^* resonance did not appear to produce a significant change in the PADs, just as it did not induce a shift in the eKE distribution of the direct detachment feature.

5.4. Effect of Hydration

We now shift focus to larger uracil-water cluster anions, $U^-(H_2O)_{n \geq 2}$. Using the resonance identification techniques highlighted in Section 5.3, the energies of the π_2^* and π_3^* resonances can be tracked (relative to the π_1^* ground state) with the incremental increase in hydration. We aimed to acquire enough data to perform an extrapolation to the bulk limit, building up a picture of the electron attachment capabilities of aqueous uracil.

5.4.1. FRPES of $U^-(H_2O)_n$

2DPES of uracil-water cluster anions, $U^-(H_2O)_n$, with $n = 2, 3, 4, 6, 8,$ and 10 water molecules are presented in Figure 5.6. For each, photoelectron spectra were acquired in increments of $\Delta h\nu = 0.1$ eV. The 2DPES of the $n = 2$ cluster has been described in Section 5.3. The 2DPES of the larger clusters are similar in many ways. In each, the (diagonal) $S_0 \leftarrow \pi_1^*$ direct detachment feature is prevalent. In addition, thermionic emission occurs from all clusters, at similar photon energies to those found for the dihydrate cluster anion.

The $S_0 \leftarrow \pi_1^*$ direct detachment feature has unit gradient in each 2DPES, but is shifted towards lower eKEs for the larger clusters. This shows that when the same $h\nu$ is applied, electrons are lost with less kinetic energy for incrementally larger clusters, and thus the electron binding energy (eBE) of $U^-(H_2O)_n$ increases with hydration. In other words, each clustered water molecule stabilises the π_1^* ground state of the anion to a greater degree than the S_0 ground state of the neutral, such that the ADE and VDE increase with n . Quantification of the eBE vs n is considered below in Section 5.4.2. Detachment to the first excited neutral state ($T_1 \leftarrow \pi_1^*$) is obscured for larger clusters, since the associated electron binding energy increases above the maximum implemented photon energy ($h\nu = 5.2$ eV).

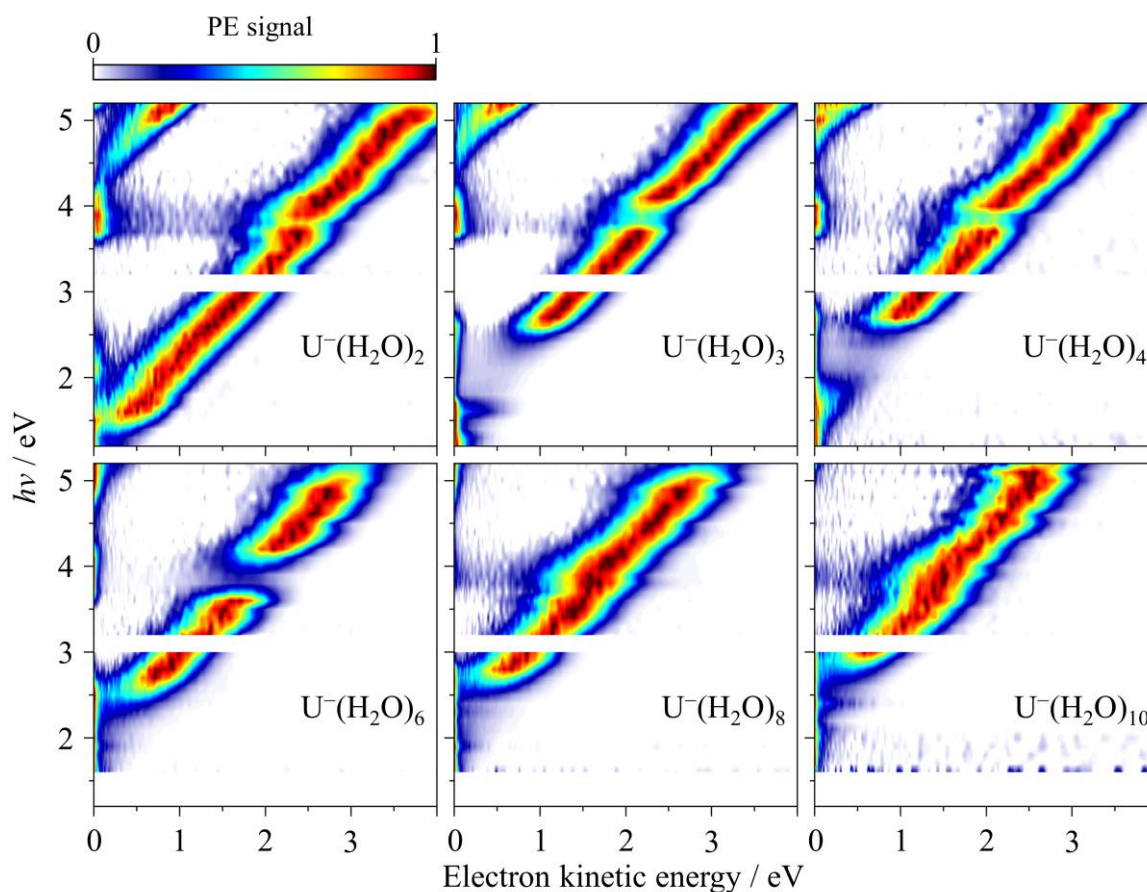


Figure 5.6: 2DPES of a series of uracil-water cluster anions, $\text{U}^-(\text{H}_2\text{O})_n$, with $n = 2-4, 6, 8$ and 10 . Each photoelectron spectrum was normalised to its maximum intensity. Photoelectron spectra were not acquired at $h\nu = 3.1$ eV due to poor laser output.

Interestingly, the positions of the excited state resonances do not appear to shift in the 2DPES, indicating that the vertical excitation energies are the same for each uracil-water cluster anion. To examine this further, $I_{\text{TE}}/I_{\text{DD}}$ is presented for each cluster in Figure 5.7, following the same procedure to that detailed in Section 5.3.2. Indeed, the sharp peak corresponding to π_3^* excitation is centred between $3.8 \leq h\nu \leq 3.9$ eV for each $\text{U}^-(\text{H}_2\text{O})_n$ measured. Herein lies the justification for correlating the two observed excited states with the π_2^* and π_3^* resonances found in electron scattering experiments.¹⁷⁴ For example, the $\pi_1^*-\pi_3^*$ energy gap found through electron transmission spectroscopy is ~ 3.6 eV, slightly smaller than the ~ 3.85 eV observed in our experiments. However, the former was measured beginning with the equilibrium geometry of neutral uracil, whereas we begin with the equilibrium geometry of the

(microhydrated) uracil anion, so some deviation is expected. We observe that hydration does not otherwise affect the excitation energy, and therefore it is appropriate to assign these resonance states.

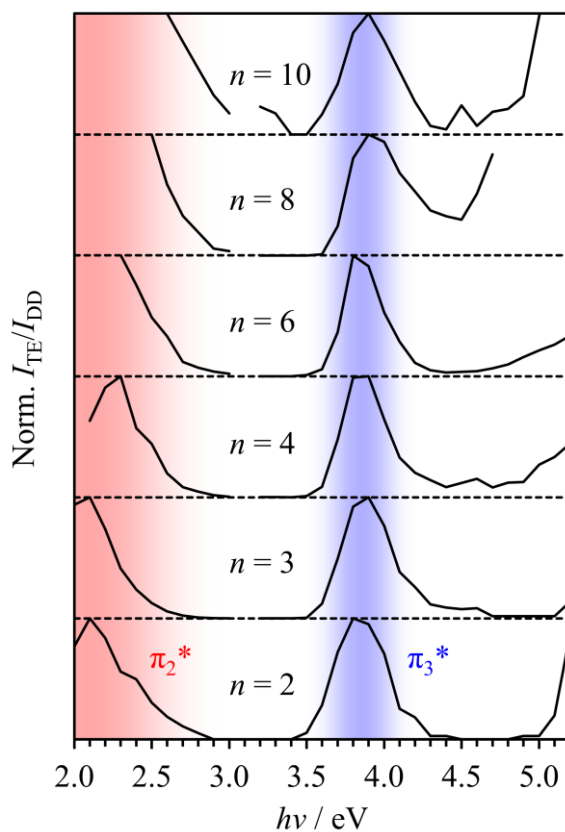


Figure 5.7: Ratio of integrated photoelectron signal associated with thermionic emission to direct detachment, for six selected $U^-(H_2O)_n$ cluster anions. The photon energies corresponding to photoexcitation from the π_1^* ground state to the π_2^* and π_3^* resonances are highlighted in red and blue, respectively. Data for each cluster was separately normalised in the region of each resonance.

As mentioned, the location of the π_2^* resonance was more difficult to track in the $U^-(H_2O)_2$ cluster, since the photodetachment cross-section associated with the direct detachment feature vanishes at low photon energies. This complication is amplified in the larger clusters, since the ADE increases with n , and thus directly detached electrons leave with even less kinetic energy. However, the high- $h\nu$ onset of the π_2^* resonance does not appear to shift with changing cluster size, so the excitation energy again appears to be unchanging. We

conclude that, in agreement with recent studies on the effect of hydration on polycyclic aromatic hydrocarbon anions,^{64,65} the excitation energies to the resonances are invariant to cluster size. Altogether, the π_1^* anion ground state is being stabilised with respect to the neutral state with increasing hydration, and the π_2^* and π_3^* resonances are stabilised at the same rate.

5.4.2. Extrapolation of Resonance Energies

In order to link our results to the condensed phase, is it possible to extrapolate the resonance state energies to the bulk aqueous limit? To attempt such an extrapolation, larger clusters needed to be measured. Performing FRPES on even larger uracil-water cluster anions ($n > 10$) would have been prohibitively time-consuming. Instead, we recognise that we have shown that the anion resonance states stabilise at the same rate as π_1^* with increasing hydration, and thus we need only track the stabilisation of the ground state. This requires a single photoelectron spectrum for each cluster, where the necessary eBE is extracted from the $S_0 \leftarrow \pi_1^*$ direct detachment feature. At a fixed photon energy of $h\nu = 3.6$ eV, photoelectron spectra were acquired for uracil-water clusters up to $n = 35$. This photon energy was selected because it was: higher than the eBE of the largest clusters; produced from the OPO with sufficiently good laser power; and (mostly) non-resonant with any excited states. The series of fixed-wavelength photoelectron spectra are displayed in Figure 5.8.

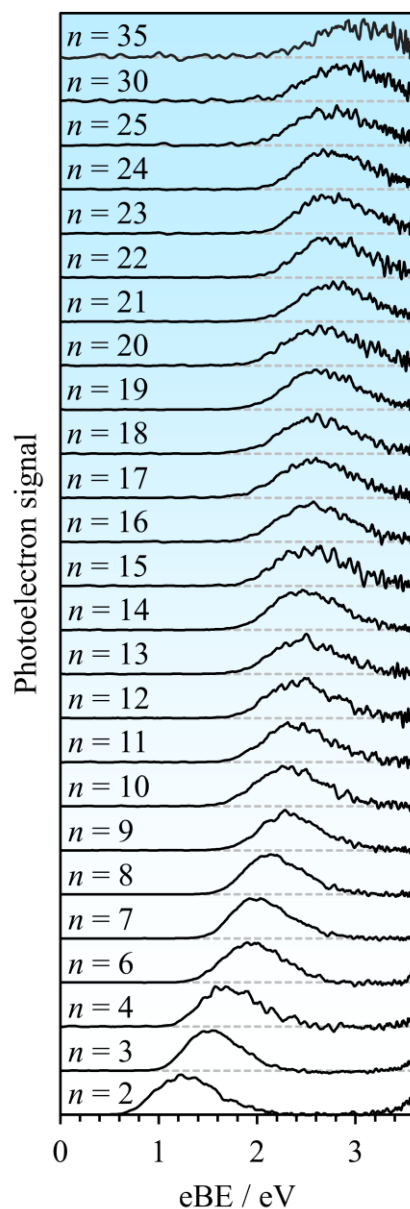


Figure 5.8: Normalised photoelectron spectra of $\text{U}^-(\text{H}_2\text{O})_n$ acquired with $h\nu = 3.6$ eV nanosecond laser pulses.

The electron binding energy of $\text{U}^-(\text{H}_2\text{O})_n$ can be defined in terms of ADE or VDE. For each spectrum displayed in Figure 5.8, the cluster-dependent ADE was extracted from the low-eBE onset (10% of peak height) of the photoelectron signal. Similarly for each cluster, the VDE was given by the eBE at which there was most photoelectron signal. Clearly, both the ADE and the VDE increase with cluster size, confirming that for very large clusters, the π_1^* state continues to be stabilised with respect to the neutral ground state. This information is

reformatted as an energy level diagram in Figure 5.9. All energies are relative to the S_0 neutral ground state, and the corresponding energy of the π_1^* state is shown in terms of both ADE and VDE.

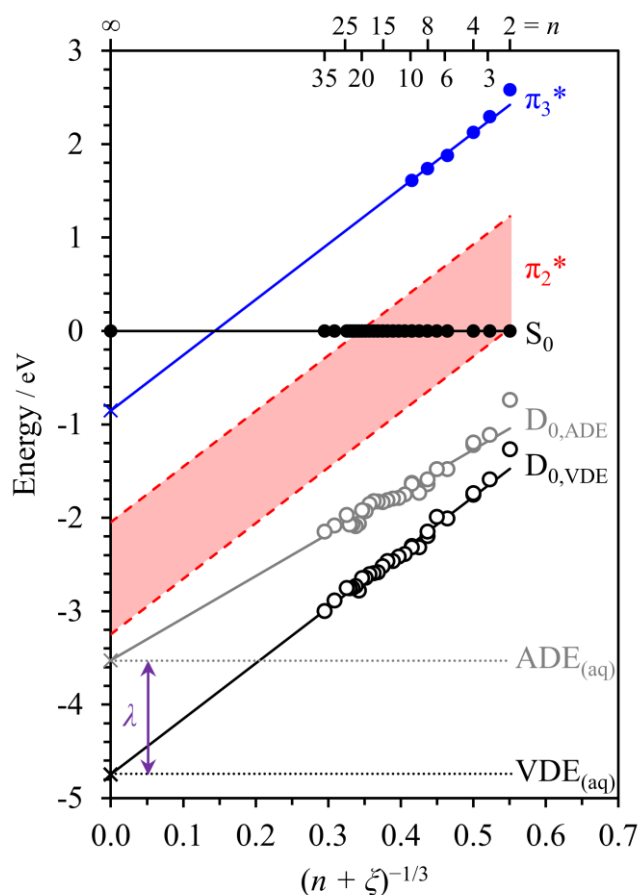


Figure 5.9: Energy level diagram for $U^-(H_2O)_n$ clusters, relative to the ground state of the neutral clusters, S_0 , plotted as a function of cluster size, $(n + \zeta)^{-1/3}$. Circles represent data taken from Figures 5.7 and 5.8 for the π_1^* ground state and the π_3^* resonance, and the dashed lines represent the extracted range of the π_2^* resonance. Linear fits (considering $n \geq 3$) to the vertical detachment energy, VDE, and adiabatic detachment energy, ADE, are extended to their respective bulk limits, shown with crosses. The difference between these extrapolated energies, $VDE_{(aq)}$ and $ADE_{(aq)}$, corresponds to the reorganisation energy, λ . The gradients of the lines fitting the π_2^* and π_3^* resonances were matched to that of the VDE.

For sufficiently large clusters, the ADE and VDE each evolve linearly as a function of $n^{-1/3}$, as observed in earlier cluster studies.⁴ However, the gradient of the $U^-(H_2O)_n$ VDE as a function of $n^{-1/3}$ did not agree with the expected gradient from continuum dielectric theory in the bulk aqueous limit.^{153,324} This was because the volume that U^- occupies in the cluster had

not been accounted for. Therefore, the energies in Figure 5.9 are plotted against $(n + \zeta)^{-1/3}$, where ζ is the ratio of volumes between U^- and a single water molecule. A value of $\zeta = 4$ produces a VDE gradient in agreement with the dielectric sphere model (whether U^- is surface or internally solvated).³²⁵ This choice of ζ is also supported by considering the relative (partial) molar volumes of U and H_2O , where $V_U = 72 \text{ cm}^3 \text{ mol}^{-1}$ (corresponding to $\zeta = 4$, since $V_{H_2O} = 18 \text{ cm}^3 \text{ mol}^{-1}$) for neutral uracil,³²⁶ which is likely to be a reasonable estimate for U^- (based off of the modest effects of electrostriction in the adenine nucleobase).³²⁷ Exploratory electronic structure calculations (CAM-B3LYP/aug-cc-pVDZ offered further justification; by defining the molecular volume as the volume contained within a contour of 0.001 electrons/Bohr³, we calculated ζ to range from 3–5, depending on the degree of microsolvation. Taken together, $\zeta = 4 \pm 1$ is a reasonable estimate for the excluded volume of U^- , and the analysis below includes consideration of this uncertainty.

Extrapolation of the ADE and VDE to the bulk limit ($n = \infty$) was performed, yielding the respective binding energies for U^- in aqueous solution: $ADE_{(aq)} = 3.53 \pm 0.20 \text{ eV}$ and $VDE_{(aq)} = 4.75 \pm 0.20 \text{ eV}$. These bulk properties are inherently difficult to measure by any other experimental technique (e.g. liquid-microjet spectroscopy) due to the unstable open-shell nature of U^- . Our extracted $ADE_{(aq)}$ and $VDE_{(aq)}$ both compare excellently with recent computed values.³²⁸ The smallest cluster ($n = 2$) was not incorporated into the linear fits as it was observed to significantly deviate from the linear trend (which was not unexpected), but all other clusters were included. The 0.20 eV uncertainties were predominantly associated with the choice in ζ . Notably, consideration of *only* the larger clusters (e.g. $n \geq 16$, which are more representative of $U^-_{(aq)}$) also produced bulk binding energies within the stated uncertainty.

Figure 5.9 also displays the energies of the π_2^* and π_3^* resonances, with respect to S_0 . Although we only obtained data for relatively smaller clusters ($n \leq 10$), the gradient as a function of $(n + \zeta)^{-1/3}$ for the π_3^* resonance is similar to that of the VDE. The stabilisation of

the resonance energies follow the VDE rather than the ADE because photoexcitation and direct detachment ($S_0 \leftarrow \pi_1^*$) are both transitions within the equilibrium geometry of the anion. Figure 5.9 illustrates that with increasing hydration, and with respect to the neutral S_0 ground state, the π_2^* and π_3^* resonances continue to become stabilised by an extent similar to that of the anion ground state.⁶⁴ From the aforementioned similar gradients (between π_3^* and VDE), we have confidence that the resonance energies can also be extrapolated to even larger sizes. Full extrapolation of the resonance energies to the bulk limit show that both the π_2^* and π_3^* resonances become bound states in $U^-_{(aq)}$, with the latter stable by ~ 0.85 eV. However, it is important to recognise that the current work considers the resonances within the geometry and hydration sphere of the U anion, whereas electron attachment to U will produce the anion in the geometry and hydration sphere of the neutral. Therefore, we must address the corresponding geometric anion-to-neutral reorganisation if we wish to link our results to the mechanism of electron attachment.

5.4.3. Electron Attachment to Aqueous Uracil

The reorganisation energy, $\lambda(n)$, is the energy difference between $U(H_2O)_n$ in its natural geometry and hydration sphere, and $U(H_2O)_n$ in the geometry and hydration sphere of the anionic cluster. The reorganisation energy is expected to increase with a higher degree of solvation, as larger clusters contain more solvent molecules which undergo rearrangement. Recalling that the difference in ADE and VDE is reflective of anion-to-neutral geometry changes, the increasing reorganisation energy (with n) is observed in the diverging gradients of the ADE and VDE in Figure 5.9 (and equivalently, in the spectral broadening exhibited in the one-colour photoelectron spectra in Figure 5.8). In the bulk limit, we can obtain an estimate for $\lambda_{(aq)}$ from the difference between the $ADE_{(aq)}$ and $VDE_{(aq)}$. This is shown pictorially as a Marcus-type plot in Figure 5.10, where the potential energy surfaces of each state are treated

as harmonic (in some reorganisation coordinate). From the $\text{ADE}_{(\text{aq})}$ and $\text{VDE}_{(\text{aq})}$ stated above, we find that $\lambda_{(\text{aq})} = 1.2 \text{ eV}$.

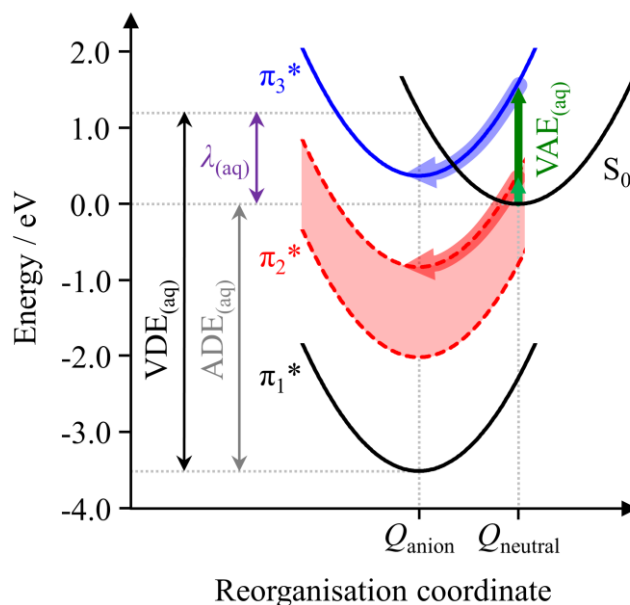


Figure 5.10: Schematic Marcus picture showing aqueous-phase energy curve, with energies determined from the extrapolation of uracil-water cluster anions. The $\text{VDE}_{(\text{aq})}$ and $\text{ADE}_{(\text{aq})}$ correspond to the aqueous vertical and adiabatic detachment energies, respectively. The reorganisation energy is defined by $\lambda_{(\text{aq})}$. Upwards block arrows show the vertical electron attachment energies ($\text{VAE}_{(\text{aq})}$) to the aqueous neutral uracil, with horizontal block arrows showing the dynamical evolution following electron attachment, which stabilise the generated anion resonances through reorganisation.

We now compare the *aqueous* anion resonance energies in the equilibrium geometry and hydration sphere of the anion, Q_{anion} , to that of the neutral, Q_{neutral} , within linear response theory.⁴³ Relative to S_0 , the π^* resonances in the Q_{neutral} geometry are $2\lambda_{(\text{aq})}$ (i.e. 2.4 eV) higher in energy than they are in Q_{anion} . For example, as illustrated in Figure 5.10, the π_3^* state is $\sim 0.9 \text{ eV}$ below S_0 in Q_{anion} , but is $\sim 1.5 \text{ eV}$ above S_0 in Q_{anion} . Hence, the π_3^* resonance of $U_{(\text{aq})}$ is capable of capturing electrons with a vertical attachment energy of $\text{VAE}_{(\text{aq})} \sim 1.5 \text{ eV}$. Similarly, the high-energy edge of the π_2^* resonance shifts to be above S_0 in the neutral geometry so that it too is a resonance, which can be populated by electrons with very low energy ($\text{VAE}_{(\text{aq})} < 0.4 \text{ eV}$, approximately). Upon formation of either resonance, solvation will

act rapidly (on a timescale of less than 100 fs)^{329,330} to accommodate the change in charge state of the nucleobase, dynamically shifting the resonance to lower energy (curved arrows in Figure 5.10). This enables the π_2^* and π_3^* resonances to adiabatically evolve into bound states. While the resonances were generally unbound in the cluster studies presented here, internal conversion can also take place to form the bound anion ground state, as evidenced by the widespread thermionic emission. Such internal conversion to the π_1^* ground state is also very likely possible in solution, providing further stabilisation of anions formed through electron attachment. Note also that the π_2^* state could participate in the electron capture mechanism of the π_3^* resonance by serving as an intermediate to the π_1^* state. In summary, through extrapolation, we show that the aqueous uracil molecule is capable of accepting low-energy electrons and appears to subsequently form a stable anion through geometric reorganisation and internal conversion.

Our findings are broadly consistent with those from Kočišek *et al.*, who showed that neutral $U(H_2O)_n$ clusters attached electrons over a relatively narrow range of < 2 eV, which subsequently leads to the evaporation of H_2O molecules.³¹⁸ As mentioned earlier, direct connection of their results to certain resonance states was not possible due to their limited cluster size specificity, but we show that such excitation could be consistent with attachment into the π_2^* resonance. Conversely, from Figure 5.10 and with accountment for the reorganisation energy $\lambda(n)$, the π_3^* resonance is inaccessible with electrons energies < 2 eV, except for the very largest clusters, which were unlikely to form in their experiments.³¹⁸

Electron capture to a nucleobase is the first step in the generally accepted mechanism for low-energy electron-induced DNA damage. The π^* resonances considered here could therefore serve as the entrance channel that triggers backbone fragmentation in aqueous RNA. The results presented in Section 5.5 on the other nucleobases will confirm that we expect similar low-energy electron accepting properties in aqueous DNA. Indeed, a clear and

surprisingly narrow peak centred at ~ 0.6 eV is observed in the yield of single-strand breaks of deposited DNA containing its structural water¹⁷⁰ and a similar, though less pronounced peak, at very low energy to DNA in cells.¹⁶⁸ Moreover, recent transient ultrafast radiology experiments have shown that radical anions are formed by low-energy electron attachment to the nucleobases and nucleotides in aqueous solution.³³¹ Hence, our gas-phase measurements appear to link up with observations in the bulk and potentially in biological environments, demonstrating the value of the bottom-up approach and FRPES as a tool to probe resonances in complex environments.

In conclusion, both the π_2^* and π_3^* shape resonances, which are well-known from electron transmission spectroscopy of isolated U,¹⁷⁴ have been observed in the water clusters. As evidenced by thermionic emission, a significant fraction of these resonances decay to form the ground state anion in all clusters studied (up to $n = 10$). Extrapolation with increasing $U^-(H_2O)_n$ cluster size of the resonances, ADEs, and VDEs, offered a picture of the energetics and available resonances in a bulk aqueous environment. For $U_{(aq)}$, the π_2^* and π_3^* resonances were found to be capable of electron capture with vertical attachment energies below 2 eV, and both become bound states of $U^-(aq)$ with sufficient (spontaneous) solute/solvent rearrangement. These results, relating to uracil in an aqueous environment, provide a vital step towards identifying the anion resonance states involved in low-energy electron attachment to the nucleobases in a DNA/RNA environment.

5.4.4. Decomposition of the Reorganisation Energy

As a final note on the $U^-(H_2O)_n$ data presented here, the reorganisation energy λ is examined in greater detail. The reorganisation energy can be decomposed into two individual components: $\lambda = \lambda_{IS} + \lambda_{OS}$, where λ_{IS} is the (inner-sphere) *intramolecular* reorganisation energy associated with the geometry change of the uracil solute upon the addition of an electron, and

λ_{OS} is the (outer-sphere) *intermolecular* reorganisation energy associated with the rearrangement of the surrounding water molecules induced by the extra charge. As seen in the diverging gradient of the ADE and VDE in Figure 5.9, the reorganisation energy is cluster size dependent: $\lambda(n)$, and through extrapolation we obtained the reorganisation energy in the bulk limit $\lambda_{(aq)} = 1.2$ eV. λ_{OS} can be assumed to be responsible for the n -dependence in λ , since the changing solvation sphere is expected to have very little effect on the overall structural changes exhibited in the U molecule upon the addition of an electron.

We expect a notable intramolecular reorganisation energy (λ_{IS}) between the neutral uracil molecule and its valence-bound anion, since the equilibrium geometry of the (S_0) neutral species is planar whereas that of the anionic π_1^* valence-bound state is bent.³³² The π_1^* state of U^- does not form over the DBS in the gas phase, so the intramolecular reorganisation energy had not been previously reported. Fortunately, the photoelectron spectra acquired for the small $U^-(Ar)_n$ and $U^-(N_2)_n$ anion clusters, presented in Chapter 4, allow us to estimate λ_{IS} via extrapolation. We find that $\lambda_{IS} = VDE(U^-) - ADE(U^-) = 0.2$ eV.²⁶⁸

The remaining contribution to the reorganisation energy of aqueous uracil is therefore $\lambda_{OS} = 1.0$ eV. We conclude that the dominant contribution to the neutral-to-anion reorganisation energy of $U^-_{(aq)}$ arises from restructuring of the intermolecular hydration sphere, i.e. from the solvent response, rather than the solute. These values for the deconvoluted reorganisation energies should serve as a useful benchmark for computational work aimed at understanding electronic resonances in bulk aqueous environments.^{333–335}

5.5. Other Nucleobase-Water Clusters

After demonstrating that the excited resonance states of the RNA nucleobase uracil were stabilised with an increasing degree of hydration, we sought to examine if this behaviour was also true of DNA nucleobases. FRPES is time-consuming and thus we focussed on a smaller selection of clusters than in the $U^-(H_2O)_n$ studies above. Unfortunately, large DNA nucleobase-water clusters were more difficult to study, sometimes due to poor ion formation yields in our source region, and other times because the mass of the larger clusters would coincide with other species being formed (e.g. thymine is nearly identical in mass to seven water molecules, such that the thymine dimer interfered with measurements on larger clusters).

5.5.1. Thymine-Water Anion Clusters

Thymine (T) is a methylated form of the U nucleobase (see Figure 5.1). We can therefore expect the two to have very similar electronic structural properties. Indeed, gas-phase electron transmission spectroscopic studies on neutral T found the same three π^* resonances that are present in U, located at similar energies (within $\sim 0.1\text{--}0.2$ eV).¹⁷⁴ Also as with U, solvation by even a single water molecule is sufficient to stabilise the lowest resonance state, π_1^* , to be the ground state of the $T^-(H_2O)_n$ anions.

Figure 5.11 displays 2DPES acquired for four $T^-(H_2O)_n$ anion clusters, with $n = 2, 3, 4,$ and 6. The quality of the data for the $n = 6$ cluster is poorer than the smaller clusters due to limited ion production. As expected, the 2DPES are strikingly similar to those of $U^-(H_2O)_n$ (Figure 5.6). Each is dominated by the $S_0 \leftarrow \pi_1^*$ direct detachment feature, running diagonally. The photoelectron signal has been normalised to the height of this feature, accentuating any shifts in the eKE distribution, as discussed in Section 5.3.3. Clearly, a distinct shift arising from autodetachment is present in each 2DPES around $h\nu \sim 3.6$ eV, which coincides with the

emergence of thermionic emission. Once again, we attribute these changes in the spectra to $\pi_3^* \leftarrow \pi_1^*$ photoexcitation. Thermionic emission was also present at lower photon energies, particularly for the larger clusters, and we assign this to population of the π_2^* anion resonance state.

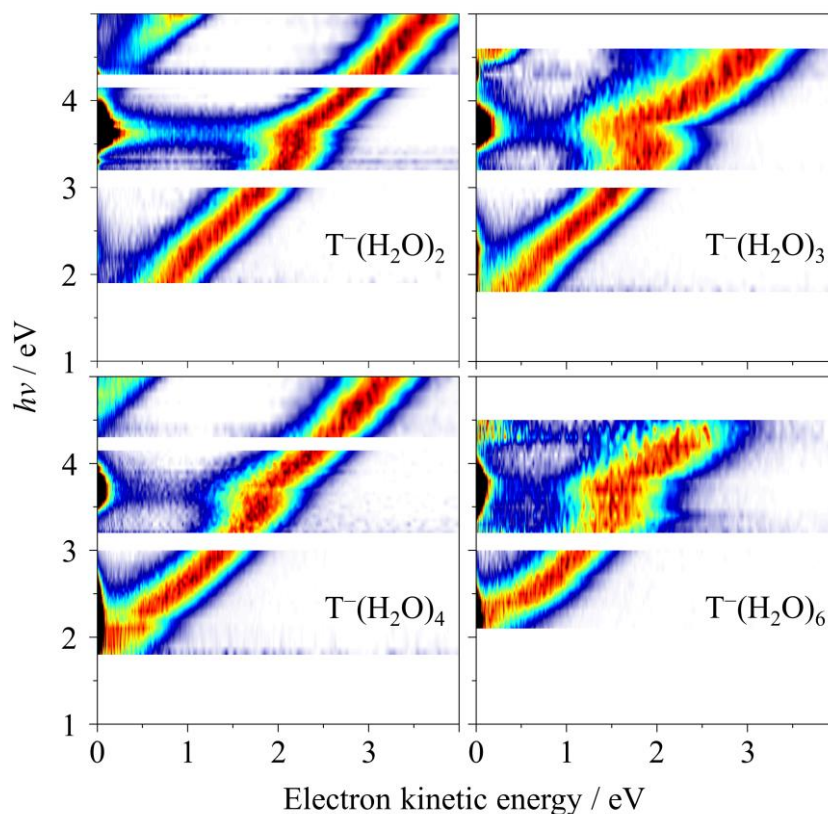


Figure 5.11: 2DPES of a series of thymine-water cluster anions, $T^-(H_2O)_n$, with $n = 2, 3, 4$, and 6. Each photoelectron spectrum was normalised to the maximum intensity of the $S_0 \leftarrow \pi_1^*$ feature.

The ADE and VDE of the $T^-(H_2O)_n$ clusters reflect those of the uracil-water anion clusters very closely. This is highlighted in Figure 5.12(a), where additional cluster data has been included using single-colour photoelectron spectra acquired at $h\nu = 4.7$ eV. The VDEs are almost identical, so the π_1^* state of $T^-(H_2O)_n$ is just as stable with respect to its neutral ground state (S_0) as in the case of $U^-(H_2O)_n$. There appears to be a small difference in the ADEs, which are slightly lower in (the majority of) the thymine-water anion clusters, as also observed in

earlier studies.¹⁸⁰ Therefore, $T^-(H_2O)_n$ clusters have a slightly larger reorganisation energy $\lambda(n)$, compared with their uracil analogues. This is consistent with the increased steric bulk of the thymine molecule, which commands more reorganisation in the bent-to-planar geometric change upon electron loss. Although we were only able to measure up to $T^-(H_2O)_{12}$, the overall similarity of the detachment energies suggests that these relationships hold also for larger clusters. Therefore for $T^-(aq)$, the extrapolated values of $ADE_{(aq)}$, $VDE_{(aq)}$, and the bulk reorganisation energy $\lambda_{(aq)}$, are likely to be comparable to those presented in Section 5.4.

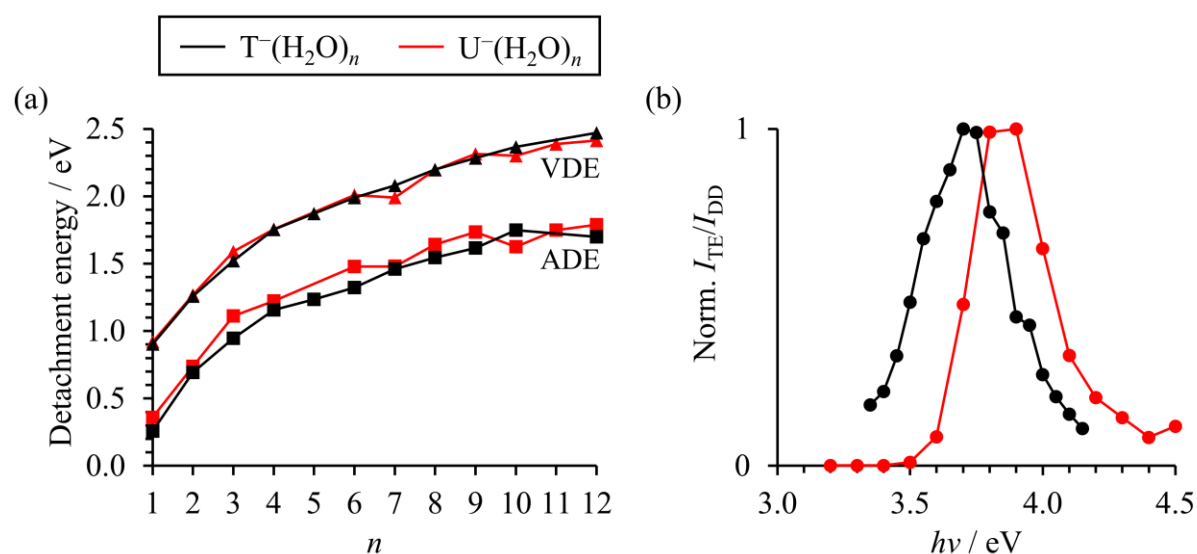


Figure 5.12: Comparison between properties in the 2DPES of $T^-(H_2O)_n$ (black) and $U^-(H_2O)_n$ (red) anion clusters. (a) Trend across cluster size in the adiabatic and vertical detachment energies, ADE (squares) and VDE (triangles), respectively. (b) Normalised ratio of thermionic emission to direct photodetachment in the $n = 4$ clusters, indicating the energy associated with photoexcitation to the π_3^* resonance.

Conversely, there is a notable difference in the position of the π_3^* resonance. Figure 5.12(b) demonstrates that the thermionic emission associated with $\pi_3^* \leftarrow \pi_1^*$ photoexcitation of $T^-(H_2O)_4$ (relative to the direct detachment feature) is maximised at a photon energy of $h\nu \approx 3.65$ eV, and is therefore red-shifted by ~ 0.2 eV to that of $U^-(H_2O)_4$. This was somewhat surprising, as electron transmission spectroscopy has shown that the $\pi_1^* - \pi_3^*$ energy

gap is approximately 0.1 eV *larger* for the thymine monomer than for uracil.¹⁷⁴ However, as mentioned previously, those experiments reveal resonance energies in the planar geometry of the neutral nucleobase molecules, whereas we probe the buckled anionic species. It appears that in the equilibrium geometry of the thymine-water cluster anions, the π_3^* resonance is slightly more stable with respect to the ground state anion, and therefore (from their similar VDEs) more stable with respect to electron loss.

A similar analysis was performed for all $T^-(H_2O)_n$ clusters studied by FRPES, extended to include the π_2^* resonance, as shown in Figure 5.13. Once again, the energetic position of the resonance states did not appear to depend on cluster size, however the data were not as extensive as in the case of $U^-(H_2O)_n$, and some data points in the $T^-(H_2O)_2$ and $T^-(H_2O)_6$ clusters showed notable deviation. To offer more confidence in this conclusion, we attempted to remeasure I_{TE}/I_{DD} using a different approach, focusing on the π_3^* resonance. I_{TE} was instead quantified by summing all the intensity of the photoelectron image within a 50 pixel radius. This corresponded to counting all photoelectrons with $eKE < 70$ meV. Some photoelectrons of higher energy (with velocity vectors outside the plane of the electron detector) would also be counted, but these counts were relatively small compared to the intensity of the thermionic emission feature. I_{DD} was taken as the summed intensity of the remaining photoelectron image, since prompt photodetachment was the only other observable feature. In this alternative approach, an approximate I_{TE}/I_{DD} was measured in real-time whilst the wavelength of our OPO laser was scanned. This brought two notable benefits: the resulting I_{TE}/I_{DD} was recorded continuously in photon energy, effectively producing a set of data with far smaller $\Delta h\nu$; and the procedure could be performed in a fraction of the time required for FRPES, allowing us to efficiently acquire results for additional clusters.

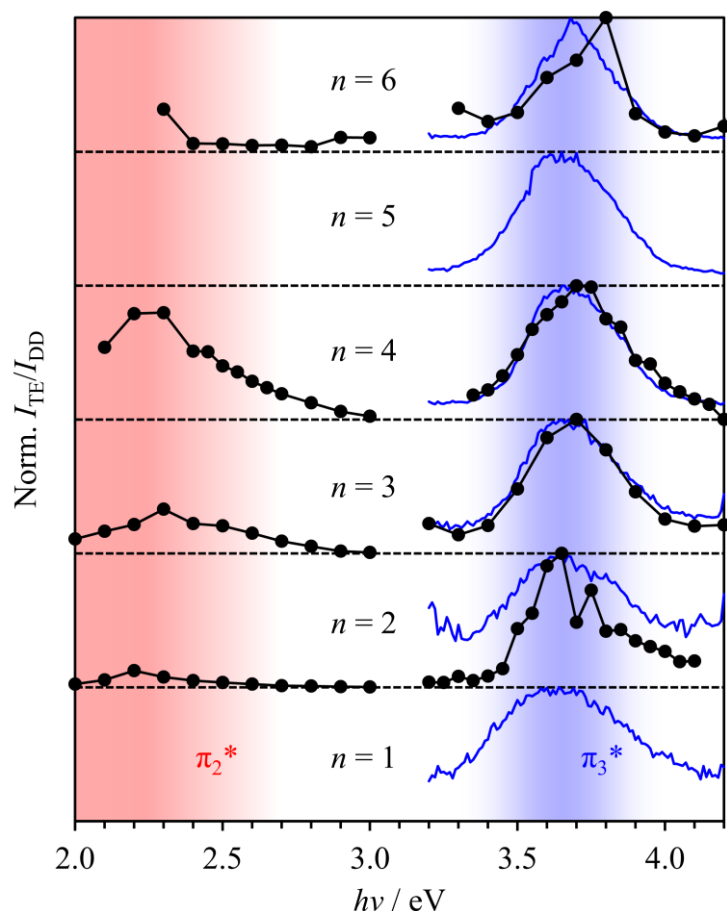


Figure 5.13: Ratio of normalised integrated photoelectron signal associated with thermionic emission to direct detachment, for $T^-(H_2O)_n$ cluster anions with $n = 1-6$. Black circles show I_{TE}/I_{DD} calculated from the FRPES presented above. Blue lines show the approximate I_{TE}/I_{DD} extracted from a continuous wavelength scan of the laser, following the procedure described in the body text. The photon energies corresponding to photoexcitation from the π_1^* ground state to the π_2^* and π_3^* resonances are highlighted in red and blue, respectively.

Figure 5.13 contains the extracted I_{TE}/I_{DD} using our alternative ‘scanning’ approach (blue lines). For $T^-(H_2O)_3$ and $T^-(H_2O)_4$, there is excellent agreement with the original FRPES approach, demonstrating the validity of our approximation. Further, the new I_{TE}/I_{DD} of $T^-(H_2O)_2$ and $T^-(H_2O)_6$ appear to be much smoother than through the FRPES approach, and reinforce the stationary behaviour of the π_3^* resonance. Additional scans were taken for the $n = 1$ and $n = 5$ clusters, which were not studied by FRPES. These too demonstrated consistency in the energetic position of the resonance states.

We conclude that the behaviours of uracil- and thymine-water cluster anions are generally very similar, as expected from their kindred molecular structures. For example, the cluster size-dependent VDEs were found to be nearly identical. However, photoexcitation to the π_3^* resonance occurs at slightly lower energy for $T^-(H_2O)_n$ than $U^-(H_2O)_n$ (by ~ 0.2 eV). Following from the analysis in Section 4.4, extrapolation of the π_3^* resonance of $T^-(H_2O)_n$ to the bulk aqueous limit reveals that, like in $U_{(aq)}$, this state is likely to be accessible through low-energy electron attachment to $T_{(aq)}$, but is also vertically bound upon geometric relaxation of the molecule and surrounding solvation sphere. Moreover, the 0.2 eV red-shift (compared to the uracil case) implies that the relaxed π_3^* state is vertically bound to a slightly greater extent in $T_{(aq)}$, providing extra resistance against ultrafast autodetachment. Our results on thymine-water anion clusters confirm that comparable electron dynamics are expected to occur on both RNA and DNA strands, and thereby provide a critical step towards identifying the resonances involved in the electron capture of DNA mediated by the nucleobases.

5.5.2. Adenine-Water Anion Clusters

Adenine (A), being a purine DNA base, has a very different chemical structure to the pyrimidine nucleobases discussed above (see Figure 5.1). The molecule consists of a double ring structure possessing extended conjugation, and consequently the anion shape resonances have different energies. Low-energy electron transmission spectroscopy found three π^* shape resonances at energies $E(\pi_1^*) = 0.54$ eV, $E(\pi_2^*) = 1.36$ eV, and $E(\pi_3^*) = 2.17$ eV.¹⁷⁴ The next resonance of similar character, π_4^* , has been calculated to reside at much higher energy, $E(\pi_4^*) \approx 6$ eV.³³⁶ Therefore, we anticipate that FRPES may identify multiple anion resonances accessible with IR/visible laser pulses, but none in our measurable UV region ($3 \leq h\nu \leq 5$ eV). However, it should be noted that Feshbach resonances may also be accessed in our experiment, but are generally not observable in electron transmission spectroscopy.

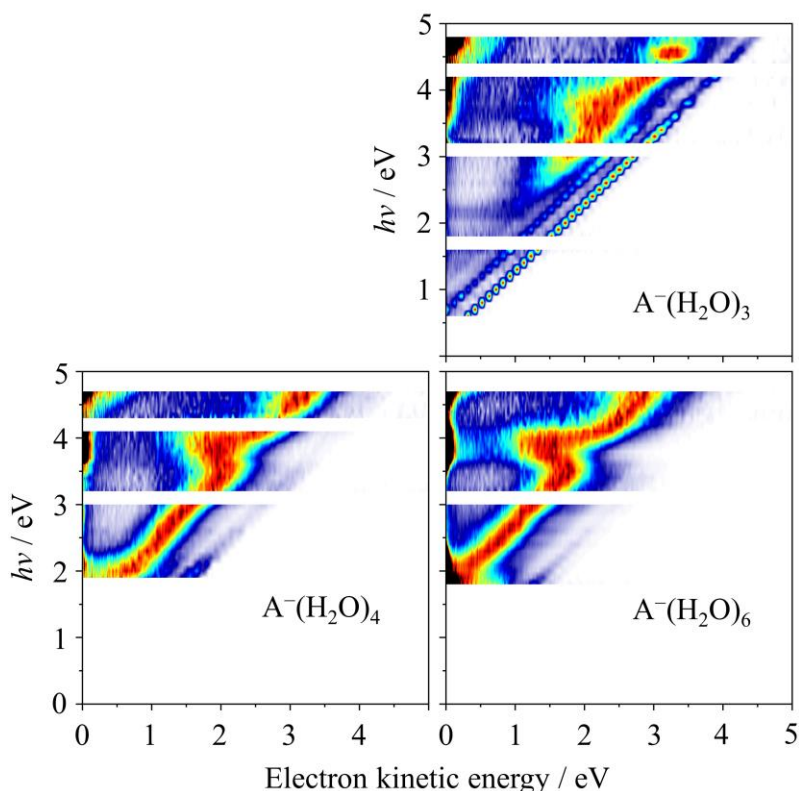


Figure 5.14: 2DPES of a series of adenine-water cluster anions, $A^-(H_2O)_n$, with $n = 3, 4$, and 6 . Each photoelectron spectrum was normalised to the maximum intensity, excluding the thermionic emission feature.

Figure 5.14 displays 2DPES for $A^-(H_2O)_3$, $A^-(H_2O)_4$, and $A^-(H_2O)_6$. The discussion will begin with the two larger clusters, $n = 4$ and $n = 6$, which show greater similarity to the previously studied nucleobases-water clusters. The distinct $S_0 \leftarrow \pi_1^*$ direct detachment feature is present once more, as the valence π_1^* state of A also becomes bound upon microhydration. The VDEs of these features are in good agreement with earlier studies on $A^-(H_2O)_n$.¹⁸¹ Thermionic emission is present across essentially the entire visible range $h\nu \leq 3.0$ eV, but particularly at the lower end, in broad agreement with excitation to the π_2^* or π_3^* excited states of adenine.¹⁷⁴

However, there is also a clear signature of autodetachment and thermionic emission in the UV region, despite the lack of π^* states expected in this energy region. Moreover, there are additional features towards higher eKE than the $S_0 \leftarrow \pi_1^*$ feature, which appear to be relatively

sharp. These are particularly prevalent in the 2DPES of $A^-(H_2O)_3$, where across the entire measured IR/visible wavelength range, the sharp high-eKE signals dominate. Clearly, there is something unexpected occurring with the $A^-(H_2O)_n$ anion clusters. We will first focus on explaining the photoexcitation taking place at UV wavelengths.

UV Autodetachment: Evidence for Tautomers

Adenine has several low-energy tautomers.³³⁷ Some have different functionality, such as tautomerisation from the canonical amine form to the imine. Adenine also possesses a labile proton on the double ring which is capable of bonding to the different nitrogen sites. Three of these prototropic tautomers have been shown to coexist in aqueous solution:^{338–340} these are denoted N3, N7, and N9 (which is the canonical form of adenine), and their corresponding chemical structures are displayed in Figure 5.15. Whilst the canonical N9 tautomer is the most stable in isolation³³⁷ and therefore the only form generally observed in gas-phase experiments, computational studies have indicated that microhydration (i) stabilises the N3 and N7 tautomers to a greater extent than N9 (although N9 remains the most stable form),³⁴¹ and (ii) reduces the energy barrier required for prototropic tautomerisation.³⁴² Taken together, it is reasonable to consider that there may be other tautomers of adenine present in the $A^-(H_2O)_n$ clusters formed in our experiment.

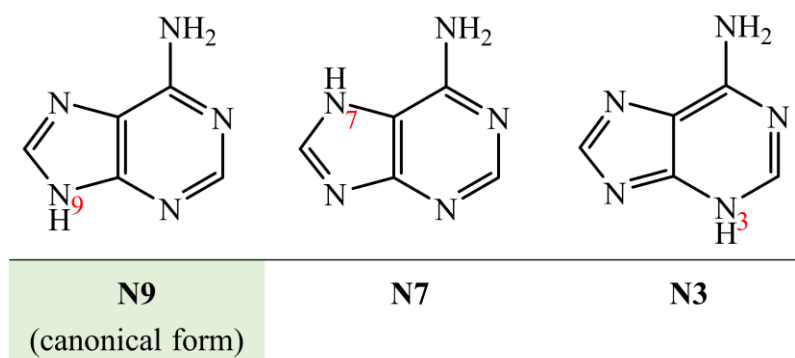


Figure 5.15: Prototropic tautomers of adenine that have been previously observed in aqueous solution.

The excitation energies of different tautomers of the adenine anion are expected to differ, and therefore the presence of different tautomers has potential to explain the autodetachment exhibited in the UV region. Before discussing the excitation energies of the three adenine tautomers, we first quantify the position of the resonance in the UV region using the techniques outlined above. Figure 5.16 demonstrates the resonance position of $A^-(H_2O)_6$ located through I_{TE}/I_{DD} , where I_{DD} in this case represents directly detaching and autodetaching electrons. Figure 5.16 also shows the shifts in the mean eKE of the $S_0 \leftarrow \pi_1^*$ feature, $\langle eKE \rangle$, which embodies the relative degree of autodetachment. In both cases, the resonance is identified to sit approximately 3.8 eV higher than the π_1^* ground state, although the onset of photoexcitation is slightly lower around $h\nu = 3.5$ eV.

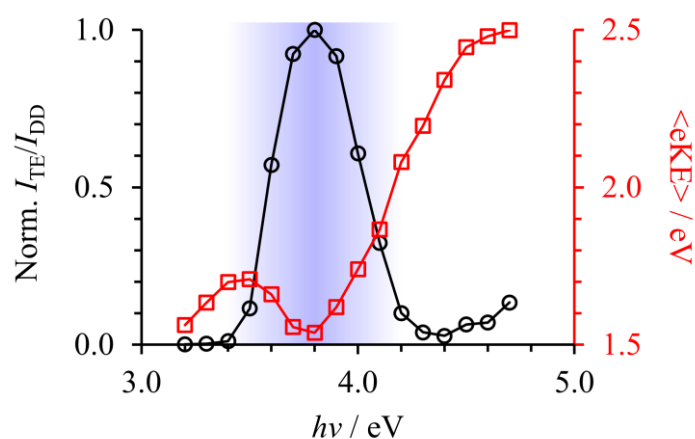


Figure 5.16: Normalised ratio of thermionic emission to other photoelectron signal in the 2DPES of $A^-(H_2O)_6$ (black circles). Overlaid with the mean eKE of the $S_0 \leftarrow \pi_1^*$ feature, $\langle eKE \rangle$ (red squares). The resonance position is highlighted in blue.

In the studies on $U^-(H_2O)_n$ and $T^-(H_2O)_n$, photoexcitation energies were compared with the position of electron scattering resonances with the neutral nucleobases. Such measurements have not been performed for the N3 and N7 tautomers of adenine, and therefore we calculate the expected position of the electron scattering resonances. To do this, the stabilisation method²³⁰ was applied, following the methodology of Cheng and Chen.¹⁷⁶ In short, the energies of the virtual molecular orbitals of each adenine tautomer were tracked as the diffuseness of

the aug-cc-pVDZ basis set was adjusted by a parameter α . Anion resonance states of the molecule are fairly insensitive to the change in α , whereas the energy of discretised continuum orbitals (DCOs) increase significantly with reduced diffuseness of the basis set, corresponding to a higher α . Since the resonance positions of the N9 tautomer have been measured by electron transmission spectroscopy,¹⁷⁴ this tautomer provides a useful point of comparison for the accuracy of the method. The stabilisation curve of N9 adenine is presented in Figure 5.17(a), and shows good agreement with earlier computations.³⁴³ Three π^* resonances were observed, clearly identifiable by their electronic structure, visualised on the right of Figure 5.17(a). The $\pi_1^* - \pi_2^*$ and $\pi_1^* - \pi_3^*$ energy gaps match well with those found in electron transmission spectroscopy (see Table 5.1). Therefore, application of the stabilisation method appears to be appropriate for calculation of the anion resonance energies of adenine.

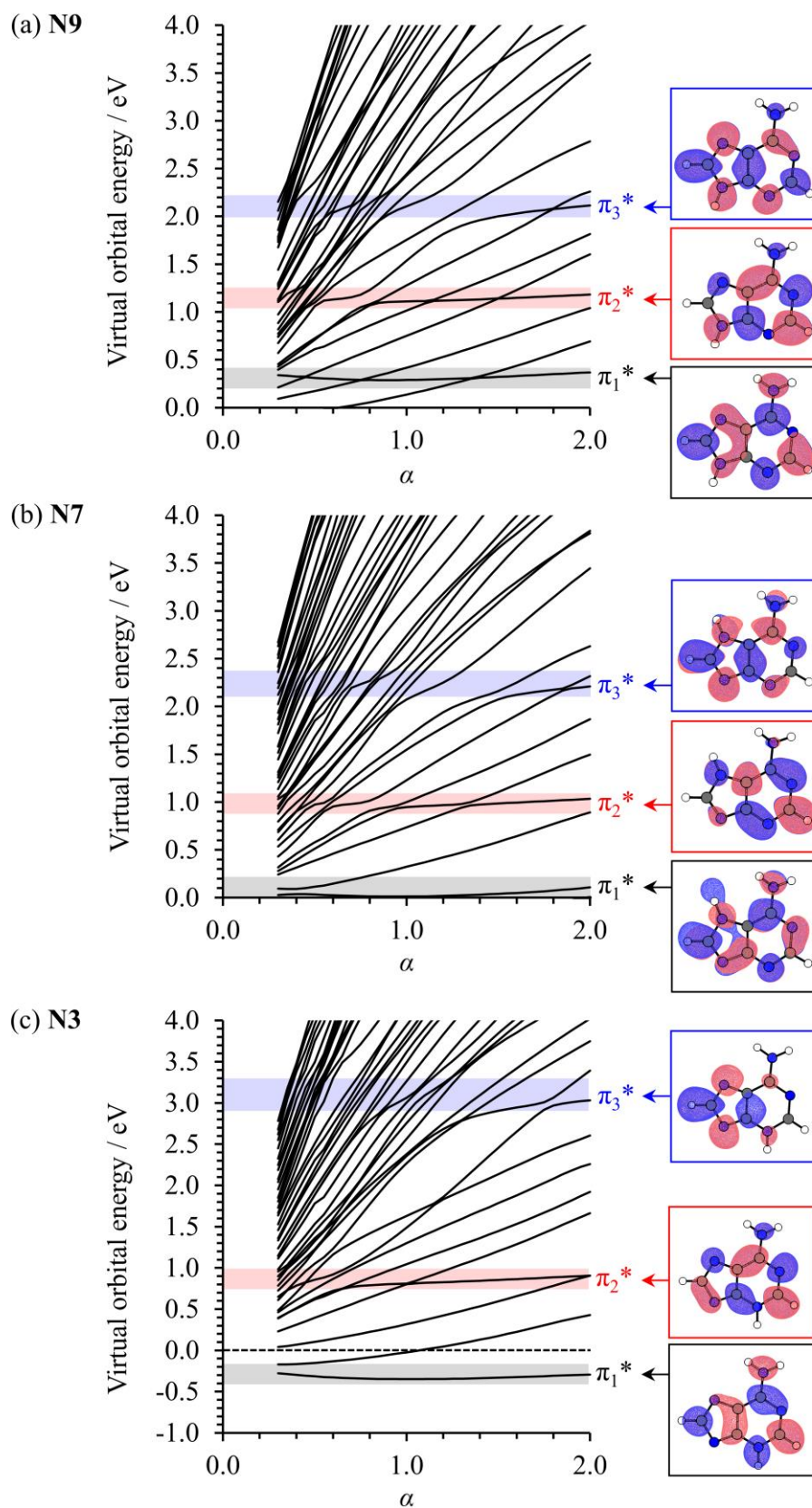


Figure 5.17: Stabilisation curves for the (a) N9, (b) N7, and (c) N3 tautomers of adenine, calculated using CAM-B3LYP/aug-cc-pVDZ with the diffuseness adjusted by parameter α . The electronic structures for each identified resonance are shown on the right (isovalue 0.03).

Table 5.1: Approximate anion resonance energy spacing of different adenine tautomers, calculated using the stabilisation method (calc.). Measured energy separation by electron transmission spectroscopy¹⁷⁴ is also shown (exp.).

Tautomer	Energy relative to π_1^* / eV			
	π_2^* (calc.)	π_2^* (exp.)	π_3^* (calc.)	π_3^* (exp.)
N9	0.8	0.82	1.8	1.63
N7	0.9		2.2	
N3	1.2		3.4	

Similar stabilisation curves were calculated for the N3 and N7 tautomers of adenine, as shown in Figures 5.17(b) and 5.17(c). The anion resonance states of N7 are generally similar to those of N9 both in appearance and in energy. This is unsurprising, as the reorganised H atom remains on the imidazole moiety of adenine, and therefore does little to alter the overall electronic structure. Conversely, the N3 tautomer, which has the H atom on the pyrimidine moiety, exhibits a very different energy spacing between the anion states. In particular, the π_1^* - π_3^* energy gap is far greater than for the other tautomers, consistent with the electronic structure of the π_3^* orbital (Figure 5.17(c), right), where the electron density appears to be predominantly confined to the imidazole moiety. Moreover, the π_1^* - π_3^* energy gap of 3.4 eV is very close to the photon energy at which thermionic emission begins to occur, and is only slightly below the energy of maximum autodetachment and thermionic emission. Notably, this was also the case for $U^-(H_2O)_n$, where the π_1^* - π_3^* energy gap found in electron transmission spectroscopy was slightly lower than the photon energy at which there was the most photoexcitation. To further verify that the $\pi_3^* \leftarrow \pi_1^*$ excitation energy – within the natural anionic geometry of the N3 tautomer – aligns reasonably well with the observed UV excitation feature, time-dependent DFT calculations were performed. The less diffuse cc-pVDZ basis set was used, in an attempt to suppress contributions from DCOs. Unfortunately, there appeared to be a significant contamination nonetheless, even with using two different functionals. Nonetheless, the computed transition energy at the B3LYP level^{215,216} was 4.05 eV with an

associated oscillator strength of 0.064, although the excitation also contained a ~25% contribution of $\pi\pi_1^*$ character. Using the long-range corrected CAM-B3LYP functional²¹⁷ gave slightly worse agreement, with a 4.56 eV excitation energy but with a comparable oscillator strength (0.056). More comprehensive computations are currently underway, but it is encouraging that the calculated excitation energies are fairly close to the experimentally observed value, and that the oscillator strength looks to be significant.

It appears that the presence of the N3 tautomer in our generated $A^-(H_2O)_n$ clusters is capable of explaining the enhanced autodetachment and thermionic emission in the UV region. As the autodetachment appears to be more severe in the larger clusters (especially $A^-(H_2O)_6$), this may reflect changing tautomeric distributions with increasing cluster size. Indeed, the N3 tautomer of adenine is predicted to be stabilised by small microhydration ($n = 1$ and 2) more than both the N7 and N9 tautomers are stabilised.³⁴¹ We emphasise that the presence of the N3 tautomer does not imply that the other tautomers are absent. Instead, we only claim that the N3 tautomer best explains the observed photoexcitation in the UV region. It is difficult to directly compare the cross-sections associated with $\pi_3^* \leftarrow \pi_1^*$ photoexcitation to $S_0 \leftarrow \pi_1^*$ photodetachment, but the acquired spectra suggest that the former process is particularly efficient.

Non-valence States of Adenine-Water Cluster Anions

Sharp features toward higher electron kinetic energies were also present in the 2DPES of $A^-(H_2O)_n$ (Figure 5.14). The presence of these features was very unexpected, as earlier photoelectron spectroscopy on adenine-water cluster anions had only observed the $S_0 \leftarrow \pi_1^*$ feature.¹⁸¹ As shown in Figure 5.18, each high-eKE peak displays substantial positive anisotropy ($\beta_2 \approx +2.0$), implying the electrons were detached from a different electronic state than π_1^* . Taken together; the relatively high eKE (i.e. low electron binding energy), the narrow

lineshape, and the distinct positive anisotropy; are characteristics of photodetachment from non-valence states (see Section 1.2.1). Therefore, it appears, just as there were different tautomers of adenine present in the generated $A^-(H_2O)_n$ clusters, different electronic states were formed too. Moreover, as each cluster displayed several diagonal non-valence features (see Figure 5.14), this may imply that different tautomers of adenine were capable of forming in their non-valence states independently, leading to different electron binding energies (offsets in the diagonal features). It should be noted that the presence of these non-valence states is unlikely to contribute to the autodetachment features in the 2DPES, as oscillator strengths associated with non-valence to valence optical transitions are expected to be relatively small. Chapter 6 investigates the non-valence states of nucleobase-water anion clusters in greater detail.

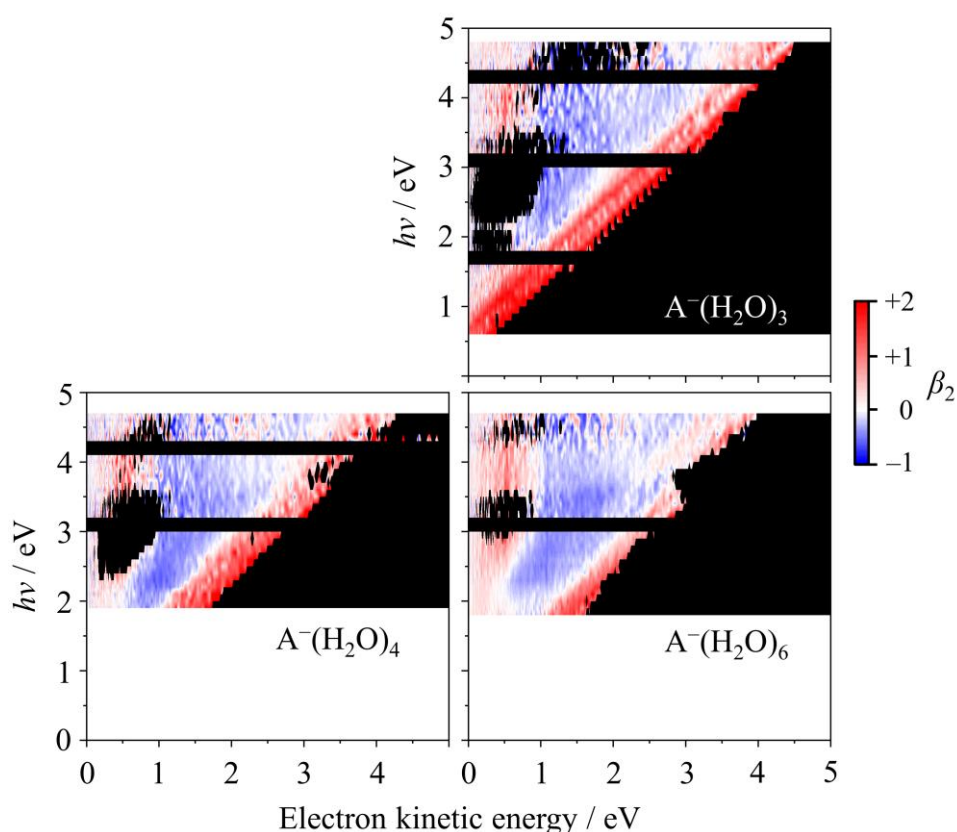


Figure 5.18: Photoelectron angular distributions for the 2DPES of $A^-(H_2O)_n$. PADs are not shown for regions with $<10\%$ photoelectron signal on the low-energy side of the $S_0 \leftarrow \pi_1^*$ feature, and $<1\%$ on the high-energy side.

5.6. Closing Remarks

Conclusions

The nucleobases are understood to be the prime site for low-energy electron attachment into DNA strands, which can lead to irreparable damage. Enhanced electron attachment occurs at specific incident electron energies associated with the anion resonance states of the nucleobases. Our results probe the effect of hydration on these anion resonances in an incremental fashion. Through extrapolation, we predict that the lowest two π^* shape resonances of aqueous uracil and thymine become adiabatically bound, whilst the π_3^* resonance remains unstable. However, by considering the effect of nuclear reorganisation within a Marcus picture (which is mostly comprised of a solvent response), we can also conclude that both the π_2^* and π_3^* resonances are accessible via very low-energy (<1.5 eV) electron attachment to aqueous U (or T). Through the observation of thermionic emission, we anticipate that both of these states undergo efficient relaxation to the more adiabatically stable π_1^* state. It remains unclear whether low-energy electrons can populate anion resonances of the canonical tautomer of aqueous adenine. Altogether, the DNA/RNA environment that surrounds biologically-occurring nucleobases is likely to have a less stabilising effect than bulk water, due to having fewer proximate water molecules and also due to Coulombic repulsion from the nearby phosphate backbone. Therefore, our extrapolated results represent an extreme, and the ‘true’ position of the biologically-occurring nucleobase anion resonances may instead be more similar to the positions for one of the cluster anions studied here.

Outlook

The results presented in this chapter shed light on the behaviour of nucleobase anion resonances in aqueous solution. However, this remains an inaccurate portrayal of the macromolecular environment of DNA. The nucleobases are covalently bonded to a ribose sugar group, which may subtly affect resonance positions and anion dynamics subsequent to electron attachment. Additionally, hydrogen bonds between opposite base pairs in the double helical structure are present, and charge-transfer between different nucleobases is a possibility. To further explore these possibilities, it would be interesting to study other forms of nucleobase clusters. For example, heterogenous nucleobase dimers, such as the adenine-thymine anion, $[\text{AT}]^-$, could represent a more accurate portrayal of the DNA environment, especially when clustered with water molecules. However, there is no guarantee that the geometry of the isolated $[\text{AT}]^-$ dimer anion would match the hydrogen-bonded structure found biologically, and it may instead preferentially π -stack. Even in this case, the dimers could act as interesting tools to probe of the electron transfer mechanism across adjacent base pairs. Alternatively, the study of nucleoside-water anion clusters is equally interesting, although will require more careful injection into the gas phase.³⁴⁴⁻³⁴⁶ Theory predicts a charge-transfer mechanism from the π^* resonances of the nucleobase across to the sugar group,¹⁷³ which may give different traces of autodetachment, particularly in the measured PADs. Hydration may inhibit (or even encourage) this internal conversion process, but this remains to be probed. In addition, solvation is predicted to increase energy barriers for cleavage of the C–O sugar-phosphate bond in the nucleotides.³⁴⁷ FRPES of nucleotide-water anion clusters could shed light on the propensity for strand damage upon $\pi\pi^*$ excitation, particularly if coupled with a reflectron mass analyser.

An obvious experiment that is lacking from this chapter is the TRPES of $\text{U}^-(\text{H}_2\text{O})_n$. From the observation of thermionic emission, we could infer that the π_2^*/π_3^* states underwent ultrafast internal conversion to the anion ground state. However, the exact mechanism for this

process remains an open question, yet has implications for the electron capture dynamics of nucleobases. In particular, it would be interesting to measure the timescale at which the π_3^* resonance becomes vertically bound with respect to electron loss, and compare how this measures against the rate of internal conversion. As hinted at in studies by Kočišek *et al.*,³¹⁸ within excited nucleobase-water anion clusters, there may also be competition from evaporative processes. Although we did not observe clear signatures of evaporative processes upon photoexcitation to resonances, these may be better unveiled using time-resolved techniques. Overall, there is much to learn about the anion resonance state dynamics of nucleobases, nucleosides/nucleotides, their water clusters and their various pairings, through the application of TRPES.

Chapter 6 – Solvent-Mediated Formation of a Hydrated Electron from a Contact Pair

This chapter details and builds upon the following publications:

C. J. Clarke, E. M. Burrow and J. R. R. Verlet, *in preparation*

All experimental work was performed by C. J. Clarke and E. M. Burrow. All computational work was performed by C. J. Clarke.

6.1. Introduction

As demonstrated in Chapter 4, the ground state of the uracil anion U^- is a non-valence dipole-bound state (DBS). Non-valence states are receiving growing interest as ‘doorway’ states for efficient electron attachment to isolated molecules (such as polycyclic aromatic hydrocarbons in the interstellar medium),^{123,276,348,349} However, it is typically thought that DBSs are suppressed in a bulk environment, simply due to spatial restrictions.² This has important ramifications for electron attachment to DNA (or RNA) nucleobases, since it remains an open question whether such non-valence states play any role in facilitating low-energy electron-induced damage.^{132,164}

Recent spectroscopic studies have suggested that non-valence DBSs may be more resilient to surrounding molecules than expected. The phenolate anion can form an excited DBS where the excess electron localises outside the ring, near the *para* position; it was shown that *para*-alkylphenolates remained capable of forming the DBS, despite the alkyl chains overlapping with the dipole-bound electron orbital.³⁵⁰ Non-valence states have also been observed in heterogenous anion-water clusters: indole forms a DBS upon clustering with one or two water molecules,³⁵¹ even though isolated indole does not possess a sufficiently strong dipole moment ($\mu < 2.5$ D)^{99,352,353}; and hydrated amino acid clusters also form DBSs, attributed to their zwitterionic character.³⁵⁴ In the previous chapter, we observed that adenine anions can display non-valence character when solvated with three, four, or six water molecules. Unfortunately, adenine was also observed to form different tautomers, complicating further analysis. However, we also found the smallest uracil-water cluster, $U^-(H_2O)_1$, to form a non-valence state (see Section 4.4.2),³¹¹ in addition to its natural π_1^* valence ground state. Therefore, to further explore the effect of hydration on a non-valence DBS, we attempted to produce larger $U^-(H_2O)_n$ clusters in their non-valence states.

Since we will be attempting to explore the effects of hydration on a non-valence state, it is also useful to place non-valence anions into the context of the aqueous phase. The DBS of U^- can be described as a molecule-electron contact pair, where the electron is suspended in a distant orbital. Metastable contact pairs also exist in the bulk solution (i.e. $[U:e^-]_{(aq)}$, for uracil), typically formed following (photo)oxidation of an anion.³⁵⁵ These aqueous contact pairs can decay through two competing pathways: geminate recombination to reform the parent anion, or dissociation into the neutral molecule and a hydrated electron, $e^-_{(aq)}$.¹⁵⁸ The study of hydrated non-valence states may therefore aid our understanding of the solvent-driven coordinate that underpins the formation of the hydrated electron – a species that plays a pivotal role in radiation chemistry and serves as the archetypical quantum solute.^{356,357} Whilst computational studies have reproduced the timescales of contact pair dissociation,^{358,359} it is more difficult for experiments to mechanistically probe $e^-_{(aq)}$ formation at a molecular level, in part due to the inevitable competition from the geminate recombination channel. By studying these clusters with photoelectron spectroscopy, we can gain insight into hydration of non-valence states, and incrementally probe a representative contact pair dissociation coordinate.

6.2. Methodology

6.2.1. Experimental

All experiments were conducted on the cluster instrument.¹⁸⁸ Uracil-water cluster anions, $U^-(H_2O)_n$ or $U(H_2O)_n^-$, were generated in a supersonic expansion (produced by a pulsed Even-Lavie valve¹⁸⁹) coupled with a ring filament ioniser. Argon was used as the backing gas, with the pressure increased up to 11 bar, encouraging the formation of kinetically trapped non-valence states. Anion clusters underwent time-of-flight mass separation, before being intersected with nanosecond laser pulses from the Nd:YAG systems described in Chapter 2. Mass spectrometry was not capable of separating structural isomers of the same $U^-(H_2O)_n$ or $U(H_2O)_n^-$ cluster. The resolution of the VMI electron spectrometer was below $\Delta eKE/eKE = 3\%$, and images were reconstructed using the MELEXIR algorithm.¹⁹⁷

6.2.2. Computational

In the calculation of non-valence states, it is typically necessary to utilise a custom, extra-diffuse basis set. In line with other similar studies,³³² the aug-cc-pVDZ Dunning basis set was used,²²¹ appended with additional diffuse functions that were affixed onto the N1 and C6 atoms (see Figure 6.1), which are located on the positive side of U. Even-tempered (scaling factor of $3^{0.5}$) basis functions were added: m of s character and n of p character, and we denote the basis set aug-cc-pVDZ+ $msnp$. Table 6.1 shows the DFT/CAM-B3LYP²¹⁷ electronic energies of U^- and neutral U, calculated at the optimised geometry of the anion, with different numbers of diffuse functions added. The difference between the anion and neutral energies is equal to the vertical detachment energy (VDE). After three s and p functions, the VDE was not found to change enough to justify the computational expense of further diffuse basis functions, and so the aug-cc-pVDZ+3s3p basis set was selected going forward.

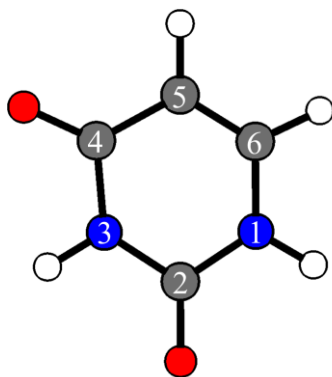


Figure 6.1: Labelled atoms of the uracil molecule. Coloured by atom type: H (white), C (grey), N (blue), O (red).

Table 6.1: DFT/CAM-B3LYP computed electronic energy and vertical detachment energy (VDE) of U^- , using the aug-cc-pVDZ basis set with different numbers of appended even-tempered extra-diffuse basis functions.

Basis set	Energy of U^- / Har	Energy of U / Har	VDE / meV
aug-cc-pVDZ+1s1p	-414.70448	-414.70713	-72.2
aug-cc-pVDZ+2s2p	-414.70993	-414.70716	75.3
aug-cc-pVDZ+3s3p	-414.71110	-414.70717	107.0
aug-cc-pVDZ+4s4p	-414.71130	-414.70717	112.5

In order to assign molecular cluster structures to each non-valence feature in the photoelectron spectra of the $U(H_2O)_n^-$ anion clusters, a two-step procedure was implemented. First, relaxed optimisations of candidate cluster structures were performed, and second, the VDE of the non-valence state was calculated at these optimised geometries. In the first step, density functional theory (DFT) with the long-range corrected CAM-B3LYP functional was used to find the optimised geometries of the $U(H_2O)_n^-$ anion clusters. DFT was selected for its efficiency and thus high-throughput capabilities, allowing a wide sample of initial geometries for each cluster to be optimised, leading to an extensive list of possible structures. It should be noted that this list was likely not exhaustive, but was sufficient to provide satisfactory explanations of the experimental observations. In particular, where water molecules solvated the dipole-bound electron, the potential energy surface along some water translation

coordinates was very shallow, leading to many possible optimised structures. However, in these cases, the exact position of the water had little effect on the VDE of the non-valence state.

For more accurate determination of the VDE in the DFT-optimised structure, we performed *ab initio* CCSD(T) calculations.^{360,361} To ensure that the electron binding energies of the calculated non-valence states were reliable, we here demonstrate some basic benchmarking results for several non-valence states that have experimentally determined VDEs. The chosen non-valence anions were $(\text{H}_2\text{O})_{2-6}^-$ and U^- , representing a wide range of binding energies. Table 6.2 shows the calculated (and experimental) VDEs for the benchmark DBSs, using improving levels of theory. For each non-valence state, the DFT (CAM-B3LYP) energy dramatically overestimated the VDE. Conversely, each *ab initio* method underestimated the experimental VDEs, but became more accurate as higher levels of theory were applied. Ultimately, the VDEs calculated with CCSD(T) theory were accurate to within some 10s of meV for each non-valence anion, and could be considered slight underestimates. We believe our methodology is appropriate for distinguishing between structural isomers that differ in electron binding energies by ~ 100 meV, as was the case for the measured $\text{U}(\text{H}_2\text{O})_n^-$ clusters.

Table 6.2: Computed vertical detachment energies (VDEs) of several DBS anions, using different levels of theory and the aug-cc-pVDZ+3s3p basis set. Corresponding experimentally measured values are also shown.

Level of theory	VDE / meV					
	U^-	$(\text{H}_2\text{O})_2^-$	$(\text{H}_2\text{O})_3^-$	$(\text{H}_2\text{O})_4^-$	$(\text{H}_2\text{O})_5^-$	$(\text{H}_2\text{O})_6^-$
CAM-B3LYP	107.0	126.5	254.7	471.6	482.3	1494
HF	25.9	1.0	68.3	199.1	173.7	225.7
MP2	45.0	21.0	113.4	289.9	282.9	354.8
CCSD	62.9	33.4	139.2	323.8	323.3	396.1
CCSD(T)	68.0	39.1	151.4	344.6	348.4	424.3
Exp.	75 ± 6^a	45 ± 5^b	160^c	350 ± 20^c	350^c	480^d

Taken from ref. ^a 268 and current work, ^b 362, ^c 363, ^d 140. Uncertainties provided where available.

6.3. The Non-Valence States of $\text{U}(\text{H}_2\text{O})_n^-$

6.3.1. Characterising $\text{U}(\text{H}_2\text{O})_1^-$

We begin by examining $\text{U}^-(\text{H}_2\text{O})_1$, which was earlier shown to exhibit an additional photoelectron spectral feature that correlated with a non-valence state (see Chapter 4).²⁶⁸ As the exact electron binding motif is not known *a priori* for this anion cluster, we refer to this signal as arising from a non-valence state, rather than a DBS as in the case of U^- . But before seeking to better characterise the non-valence state that is being photodetached, we must first establish whether this photoelectron signal is being produced from a different isomer of $\text{U}^-(\text{H}_2\text{O})_1$, or if it proceeds via an initial photoexcitation of the π_1^* valence state. This is easily verified by monitoring the two photoelectron signals as the ion source conditions are altered, since isomeric distributions tend to be very sensitive to such changes.³⁶⁴

Figure 6.2 displays photoelectron spectra of $\text{U}^-(\text{H}_2\text{O})_1$ acquired at $h\nu = 2.33$ eV for a range of (Ar) backing gas pressures. Signal is plotted against electron binding energy (equal to $h\nu$ minus the electron kinetic energy). As a reminder, photodetachment from the π_1^* valence state produces the broad feature around $\text{VDE} \approx 1.0$ eV, as observed previously.^{180,181,307} The spectral breadth arises from the disparate geometries between the initial (buckled) anion and final (planar) neutral molecule. Additionally, the PAD (inset Figure 6.2) peaks perpendicular to the polarisation vector of the laser light-field, corresponding to a negative anisotropy parameter, $\beta_2 < 0$.^{11,12} The photoelectron signal arising from the non-valence state is in stark contrast: the narrow feature is centred at much lower binding energy, $\text{VDE} \approx 0.25$ eV; and the signal is maximally anisotropic parallel to the polarisation vector ($\beta_2 \approx +2$), consistent with electron emission from a nodeless s-like orbital.^{276,298} As demonstrated in Figure 6.2, the relative intensity of the two signals is indeed sensitive to changes in the backing gas pressure, suggesting (at least) two isomers of $\text{U}^-(\text{H}_2\text{O})_1$ are generated in our anion source region. In

particular, it appears that formation of the non-valence isomer of $U^-(H_2O)_1$ is enhanced when higher backing pressures are implemented, which generally correlates with more efficient cooling in the molecular beam. Hence, we conclude that a larger fraction of the non-valence anions are formed at lower cluster temperatures, indicating that the non-valence state isomers are kinetically trapped, similar to observations of different isomers of $(H_2O)_n^-$.^{144,146,364}

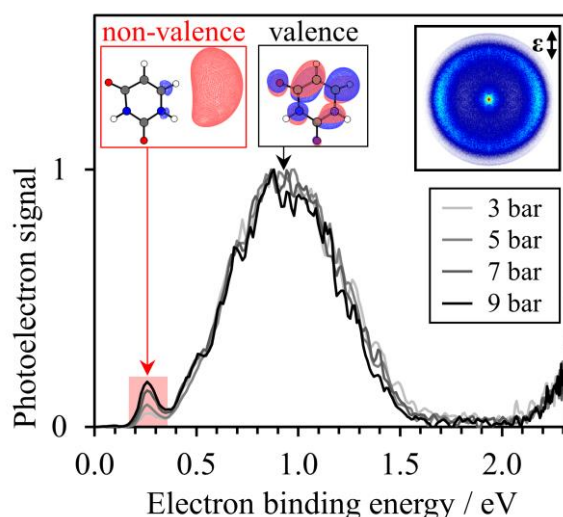


Figure 6.2: Photoelectron spectrum of $U^-(H_2O)_1$ acquired at $h\nu = 2.33$ eV and at different backing gas pressures. Electronic structures of the anions responsible for each peak are shown inset, along with the corresponding photoelectron image at 9 bar Ar (with laser polarisation vector indicated by ϵ).

In Figure 6.2, the photoelectron signal associated with the non-valence state of $U^-(H_2O)_1$ is substantially weaker than that from the π_1^* valence state (even at high backing pressure). However, this is not necessarily reflective of the relative populations of the two isomers in the molecular beam, as the photodetachment cross-sections are unlikely to be equal for the two states. In particular, the photodetachment cross-section of a non-valence state becomes enhanced at lower photon energies, since the de Broglie wavelength of the outgoing electron wave becomes similar to the size of the non-valence orbital.^{224,365,366} Figure 6.3 shows a selection of photoelectron spectra of $U^-(H_2O)_1$ acquired at different photon energies, $1.9 \leq h\nu \leq 2.3$ eV, and it is clear that photodetachment of the non-valence state is more

pronounced at lower $h\nu$. Therefore, as we wish to study non-valence states of $\text{U}^-(\text{H}_2\text{O})_n$, it is beneficial to implement lower photon energies to maximise their detection.

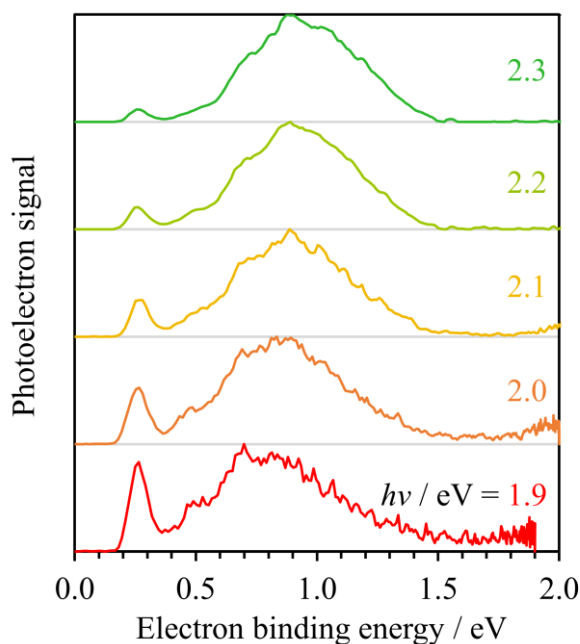


Figure 6.3: Photoelectron spectra of $\text{U}^-(\text{H}_2\text{O})_1$ acquired at different photon energies, each normalised to the maximum signal.

At the much lower photon energy of $h\nu = 0.7$ eV, the only observable feature in the photoelectron spectrum of $\text{U}^-(\text{H}_2\text{O})_1$ stems from the non-valence isomer. This is shown in Figure 6.4 (where the cluster is written as $\text{U}(\text{H}_2\text{O})_1^-$, as explained below), which also presents the similarly acquired photoelectron spectrum of U^- . As earlier demonstrated in Chapter 4, the photoelectron spectrum from the DBS of U^- is narrow and centred at $\text{VDE}_0 = 75 \pm 6$ meV (where the subscript is used to indicate cluster size, n). For $\text{U}^-(\text{H}_2\text{O})_1$, the non-valence electron is comparably more bound, with $\text{VDE}_1 = 255 \pm 20$ meV. Between VDE_0 and VDE_1 , the 180 meV increase in electron binding energy therefore reflects the water-induced stabilisation of the non-valence electron in $\text{U}^-(\text{H}_2\text{O})_1$. While the differential stabilisation is less than that for the valence-bound anion (~ 0.5 eV for the addition of one water molecule²⁶⁸), it is greater than the stabilisation expected by combining the dipole moments of U and H_2O .³⁶⁷ Hence, the clustered water molecule is likely to be solvating the non-valence electron directly.

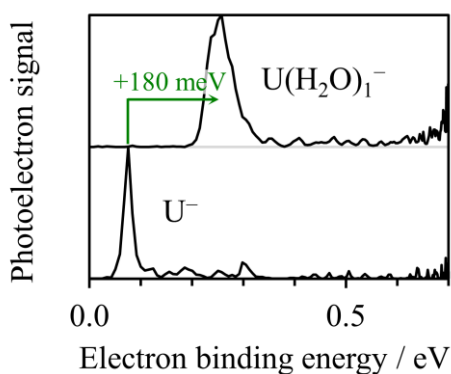


Figure 6.4: Normalised photoelectron spectra of U^- and $U(H_2O)_1^-$, acquired using $h\nu = 0.7$ eV laser pulses.

In order to characterise the binding motif of the single water molecule in $U^-(H_2O)_1$, we performed supporting quantum chemical calculations. The binding sites for a water molecule in $U^-(H_2O)_1$, some of which have been identified in earlier computational studies,²²⁵ can be broadly grouped into three categories (as shown in Figure 6.5): sites that solvate the nucleobase ring (R_m where m indicates the specific binding location); in the void between U and the dipole-bound electron (Q); or at the outer periphery of the dipole-bound orbital (P). The optimised structure of each isomer was found using density functional theory (CAM-B3LYP/aug-cc-pVDZ), initiated from a wide range of configurations, and then VDE_1 was computed at the higher CCSD(T) level of theory.

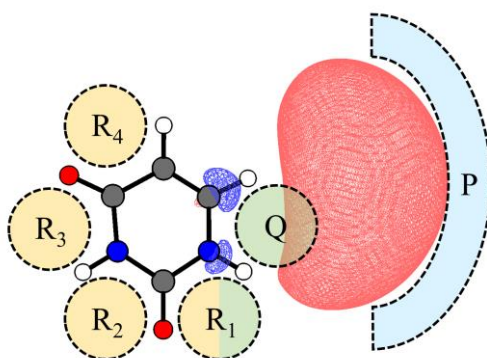


Figure 6.5: Electronic structure of the dipole-bound anion, U^- . Binding sites for clustered water molecules are labelled.

Unconstrained geometry optimisations for all R_m isomers of $U^-(H_2O)_1$ converged to valence anions. This is unsurprising, as the π_1^* state is the electronic ground state. However, since there is a large buckling geometry change that separates the valence and non-valence states of U^- , we were able to find optimised non-valence structures for some of the R-isomers by constraining the uracil ring to remain planar. In each case (R_2 and R_4), we found $VDE_1(R_m) < 100$ meV, inconsistent with the observed $VDE_1 = 255 \pm 20$ meV. Altogether, we conclude that R-isomers adiabatically convert to the valence-bound anion of $U^-(H_2O)_1$ within the timescale of the experiment, and are likely principally responsible for the dominant π_1^* state signal in Figure 6.2.

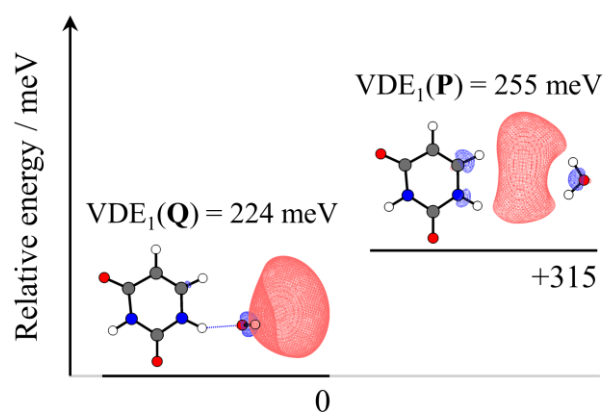


Figure 6.6: Relative energies and VDEs, computed with CCSD(T)/aug-cc-pVDZ+3s3p, of the most stable P- and Q-isomers structures of $U^-(H_2O)_1$. Isovalues were chosen to be 75% of the maximum electron density of the non-valence state.

Conversely, fully-relaxed optimisations of an extensive range of Q- and P-isomers readily converged to non-valence anions. The most stable calculated Q- and P-isomers are shown in Figure 6.6. We found that $VDE_1(Q) = 224$ meV and $VDE_1(P) = 255$ meV, such that both isomers are consistent with the observed photoelectron signal. Although the P-isomer appears to match better with the experimentally determined VDE_1 , it should be noted that our benchmarking studies (see Section 6.2.2) demonstrated that the CCSD(T)-calculated VDEs tended to be slight underestimates, and thus the Q-isomer should be considered to match

equally well. Furthermore, the Q-isomer is more stable than the P-isomer by 315 meV, suggesting it may even be the more likely structure. This would align with our expectations of the most likely isomers to form in our anion source region: we expect $U^-(H_2O)_1$ to be generated via electron attachment to the preformed cluster, $U(H_2O)_1$, or electron attachment to a larger $U(H_2O)_n$ cluster followed by evaporation. In either case, the P-isomer is not capable of forming without the dipole-bound electron already in place. Of course, this does not rule out formation of the P-isomer through rearrangement of the water molecule, but this too is unlikely as the Q-isomer is calculated to be significantly more stable. Nonetheless, whether the water molecule presides in the Q- or P-site, it is apparent that, in the non-valence state of $U^-(H_2O)_1$, the water is oriented to directly solvate the dipole-bound electron, rather than the U molecule. Henceforth, we therefore denote the non-valence state of the uracil monohydrate anion as $U(H_2O)_1^-$, making a distinction from the π_1^* valence state, which will remain written as $U^-(H_2O)_1$.

6.3.2. Non-valence States of Larger Cluster Anions, $U(H_2O)_n^-$

With the knowledge that we could form non-valence $U(H_2O)_1^-$ clusters that were kinetically trapped over the timescale to perform our experiment ($\sim 200 \mu s$), we sought to generate non-valence isomers of larger clusters too, which we will denote $U(H_2O)_n^-$. Two main changes were made to the experiments described in Chapter 5: an increased backing pressure of 11 bar of Ar was applied to encourage formation of kinetically trapped states; and lower photon energies were implemented, increasing the photodetachment cross-section associated with any non-valence states that formed. With the new conditions, we observed photoelectron signals arising from non-valence anions of $U(H_2O)_{n \leq 4}^-$, as shown in Figure 6.7. Labels refer to structural isomer assignments, presented below. The lower photon energies ($h\nu = 0.70$ eV for $n = 0-2$, and $h\nu = 1.20$ eV for $n = 3, 4$) also actively discriminated against detachment from the

$U^-(H_2O)_{1-4}$ valence states, since the photodetachment cross-section diminishes on account of Wigner's threshold law.¹³

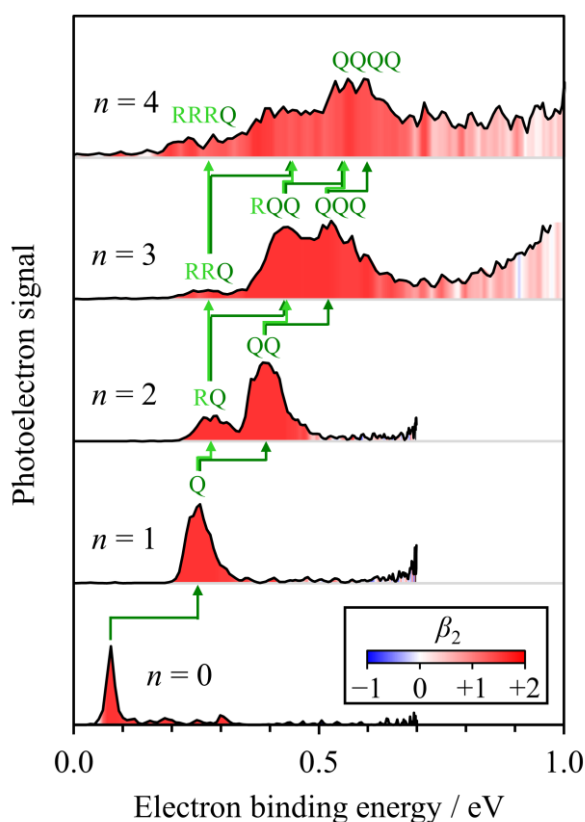


Figure 6.7: Photoelectron spectra of $U(H_2O)_n^-$ acquired at low photon energies, selectively detaching the non-valence state. Peaks are coloured by the measured photoelectron anisotropy (β_2). Dark and light green arrows highlight the increase in electron binding energy upon addition of an electron- or ring-solvating water molecule, respectively.

The photoelectron spectra of U^- and $U(H_2O)_1^-$ are described above; the only difference in Figure 6.7 is that the features have been coloured by their respective anisotropy parameters (β_2) at each electron binding energy, emphasising their non-valence origin. The photoelectron spectrum of $U(H_2O)_2^-$ shows two features, seemingly arising from different structural isomers. Both peaks are relatively narrow and the corresponding angular distributions are consistent with photodetachment from non-valence states.^{276,298} The binding energies are greater than that of $U(H_2O)_1^-$, we extract $VDE_2 = 395 \pm 30$ meV and 278 ± 30 meV. For the higher binding energy feature, the difference between VDE_1 and VDE_2 is ~ 140 meV (dark green arrow in

Figure 6.7). Recalling that the VDE increased by 180 meV from U^- to $U(H_2O)_1^-$, we might anticipate that the structural isomer with the larger VDE_2 contains two electron-solvating water molecules, with the second water molecule offering similar, but slightly lower stabilisation, as generally seen in clustering studies.^{4,152} On the other hand, the isomer with the lower VDE_2 has a second water molecule that exerts very little stabilisation (~ 20 meV; light green arrow in Figure 6.7), which may indicate this water molecule does not solvate the electron directly. To assign the anionic cluster isomers that lead to the non-valence signals, we performed further quantum chemical calculations.

A range of isomers are possible with permutations XY, where X, Y = R_m, Q, or P. All trialled RR-isomers were found to converge to the valence-bound anion, consistent with the analogous calculations on $U^-(H_2O)_1$. Hence, the structures that lead to the non-valence $U(H_2O)_2^-$ signals in Figure 6.7 must contain at least one water molecule occupying a site different to R.

We first consider the most likely structure of the isomer with $VDE_2 = 395 \pm 30$ meV, in which both water molecules are expected to solvate the excess non-valence electron. Whilst fully-relaxed geometry optimisations (from many different starting structures) led to a variety of structures, we focus on the lowest energy structures for each XY permutation, which are shown in Figure 6.8. The most stable isomer is QQ, owing to the supporting hydrogen bonding network. The QP- and PP-isomers are 275 and 402 meV higher in energy, respectively. For each isomer, the computed maximum in the photoelectron spectrum is predicted to be at $VDE_2(QQ) = 372$ meV, $VDE_2(QP) = 526$ meV, and $VDE_2(PP) = 499$ meV. Overall, the calculations suggest that the experimentally observed isomer with $VDE_2 = 395 \pm 30$ meV is the QQ-isomer, and thus the non-valence electron becomes more distant from the U molecule as it is preferentially solvated through the space dividing to the two. This conclusion also

supports the previous supposition that the Q-isomer is the dominant non-valence isomer in $U(H_2O)_1^-$.

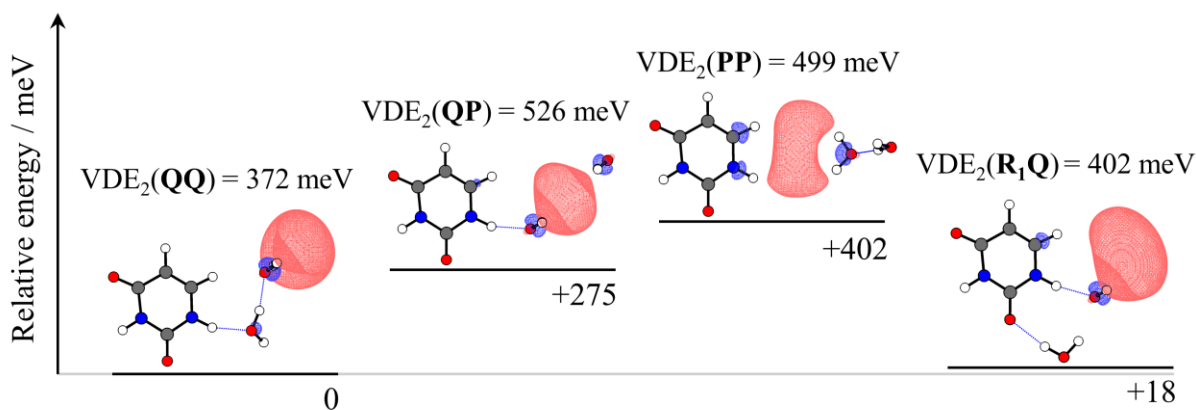


Figure 6.8: Relative energies (to the QQ-isomer) and VDEs, computed with CCSD(T)/aug-cc-pVDZ+3s3p, of candidate optimised structures for the more strongly bound isomer of $U(H_2O)_2^-$. Isovalues were chosen to be 75% of the maximum electron density of the non-valence state.

Considering the origin of the photoelectron peak at $VDE_2 = 278 \pm 30$ meV for $U(H_2O)_2^-$ in Figure 6.7, we considered a range of R_mQ -isomers. The R_2Q -, R_3Q - and R_4Q -isomers are 25, 25, and 103 meV higher in energy than the QQ-isomer, respectively, and their optimised structures are shown in Figure 6.9. The corresponding VDEs range between 270–282 meV, such that all are close to the observed experimental $VDE_2 \approx 278$ meV. We conclude that some combination of the R_2Q -, R_3Q - and R_4Q -isomers are candidates for this observed photoelectron signal. In contrast to $U^-(H_2O)_1$, the R-site water molecule does not induce the adiabatic formation of valence $U^-(H_2O)_2$ on the timescale of the experiment. Instead, it appears that the Q-site water molecule is ‘locking’ the excess electron into the non-valence state, with the R-site water molecule simply solvating neutral U, leading to the small additional increase in VDE. Since neutral U is planar and the excess electron is held at a distance, there is little driving force for the buckling motion that would otherwise encourage charge-transfer to U and the formation of the valence-bound anion.

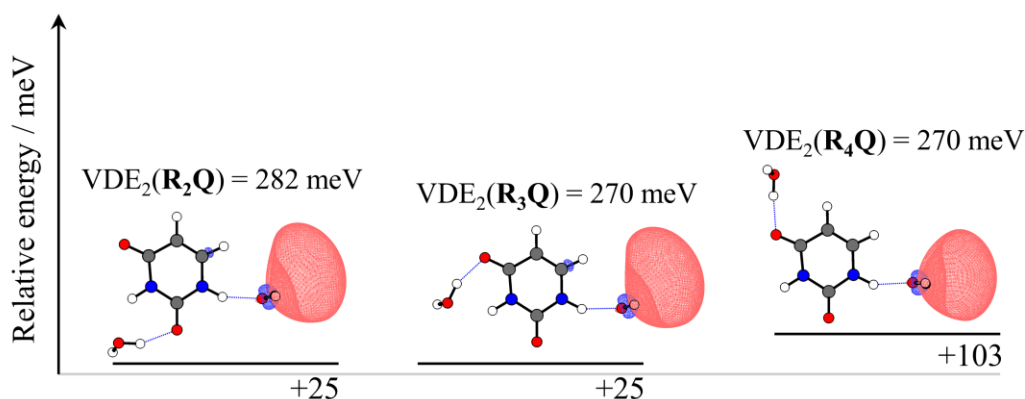


Figure 6.9: Relative energies (to the QQ-isomer) and VDEs, computed with CCSD(T)/aug-cc-pVDZ+3s3p, of candidate optimised structures for the less strongly bound isomer of $\text{U}(\text{H}_2\text{O})_2^-$. Isovalues were chosen to be 75% of the maximum electron density of the non-valence state.

Finally, we also consider the R_1Q -isomer. The optimised structure was calculated to have $\text{VDE}_2(\text{R}_1\text{Q}) = 402$ meV, with a relative energy only 18 meV above the QQ-isomer. Therefore, the feature with $\text{VDE}_2 = 395 \pm 30$ meV could also contain contributions from the R_1Q isomer, particularly on the edge of higher binding energy (where there is indeed a possible shoulder to the peak). Similar to the Q-site, the R_1 -site offers direct solvation of the excess electron such that the uracil-electron complex is viewed more appropriately as a “solvent-shared” state,³⁵⁵ intermediate to ring- and electron-solvating. Therefore, the potential presence of this isomer remains consistent with the idea that the excess electron preferentially solvated from the region between the nucleobase and the non-valence electron.

Non-valence states of $\text{U}(\text{H}_2\text{O})_3^-$ were also observed in the photoelectron spectrum shown in Figure 6.7. There are three distinct but relatively broad, anisotropic features, discernible at $\text{VDE}_3 = 530 \pm 50$ meV, 430 ± 50 meV and 260 ± 30 meV. These three peaks are likely a continuation of the two non-valence features observed from $\text{U}(\text{H}_2\text{O})_2^-$, where the additional water molecule either provides a small stabilisation by solvating the uracil ring (light green arrows in Figure 6.7), or a large stabilisation by solvating the non-valence electron (dark green arrows in Figure 6.7). Moreover, as electron-solvation has (for the smaller clusters)

preferentially occurred in the gap between the nucleobase and excess electron, we expect the highest binding energy feature at $VDE_3 = 530 \pm 30$ meV to arise from a QQQ-type isomer (or R_1QQ). In addition, the feature at $VDE_3 \approx 430$ meV is likely an RQQ isomer, and the feature at $VDE_3 \approx 260$ meV an RRQ isomer. Whilst there is also some photoelectron signal present at binding energies >0.7 eV, this signal has starkly different angular distributions that can be correlated to electron emission originating from the valence anion – mostly through thermionic emission processes.

Calculations on the larger $U(H_2O)_3^-$ anion cluster are more challenging, as many more isomeric structures become available. Nonetheless, we were able to verify that the above predictions are indeed consistent with the calculated structures. For the most stable computed QQQ-type isomer, $VDE_3(QQQ) = 517$ meV, in excellent agreement with the observed $VDE_3 = 530 \pm 30$ meV. Conversely, the optimised PPP-isomer had a much higher $VDE_3(PPP) = 772$ meV, and is 424 meV higher in energy than the QQQ-isomer, providing further assurance that additional water molecules do not solvate the excess electron from its outer periphery, but rather by wedging between the U molecule and the non-valence orbital. The lowest energy RQQ structure was found to be R_3QQ , with $VDE_3(R_3QQ) = 412$ meV, matching well with the measured central feature at $VDE_3 = 430 \pm 50$ meV. Interestingly, the computed R_3QQ -isomer was slightly lower in energy than the optimised QQQ-isomer, which may offer insight into the similar intensities of the two higher-energy peaks in the photoelectron spectrum of $U(H_2O)_3^-$ (as opposed to the spectrum of $U(H_2O)_2^-$, for which the peak associated with the QQ-isomer was clearly more intense). Finally, the measured feature at $VDE_3 = 260 \pm 30$ meV was expected to stem from an RRQ-isomer: the optimised R_2R_4Q -isomer appeared to be a good candidate, with $VDE_3(R_2R_4Q) = 307$ meV. In general, as evidenced by the substantial widths of each observed peak, it is likely that many other isomeric structures (especially other RRQ- and RQQ-isomers) also contribute to the observed

photoelectron signals. We can again conclude that clustered water molecules preferentially solvate the non-valence electron from *within* the cluster, and that even a single electron-solvating water molecule is sufficient to prevent the excess electron from transferring onto the uracil ring.

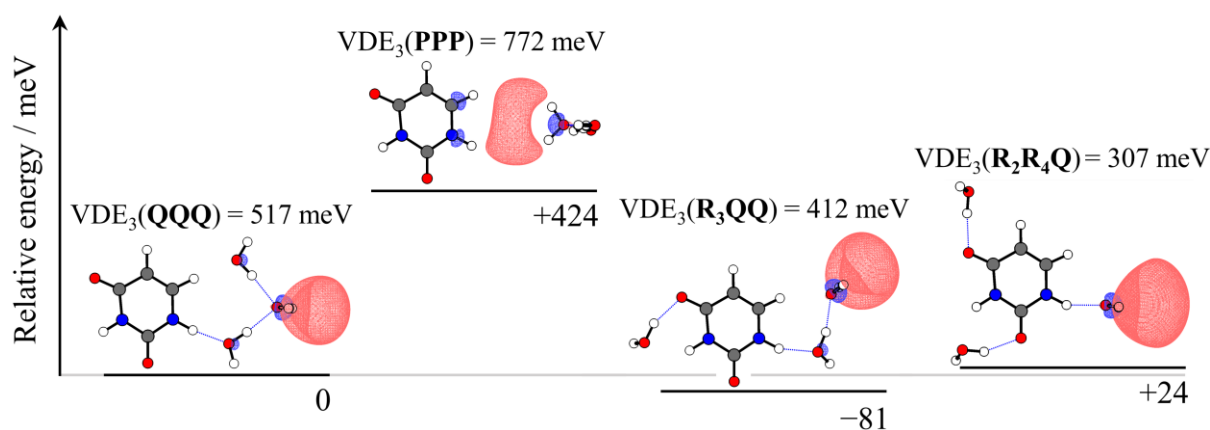


Figure 6.10: Relative energies (to the QQQ-isomer) and VDEs, computed with CCSD(T)/aug-cc-pVDZ+3s3p, of candidate optimised structures of $\text{U}(\text{H}_2\text{O})_3^-$. Isovalues were chosen to be 75% of the maximum electron density of the non-valence state.

Calculations were not performed for $\text{U}(\text{H}_2\text{O})_4^-$, although the photoelectron spectrum of this anion cluster did show several partially resolved peaks associated with non-valence anion detachment. From the combined experimental and computational results for $\text{U}(\text{H}_2\text{O})_{0-3}^-$, the low binding energy edge of the photoelectron spectrum likely correlates with RRRQ-isomers, and the highest edge is likely attributable to QQQQ-isomers. Several combinations of R and Q are expected to constitute the remainder of the broad signal. We were not able to generate larger ($n > 4$) clusters with clear signals assignable to non-valence states, suggesting that the kinetically trapped species for $\text{U}(\text{H}_2\text{O})_{n>4}^-$, if formed, had converted to valence anions on the timescale of our experiments.

6.3.3. From Contact Pair to Hydrated Electron

Our results show that the addition of a single water molecule to the dipole-bound electron of U^- drives separation of the U molecule and the excess electron. The water molecule in the Q-site binds by donating both its H-atoms to the excess electron distribution (e.g. see Figure 6.6). This motif is reminiscent of the binding of the excess electron in small water cluster anions, $(H_2O)_n^-$, the structures of which have been determined by IR action spectroscopy.^{140,141} In these, a single water molecule near the edge of the water cluster interacts closely with the non-valence electron through a similar double H-bond acceptor motif. For larger $(H_2O)_n^-$ clusters, the electron binding is enhanced and the non-valence electron orbital becomes more confined.³⁶⁸ A similar confinement of the non-valence electron density with increasing hydration occurs for all-Q isomers of $U(H_2O)_n^-$, as demonstrated by the orbital size in the calculated electronic structures presented above. The connection between $U(H_2O)_n^-$ and $(H_2O)_n^-$ is further supported by considering the differential increase in binding energy with cluster size. In Figure 6.11, the VDE_n is plotted as a function of $n^{-1/3}$ (i.e. cluster size⁴) for the most stable non-valence isomers of $U(H_2O)_n^-$ and $(H_2O)_n^-$,¹⁴⁴ revealing similar gradients in the same range of VDE (~ 0.5 eV). Clearly, the dipolar U molecule acts to stabilise the non-valence electron, but the similar gradients indicate that this effect is essentially independent of n , suggesting that U has less influence on the electron binding as solvation is increased. This is consistent with the overall picture that additional water molecules solvate the electron from the Q-site, moving the non-valence electron further away from U. A computational study has predicted similar behaviour, albeit for larger clusters:²⁹² the dipole-bound anion of the model H_3BNH_3 molecule ($\mu = 5.4$ D) was subject to clustering of tens of water molecules and was found to localise the non-valence electron on the surface of the water cluster. Our observation of all-Q isomers broadly supports this and suggests that even a single water molecule is sufficient to instigate this transition.

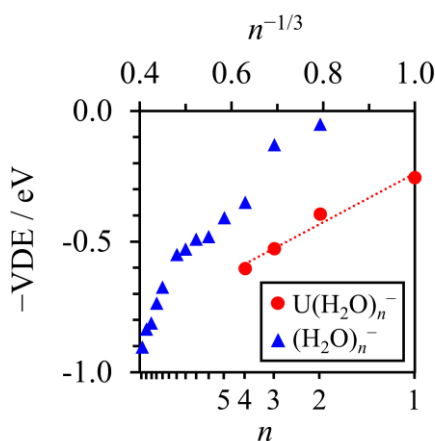


Figure 6.11: Vertical detachment energies (VDEs) associated with the most stable isomers of $(\text{H}_2\text{O})_n^-$ (blue triangles) and $\text{U}(\text{H}_2\text{O})_n^-$ (red circles). The red dotted line shows a linear fit to the VDEs of $\text{U}(\text{H}_2\text{O})_n^-$.

From the perspective of incrementally increasing solvation, water cluster anions $(\text{H}_2\text{O})_n^-$ are precursors to the hydrated electron. The all-Q isomers of $\text{U}(\text{H}_2\text{O})_n^-$ can also be viewed as precursors to $e^-_{(\text{aq})}$, with a similar electron binding motif, but in the presence of a dipolar solute. Considering that the DBS of U^- is broadly representative of a molecule-electron contact pair, we can therefore correlate the kinetically trapped non-valence $\text{U}(\text{H}_2\text{O})_n^-$ clusters with solvent-induced dissociation of the contact pair. Figure 6.12 presents a visual aid, where the different isomers of $\text{U}(\text{H}_2\text{O})_n^-$ form local minima along the a generalised $\text{U}-e^-$ separation (dissociation) coordinate. In this sense, the non-valence anion clusters studied here offer incremental snapshots of contact pair dissociation, or in other words, the hydrated electron solvation coordinate. The electron is most quickly stabilised by an initial water molecule wedging in between the U molecule and the non-valence electron, to which further water molecules push in and drive the electron further from the parent into $e^-_{(\text{aq})}$. This solvent-induced mechanism is in accord with earlier suggestions of a diffusion controlled dissociation, where the motion of a single diffusing water can be important.³⁵⁸

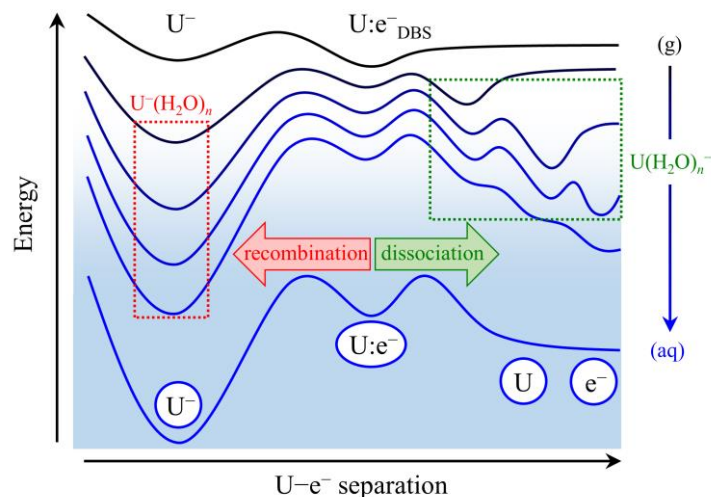


Figure 6.12: Sketch illustrating the evolution of the non-valence DBS of uracil ($U:e^-$) into its aqueous analogue, the contact pair, within the context of the potential energy along a generalised $U-e^-$ separation coordinate. Rearrangement of the solvating water molecules can provoke either recombination into a valence anion U^- , or dissociation of the contact pair. Clusters permit probing of the solvent-induced dissociation coordinate via kinetically-trapped local minima.

Valence anions of $U^-(H_2O)_n$ were also formed in our experiment (as showcased in Chapter 5), representing the opposite direction along the $U-e^-$ separation coordinate mentioned above, i.e. geminate recombination of the contact pair. From the contact pair, formation of $U^-(H_2O)_n$ and $U(H_2O)_n^-$ occur in competition, and this competition is dependent on cluster size. For $n \geq 1$, recombination is the energetically favoured pathway, as evidenced by the higher electron affinities associated with $U^-(H_2O)_n$ relative to those of $U(H_2O)_n^-$, shown in Figure 6.13. Since the valence state is stabilised more with increasing solvation than the non-valence state, the energetic barrier separating the two states is generally expected to decrease (in a normal regime Marcus picture of charge-transfer³⁶⁹). This may offer an explanation for the absence of larger $U(H_2O)_{n>4}^-$ clusters from our anion source, as these non-valence states could not be kinetically trapped for a sufficient period. However, at least for the smaller clusters, our computations suggest that the energetic barrier between valence and non-valence states is also dictated by the solvation motif: for example, relaxed geometry optimisations from

ring-solvated (R_m) non-valence $U(H_2O)_1^-$ readily formed valence-bound $U^-(H_2O)_1$, whereas optimisations of electron-solvated (Q or P) $U(H_2O)_1^-$ retained the non-valence description. Altogether, it is likely that the response of the water molecules which are closest to the contact pair electron that have the greatest influence on the decay pathway.

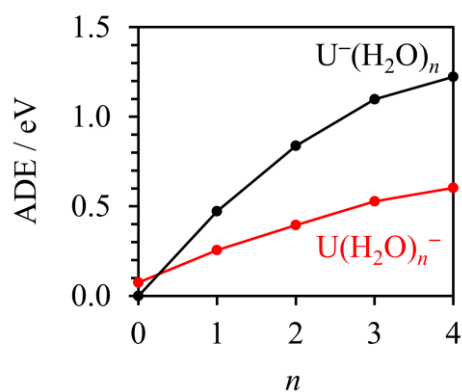


Figure 6.13: Adiabatic detachment energies (ADEs) of valence $U^-(H_2O)_n$ (black) and non-valence $U(H_2O)_n^-$ (red) anion clusters

6.4. Closing Remarks

Conclusions

Dipole-bound states are thought to be incapable of forming in aqueous solution, due to disruption from the surrounding water molecules. Despite this, through the observation of non-valence $U(H_2O)_n^-$ clusters and with supporting quantum chemical calculations, we have shown that the addition of a few (up to four) water molecules can act to significantly stabilise the non-valence electron. However, the electron binding motif of the non-valence states of $U(H_2O)_n^-$ bears greater resemblance to $(H_2O)_n^-$ cluster anions than to a pure DBS, since the diffuse electron accepts a double hydrogen bond from a water molecule. Interestingly, the direct solvation of the non-valence electron appears to preferentially occur from the volume between the U molecule and the electron, which effectively acts to drive the electron away from the molecule as the degree of solvation is increased. By drawing comparisons between the DBS of U^- and an aqueous molecule-electron contact pair, our cluster-based approach provides insight into the solvent-driven contact pair dissociation coordinate, and thus also insight into the initial steps of $e^-_{(aq)}$ formation. The response of even a single water molecule plays a critical role in stabilising the non-valence electron further away from the nucleobase, and in inhibiting geminate recombination. Overall, our application of anion-water clusters offers a new route to probing the molecular-level hydration coordinate that determines the fate of the non-valence electron in a contact pair and creation of $e^-_{(aq)}$.

Outlook

Hydration of other molecules that form DBSs are expected to evoke a similar solvation response to the presence of the non-valence electron. For instance, non-valence adenine-water cluster anions, $A(H_2O)_n^-$, were observed in the experiments described in Chapter 5.

Unfortunately, adenine could form multiple tautomeric structures such that characterisation of the non-valence states is more challenging and has not yet been performed. Nonetheless, it seems that these hydrated non-valence states, which can be treated as precursors to $e^-_{(aq)}$, may be a quite general phenomenon.

The most stable non-valence states of $U(H_2O)_n^-$ generally arose from all-Q isomers, which benefitted from hydrogen bonding between the nucleobase and the clustered water molecules. It would be interesting to test whether a polar molecule that is incapable of forming H-bonds will act similarly. If the Q- and P-isomers are brought sufficiently close in energy, it may be possible to form both structures in the molecular beam source and distinguish them by their different electron binding energies. On a different note, it could be equally interesting to change the identity of the solvent. Solvated electrons are not exclusive to water, and the response of other solvents may differ to the ‘wedging’ response that was demonstrated above. In particular, larger solvent molecules, such as ethanol, may not be able to localise between U and the non-valence electron as easily, such that the response leading to contact pair dissociation could be hindered.

Small non-valence anion clusters of $U(H_2O)_n^-$ are kinetically trapped states and may be expected to decay to $U^-(H_2O)_n$ on a timescale longer than the duration of the experiment. However, it may be possible to prompt this charge-transfer via photoexcitation to a valence-bound state (e.g. the π^* resonances). If so, the relaxation dynamics following electron attachment into a (partially) hydrated nucleobase could therefore be studied by TRPES. As the nucleobase in non-valence $U(H_2O)_n^-$ has the same planar geometry as neutral U, the light-driven charge-transfer is a good approximation to low-energy electron attachment. On the other hand, the reverse photoexcitation from $U^-(H_2O)_n$ to $U(H_2O)_n^-$ may also be possible. This potentially allows the dynamics of the solvent response to be probed through TRPES, since structural isomers are distinguishable through their electron binding energies.

Chapter 7 – Conclusion

Frequency-resolved photoelectron spectroscopy (FRPES) is an effective tool for determining the energetic positions of anion resonance states. In Chapter 3, the pyruvate anion was studied by FRPES, where UV photoexcitation was observed to induce fragmentation of the small molecule. This has implications for the ability of the pyruvate anion to persist in the atmosphere, although the photodissociation channel may become inhibited by the bulk aqueous environment that generally accommodates the anion.

The nucleobases are the prime target sites for low-energy electron attachment to DNA, which induces strand breakages. However, it remains unclear which anion resonance states participate most in the initial electron attachment step. For each nucleobase, the energies of the lowest anion resonances have been determined in the gas phase – the results in Chapter 4 contributed to this understanding by highlighting that the π_1^* valence state of the uracil (U) nucleobase anion is not as adiabatically bound as has previously been suggested.

Despite this knowledge, electron attachment to the nucleobases within DNA is expected to occur with different incident electron energies (compared to in the gas phase), as the surrounding environment of the helical structure will both stabilise and destabilise the anion resonance states. We began to tackle this problem in Chapter 5 by studying nucleobase-water anion clusters with FRPES, incrementally probing the effect of hydration on the low-energy shape resonances. By examining sufficiently large $U^-(H_2O)_n$ clusters, we could extrapolate our measured energies to the bulk aqueous limit, where we found that the π_2^* and π_3^* resonances remained accessible with very low energy electrons (< 2 eV), yet were also adiabatically bound states of $U^-_{(aq)}$. Thymine-water anion clusters were observed to exhibit similar behaviour. Moreover, there was also evidence of these π_2^* and π_3^* resonances undergoing ultrafast internal

conversion to the ground π_1^* state, which may aid long-term electron capture within the DNA environment.

Curiously, our experiment was also capable of forming a different class of uracil-water cluster anions: non-valence states, $U(H_2O)_n^-$. Chapter 6 examined the effect of incremental hydration on these exotic states, which have generally been postulated as efficient ‘doorways’ for electron capture. With the aid of computations, it appeared that solvation preferentially occurred from between U and the electron, leading to a binding motif similar to $(H_2O)_n^-$, i.e. precursors to the hydrated electron. Although non-valence states are not believed to participate in low-energy electron attachment to DNA (despite all nucleobase anions having a propensity to form DBSs in isolation), the placement of even a single water molecule can have drastic consequences for the stability and persistence of non-valence states.

Altogether, the work presented in this thesis demonstrates how frequency-resolved photoelectron spectroscopy can be applied to map out the position of excited anion resonance states, indirectly providing information on their relaxation dynamics. Applied to nucleobase-water clusters, we identified resonance states that can be populated through low-energy electron attachment to aqueous nucleobases, and demonstrated that these states are expected to undergo very fast relaxation to the anion ground state. These findings contribute to our understanding of electron attachment to nucleobases in condensed phases, such as within living cells. Furthermore, we highlighted the important stabilising effect that water molecules impose on non-valence states of anions, although it remains contentious that non-valence states play any role in electron attachment to DNA. Instead, our measurements on non-valence states of nucleobase-water clusters appear to offer an unprecedented view into the process of molecule-electron contact pair dissociation in an aqueous environment.

References

- 1 J. Simons, *J. Phys. Chem. A*, 2008, **112**, 6401–6511.
- 2 J. Simons, *J. Phys. Chem. A*, 2023, **127**, 3940–3957.
- 3 N. B. Cech and C. G. Enke, *Mass Spectrom. Rev.*, 2001, **20**, 362–387.
- 4 J. Jortner, *Z Phys D*, 1992, **24**, 247–275.
- 5 J. R. R. Verlet, *Chem. Soc. Rev.*, 2008, **37**, 505–517.
- 6 A. Henley and H. H. Fielding, *Int. Rev. Phys. Chem.*, 2019, **38**, 1–34.
- 7 D. W. Chandler and P. L. Houston, *J. Chem. Phys.*, 1987, **87**, 1445–1447.
- 8 A. T. J. B. Eppink and D. H. Parker, *Rev. Sci. Instrum.*, 1997, **68**, 3477–3484.
- 9 A. Sanov and R. Mabbs, *Int. Rev. Phys. Chem.*, 2008, **27**, 53–85.
- 10 K. L. Reid, *Annu. Rev. Phys. Chem.*, 2003, **54**, 397–424.
- 11 J. Cooper and R. N. Zare, *J. Chem. Phys.*, 1968, **48**, 942–943.
- 12 A. Sanov, *Annu. Rev. Phys. Chem.*, 2014, **65**, 341–363.
- 13 E. P. Wigner, *Phys. Rev.*, 1948, **73**, 1002–1009.
- 14 K. D. Jordan and P. D. Burrow, *Acc. Chem. Res.*, 1978, **11**, 341–348.
- 15 K. J. Reed, A. H. Zimmerman, H. C. Andersen and J. I. Brauman, *J. Chem. Phys.*, 1976, **64**, 1368–1375.
- 16 D. Khuseynov, C. C. Blackstone, L. M. Culberson and A. Sanov, *J. Chem. Phys.*, 2014, **141**, 124312.
- 17 E. R. Grumbling and A. Sanov, *J. Chem. Phys.*, 2011, **135**, 164302.
- 18 A. Sanov, E. R. Grumbling, D. J. Goebbert and L. M. Culberson, *J. Chem. Phys.*, 2013, **138**, 054311.
- 19 C. C. Blackstone, A. A. Wallace and A. Sanov, *Mol. Phys.*, 2021, **119**, e1831636.
- 20 C. M. Oana and A. I. Krylov, *J. Chem. Phys.*, 2007, **127**, 234106.
- 21 C. M. Oana and A. I. Krylov, *J. Chem. Phys.*, 2009, **131**, 124114.
- 22 S. Gozem, A. O. Gunina, T. Ichino, D. L. Osborn, J. F. Stanton and A. I. Krylov, *J. Phys. Chem. Lett.*, 2015, **6**, 4532–4540.
- 23 S. Gozem and A. I. Krylov, *Wiley Interdiscip. Rev. Comput. Mol. Sci.*, 2022, **12**, e1546.
- 24 T. Seideman, *Annu. Rev. Phys. Chem.*, 2002, **53**, 41–65.
- 25 J. Lecointre, G. M. Roberts, D. A. Horke and J. R. R. Verlet, *J. Phys. Chem. A*, 2010, **114**, 11216–11224.
- 26 D. Popova-Gorelova, J. Küpper and R. Santra, *Phys. Rev. A*, 2016, **94**, 013412.
- 27 C. S. Anstöter, B. F. E. Curchod and J. R. R. Verlet, *Nat. Commun.*, 2020, **11**, 2827.
- 28 G. J. Schulz, *Rev. Mod. Phys.*, 1973, **45**, 423–486.
- 29 D. A. Horke, Q. Li, L. Blancafort and J. R. R. Verlet, *Nat. Chem.*, 2013, **5**, 711–717.
- 30 M. Krauss and F. H. Mies, *Phys. Rev. A*, 1970, **1**, 1592–1598.
- 31 M. Bixon and J. Jortner, *J. Chem. Phys.*, 1968, **48**, 715–726.
- 32 M. Klessinger and J. Michl, *Excited States and Photochemistry of Organic Molecules*, VCH, New York, 1995.
- 33 M. Born and J. R. Oppenheimer, *Ann. Phys.*, 1927, **84**, 457–484.
- 34 R. Englman and J. Jortner, *Mol. Phys.*, 1970, **18**, 145–164.
- 35 G. A. Worth and L. S. Cederbaum, *Annu. Rev. Phys. Chem.*, 2004, **55**, 127–158.
- 36 K. S. Zinchenko, F. Ardana-Lamas, I. Seidu, S. P. Neville, J. van der Veen, V. U. Lanfaloni, M. S. Schuurman and H. J. Wörner, *Science*, 2021, **371**, 489–494.
- 37 W. Domcke and D. R. Yarkony, *Annu. Rev. Phys. Chem.*, 2012, **63**, 325–352.
- 38 S. Matsika, *Chem. Rev.*, 2021, **121**, 9407–9449.
- 39 D. Boyall and K. L. Reid, *Chem. Soc. Rev.*, 1997, **26**, 223–232.
- 40 D. J. Nesbitt and R. W. Field, *J. Phys. Chem.*, 1996, **100**, 12735–12756.
- 41 T. Uzer and W. H. Miller, *Phys. Rep.*, 1991, **199**, 73–146.
- 42 P. R. Stannard and W. M. Gelbart, *J. Phys. Chem.*, 1981, **85**, 3592–3599.
- 43 R. A. Marcus, *Faraday Discuss. Chem. Soc.*, 1983, **75**, 103–115.
- 44 L. J. Butler and D. M. Neumark, *J. Phys. Chem.*, 1996, **100**, 12801–12816.
- 45 C. W. West, J. N. Bull and J. R. R. Verlet, *J. Phys. Chem. Lett.*, 2016, **7**, 4635–4640.

- 46 J. A. Gibbard, E. Castracane, A. I. Krylov and R. E. Continetti, *Phys. Chem. Chem. Phys.*, 2021, **23**, 18414–18424.
- 47 J. A. Gibbard and J. R. R. Verlet, *J. Chem. Phys.*, 2023, **158**, 154306.
- 48 M. Kasha, *Discuss. Faraday Soc.*, 1950, **9**, 14–19.
- 49 M. Y. Berezin and S. Achilefu, *Chem. Rev.*, 2010, **110**, 2641–2684.
- 50 L. Sanche and G. J. Schulz, *J. Chem. Phys.*, 1973, **58**, 479–493.
- 51 K. D. Jordan and P. D. Burrow, *Chem. Rev.*, 1987, **87**, 557–588.
- 52 M. Allan, *J. Electron Spectros. Relat. Phenomena*, 1989, **48**, 219–351.
- 53 K. Regeta and M. Allan, *Phys. Rev. Lett.*, 2013, **110**, 203201.
- 54 S. J. P. Marlton and A. J. Trevitt, *Chem. Commun.*, 2022, **58**, 9451–9467.
- 55 J. A. Gibbard, C. J. Clarke and J. R. R. Verlet, *Phys. Chem. Chem. Phys.*, 2021, **23**, 18425–18431.
- 56 C. S. Anstöter, J. N. Bull and J. R. R. Verlet, *Int. Rev. Phys. Chem.*, 2016, **35**, 509–538.
- 57 G. Ganteför, W. Eberhardt, H. Weidele, D. Kreisle and E. Recknagel, *Phys. Rev. Lett.*, 1996, **77**, 4524–4527.
- 58 J. C. Pinaré, B. Baguenard, C. Bordas and M. Broyer, *Phys. Rev. Lett.*, 1998, **81**, 2225–2228.
- 59 Y. Shi, V. A. Spasov and K. M. Ervin, *J. Chem. Phys.*, 1999, **111**, 938–949.
- 60 A. E. Bragg, J. R. R. Verlet, A. Kammrath, O. Cheshnovsky and D. M. Neumark, *J. Am. Chem. Soc.*, 2005, **127**, 15283–15295.
- 61 M. A. Parkes, C. Phillips, M. J. Porter and H. H. Fielding, *Phys. Chem. Chem. Phys.*, 2016, **18**, 10329–10336.
- 62 C. McLaughlin, M. Assmann, M. A. Parkes, J. L. Woodhouse, R. Lewin, H. C. Hailes, G. A. Worth and H. H. Fielding, *Chem. Sci.*, 2017, **8**, 1621–1630.
- 63 C. S. Anstöter and J. R. R. Verlet, *Mol. Phys.*, 2021, **119**, e1821921.
- 64 A. Lietard, G. Mensa-Bonsu and J. R. R. Verlet, *Nat. Chem.*, 2021, **13**, 737–742.
- 65 A. Lietard and J. R. R. Verlet, *J. Phys. Chem. Lett.*, 2022, **13**, 3529–3533.
- 66 C. R. Sagan, C. S. Anstöter, M. Thodika, K. D. Wilson, S. Matsika and E. Garand, *J. Phys. Chem. Lett.*, 2022, **13**, 10245–10252.
- 67 Y. Zhao, E. de Beer, C. Xu, T. Taylor and D. M. Neumark, *J. Chem. Phys.*, 1996, **105**, 4905–4919.
- 68 B. Concina and C. Bordas, *J. Phys. Chem. A*, 2022, **126**, 7442–7451.
- 69 E. E. B. Campbell and R. D. Levine, *Annu. Rev. Phys. Chem.*, 2000, **51**, 65–98.
- 70 B. Baguenard, J. C. Pinaré, F. Lépine, C. Bordas and M. Broyer, *Chem. Phys. Lett.*, 2002, **352**, 147–153.
- 71 J. Troe, T. M. Miller and A. A. Viggiano, *J. Chem. Phys.*, 2009, **130**, 244303.
- 72 B. Concina, B. Baguenard, F. Calvo and C. Bordas, *J. Chem. Phys.*, 2010, **132**, 104307.
- 73 G.-Z. Zhu and L.-S. Wang, *Chem. Sci.*, 2019, **10**, 9409–9423.
- 74 C. S. Anstöter, G. Mensa-Bonsu, P. Nag, M. Ranković, R. Kumar T. P., A. N. Boichenko, A. V. Bochenkova, J. Fedor and J. R. R. Verlet, *Phys. Rev. Lett.*, 2020, **124**, 203401.
- 75 C. L. Adams, K. Hansen and J. M. Weber, *J. Phys. Chem. A*, 2019, **123**, 8562–8570.
- 76 R. E. Continetti and H. Guo, *Chem. Soc. Rev.*, 2017, **46**, 7650–7667.
- 77 L.-S. Wang and X.-B. Wang, *J. Phys. Chem. A*, 2000, **104**, 1978–1990.
- 78 A. Dreuw and L. S. Cederbaum, *Chem. Rev.*, 2002, **102**, 181–200.
- 79 X.-B. Wang and L.-S. Wang, *Annu. Rev. Phys. Chem.*, 2009, **60**, 105–126.
- 80 L.-S. Wang, *J. Chem. Phys.*, 2015, **143**, 040901.
- 81 J. A. Gibbard and J. R. R. Verlet, *J. Phys. Chem. A*, 2022, **126**, 3495–3501.
- 82 X.-B. Wang, C.-F. Ding and L.-S. Wang, *Phys. Rev. Lett.*, 1998, **81**, 3351–3354.
- 83 A. Dreuw and L. S. Cederbaum, *Phys. Rev. A*, 2000, **63**, 012501.
- 84 J. R. R. Verlet, D. A. Horke and A. S. Chatterley, *Phys. Chem. Chem. Phys.*, 2014, **16**, 15043–15052.
- 85 X.-B. Wang, C.-F. Ding and L.-S. Wang, *Chem. Phys. Lett.*, 1999, **307**, 391–396.
- 86 P. D. Dau, H.-T. Liu, J.-P. Yang, M.-O. Winghart, T. J. A. Wolf, A.-N. Unterreiner, P. Weis, Y.-R. Miao, C.-G. Ning, M. M. Kappes and L.-S. Wang, *Phys. Rev. A*, 2012, **85**, 064503.
- 87 J. A. Gibbard and J. R. R. Verlet, *J. Phys. Chem. Lett.*, 2022, **13**, 7797–7801.
- 88 A. H. Zewail, *J. Phys. Chem. A*, 2000, **104**, 5660–5694.

- 89 D. M. Neumark, *Annu. Rev. Phys. Chem.*, 2001, **52**, 255–277.
- 90 A. Stolow, A. E. Bragg and D. M. Neumark, *Chem. Rev.*, 2004, **104**, 1719–1758.
- 91 M. S. Schuurman and V. Blanchet, *Phys. Chem. Chem. Phys.*, 2022, **24**, 20012–20024.
- 92 G. Wu, P. Hockett and A. Stolow, *Phys. Chem. Chem. Phys.*, 2011, **13**, 18447–18467.
- 93 A. Assion, M. Geisler, J. Helbing, V. Seyfried and T. Baumert, *Phys. Rev. A*, 1996, **54**, R4605–R4608.
- 94 H. Okuyama, Y.-I. Suzuki, S. Karashima and T. Suzuki, *J. Chem. Phys.*, 2016, **145**, 074502.
- 95 A. Kunin and D. M. Neumark, *Phys. Chem. Chem. Phys.*, 2019, **21**, 7239–7255.
- 96 A. V. Davis, R. Wester, A. E. Bragg and D. M. Neumark, *J. Chem. Phys.*, 2003, **118**, 999–1002.
- 97 R. F. Stebbings and F. B. Dunning, *Rydberg States of Atoms and Molecules*, Cambridge University Press, 1983.
- 98 O. H. Crawford, *Mol. Phys.*, 1971, **20**, 585–591.
- 99 C. Desfrancois, H. Abdoul-Carime and J.-P. Schermann, *Int. J. Mod. Phys. B*, 1996, **10**, 1339–1395.
- 100 G.-Z. Zhu, Y. Liu and L.-S. Wang, *Phys. Rev. Lett.*, 2017, **119**, 023002.
- 101 G. Liu, S. M. Ciborowski, J. D. Graham, A. M. Buytendyk and K. H. Bowen, *J. Chem. Phys.*, 2019, **151**, 101101.
- 102 G. Liu, S. M. Ciborowski, C. Ross Pitts, J. D. Graham, A. M. Buytendyk, T. Lectka and K. H. Bowen, *Phys. Chem. Chem. Phys.*, 2019, **21**, 18310–18315.
- 103 Y. Liu, G.-Z. Zhu, D.-F. Yuan, C.-H. Qian, Y.-R. Zhang, B. M. Rubenstein and L.-S. Wang, *J. Am. Chem. Soc.*, 2020, **142**, 20240–20246.
- 104 D. H. Kang, J. Kim, M. Cheng and S. K. Kim, *J. Phys. Chem. Lett.*, 2021, **12**, 1947–1954.
- 105 T. Sommerfeld, B. Bhattarai, V. P. Vysotskiy and L. S. Cederbaum, *J. Chem. Phys.*, 2010, **133**, 114301.
- 106 V. K. Voora, L. S. Cederbaum and K. D. Jordan, *J. Phys. Chem. Lett.*, 2013, **4**, 849–853.
- 107 V. K. Voora and K. D. Jordan, *J. Phys. Chem. Lett.*, 2015, **6**, 3994–3997.
- 108 J. N. Bull and J. R. R. Verlet, *Sci. Adv.*, 2017, **3**, e1603106.
- 109 D. H. Kang, J. Kim, H. J. Eun and S. K. Kim, *Acc. Chem. Res.*, 2022, **55**, 3032–3042.
- 110 D.-F. Yuan, Y. Liu, Y.-R. Zhang and L.-S. Wang, *J. Am. Chem. Soc.*, 2023, **145**, 5512–5522.
- 111 J. N. Bull and J. R. R. Verlet, *Phys. Chem. Chem. Phys.*, 2017, **19**, 26589–26595.
- 112 T. Sugiura and A. Arakawa, *Proceedings of the International Conference on Mass Spectrometry*, Univ. of Tokyo, Tokyo, 1970.
- 113 J. A. Stockdale, F. J. Davis, R. N. Compton and C. E. Klots, *J. Chem. Phys.*, 1974, **60**, 4279–4285.
- 114 C. Desfrancois, *Phys. Rev. A*, 1995, **51**, 3667–3675.
- 115 H.-T. Liu, C.-G. Ning, D.-L. Huang and L.-S. Wang, *Angew. Chem.*, 2014, **53**, 2464–2468.
- 116 M. Ranković, P. Nag, C. S. Anstöter, G. Mensa-Bonsu, R. Kumar T. P., J. R. R. Verlet and J. Fedor, *J. Chem. Phys.*, 2022, **157**, 064302.
- 117 V. K. Voora and K. D. Jordan, *J. Phys. Chem. A*, 2014, **118**, 7201–7205.
- 118 F. Carelli, F. A. Gianturco, R. Wester and M. Satta, *J. Chem. Phys.*, 2014, **141**, 054302.
- 119 D. H. Kang, J. Kim, H. J. Eun and S. K. Kim, *J. Am. Chem. Soc.*, 2022, **144**, 16077–16085.
- 120 M. A. Yandell, S. B. King and D. M. Neumark, *J. Am. Chem. Soc.*, 2013, **135**, 2128–2131.
- 121 J. P. Rogers, Doctoral, Durham University, 2017.
- 122 J. P. Rogers, C. S. Anstöter and J. R. R. Verlet, *Nat. Chem.*, 2018, **10**, 341–346.
- 123 P. J. Sarre, *Mon. Not. R. Astron. Soc.*, 2000, **313**, L14–L16.
- 124 R. C. Fortenberry, *J. Phys. Chem. A*, 2015, **119**, 9941–9953.
- 125 M. C. McCarthy, C. A. Gottlieb, H. Gupta and P. Thaddeus, *ApJ*, 2006, **652**, L141.
- 126 J. Cernicharo, M. Guélin, M. Agúndez, K. Kawaguchi, M. McCarthy and P. Thaddeus, *A&A*, 2007, **467**, L37–L40.
- 127 S. Brünken, H. Gupta, C. A. Gottlieb, M. C. McCarthy and P. Thaddeus, *ApJ*, 2007, **664**, L43.
- 128 P. Thaddeus, C. A. Gottlieb, H. Gupta, S. Brünken, M. C. McCarthy, M. Agúndez, M. Guélin and J. Cernicharo, *ApJ*, 2008, **677**, 1132.
- 129 J. Cernicharo, M. Guélin, M. Agúndez, M. C. McCarthy and P. Thaddeus, *ApJ*, 2008, **688**, L83.

- 130 M. Agúndez, J. Cernicharo, M. Guélin, C. Kahane, E. Roueff, J. Klos, F. J. Aoiz, F. Lique, N. Marcelino, J. R. Goicoechea, M. G. García, C. A. Gottlieb, M. C. McCarthy and P. Thaddeus, *A&A*, 2010, **517**, L2.
- 131 A. G. G. M. Tielens, *Annu. Rev. Astron. Astrophys.*, 2008, **46**, 289–337.
- 132 J. Narayanan S J, D. Tripathi, P. Verma, A. Adhikary and A. K. Dutta, *ACS Omega*, 2023, **8**, 10669–10689.
- 133 A. M. Scheer, K. Aflatooni, G. A. Gallup and P. D. Burrow, *Phys. Rev. Lett.*, 2004, **92**, 068102.
- 134 G. H. Patterson, S. M. Knobel, W. D. Sharif, S. R. Kain and D. W. Piston, *Biophys. J.*, 1997, **73**, 2782–2790.
- 135 C. R. S. Mooney, D. A. Horke, A. S. Chatterley, A. Simperler, H. H. Fielding and J. R. Verlet, *Chem. Sci.*, 2013, **4**, 921–927.
- 136 A. Svendsen, H. V. Kiefer, H. B. Pedersen, A. V. Bochenkova and L. H. Andersen, *J. Am. Chem. Soc.*, 2017, **139**, 8766–8771.
- 137 K. H. Bowen and J. G. Eaton, in *The Structure of Small Molecules and Ions*, eds. R. Naaman and Z. Vager, Springer US, Boston, MA, 1988, pp. 147–169.
- 138 J. V. Coe, G. H. Lee, J. G. Eaton, S. T. Arnold, H. W. Sarkas, K. H. Bowen, C. Ludewigt, H. Haberland and D. R. Worsnop, *J. Chem. Phys.*, 1990, **92**, 3980–3982.
- 139 J. Kim, I. Becker, O. Cheshnovsky and M. A. Johnson, *Chem. Phys. Lett.*, 1998, **297**, 90–96.
- 140 N. I. Hammer, J. R. Roscioli and M. A. Johnson, *J. Phys. Chem. A*, 2005, **109**, 7896–7901.
- 141 N. I. Hammer, J.-W. Shin, J. M. Headrick, E. G. Diken, J. R. Roscioli, G. H. Weddle and M. A. Johnson, *Science*, 2004, **306**, 675–679.
- 142 K. R. Asmis, G. Santambrogio, J. Zhou, E. Garand, J. Headrick, D. Goebbert, M. A. Johnson and D. M. Neumark, *J. Chem. Phys.*, 2007, **126**, 191105.
- 143 C.-C. Zho, V. Vlček, D. Neuhauser and B. J. Schwartz, *J. Phys. Chem. Lett.*, 2018, **9**, 5173–5178.
- 144 J. R. R. Verlet, A. E. Bragg, A. Kammrath, O. Cheshnovsky and D. M. Neumark, *Science*, 2005, **307**, 93–96.
- 145 J. V. Coe, S. M. Williams and K. H. Bowen, *Int. Rev. Phys. Chem.*, 2008, **27**, 27–51.
- 146 L. Ma, K. Majer, F. Chirot and B. von Issendorff, *J. Chem. Phys.*, 2009, **131**, 144303.
- 147 K. Majer, L. Ma and B. von Issendorff, *J. Phys. Chem. A*, 2021, **125**, 8426–8433.
- 148 D. Luckhaus, Y. Yamamoto, T. Suzuki and R. Signorell, *Sci. Adv.*, 2017, **3**, e1603224.
- 149 J. Nishitani, Y. Yamamoto, C. W. West, S. Karashima and T. Suzuki, *Sci. Adv.*, 2019, **5**, eaaw6896.
- 150 J. V. Coe, *Int. Rev. Phys. Chem.*, 2001, **20**, 33–58.
- 151 G. Markovich, R. Giniger, M. Levin and O. Cheshnovsky, *J. Chem. Phys.*, 1991, **95**, 9416–9419.
- 152 G. Markovich, S. Pollack, R. Giniger and O. Cheshnovsky, *J. Chem. Phys.*, 1994, **101**, 9344–9353.
- 153 J. V. Coe, *J. Phys. Chem. A*, 1997, **101**, 2055–2063.
- 154 X. Yang, B. Kiran, X.-B. Wang, L.-S. Wang, M. Mucha and P. Jungwirth, *J. Phys. Chem. A*, 2004, **108**, 7820–7826.
- 155 E. Surber, R. Mabbs, T. Habteyes and A. Sanov, *J. Phys. Chem. A*, 2005, **109**, 4452–4458.
- 156 Y. Wang, X. Zhang, S. Lyapustina, M. M. Nilles, S. Xu, J. D. Graham, K. H. Bowen, J. T. Kelly, G. S. Tschumper and N. I. Hammer, *Phys. Chem. Chem. Phys.*, 2015, **18**, 704–712.
- 157 M. Valiev, S. H. M. Deng and X.-B. Wang, *J. Phys. Chem. B*, 2016, **120**, 1518–1525.
- 158 X. Chen and S. E. Bradforth, *Annu. Rev. Phys. Chem.*, 2008, **59**, 203–231.
- 159 D. Serxner, C. E. H. Dessent and M. A. Johnson, *J. Chem. Phys.*, 1996, **105**, 7231–7234.
- 160 L. Lehr, M. T. Zanni, C. Frischkorn, R. Weinkauff and D. M. Neumark, *Science*, 1999, **284**, 635–638.
- 161 A. V. Davis, M. T. Zanni, C. Frischkorn and D. M. Neumark, *J. Electron Spectros. Relat. Phenomena*, 2000, **108**, 203–211.
- 162 A. Kammrath, J. R. R. Verlet, A. E. Bragg, G. B. Griffin and D. M. Neumark, *J. Phys. Chem. A*, 2005, **109**, 11475–11483.
- 163 R. M. Young and D. M. Neumark, *Chem. Rev.*, 2012, **112**, 5553–5577.

- 164 B. Boudaïffa, P. Cloutier, D. Hunting, M. A. Huels and L. Sanche, *Science*, 2000, **287**, 1658–1660.
- 165 I. Baccarelli, I. Bald, F. A. Gianturco, E. Illenberger and J. Kopyra, *Phys. Rep.*, 2011, **508**, 1–44.
- 166 E. Alizadeh, T. M. Orlando and L. Sanche, *Annu. Rev. Phys. Chem.*, 2015, **66**, 379–398.
- 167 Y. Dong, Y. Gao, W. Liu, T. Gao, Y. Zheng and L. Sanche, *J. Phys. Chem. Lett.*, 2019, **10**, 2985–2990.
- 168 Y. Gao, Y. Zheng and L. Sanche, *Int. J. Mol. Sci.*, 2021, **22**, 7879.
- 169 X. Luo, Y. Zheng and L. Sanche, *J. Chem. Phys.*, 2014, **140**, 155101.
- 170 F. Martin, P. D. Burrow, Z. Cai, P. Cloutier, D. Hunting and L. Sanche, *Phys. Rev. Lett.*, 2004, **93**, 068101.
- 171 C. Liu, Y. Zheng and L. Sanche, *Photochem. Photobiol.*, 2022, **98**, 546–563.
- 172 J. Berdys, I. Anusiewicz, P. Skurski and J. Simons, *J. Am. Chem. Soc.*, 2004, **126**, 6441–6447.
- 173 J. Simons, *Acc. Chem. Res.*, 2006, **39**, 772–779.
- 174 K. Aflatooni, G. A. Gallup and P. D. Burrow, *J. Phys. Chem. A*, 1998, **102**, 6205–6207.
- 175 T. Sommerfeld, *J. Phys. Chem. A*, 2004, **108**, 9150–9154.
- 176 H.-Y. Cheng and C.-W. Chen, *J. Phys. Chem. A*, 2011, **115**, 10113–10121.
- 177 I. González-Ramírez, J. Segarra-Martí, L. Serrano-Andrés, M. Merchán, M. Rubio and D. Roca-Sanjuán, *J. Chem. Theory Comput.*, 2012, **8**, 2769–2776.
- 178 H. Abdoul-Carime, S. Gohlke and E. Illenberger, *Phys. Rev. Lett.*, 2004, **92**, 168103.
- 179 P. D. Burrow, G. A. Gallup, A. M. Scheer, S. Denifl, S. Ptasinska, T. Märk and P. Scheier, *J. Chem. Phys.*, 2006, **124**, 124310.
- 180 J. Schiedt, R. Weinkauff, D. M. Neumark and E. W. Schlag, *Chem. Phys.*, 1998, **239**, 511–524.
- 181 S. Eustis, D. Wang, S. Lyapustina and K. H. Bowen, *J. Chem. Phys.*, 2007, **127**, 224309.
- 182 S. B. King, M. A. Yandell and D. M. Neumark, *Faraday Discuss.*, 2013, **163**, 59–72.
- 183 S. B. King, M. A. Yandell, A. B. Stephansen and D. M. Neumark, *J. Chem. Phys.*, 2014, **141**, 224310.
- 184 A. B. Stephansen, S. B. King, Y. Yokoi, Y. Minoshima, W.-L. Li, A. Kunin, T. Takayanagi and D. M. Neumark, *J. Chem. Phys.*, 2015, **143**, 104308.
- 185 A. Kunin, W.-L. Li and D. M. Neumark, *J. Chem. Phys.*, 2018, **149**, 084301.
- 186 A. Kunin, V. S. McGraw, K. G. Lunny and D. M. Neumark, *J. Chem. Phys.*, 2019, **151**, 154304.
- 187 G. M. Roberts, Doctoral, Durham University, 2010.
- 188 J. P. Rogers, C. S. Anstöter, J. N. Bull, B. F. E. Curchod and J. R. R. Verlet, *J. Phys. Chem. A*, 2019, **123**, 1602–1612.
- 189 U. Even, *EPJ Techn. Instrum.*, 2015, **2**, 17.
- 190 W. C. Wiley and I. H. McLaren, *Rev. Sci. Instrum.*, 1955, **26**, 1150–1157.
- 191 A. M. Rijs, E. H. G. Backus, C. A. de Lange, N. P. C. Westwood and M. H. M. Janssen, *J. Electron Spectros. Relat. Phenomena*, 2000, **112**, 151–162.
- 192 I. León, Z. Yang, H.-T. Liu and L.-S. Wang, *Rev. Sci. Instrum.*, 2014, **85**, 083106.
- 193 S. J. Kregel, G. K. Thurston, J. Zhou and E. Garand, *J. Chem. Phys.*, 2017, **147**, 094201.
- 194 G. A. Garcia, L. Nahon and I. Powis, *Rev. Sci. Instrum.*, 2004, **75**, 4989–4996.
- 195 G. M. Roberts, J. L. Nixon, J. Lecointre, E. Wrede and J. R. R. Verlet, *Rev. Sci. Instrum.*, 2009, **80**, 053104.
- 196 B. Dick, *Phys. Chem. Chem. Phys.*, 2013, **16**, 570–580.
- 197 B. Dick, *Phys. Chem. Chem. Phys.*, 2019, **21**, 19499–19512.
- 198 C. Sparling, A. Ruget, J. Leach and D. Townsend, *Rev. Sci. Instrum.*, 2022, **93**, 023303.
- 199 G. A. Cooper, Doctoral, University of Oxford, 2016.
- 200 G. R. Harrison, J. C. Vaughan, B. Hidle and G. M. Laurent, *J. Chem. Phys.*, 2018, **148**, 194101.
- 201 C. W. West, Doctoral, Durham University, 2016.
- 202 L. H. Stanley, Doctoral, Durham University, 2017.
- 203 C. S. Anstöter, Doctoral, Durham University, 2019.
- 204 G. I. Taylor, *Proc. R. Soc. London A*, 1964, **280**, 383–397.
- 205 J. B. Fenn, M. Mann, C. K. Meng, S. F. Wong and C. M. Whitehouse, *Science*, 1989, **246**, 64–71.

- 206 A. S. Chatterley, C. W. West, V. G. Stavros and J. R. R. Verlet, *Chem. Sci.*, 2014, **5**, 3963–3975.
- 207 A. Szabo and N. S. Ostlund, *Modern Quantum Chemistry: Introduction to Advanced Electronic Structure Theory*, Courier Corporation, 2012.
- 208 J. C. Slater, *Phys. Rev.*, 1951, **81**, 385–390.
- 209 D. J. Griffiths and D. F. Schroeter, *Introduction to Quantum Mechanics*, Cambridge University Press, 2018.
- 210 C. David Sherrill and H. F. Schaefer, in *Advances in Quantum Chemistry*, eds. P.-O. Löwdin, J. R. Sabin, M. C. Zerner and E. Brändas, Academic Press, 1999, vol. 34, pp. 143–269.
- 211 Chr. Møller and M. S. Plesset, *Phys. Rev.*, 1934, **46**, 618–622.
- 212 J. Čížek, *J. Chem. Phys.*, 1966, **45**, 4256–4266.
- 213 In *Density Functional Theory*, John Wiley & Sons, Ltd, 2009, pp. 1–33.
- 214 J. P. Perdew, K. Burke and Y. Wang, *Phys. Rev. B*, 1996, **54**, 16533–16539.
- 215 A. D. Becke, *J. Chem. Phys.*, 1993, **98**, 5648–5652.
- 216 P. J. Stephens, F. J. Devlin, C. F. Chabalowski and M. J. Frisch, *J. Phys. Chem.*, 1994, **98**, 11623–11627.
- 217 T. Yanai, D. P. Tew and N. C. Handy, *Chem. Phys. Lett.*, 2004, **393**, 51–57.
- 218 J.-D. Chai and M. Head-Gordon, *Phys. Chem. Chem. Phys.*, 2008, **10**, 6615–6620.
- 219 B. P. Pritchard, D. Altarawy, B. Didier, T. D. Gibson and T. L. Windus, *J. Chem. Inf. Model.*, 2019, **59**, 4814–4820.
- 220 T. H. Dunning Jr., *J. Chem. Phys.*, 1989, **90**, 1007–1023.
- 221 R. A. Kendall, T. H. Dunning Jr. and R. J. Harrison, *J. Chem. Phys.*, 1992, **96**, 6796–6806.
- 222 G. L. Gutsev and L. Adamowicz, *J. Phys. Chem.*, 1995, **99**, 13412–13421.
- 223 P. Skurski, M. Gutowski and J. Simons, *Int. J. Quantum Chem.*, 2000, **80**, 1024–1038.
- 224 K. D. Jordan and F. Wang, *Annu. Rev. Phys. Chem.*, 2003, **54**, 367–396.
- 225 C. S. Anstöter and S. Matsika, *J. Phys. Chem. A*, 2020, **124**, 9237–9243.
- 226 G. Thiam and F. Rabilloud, *J. Chem. Theory Comput.*, 2023, **19**, 2842–2849.
- 227 A. Lietard, J. R. R. Verlet, S. Slimak and K. D. Jordan, *J. Phys. Chem. A*, 2021, **125**, 7004–7013.
- 228 T. Jagau, *Nachr. Chem.*, 2020, **68**, 50–54.
- 229 T.-C. Jagau, *Chem. Commun.*, 2022, **58**, 5205–5224.
- 230 A. U. Hazi and H. S. Taylor, *Phys. Rev. A*, 1970, **1**, 1109–1120.
- 231 B. J. Carlson, M. F. Falcetta, S. R. Slimak and K. D. Jordan, *J. Phys. Chem. Lett.*, 2021, **12**, 1202–1206.
- 232 A. Dreuw and M. Head-Gordon, *Chem. Rev.*, 2005, **105**, 4009–4037.
- 233 A. Lange and J. M. Herbert, *J. Chem. Theory Comput.*, 2007, **3**, 1680–1690.
- 234 C. J. Clarke, J. A. Gibbard, L. Hutton, J. R. R. Verlet and B. F. E. Curchod, *Nat. Commun.*, 2022, **13**, 937.
- 235 R. Atkinson and J. Arey, *Chem. Rev.*, 2003, **103**, 4605–4638.
- 236 J. J. Orlando, G. S. Tyndall and T. J. Wallington, *Chem. Rev.*, 2003, **103**, 4657–4690.
- 237 A. Hirsikko, T. Nieminen, S. Gagné, K. Lehtipalo, H. E. Manninen, M. Ehn, U. Hörrak, V.-M. Kerminen, L. Laakso, P. H. McMurry, A. Mirme, S. Mirme, T. Petäjä, H. Tammet, V. Vakkari, M. Vana and M. Kulmala, *Atmos. Chem. Phys.*, 2011, **11**, 767–798.
- 238 C. E. Lund Myhre and C. J. Nielsen, *Atmos. Chem. Phys.*, 2004, **4**, 1759–1769.
- 239 P. G. Eger, J. Schuladen, N. Sobanski, H. Fischer, E. Karu, J. Williams, M. Riva, Q. Zha, M. Ehn, L. L. J. Quéléver, S. Schallhart, J. Lelieveld and J. N. Crowley, *Atmos. Chem. Phys.*, 2020, **20**, 3697–3711.
- 240 A. E. Reed Harris, B. Ervens, R. K. Shoemaker, J. A. Kroll, R. J. Rapf, E. C. Griffith, A. Monod and V. Vaida, *J. Phys. Chem. A*, 2014, **118**, 8505–8516.
- 241 A. E. Reed Harris, M. Cazaunau, A. Gratien, E. Pangui, J.-F. Doussin and V. Vaida, *J. Phys. Chem. A*, 2017, **121**, 8348–8358.
- 242 K. J. Kappes, A. M. Deal, M. F. Jepsen, S. L. Blair, J.-F. Doussin, M. Cazaunau, E. Pangui, B. N. Hopper, M. S. Johnson and V. Vaida, *J. Phys. Chem. A*, 2021, **125**, 1036–1049.
- 243 E. C. Griffith, B. K. Carpenter, R. K. Shoemaker and V. Vaida, *Proc. Natl. Acad. Sci.*, 2013, **110**, 11714–11719.

- 244 S. Yamamoto and R. A. Back, *Can. J. Chem.*, 1985, **63**, 549–554.
- 245 P. R. Schreiner, H. P. Reisenauer, D. Ley, D. Gerbig, C.-H. Wu and W. D. Allen, *Science*, 2011, **332**, 1300–1303.
- 246 X.-P. Chang, Q. Fang and G. Cui, *J. Chem. Phys.*, 2014, **141**, 154311.
- 247 A. E. Reed Harris, J.-F. Doussin, B. K. Carpenter and V. Vaida, *J. Phys. Chem. A*, 2016, **120**, 10123–10133.
- 248 B. R. Samanta, R. Fernando, D. Rösch, H. Reisler and D. L. Osborn, *Phys. Chem. Chem. Phys.*, 2021, **23**, 4107–4119.
- 249 E. C. Griffith, R. K. Shoemaker and V. Vaida, *Orig. Life Evol. Biosph.*, 2013, **43**, 341–352.
- 250 M. Fischer and P. Warneck, *Ber. Bunsenges. Phys. Chem.*, 1991, **95**, 523–527.
- 251 I. Khan, P. Brimblecombe and S. L. Clegg, *J. Atmos. Chem.*, 1995, **22**, 285–302.
- 252 D. A. Horke, G. M. Roberts, J. Lecointre and J. R. R. Verlet, *Rev. Sci. Instrum.*, 2012, **83**, 063101.
- 253 K. A. Peterson, D. E. Woon and T. H. Dunning, *J. Chem. Phys.*, 1994, **100**, 7410–7415.
- 254 T. B. Adler, G. Knizia and H.-J. Werner, *J. Chem. Phys.*, 2007, **127**, 221106.
- 255 M. Frisch, G. Trucks, H. Schlegel, G. Scuseria, M. Robb, J. Cheeseman, G. Scalmani, V. Barone, B. Mennucci, G. Petersson, and others, *See also: <http://www.gaussian.com>*.
- 256 H.-J. Werner, P. J. Knowles, G. Knizia, F. R. Manby and M. Schütz, *Wiley Interdiscip. Rev. Comput. Mol. Sci.*, 2012, **2**, 242–253.
- 257 M. Barbatti, M. Ruckebauer, F. Plasser, J. Pittner, G. Granucci, M. Persico and H. Lischka, *Wiley Interdiscip. Rev. Comput. Mol. Sci.*, 2014, **4**, 26–33.
- 258 F. Furche, R. Ahlrichs, C. Hättig, W. Klopper, M. Sierka and F. Weigend, *Wiley Interdiscip. Rev. Comput. Mol. Sci.*, 2014, **4**, 91–100.
- 259 M. R. Nimlos, J. A. Soderquist and G. B. Ellison, *J. Am. Chem. Soc.*, 1989, **111**, 7675–7681.
- 260 A. M. Oliveira, Y.-J. Lu, J. H. Lehman, P. B. Changala, J. H. Baraban, J. F. Stanton and W. C. Lineberger, *J. Am. Chem. Soc.*, 2015, **137**, 12939–12945.
- 261 V. Vuitton, P. Lavvas, R. V. Yelle, M. Galand, A. Wellbrock, G. R. Lewis, A. J. Coates and J.-E. Wahlund, *Planet. Space Sci.*, 2009, **57**, 1558–1572.
- 262 W. R. Stockwell, C. V. Lawson, E. Saunders and W. S. Goliff, *Atmosphere*, 2012, **3**, 1–32.
- 263 L. Campbell and M. J. Brunger, *Int. Rev. Phys. Chem.*, 2016, **35**, 297–351.
- 264 O. Ingólfsson, *Low-Energy Electrons: Fundamentals and Applications*, CRC Press, 2019.
- 265 A. J. Eugene, E. A. Pillar-Little, A. J. Colussi and M. I. Guzman, *Langmuir*, 2018, **34**, 9307–9313.
- 266 W. Cao, Z. Hu, X. Peng, H. Sun, Z. Sun and X.-B. Wang, *J. Am. Chem. Soc.*, 2022, **144**, 19317–19325.
- 267 R. J. Rapf, M. R. Dooley, K. Kappes, R. J. Perkins and V. Vaida, *J. Phys. Chem. A*, 2017, **121**, 8368–8379.
- 268 C. J. Clarke, E. M. Burrow and J. R. R. Verlet, *Phys. Chem. Chem. Phys.*, 2024, **26**, 20037–20045.
- 269 J. Gu, Y. Xie and H. F. Schaefer, *J. Am. Chem. Soc.*, 2006, **128**, 1250–1252.
- 270 J. Gu, J. Leszczynski and H. F. I. Schaefer, *Chem. Rev.*, 2012, **112**, 5603–5640.
- 271 J. H. Hendricks, S. A. Lyapustina, H. L. de Clercq, J. T. Snodgrass and K. H. Bowen, *J. Chem. Phys.*, 1996, **104**, 7788–7791.
- 272 C. Desfrancois, H. Abdoul-Carime and J. P. Schermann, *J. Chem. Phys.*, 1996, **104**, 7792–7794.
- 273 T. Sommerfeld, *J. Phys.: Conf. Ser.*, 2005, **4**, 245.
- 274 J. N. Bull, C. S. Anstöter and J. R. R. Verlet, *Nat. Commun.*, 2019, **10**, 5820.
- 275 G. Liu, S. M. Ciburowski, J. D. Graham, A. M. Buytendyk and K. H. Bowen, *J. Chem. Phys.*, 2020, **153**, 044307.
- 276 J. R. R. Verlet, C. S. Anstöter, J. N. Bull and J. P. Rogers, *J. Phys. Chem. A*, 2020, **124**, 3507–3519.
- 277 C. J. Clarke and J. R. R. Verlet, *Annu. Rev. Phys. Chem.*, 2024, **75**, 89–110.
- 278 C. Desfrancois, V. Periquet, Y. Bouteiller and J. P. Schermann, *J. Phys. Chem. A*, 1998, **102**, 1274–1278.
- 279 A. O. Colson, B. Besler, D. M. Close and M. D. Sevilla, *J. Phys. Chem.*, 1992, **96**, 661–668.
- 280 M. D. Sevilla, B. Besler and A.-O. Colson, *J. Phys. Chem.*, 1995, **99**, 1060–1063.

- 281 R. A. Bachorz, J. Rak and M. Gutowski, *Phys. Chem. Chem. Phys.*, 2005, **7**, 2116–2125.
- 282 P. Dedíková, L. Demovič, M. Pitoňák, P. Neogrady and M. Urban, *Chem. Phys. Lett.*, 2009, **481**, 107–111.
- 283 H. Motegi and T. Takayanagi, *J. Mol. Structure: THEOCHEM*, 2009, **907**, 85–92.
- 284 N. Russo, M. Toscano and A. Grand, *J. Comput. Chem.*, 2000, **21**, 1243–1250.
- 285 S. D. Wetmore, R. J. Boyd and L. A. Eriksson, *Chem. Phys. Lett.*, 2000, **322**, 129–135.
- 286 N. J. Saettel and O. Wiest, *J. Am. Chem. Soc.*, 2001, **123**, 2693–2694.
- 287 S. S. Wesolowski, M. L. Leininger, P. N. Pentchev and H. F. Schaefer, *J. Am. Chem. Soc.*, 2001, **123**, 4023–4028.
- 288 R. A. Bachorz, W. Klopper and M. Gutowski, *J. Chem. Phys.*, 2007, **126**, 085101.
- 289 D. Roca-Sanjuán, M. Merchán, L. Serrano-Andrés and M. Rubio, *J. Chem. Phys.*, 2008, **129**, 095104.
- 290 J. M. L. Martin and G. de Oliveira, *J. Chem. Phys.*, 1999, **111**, 1843–1856.
- 291 J. Gu, Y. Xie and H. F. Schaefer, *J. Chem. Theory Comput.*, 2014, **10**, 609–612.
- 292 I. Anusiewicz, P. Skurski and J. Simons, *J. Phys. Chem. A*, 2020, **124**, 2064–2076.
- 293 J. H. Hendricks, S. A. Lyapustina, H. L. de Clercq and K. H. Bowen, *J. Chem. Phys.*, 1998, **108**, 8–11.
- 294 D. Hanstorp and M. Gustafsson, *J. Phys. B: At. Mol. Opt. Phys.*, 1992, **25**, 1773.
- 295 J. E. Sansonetti and W. C. Martin, *J. Phys. Chem. Ref. Data*, 2005, **34**, 1559–2259.
- 296 M. J. Frisch et al., Gaussian 16, Revision C.01 Gaussian, Inc., Wallingford CT 2016.
- 297 R. N. Zare, *Mol. Photochem.*, 1972, **4**, 1–37.
- 298 J. Simons, *J. Phys. Chem. A*, 2020, **124**, 8778–8797.
- 299 S. T. Arnold, J. H. Hendricks and K. H. Bowen, *J. Chem. Phys.*, 1995, **102**, 39–47.
- 300 J. H. Hendricks, H. L. de Clercq, C. B. Freidhoff, S. T. Arnold, J. G. Eaton, C. Fancher, S. A. Lyapustina, J. T. Snodgrass and K. H. Bowen, *J. Chem. Phys.*, 2002, **116**, 7926–7938.
- 301 T. Lenzer, I. Yourshaw, M. R. Furlanetto, N. L. Pivonka and D. M. Neumark, *J. Chem. Phys.*, 2001, **115**, 3578–3589.
- 302 I. Yourshaw, Y. Zhao and D. M. Neumark, *J. Chem. Phys.*, 1996, **105**, 351–373.
- 303 K. R. Asmis, T. R. Taylor, C. Xu and D. M. Neumark, *J. Chem. Phys.*, 1998, **109**, 4389–4395.
- 304 J. K. Song, N. K. Lee and S. K. Kim, *J. Chem. Phys.*, 2002, **117**, 1589–1594.
- 305 T. N. Olney, N. M. Cann, G. Cooper and C. E. Brion, *Chem. Phys.*, 1997, **223**, 59–98.
- 306 A. Halkier, S. Coriani and P. Jørgensen, *Chem. Phys. Lett.*, 1998, **294**, 292–296.
- 307 G. A. Cooper, C. J. Clarke and J. R. R. Verlet, *J. Am. Chem. Soc.*, 2023, **145**, 1319–1326.
- 308 Y. Yokoi, K. Kano, Y. Minoshima and T. Takayanagi, *Comput. Theor. Chem.*, 2014, **1046**, 99–106.
- 309 V. Periquet, A. Moreau, S. Carles, J. P. Schermann and C. Desfrancois, *J. Electron Spectros. Relat. Phenomena*, 2000, **106**, 141–151.
- 310 M. Kobyłecka, J. Leszczynski and J. Rak, *J. Am. Chem. Soc.*, 2008, **130**, 15683–15687.
- 311 G. A. Cooper, C. J. Clarke and J. R. R. Verlet, *J. Phys. B: At. Mol. Opt. Phys.*, 2023, **56**, 185102.
- 312 J. Cadet, T. Delatour, T. Douki, D. Gasparutto, J.-P. Pouget, J.-L. Ravanat and S. Sauvaigo, *Mutat. Res.*, 1999, **424**, 9–21.
- 313 S. M. Pimblott and J. A. LaVerne, *Rad. Phys. Chem.*, 2007, **76**, 1244–1247.
- 314 S. Kouass Sahbani, P. Cloutier, A. D. Bass, D. J. Hunting and L. Sanche, *J. Phys. Chem. Lett.*, 2015, **6**, 3911–3914.
- 315 Y. Zheng and L. Sanche, *Rev. Nanosci. Nanotechnol.*, 2013, **2**, 1–28.
- 316 A. Kumar, D. Becker, A. Adhikary and M. D. Sevilla, *Int. J. Mol. Sci.*, 2019, **20**, 3998.
- 317 M. Théodore, M. Sobczyk and J. Simons, *Chem. Phys.*, 2006, **329**, 139–147.
- 318 J. Kočišek, A. Pysanenko, M. Fárník and J. Fedor, *J. Phys. Chem. Lett.*, 2016, **7**, 3401–3405.
- 319 S. Denifl, S. Ptasińska, G. Hanel, B. Gstir, M. Probst, P. Scheier and T. D. Märk, *J. Chem. Phys.*, 2004, **120**, 6557–6565.
- 320 S. Denifl, S. Ptasińska, G. Hanel, B. Gstir, P. Scheier, M. Probst, B. Farizon, M. Farizon, S. Matejcik, E. Illenberger and T. D. Märk, *Phys. Scr.*, 2004, **2004**, 252.
- 321 S. Ptasińska, S. Denifl, B. Mróz, M. Probst, V. Grill, E. Illenberger, P. Scheier and T. D. Märk, *J. Chem. Phys.*, 2005, **123**, 124302.

- 322 R. Abouaf and H. Dunet, *Eur. Phys. J. D*, 2005, **35**, 405–410.
- 323 P. D. Burrow, A. E. Howard, A. R. Johnston and K. D. Jordan, *J. Phys. Chem.*, 1992, **96**, 7570–7578.
- 324 R. A. Marcus, *J. Chem. Phys.*, 1956, **24**, 966–978.
- 325 G. Makov and A. Nitzan, *J. Phys. Chem.*, 1994, **98**, 3459–3466.
- 326 A. F. Fucaloro, K. Dewey, G. Fan, K. Imuta, D. Jensen and M. Muranaka, *J. Solution Chem.*, 2008, **37**, 1289–1304.
- 327 A. R. Lowe, J. S. Cox and P. R. Tremaine, *J. Chem. Thermodyn.*, 2017, **112**, 129–145.
- 328 M. Mukherjee, D. Tripathi, M. Brehm, C. Riplinger and A. K. Dutta, *J. Chem. Theory Comput.*, 2021, **17**, 105–116.
- 329 H. J. Bakker, Y. L. A. Rezus and R. L. A. Timmer, *J. Phys. Chem. A*, 2008, **112**, 11523–11534.
- 330 C. S. Anstöter, M. DelloStritto, M. L. Klein and S. Matsika, *J. Phys. Chem. A*, 2021, **125**, 6995–7003.
- 331 J. Ma, F. Wang, S. A. Denisov, A. Adhikary and M. Mostafavi, *Sci. Adv.*, 2017, **3**, e1701669.
- 332 C. S. Anstöter and S. Matsika, *J. Phys. Chem. A*, 2020, **124**, 9237–9243.
- 333 A. Sieradzka and J. D. Gorfinkiel, *J. Chem. Phys.*, 2017, **147**, 034302.
- 334 A. Sieradzka and J. D. Gorfinkiel, *J. Chem. Phys.*, 2017, **147**, 034303.
- 335 P. Verma, D. Ghosh and A. K. Dutta, *J. Phys. Chem. A*, 2021, **125**, 4683–4694.
- 336 F. Kossoski, J. Kopyra and M. T. D. N. Varella, *Phys. Chem. Chem. Phys.*, 2015, **17**, 28958–28965.
- 337 C. Fonseca Guerra, F. M. Bickelhaupt, S. Saha and F. Wang, *J. Phys. Chem. A*, 2006, **110**, 4012–4020.
- 338 M. T. Chenon, R. J. Pugmire, D. M. Grant, R. P. Panzica and L. B. Townsend, *J. Am. Chem. Soc.*, 1975, **97**, 4636–4642.
- 339 A. Laxer, D. T. Major, H. E. Gottlieb and B. Fischer, *J. Org. Chem.*, 2001, **66**, 5463–5481.
- 340 T. G. Burova, V. V. Ermolenkov, G. N. Ten, R. S. Shcherbakov, V. I. Baranov and I. K. Lednev, *J. Phys. Chem. A*, 2011, **115**, 10600–10609.
- 341 M. Hanus, M. Kabeláč, J. Rejnek, F. Ryjáček and P. Hobza, *J. Phys. Chem. B*, 2004, **108**, 2087–2097.
- 342 H.-S. Kim, D.-S. Ahn, S.-Y. Chung, S. K. Kim and S. Lee, *J. Phys. Chem. A*, 2007, **111**, 8007–8012.
- 343 M. A. Fennimore and S. Matsika, *J. Phys. Chem. A*, 2018, **122**, 4048–4057.
- 344 A. Abo-riziq, B. O. Crews, I. Compagnon, J. Oomens, G. Meijer, G. Von Helden, M. Kabeláč, P. Hobza and M. S. de Vries, *J. Phys. Chem. A*, 2007, **111**, 7529–7536.
- 345 S. T. Stokes, X. Li, A. Grubisic, Y. J. Ko and K. H. Bowen, *J. Chem. Phys.*, 2007, **127**, 084321.
- 346 M. Staniforth and V. G. Stavros, *Proc. R. Soc. London A*, 2013, **469**, 20130458.
- 347 J. Gu, J. Wang and J. Leszczynski, *Nucleic Acids Res.*, 2010, **38**, 5280–5290.
- 348 M. A. Cordiner and P. J. Sarre, *A&A*, 2007, **472**, 537–545.
- 349 V. K. Voora and K. D. Jordan, *J. Phys. Chem. A*, 2014, **118**, 7201–7205.
- 350 M. Elena Castellani, C. S. Anstöter and J. R. R. Verlet, *Phys. Chem. Chem. Phys.*, 2019, **21**, 24286–24290.
- 351 A. M. Buytendyk, A. M. Buonaugurio, S.-J. Xu, J. M. Nilles, K. H. Bowen, N. Kirnosov and L. Adamowicz, *J. Chem. Phys.*, 2016, **145**, 024301.
- 352 O. Crawford and A. Dalgarno, *Chem. Phys. Lett.*, 1967, **1**, 23.
- 353 C.-H. Qian, G.-Z. Zhu and L.-S. Wang, *J. Phys. Chem. Lett.*, 2019, **10**, 6472–6477.
- 354 S. Xu, J. M. Nilles and K. H. Bowen Jr., *J. Chem. Phys.*, 2003, **119**, 10696–10701.
- 355 J. Lan, M. Chergui and A. Pasquarello, *Nat. Commun.*, 2024, **15**, 2544.
- 356 B. C. Garrett, D. A. Dixon, D. M. Camaioni, D. M. Chipman, M. A. Johnson, C. D. Jonah, G. A. Kimmel, J. H. Miller, T. N. Rescigno, P. J. Rossky, S. S. Xantheas, S. D. Colson, A. H. Laufer, D. Ray, P. F. Barbara, D. M. Bartels, K. H. Becker, K. H. Jr. Bowen, S. E. Bradforth, I. Carmichael, J. V. Coe, L. R. Corrales, J. P. Cowin, M. Dupuis, K. B. Eisenthal, J. A. Franz, M. S. Gutowski, K. D. Jordan, B. D. Kay, J. A. LaVerne, S. V. Lymar, T. E. Madey, C. W. McCurdy, D. Meisel, S. Mukamel, A. R. Nilsson, T. M. Orlando, N. G. Petrik, S. M. Pimblott, J. R. Rustad, G. K. Schenter, S. J. Singer, A. Tokmakoff, L.-S. Wang and T. S. Zwier, *Chem. Rev.*, 2005, **105**, 355–390.

- 357 J. M. Herbert and M. P. Coons, *Annu. Rev. Phys. Chem.*, 2017, **68**, 447–472.
- 358 A. Staib and D. Borgis, *J. Chem. Phys.*, 1996, **104**, 9027–9039.
- 359 W.-S. Sheu and P. J. Rossky, *J. Phys. Chem.*, 1996, **100**, 1295–1302.
- 360 K. Raghavachari, G. W. Trucks, J. A. Pople and M. Head-Gordon, *Chem. Phys. Lett.*, 1989, **157**, 479–483.
- 361 R. J. Bartlett, J. D. Watts, S. A. Kucharski and J. Noga, *Chem. Phys. Lett.*, 1990, **165**, 513–522.
- 362 A. W. Castleman and K. H. Bowen, *J. Phys. Chem.*, 1996, **100**, 12911–12944.
- 363 J.-W. Shin, N. I. Hammer, J. M. Headrick and M. A. Johnson, *Chem. Phys. Lett.*, 2004, **399**, 349–353.
- 364 A. Lietard and J. R. R. Verlet, *J. Phys. Chem. Lett.*, 2019, **10**, 1180–1184.
- 365 C. G. Bailey, C. E. H. Dessent, M. A. Johnson and K. H. Bowen, *J. Chem. Phys.*, 1996, **104**, 6976–6983.
- 366 M. Sindelka, V. Spirko, P. Jungwirth, F. Wang, S. Mahalakshmi and K. D. Jordan, *J. Chem. Phys.*, 2004, **121**, 1824–1829.
- 367 S. Slimak and K. D. Jordan, *J. Phys. Chem. Lett.*, 2022, **13**, 10331–10334.
- 368 P. Ayotte and M. A. Johnson, *J. Chem. Phys.*, 1997, **106**, 811–814.
- 369 R. A. Marcus, *Annu. Rev. Phys. Chem.*, 1964, **15**, 155–196.